# Geological Fieldwork 2018

## A Summary of Field Activities and Current Research

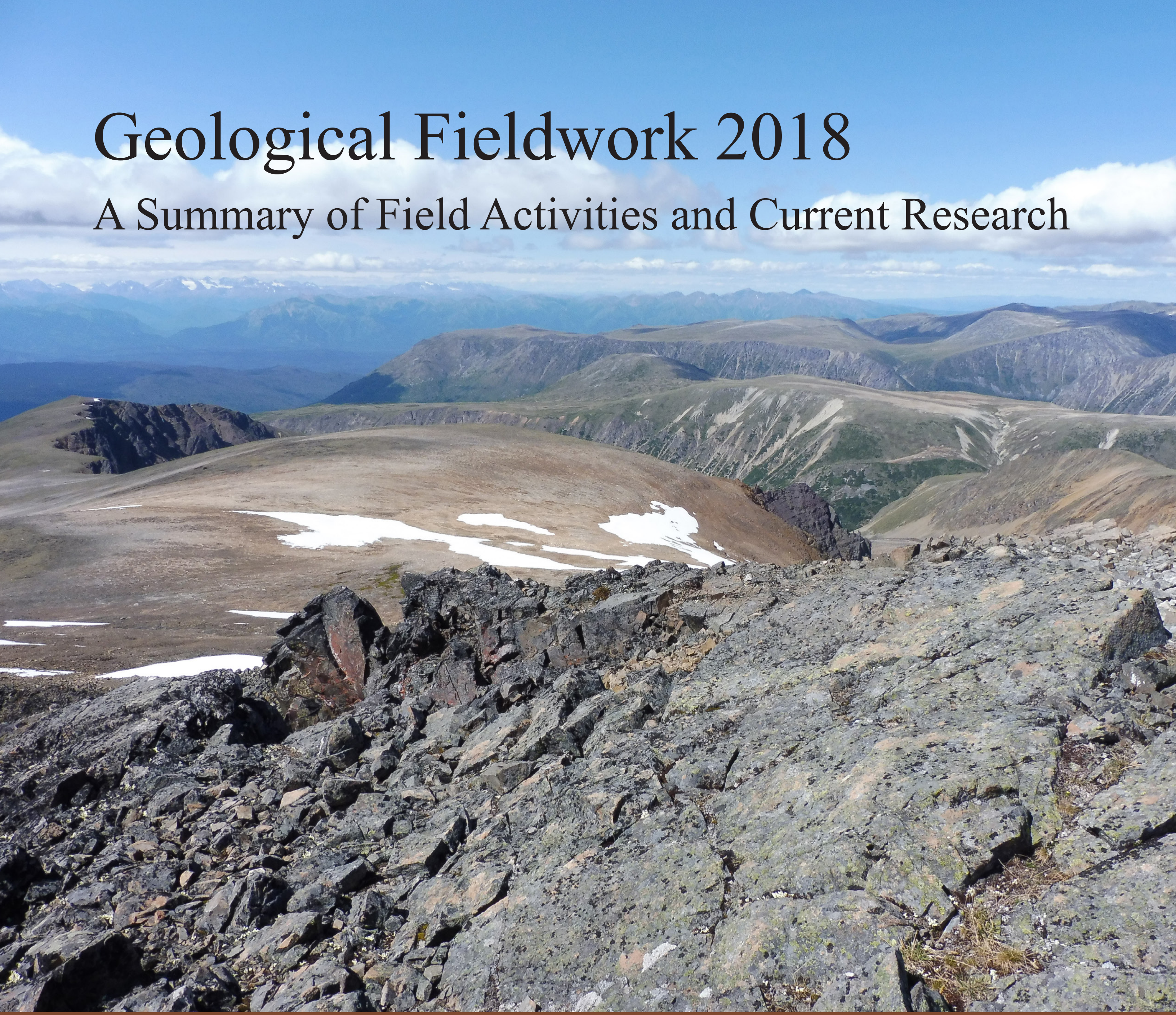

BRITISH COLUMBIA

Ministry of
Energy, Mines and
Petroleum Resources

BRITISH COLUMBIA GEOLOGICAL SURVEY

Ministry of Energy, Mines and Petroleum Resources
British Columbia Geological Survey
Paper 2019-01

Ministry of Energy, Mines and Petroleum Resources

# Geological Fieldwork 2018

## A Summary of Field Activities and Current Research


Ministry of Energy, Mines and Petroleum Resources
British Columbia Geological Survey

Paper 2019-01

# Ministry of Energy, Mines and Petroleum Resources
# Mines and Mineral Resources Division
# British Columbia Geological Survey

Recommended citation format for individual papers:

Milidragovic, D., and Grundy, R., 2019. Geochemistry and petrology of rocks in the Decar area, central British Columbia: Petrologically constrained subdivision of the Cache Creek complex. In: Geological Fieldwork 2018, British Columbia Ministry of Energy, Mines and Petroleum Resources, British Columbia Geological Survey Paper 2019-01, pp. 55-77.

**Front Cover:** Gently dipping dark grey to maroon interstratified lava flows, tuff, lapilli-tuff, lapillistone, and volcanic breccia likely correlative with the Horn Mountain Formation (late Early-Middle Jurassic, foreground) unconformably overlie the Nightout pluton (Late Triassic, background). View to the northwest from Mount Walter, near Yehiniko Lake.
See van Straaten, B.I., and Wearmouth, C., 2019. Geology of the Latham and Pallen Creek area, northwestern British Columbia: Distinguishing the Tsaybahe group, Stuhini Group, and Hazelton Group, and the onset of Triassic arc volcanism in northern Stikinia, this volume. **Photo by Bram van Straaten.**

**Back Cover:** Northern Hogem batholith area, looking east. Bedrock exposures are diorite to monzodiorite of the Thane Creek suite. Mountains, valleys, and tarn are unnamed.
See Ootes, L., Bergen, A., Milidragovic, D., Graham, B., and Simmonds, R., 2019. Preliminary geology of northern Hogem batholith, Quesnel terrane, north-central British Columbia, this volume. **Photo by Reid Simmonds.**

This publication is available, free of charge, from the British Columbia Geological Survey website:
https://www2.gov.bc.ca/gov/content/industry/mineral-exploration-mining/british-columbia-geological-survey/publications

**British Columbia Cataloguing in Publication Data**

Main entry under title:

Geological Fieldwork: - 1974 -

Annual.

Issuing body varies

Vols. for 1978-1996 issued in series: Paper / British Columbia. Ministry of Energy, Mines and Petroleum Resources; vols. for 1997 - 1998, Paper / British Columbia. Ministry of Employment and Investment; vols. for 1999-2004, Paper / British Columbia. Ministry of Energy and Mines; vols. for 2005-2009, Paper / British Columbia. Ministry of Energy, Mines and Petroleum Resources; vols. for 2010, Paper / British Columbia. Ministry of Forests, Mines and Lands; vols. for 2011, Paper / British Columbia. Ministry of Energy and Mines; vols. for 2012- , Paper / British Columbia. Ministry of Energy, Mines and Natural Gas; vols. for 2014- , Paper / British Columbia. Ministry of Energy and Mines.

Includes Bibliographical references.

ISSN 0381-243X=Geological Fieldwork

1. Geology - British Columbia - Periodicals. 2. Mines and mineral resources - British Columbia - Periodicals. 3. Geology - Fieldwork - Periodicals. 4. Geology, Economic - British Columbia - Periodicals. 5. British Columbia. Geological Survey Branch - Periodicals. I. British Columbia. Geological Division. II. British Columbia. Geological Survey Branch. III. British Columbia. Geological Survey Branch. IV. British Columbia. Dept. of Mines and Petroleum Resources. V. British Columbia. Ministry of Energy, Mines and Petroleum Resources. VI. British Columbia. Ministry of Employment and Investment. VII. British Columbia Ministry of Energy and Mines. VIII. Series: Paper (British Columbia. Ministry of Energy, Mines and Petroleum Resources). IX. Series: Paper (British Columbia. Ministry of Employment and Investment). X. Series: Paper (British Columbia Ministry of Energy and Mines). XI. Series: Paper (British Columbia Ministry of Energy, Mines and Petroleum Resources). XII. Series: Paper (British Columbia Ministry of Forests, Mines and Lands). XIII. Series: Paper (British Columbia Ministry of Energy and Mines). XIV. Series: Paper (British Columbia Ministry of Energy, Mines and Natural Gas). XV. Series: Paper (British Columbia Ministry of Energy and Mines).

QE187.46 622.1’09711 C76-083084-3 (Rev.)

Victoria
British Columbia
Canada

January 2019

# Preface

## Geological Fieldwork 2018

This, the 44th edition of **Geological Fieldwork,** is a volume of peer-reviewed papers that presents the results of geoscience research conducted by the **British Columbia Geological Survey** (BCGS) and its partners. This volume is one of three that the Survey publishes each January and is accompanied by the **Provincial Overview of Exploration and Mining in British Columbia** and the **Coal Industry Overview**. In addition to these annual publications, the Survey regularly releases Open Files, GeoFiles, Geoscience Maps, Papers, and databases, all of which are freely accessed through the recently updated BCGS website and through MapPlace, our database-driven geospatial web service.

The papers in Geological Fieldwork 2018 address a variety of geological inquires, highlighting both regional mapping and more thematic studies. Schiarizza's contribution is the latest in a series that examines the geological architecture of the Nicola Group (Triassic) in central British Columbia. From work in the north-central part of the province, Ootes et al. present the initial results from the first year of a four-year mapping program that addresses the geological evolution of the Hogem batholith and related mineral deposits, and Milidragovic and Grundy consider the geochemistry and petrology of the Trembleur ultramafite, host to the Decar nickel-iron awaruite deposit. In northwest British Columbia, van Straaten and Wearmouth continued recent Survey mapping of volcano-sedimentary successions and related intrusions of northern Stikinia near Dease Lake, and Mihalynuk et al. present geochronological data from the Granduc and Rock and Roll volcanogenic massive sulphide (VMS) deposits. Simandl et al. describe the occurrence of fersmite, a mineral rich in niobium, thorium, and rare earth elements, at the Mount Brussiloff magnesite deposit in the southeastern part of the province. The final paper in the volume, by Han et al., details the data model used at the BCGS to streamline data set handling, from compilation to product generation.

Conferences are another way that the Survey distributes the results of ongoing studies. In 2018, BCGS contributed technical presentations at annual regional meetings such as Rock Talks (Smithers), Kamloops Exploration Group (KEG; Kamloops), Minerals South (Trail) and the American Exploration and Mining Association (Spokane). The Survey continues to contribute to the technical program of the Association of Mineral Exploration's (AME) Roundup (Vancouver), organizing two technical sessions and providing technical content through presentations and posters. The Survey coordinates the Ministry presence at both Roundup and the Prospectors and Developers Association of Canada (Toronto) meetings. Unique in 2018, the BCGS was a technical partner in the Resources for Future Generations 2018 (RFG 2018), and interim International Union of Geological Sciences (IUGS) convention held in Vancouver in June. RFG was a joint meeting of IUGS, the Canadian Federation of Earth Sciences (CFES), the Canadian Institute of Mining, Metallurgy and Petroleum (CIM), the Geological Association of Canada (GAC) and the Mineralogical Association of Canada (MAC). A number of staff were on the organizing committee, presented talks, or ran field trips. BCGS also hosted its annual Open House in Victoria in November.

The Survey continues to invest in streamlining digital data collection in the field and integration into provincial datasets. The BCGS has adopted an in-house digital database that works with inexpensive software on low-cost generic tablets, enabling geologists to digitally capture data in the field while using other datasets such as geophysics and satellite imagery. Also developed in-house, the BCGS data framework model enables maps to be more efficiently integrated into the provincial geology as well as meet internationally accepted data standards.

In the last few years, the Survey has seen significant renewal by filling several vacancies. In February, former Chief Geologist and Executive Director Dr. Stephen Rowins left BCGS and assumed the role of director and professor at the Centre for Exploration Targeting at University of Western Australia. Dr. Adrian Hickin, former Director of the Cordilleran Geoscience Section, was selected as Steve's replacement and has been appointed Chief Geologist.

Adrian S. Hickin
Chief Geologist and Executive Director
British Columbia Geological Survey

# Table of Contents

# British Columbia Geological Survey annual program review 2018-2019

Filippo Ferri[1, a], Larry D. Jones[1], Gordon Clarke[2], and Adrian S. Hickin[1]

[1] British Columbia Geological Survey, Ministry of Energy, Mines and Petroleum Resources, Victoria, BC, V8W 9N3
[2] British Columbia Geological Survey, Ministry of Energy, Mines and Petroleum Resources, Vancouver, BC, V6Z 2G3
[a] corresponding author: Fil.Ferri@gov.bc.ca

Recommended citation: Ferri, F., Jones, L.D., Clarke, G., and Hickin, A.S., 2019. British Columbia Geological Survey annual program review 2018-2019. In: Geological Fieldwork 2018, Ministry of Energy, Mines and Petroleum Resources, British Columbia Geological Survey Paper 2019-01, pp. 1-14.

## 1. Introduction

Founded in 1895, the British Columbia Geological Survey (BCGS) is the oldest scientific agency in the province. The Survey conducts research to establish the geological evolution and mineral resources of the province. Drawing on continuously advancing concepts and technologies, the Survey creates knowledge to guide societal decisions centred on the Earth sciences, connecting government, the minerals industry, and communities to the province's geology and mineral resources. The information provided by the Survey is used for effective mineral exploration, sound land use management, and responsible governance. This information benefits decisions that balance the economy, the environment, and community interests. Survey activities serve government, the general public, First Nations, local communities, the minerals industry, public safety agencies, environmental scientists, and other research organizations. The Survey strives to be a leader in public government geoscience, providing geological and geomorphological information through reports, maps, and databases (Fig. 1), which can be freely accessed online. This paper highlights the activities of the Survey in 2018.

The BCGS is part of the Mines and Minerals Resource Division in the British Columbia Ministry of Energy, Mines and Petroleum Resources. Headquartered in Victoria, the Survey also operates a satellite office in Vancouver focussed on the exploration and mining industry (Mineral Development Office or MDO). Staffed by 28 people, the BCGS consists of three sections: 1) Cordilleran Geoscience; 2) Resource Information and 3) the Mineral Development Office (Fig. 2). The Cordilleran Geoscience Section delivers new geoscience, primarily through field-based bedrock and surficial geology mapping projects, regional geochemical surveys, and targeted mineral deposit studies. It also manages the Survey's laboratory and curates the provincial sample archive. The Resource Information Section is responsible for maintaining and developing geoscience databases and disseminating these data online through MapPlace 2, our geospatial web service. The Resource Information Section is also responsible for collecting, evaluating, approving, and archiving assessment reports submitted by the exploration and mining industry in order to maintain titles in good standing. As the steward of mineral and coal resources in the province, the Survey has an important role in stimulating activity, attracting investment, and providing continuous research based on a corporate memory that extends back more than 125 years. The Mineral Development Office provides investment intelligence to government and global business, connecting the national and international investment community to the Survey and to the province's mineral resources. It also produces the annual Provincial Overview of Exploration and Mining in British Columbia (e.g., British Columbia Geological Survey, 2019; Clarke et al., 2019).

The BCGS continues to evolve with several staff changes. Chief Geologist and Executive Director Dr. Stephen Rowins departed from the Survey to pursue an opportunity as director and professor at the Centre for Exploration Targeting at University of Western Australia. Dr. Adrian Hickin, former Director of the Cordilleran Geoscience Section, was selected as Steve's replacement and has been appointed Chief Geologist. With the filling of several vacancies in the last five years, the Survey is seeing significant renewal, and is working to fill other key geoscience roles in 2019. The Survey continues to invest in the next generation of geoscientists by hiring and training student assistants, supporting graduate students, and mentoring student research (Fig. 3).

## 2. Partnerships

The BCGS is small and works to make best use of limited resources. Thus, partnerships are important. BCGS and the Geological Survey of Canada (GSC) continue to deliver projects through the second iteration of the Geo-mapping for Energy and Minerals (GEM 2) program and through three Targeted Geoscience Initiative 5 (TGI 5) projects.

In 2013, the Government of Canada renewed support for the second phase of the GEM program (2013-2020) aimed at advancing geological knowledge and further developing modern geological maps and data sets. The BCGS collaborated with the GSC and the Yukon Geological Survey with a project examining Cache Creek and Stikine terranes near Atlin.

The TGI 5 program is directed at building knowledge and developing methods to better target buried mineral deposits.

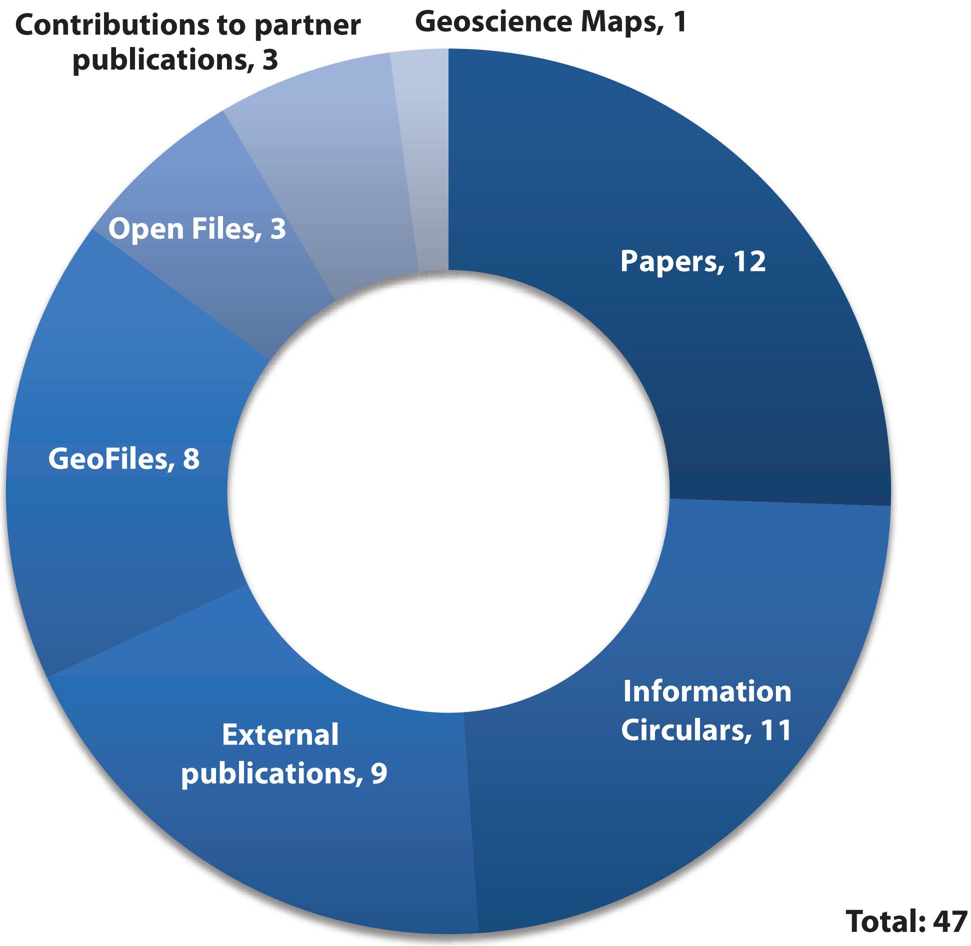


**Types of Publications by the British Columbia Geological Survey**

**Papers*:** This series is reserved for reviews and final thematic or regional works. Geological Fieldwork, our annual review of field activities and current research, is released as the first Paper of each year.

**Geoscience Maps:** This series is the BCGS vehicle for publishing final maps.

**Open Files:** These maps and reports present the interim results of ongoing research, particularly mapping projects.

**GeoFiles:** These publications enable rapid release of extensive data tables from ongoing geochemical, geochronologic, and geophysical work. As such, they serve the same function as data repositories provided by many journals, providing immediate access to raw data from specific projects.

**Information Circulars:** These publications provide accessible geoscience information to a broad audience in government, industry, and the general public. Included in the Information Circular series are the annual Provincial Overview of Exploration and Mining in British Columbia**, and the Coal Industry Overview.

**Contributions to partner publications:** This category includes reports, maps, and other products published by another agency such as the Geological Survey of Canada or Geoscience BC, but have received contributions from British Columbia Geological Survey staff.

**External publications:** These are contributions to the peer reviewed literature and published in a recognized national or international scientific journal.

*The count refers to the total number of articles authored by BCGS personnel in a volume.

**Although six articles are included in Exploration and Mining in British Columbia, it is counted as a single volume.

**Fig. 1.** British Columbia Geological Survey publications in 2018.

**Fig. 2.** Members of the British Columbia Geological Survey at Johnson Street Bridge, Victoria.

The program aims to understand the geological processes responsible for deriving, transporting, and depositing ore metals. One BCGS-TGI 5 project, in northwest British Columbia and southern Yukon, is assessing gold occurrences spatially related to the Llewellyn fault and Tally Ho shear zone. BCGS leads another TGI 5 project focused on specialty metal deposits in the province that contain rare earth elements, lithium, tantalum, and niobium. This project includes a partnership with the Geological Survey of Japan. The third TGI 5 project, also led by BCGS, is in collaboration with the University of British Columbia and is working towards a mineral deposit model for orogenic Ni-Cu-PGE mineralization. The current iteration of the TGI program is expected to conclude in 2020.

In 2018, the Survey partnered informally with the Saanich Inlet Protection Society, a Vancouver Island community group, to develop a proposal to the UNESCO Global Geoparks Network for creating a geopark dedicated to Saanich Inlet (British Columbia Geological Survey, 2018a). It also continues to work with the Tumbler Ridge Geopark Society to enhance the Tumbler Ridge Global Geopark, which UNESCO added to the Network in 2014.

## 3. Cordilleran Geoscience Section

Geologists with the Cordilleran Geoscience Section undertake single- and multi-year field-based projects that include regional mapping, mineral deposit studies, and developing

**Fig. 3.** Training the next generation of field geologists.

new exploration methods (Fig. 4). Collectively, the section provides a range of expertise that includes, regional mapping, metallogeny, coal, tectonics, surficial and Quaternary geology, geochemistry, petrology, and mineral exploration methods.

In addition to the main projects undertaken in 2018, and itemized in more detail below, Cordilleran Section geologists provided new information from previous studies. Mihalynuk et al. (2019) report U-Pb zircon data from the Granduc and Rock and Roll volcanic massive sulphide deposits in northwestern British Columbia that are consistent with previous work indicating that mineralization took place in the Late Triassic. Building on work in the Decar area of central British Columbia (Milidragovic et al., 2018), Milidragovic and Grundy (2019) provide new geochemical and petrographic data from Cache Creek terrane, concluding that volcano-sedimentary rocks of the Sowchea succession are likely oceanic plateau deposits whereas the Trembleur ultramafite (host to the Decar nickel-iron awaurite prospect) and overlying rocks of the Rubyrock igneous complex formed in a suprasubduction zone setting. Representing two fundamentally different tectonic settings, these two tectonostratigraphic packages were interleaved during Cache Creek terrane-Stikine terrane collision in the Late Jurassic. Coal geology compilation work continued, with updated releases for the East Kootenay coalfields (British Columbia Geological Survey, 2018b) and the Peace River coalfields (British Columbia Geological Survey, 2018c).

### 3.1. Mapping, regional synthesis, and compilation

#### 3.1.1. Porphyry transitions; magmatic belts of Stikinia (BCGS-GSC)

Although fieldwork on this project finished in 2016, further work is planned towards synthesizing data and updating the provincial geology compilation. This project, initiated as a collaboration with the Geological Survey of Canada through the Geo-mapping for Energy and Minerals (GEM 2), addresses the continuity of the prospective Triassic-Jurassic magmatic belt in northern Stikinia, assesses the porphyry potential of this belt, and evaluates the potential of deposits in adjacent terranes.

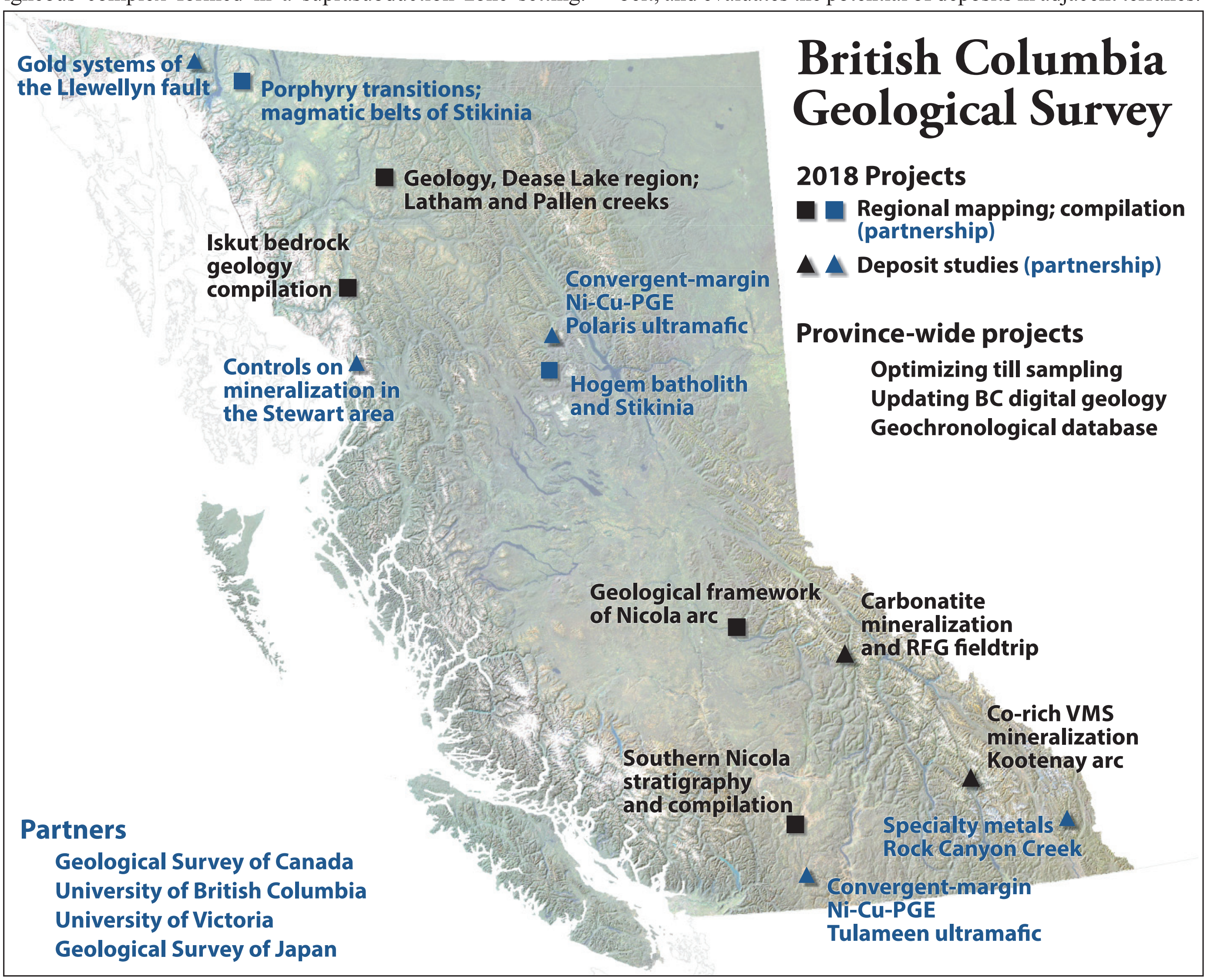


**Fig. 4.** British Columbia Geological Survey projects in 2018.

### 3.1.2. Regional mapping in the Dease Lake region

This was the third and final field season of a mapping project in the Dease Lake region that examined Upper Triassic to Middle Jurassic arc-related volcanic and sedimentary rocks and allied intrusive rocks to better understand the tectonic and metallogenic history of northern Stikinia and bounding terranes (Fig. 5). Mapping in 2018 (van Straaten and Wearmouth, 2019) focused on the Latham and Pallen Creek areas southwest of Dease Lake and distinguished three volcano-sedimentary units sitting above upper Paleozoic rocks of the Stikine assemblage: 1) the Tsaybahe group (Lower to Middle Triassic); 2) the Stuhini Group (Upper Triassic) and 3) the Hazelton Group (Lower to Middle Jurassic). The Tsaybahe group is an informal name assigned to fine-grained siliciclastic and overlying plagioclase and augite-phyric basalts that are texturally similar to the overlying Stuhini Group. They are distinguished from the Stuhini Group based on age, stratigraphic position and distinctive low magnetic susceptibility. Stuhini Group volcanic rocks are unconformably overlain by the Hazelton Group, which includes a lower sedimentary unit (Spatsizi Formation) and overlying volcanic rocks (Horn Mountain Formation). The Tsaybahe group likely represents nascent Stuhini arc magmatism. Developed within or adjacent to Upper Triassic and Middle Jurassic plutons that cut the supracrustal units are zones with locally elevated copper, gold, silver and/or molybdenum in fractures, veins, skarns, and gossans. This project will now begin a synthesizing year, and the recent mapping will be incorporated into the provincial geology compilation.

**Fig. 5.** Middle part of Horn Mountain Formation, west of Tanzilla, Dease Lake mapping project.

### 3.1.3. Iskut bedrock compilation

Part of the Golden Triangle of northwestern British Columbia (e.g., British Columbia Geological Survey 2018d), the Iskut River region hosts many significant porphyry, precious-metal and volcanogenic massive sulphide deposits that are related to the Hazelton Group and allied intrusions (latest Triassic to Middle Jurassic). Nelson et al. (2018) set out new nomenclature and definitions for the Hazelton Group, providing a unified stratigraphic framework that will assist exploration in this highly prospective region. Digital data and working files supporting the Iskut region compilation are in Nelson (2019), and new U-Pb zircon geochronologic data from the Mitchell deposit are in Febbo et al. (2019).

### 3.1.4. Hogem batholith and Stikinia

In 2018, a multi-year 1:50,000-scale mapping project was initiated in north-central British Columbia targeting northern Hogem batholith and adjacent volcanic and sedimentary rocks of Stikinia (Fig. 6). The main objectives of this project are to update the bedrock and surficial maps of northern Hogem batholith and adjacent Quesnel, Stikine, and Cache Creek terranes and to generate new geochronological data to better understand the timing of intrusive events and their relationship to mineralization. This project will provide the first detailed maps of northern Hogem batholith and update reconnaissance-level maps of adjacent terranes that date from the 1940s. Based mainly on crosscutting relationships and the presence or absence of tectonic fabrics, Ootes et al., (2019 a,b) identify four main plutonic suites (from oldest to youngest): Thane Creek (ca. 200 Ma), Duckling Creek (ca. 180 Ma), Mesilinka (ca. 135 Ma), and Osilinka (ca. 135 Ma). To the ca. 34 mineral occurrences previously known from the area, and additional 17 were discovered this summer. Most are in the Thane Creek and Osilinka suites and consist mainly of disseminated chalcopyrite and malachite staining. New gold and copper-bearing quartz veins were also discovered, and crosscut Thane Creek diorite and Osilinka granite. Work in 2019 will map the more northerly part of Hogem batholith and Cache Creek terrane to the west.

**Fig. 6.** Fly camp, Hogem batholith project.

### 3.1.5. Stratigraphic architecture of the Nicola arc

The large number of operating porphyry Cu-Au-Mo mines in Quesnel terrane marks it as the most important metallotect in the Canadian Cordillera. Despite its economic importance, the regional stratigraphic framework of the main Triassic to Jurassic arc sequences has not been well-defined. The BCGS currently has two projects that, together, will provide a coherent stratigraphic architecture for the Nicola arc: the Nicola Group stratigraphic framework project between Bonaparte Lake and Likely; and the southern Nicola arc project in the Merritt and Princeton areas (Fig. 4).

#### 3.1.5.1. Nicola Group stratigraphic framework

This project was initiated in 2015 with the primary objective of establishing a regional stratigraphic framework for Triassic rocks of the Nicola arc in the central part of the Quesnel terrane. Based on new work in the Bridge Lake-Quesnel River area in 2018, Schiarizza (2019) refines his earlier four-fold subdivision of the Nicola Group. Assemblage one is represented mainly by the Spanish Mountain unit (new informal name), which consists of Middle Triassic sedimentary rocks and local pillowed basalt with N-MORB and E-MORB geochemical characteristics. Undated, but possibly correlative rocks in the south-central part of the Nicola belt include volcaniclastic sandstone, chert, and pyroxene-phryic basalts of the Wavey Lake unit (new informal name), which is locally overlain by early Carnian siltstone of the Meridian Lake unit (new informal name). Assemblage two (Carnian and early Norian), the most widespread subunit of the Nicola Group, contains volcanic sandstone and conglomerate, locally intercalated with pyroxene-phyric basaltic rocks. Assemblage three (Norian) consists of pyroxene-phyric basalt flows and related breccias. Assemblage four (late Norian and Rhaetian) may be separated from older Nicola rocks by an unconformity or disconformity. It consists of red and maroon polymictic conglomerate with abundant hypabyssal and plutonic rock fragments, feldspathic sandstone, and distinctive analcime basalt and coarse, crowded plagioclase-phyric andesite. The Nicola Group is flanked to the east by Middle and Upper Triassic slate, siltstone and quartz sandstone of the Slocan Group (Fig. 7), part of a siliciclastic basin that formed east of, and coeval with, the Nicola arc; Middle Triassic carbonaceous shales previously included in the Nicola Group are re-assigned to the Slocan Group. Upper Triassic to Lower Jurassic calcalkaline and alkaline plutonic rocks that cut the Nicola Group are equivalent to regional plutonic suites in Quesnel terrane, and include a latest Triassic monzodiorite suite that is coeval with assemblage four and hosts significant porphyry Cu-Au deposits. Work in 2019 will entail formalizing nomenclature, generating detrital zircon geochronologic data, and correlating results with the southern Nicola arc project.

**Fig. 7.** Steeply dipping sandstone with thin interbeds of slaty siltstone, Slocan Group, southeast of Spanish Lake. Beds are overturned.

#### 3.1.5.2. Southern Nicola arc

The Southern Nicola Arc project began in 2012 as a regional mapping program along the western part of the Nicola arc between Merritt and Princeton with an aim of re-examining the three stratigraphic belts first proposed for the Nicola Group (Preto, 1979; Mihalynuk et al., 2016). This mapping, together with new biostratigraphy and geochronology has redefined the original belts and their relationships. A brief field study in 2018 measured a key section representing the lower of two major subdivisions proposed for the Nicola Group and re-examined an area containing a representative section of the upper part of the lower stratigraphic subdivision. These data will be incorporated into a new 1:50,000 scale map that will detail Nicola Group geology between Merritt and Princeton, integrated with Nicola Group studies to the north, and entered into the provincial digital geology compilation.

### 3.1.6. Surficial geology mapping and till sampling

Plouffe and Ferbey (2018) published a new 1:50,000-scale surficial geology map of the Highland Valley copper mine area, and Ferbey et al. (2018) described the geochemistry and mineralogy of 14 subsurface till samples recovered from a diamond drill hole on the Rateria porphyry Cu±Mo property. An updated index of British Columbia surficial geology maps (Arnold and Ferbey, 2016) was released in January, 2018.

## 3.2. Deposit studies

### 3.2.1. Gold and Llewellyn fault (BCGS-GSC-YGS-TGI 5)

This project is examining the nature and timing of gold mineralization spatially related to the Llewellyn fault zone. This structure is a brittle, steeply dipping, southeast-striking dextral strike-slip fault that overprints earlier ductile deformation with similar orientation and kinematics. This early ductile shear zone is similar to the Tally Ho shear zone in Yukon. Ootes et al. (2018) concluded that the early ductile fabrics formed between 120 and 75 Ma, considerably older than the brittle deformation that is bracketed between 56 and 50 Ma, and that the various styles of gold mineralization developed at distinctly different periods. Geochronologic samples collected in 2018 from southern Yukon and northern British Columbia will better establish the age of early ductile strain.

### 3.2.2. Specialty metals (BCGS-GSC-TGI 5)

Specialty metals are elements such as rare earth elements (REE), Li, Ta, Nb, Ga, Ge, In, Co, W, Mg, Cs, Rb, Rh, Be, Zr, Hf, V, Sb and Sc that are not only essential to the growth of the electronics and green-energy sector, but also critical or strategic for technologically advanced devices and industrial processes. Work in 2018 emphasized laboratory analyses of British Columbia carbonatite samples collected during the last six years, focussing on quantifying radiogenic and stable isotope levels.

Simandl et al. (2019) report on an occurrence of fersmite from the Mount Brussilof magnesite deposit in southeastern British Columbia. Fersmite is a Nb- Ta-bearing mineral commonly found as an alteration product of pre-exiting niobium-bearing minerals in carbonatites, alkaline and peralkaline intrusions, and rare earth element pegmatites. In contrast, fersmite at Mount Brussilof appears to be primary. It forms crystals on sparry dolomite, which is commonly found in Mississippi Valley-type Zn-Pb deposits, crosscutting and lining cavities in sparry magnesite. This fersmite is rich in Nb, Th and heavy rare earth elements, but poor in Ta. Chemical mapping of individual crystals shows strong zonation suggesting that the hydrothermal fluids from which fersmite precipitated evolved with time.

### 3.2.3. Tulameen-Polaris: Towards a new mineral deposit model for convergent margin Ni-Cu-PGE (BCGS-TGI 5)

This project builds on our current understanding of high-tenor Ni-Cu-PGE deposits formed at convergent margins that are found in Alaskan-type ultramafic-mafic intrusions and that are possibly genetically linked to Cu-Au porphyry systems (e.g., Nixon et al., 2017; Manor et al., 2017, Nixon 2018). One objective is to develop a new mineral deposit model encompassing the temporal evolution and ore system processes involved in the genesis of Cu-PGE recently found in the Tulameen Alaskan-type ultramafic complex (Nixon, 2018). The project continues with a study of the Polaris Alaskan-type ultramafic intrusion to better establish its age and character, to place its Ni-Cu-PGE mineralization in a geological context, and to test for possible relationships to the Hogem batholith immediately to the south (Fig. 4) and its Cu-Au mineral systems. In 2018, previously collected samples from the Tulameen body were analyzed and several weeks of fieldwork spent at the Polaris complex (Fig. 8) to examine geological relationships and collect samples for geochemical, isotopic, and geochronologic analysis.

### 3.2.4. Blue River carbonatites

Carbonatites are igneous rocks containing abundant primary carbonate minerals. These rare rocks generally form in intracratonic settings as part of crustal-scale dome and rift systems. In the Canadian Cordillera, carbonatites were emplaced episodically, at ca. 810-700, 500, and 360-330 Ma, forming part of the British Columbia alkaline province, which defines a long (at least 1000 km), narrow (ca. 200 km) orogen-parallel belt. The ca. 810-700 Ma and 500 Ma carbonatites were injected during protracted breakup of the supercontinent Rodinia and passive margin development on the western flank of Laurentia.

**Fig. 8.** In the distance, rust brown-weathering dunite, Polaris ultramafic complex.

In contrast to these and to most carbonatites globally, the 360-330 Ma carbonatites, such as the Blue River area examples, are unusual. They were emplaced near the continental margin during subduction rather than in the cratonic interior during continent breakup. The Blue River carbonatites include at least 18 carbonatite and 2 alkaline, silica-undersaturated-rock occurrences. As part of the Resources for Future Generations conference and sponsored by the Mineralogical Association of Canada, Ruhklov et al., (2018a) led a field trip that examined the characteristics, magmatic evolution, and mineralization of the Blue River carbonatites as represented by the Upper Fir complex, which hosts one of the largest and best studied Nb-Ta deposits in the Canadian Cordillera (Fig. 9). New isotopic and elemental compositions of minerals from Blue River carbonatites and related rocks (Ruhklov et al., 2018a, b) are indistinguishable from worldwide carbonatites generated by deep-mantle plumes. The 360-330 Ma Cordilleran examples formed along the western margin of Laurentia while subduction was taking place immediately to the west. Lithospheric extension related to this Late Paleozoic subduction is considered responsible for rifting the continental margin and initiating the Slide Mountain ocean as a back-arc basin. Ruhklov et al. (2018a) conclude that this same back-arc extension triggered the most prolific pulse of alkaline magmatism in the Cordillera, including emplacement of the Blue River carbonatites, which were derived from a long-lived, deep-level mantle plume that was tapped episodically since the Neoproterozoic. Further fieldwork in 2018 collected samples from the Blue River and from the Ice River complex to test this model.

### 3.2.5. Co-rich VMS mineralization, Kootenay arc

In 2018, a reconnaissance program was initiated in the Kootenay arc examining the potential for Cu-Co-Ni Beshi-type volcanogenic massive sulphide deposits in the Lardeau Group that may hold similarities to Outokupu-style polymetallic massive sulphides in Finland described by Peltonen et al. (2008).

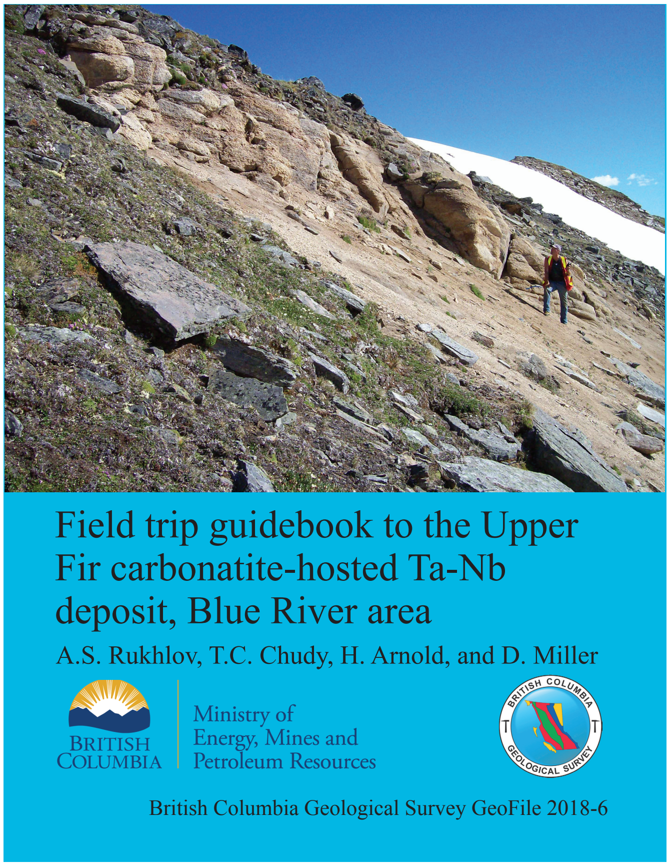


**Fig. 9.** Field trip guidebook to the Upper Fir-carbonatite-hosted Ta-Nb deposit (Rukhlov et al., 2018a). The cover photo shows a sill-like body of calcite carbonatite in the Howard Creek area.

### 3.3. Geochemical databases

Fieldwork generates vast amounts of rock, till, stream-sediment, and coal geochemical data. In the past, the British Columbia Geological Survey has modelled geochemical data sets individually. Han et al. (2019) developed a skeleton data model capable of capturing and representing the commonalities of individual sets by focusing on common entities, attributes, and relationships. They use this skeleton data model to update existing models for four province-wide data sets (lithogeochemical, regional drainage, till, and coal ash), capturing the unique characteristics of each. Applying the skeleton data model streamlines data handling steps, from data compilation to product generation, and establishes a reliable flow for managing geochemical data at the Survey.

### 3.4. BCGS Emeritus Scientists

Emeritus Scientist Ray Lett continued in his role as mentor to Survey geologists and serving as a peer reviewer. He also continued to be productive, releasing unpublished geochemical data from between Lillooet and French Bar Creek, south-central British Columbia (Lett, 2018a), the Porcher Island, Grenville Channel, and Dundas Island area, central British Columbia coast (Lett, 2018b), and the McLeod Lake area, central British Columbia (Lett, 2018c).

Shortly after her retirement in early 2018, JoAnne Nelson, the Survey's most recent Emeritus, launched a cross-country lecture tour as recipient of the 2017 Canadian Provincial and Territorial Geologists Medal and devoted to her work on the tectonic evolution of the Canadian Cordillera. JoAnne will be releasing a GeoFile digital data release (Nelson, 2019) to accompany her most recent work in the Iskut River region (Nelson et al., 2018).

## 4. Resource Information Section highlights

As custodian of all provincial public geoscience data, the Survey preserves and archives more than a century's worth of information, including geological maps and reports, thematic studies, and mineral occurrence, geochemical, and geophysical data. Survey activities are traditionally aimed at enhancing British Columbia's mineral exploration competitiveness, and delivering geoscience is a priority in making the province an attractive investment destination. The Survey continues to upgrade databases and to make geoscience information more accessible through MapPlace 2, our geospatial web service. These activities help explorers advance projects without duplicating previous work. They also help government, First Nations, and communities make decisions about mineral exploration, resource development, environmental protection, natural hazards, and land use.

### 4.1. MapPlace 2

MapPlace 2 is the BCGS geospatial web service that enables people to easily visualize, search, report, and generate custom results and maps from all province-wide geoscience databases (Cui et al., 2018a). Through MapPlace 2, multiple layers of geospatial data, such as mineral titles, assessment reports, powerlines, aquifers, topography and satellite imagery, can be accessed. Recent enhancements include the addition of OpenStreetMap as a base map, and KML downloads for selected bedrock units and other data.

### 4.2. Databases

#### 4.2.1. ARIS

ARIS (Assessment Report Index System) is an index database linking to a collection of mineral exploration assessment reports submitted in compliance with Mineral Tenure Act Regulations. The ARIS library of more than 36,700 PDF reports, dating from 1947, describes exploration work valued at more than $2.8 billion. After a one-year confidentiality period, the reports become an open resource that can be used for planning mineral exploration, investment, research, land use, and resource management. Currently, digital data are available for download from 480 assessment reports through the ARIS search application. The BCGS welcomes the submission of assessment report digital data. Data can be submitted when a report is filed or e-mailed to ARIS.digital@gov.bc.ca.

Norris and Fortin (2019) conducted a pilot project to extract geochemical data from assessment reports in the Interior Plateau region and incorporate them into a new database.

Data harvested from about 125 assessment reports submitted between 2000 and 2015 (Fig. 10) include about 1.5 million determinations from about 35,000 samples. Future assessment report-sourced databases will include information from drill holes and geophysical surveys. The BCGS is also implementing recommendations from the Exploration Assessment Data Digital Formats Proposal by PDAC to ensure that the structure of the databases will meet future national standards.

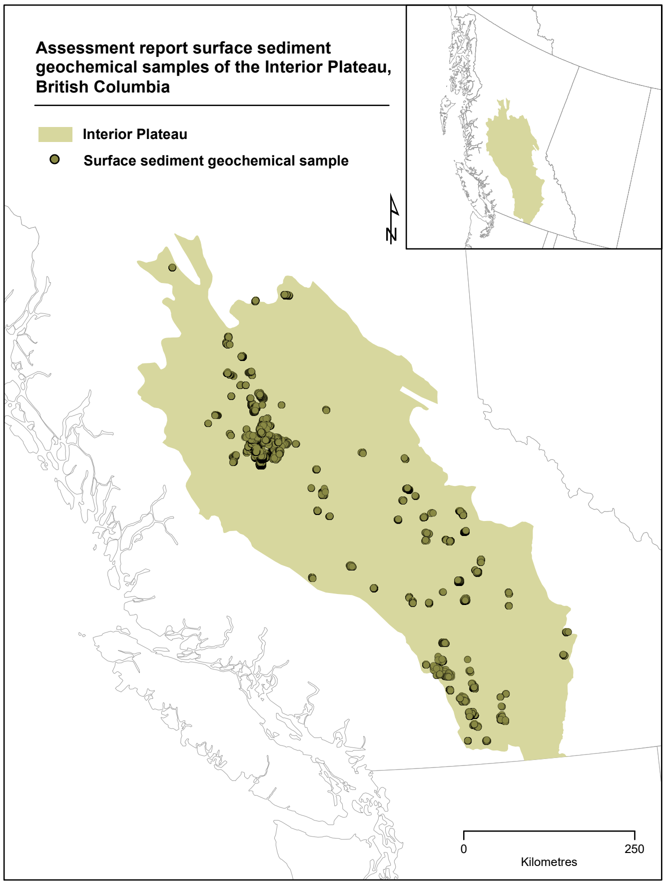


**Fig. 10.** Surface sediment geochemistry data harvested from assessment reports.

### 4.2.2. COALFILE

COALFILE includes a collection of 1010 coal assessment reports, dating from 1900. It includes data from about 15,700 boreholes, 550 bulk samples, 5600 maps, 3650 trenches, 480 coal ash chemistry analyses and links to MINFILE.

### 4.2.3. MINFILE

MINFILE is a database of more than 14,800 mineral, coal, and industrial mineral occurrences. It is widely used by the mineral industry to develop exploration strategies, plan investments, evaluate or estimate resource potential, and carry out metallogenic studies. It also serves government agencies and other organizations concerned with natural resources and land use. The MINFILE database can be queried via an online application that interacts with MapPlace 2, ARIS, and Property File.

### 4.2.4. Property File

Property File is a collection of more than 73,500 reports, maps, photos, and technical notes donated to the Survey since the late 1800s. These documents can be accessed from the Property File database using a full-text, search tool. The BCGS accepts donations to Property File.

### 4.2.5. Geochemical databases

The provincial geochemical databases hold field and geochemical data from multi-media surveys by the Geological Survey of Canada, the BCGS, and Geoscience BC. These databases are updated regularly and contain results from: 1) the Regional Geochemical Survey program (RGS) including analyses from stream-sediment, lake-sediment, moss, and water samples; 2) till surveys; and 3) rock samples. The current version of the RGS database of about 65,000 samples is compiled from 111 original sources (Han and Rukhlov, 2017) and is delivered in flat tabular XLS format for ease of use and consistency with previously published data. The till database is an XLS format compilation from about 40 reports released between 1992 and 2017 and includes geochemical data for about 10,500 samples (Bustard and Ferbey, 2017; Bustard et al., 2017). The lithogeochemical database includes data from about 2000 papers and reports published by the BCGS, GSC and universities between 1986 and 2015. The data set consists of about 11,000 samples, including a quarter million determinations analyzed by 26 different methods at 21 laboratories (Han et al., 2016). The skeleton data model developed by Han et al. (2019) is being used to update existing models for the province-wide data sets.

## 4.3. British Columbia digital geology map

BCGS offers province-wide digital coverage of bedrock geology, including details from field mapping at scales from 1:50,000 to 1:250,000 (Cui et al., 2018b). The BC digital geology continuously integrates new regional compilations as the data become available (Fig. 11). The digital geology (in GeoPackage and Esri shapefile formats) and Truetype font for

**Fig. 11.** Digital data capture in the field.

stratigraphic age symbols are freely available for download under the British Columbia Open Government License. Customized bedrock geological maps and legends can be visualized and data downloaded in KML format by spatial and non-spatial queries via MapPlace 2. The BCGS is introducing new lithology codes in the digital geology database that will capture distinguishing features on the geological processes and environments of bedrock units. The digital geology is maintained by a geospatial frame data model with techniques to simplify the integration process and shorten the time from field mapping, compilation, and integration to data delivery.

### 4.4. Website update

The BCGS has a newly designed, easier to use website (Fig. 12). The site has better navigation links and search capabilities. The search results link to over 8300 publication assets (PDF, ZIP, XLS, and various map formats). Search capabilities have been enhanced allowing one to search the content of documents for specific text strings.

### 4.5. EarthResourceML

EarthResourceML is an XML-based standard for the exchange of digital information. The BCGS is reviewing EarthResourceML and developing interoperable (data exchange capable) web services. These web services would enable access to geological data on the OneGeology portal, and allow interoperable connections of the Survey's databases. Data components have been mapped to the vocabularies adopted by the Commission for the Management and Application of Geoscience Information (CGI). The implementation of EarthResourceML would help to enhance usability of the various databases by adopting the open standard in the data models, contents, and vocabularies.

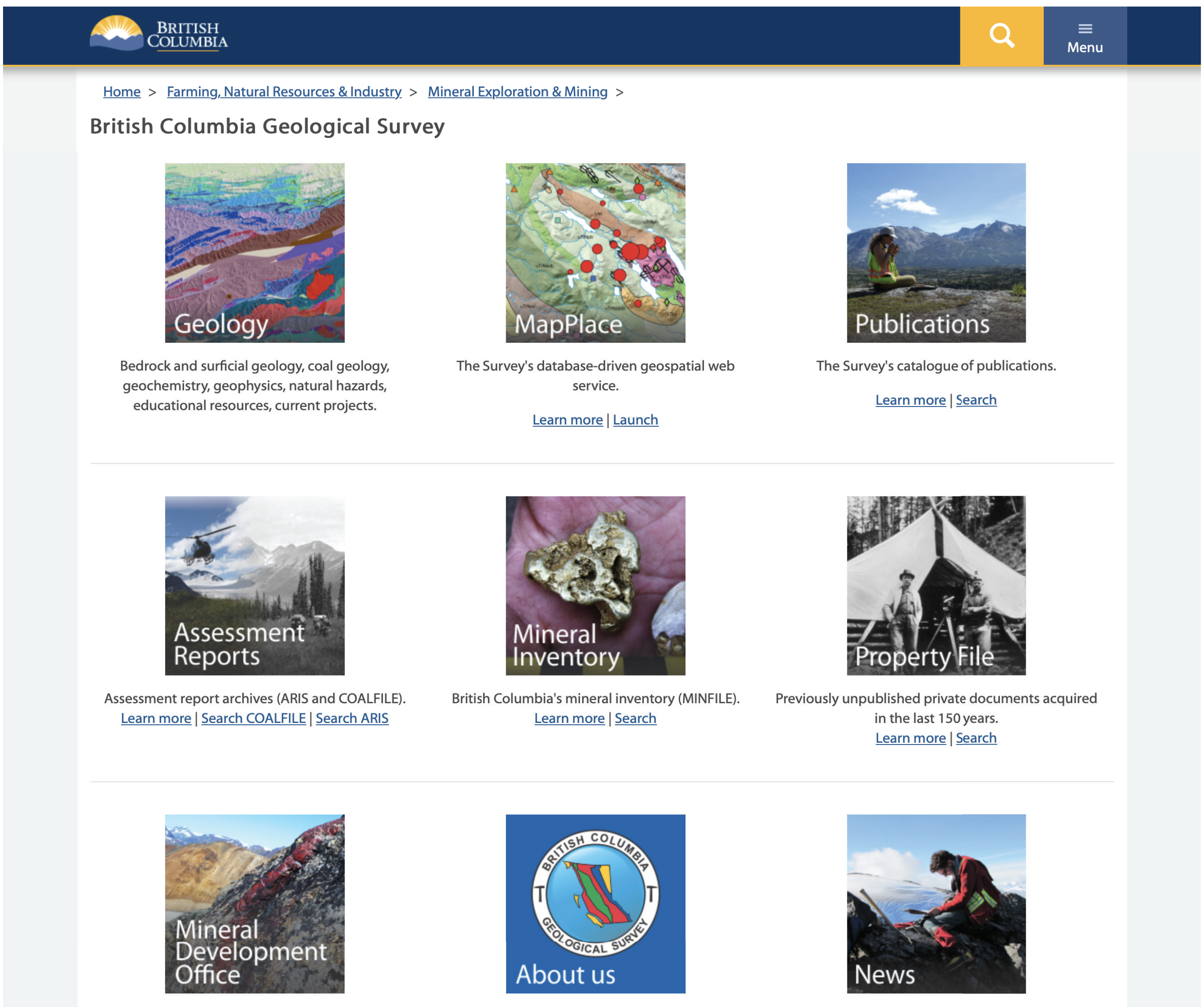


**Fig. 12.** Newly designed British Columbia Geological Survey website.

### 4.6. Three dimensional geological modelling

The British Columbia Geological Survey used 3D modelling to help analyze the Upper Fir carbonatite-hosted Ta-Nb deposit (see section 3.2.4. above, and Rukhlov et al., 2018), generating a series of cross sections to illustrate the spatial variation of rock compositions in the deposit (Fig. 13).

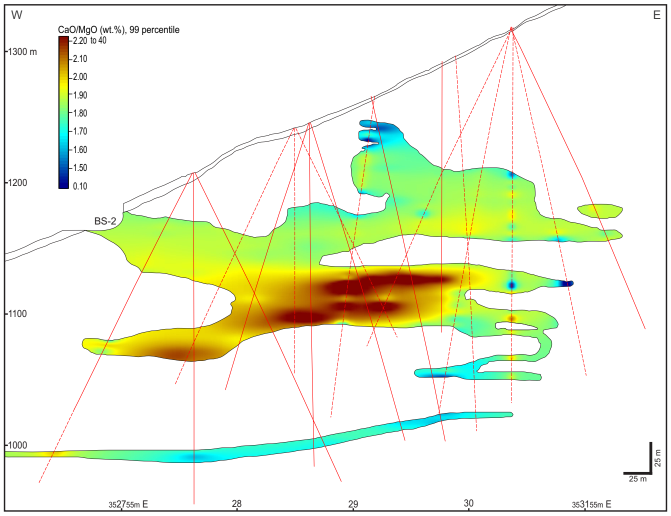


**Fig. 13.** Cross section showing the 99th percentile for CaO/MgO (wt.%) from drill-core samples (1 m intervals), gridded by the inverse-distance 3D interpolation method using GOCAD® software.

## 5. British Columbia Geological Survey Mineral Development Office (MDO)

The Mineral Development Office is the Vancouver base of the British Columbia Geological Survey. It links the more than 800 exploration and mining companies headquartered in Vancouver to provincial mineral and coal information. The MDO distributes Survey data and provides technical information and expertise about mineral opportunities to the domestic and international investment community.

The MDO monitors the activities of the mining and exploration sectors and co-ordinates production of the 'Provincial Overview of Exploration and Mining in British Columbia', an annual volume that summarizes activities in the different regions of the province and written by the Regional Geologists and the MDO (see British Columbia Geological Survey, 2019; Clarke et al., 2019). In 2018, the MDO led production of a brochure devoted to the Golden Triangle of northwestern British Columbia, which hosts most of the major gold, silver, and copper deposits in west-central Stikinia (British Columbia Geological Survey, 2018d). More than 150 mines have operated in the region since prospectors first arrived near the end of the 19th century and it currently hosts the Brucejack and Red Chris mines. The MDO also led developing a brochure about low-carbon emission energy technologies and metals mining in the province (British Columbia Geological Survey, 2018e).

Exploration expenditures in the province increased from last year and will be highlighted in the 2018 British Columbia Mineral and Coal Exploration Survey, a joint initiative amongst EY (formerly Ernst & Young), the Ministry of Energy, Mines and Petroleum Resources, and the Association for Mineral Exploration (AME). Conducted in the fall of 2018, the survey is based on data collected directly from prospectors and exploration companies. Expenditure trends suggest that exploration in British Columbia continues to undergo an exploration lifecycle 'reset' that began with an upturn in outlays in 2017.

## 6. Regional geologists

The British Columbia Regional Geologists (Table 1) represent the provincial government on geological matters at a regional level and capture information on industry activity in their jurisdictions. Within their communities, they provide information on exploration trends, possible investment opportunities, land use processes, First Nation capacity building, and public outreach.

**Table 1.** British Columbia's regional geologists.

| Regional Geologist | Office | Region |
|---|---|---|
| Vacant | Smithers | Northwest |
| John DeGrace | Prince George | Northeast and North Central |
| Vacant | Kamloops | South Central |
| Fiona Katay | Cranbrook | Southeast |
| Bruce Northcote | Vancouver | Southwest |

## Acknowledgment

We thank George Owsiacki of Total Earth Science Services (Victoria) for the desktop publishing of this volume.

## References cited

Arnold, H., and Ferbey, T, 2016. British Columbia surficial geology map index. British Columbia Ministry of Energy and Mines, British Columbia Geological Survey Open File 2016-3.

British Columbia Geological Survey, 2018a. Saanich Inlet, southern Vancouver Island: Geology of an Aspiring Global Geopark. British Columbia Ministry of Energy, Mines and Petroleum Resources, British Columbia Geological Survey Information Circular 2018-3, 8 p.

British Columbia Geological Survey, 2018b. The East Kootenay coalfields. British Columbia Ministry of Energy, Mines and Petroleum Resources, British Columbia Geological Survey Information Circular 2018-6.

British Columbia Geological Survey, 2018c. The Peace River coalfields. British Columbia Ministry of Energy, Mines and Petroleum Resources, British Columbia Geological Survey Information Circular 2018-7.

British Columbia Geological Survey, 2018d. The Golden Triangle of northwestern British Columbia. British Columbia Ministry of Energy, Mines and Petroleum Resources, British Columbia Geological Survey Information Circular 2018-5, 8 p.

British Columbia Geological Survey, 2018e. Low-carbon energy technologies and metals mining in British Columbia. British Columbia Ministry of Energy, Mines and Petroleum Resources, British Columbia Geological Survey Information Circular 2018-11, 8 p.

British Columbia Geological Survey, 2019. Provincial Overview of Exploration and Mining in British Columbia, 2018. British Columbia Ministry of Energy, Mines and Petroleum Resources, British Columbia Geological Survey, Information Circular 2019-01, 133 p.

Bustard, A.L., and Ferbey, T., 2017. An index of base and precious metal regional- to property-scale subglacial till geochemical and mineralogical surveys in British Columbia, British Columbia Ministry of Energy and Mines, British Columbia Geological Survey Open File 2016-2 (updated August 2017).

Bustard, A.L., Han, T., and Ferbey, T., 2017. Compiled till geochemical data for British Columbia, British Columbia British Columbia Ministry of Energy, Mines and Petroleum Resources, British Columbia Geological Survey GeoFile 2017-9.

Clarke, G., Northcote, B., Katay, F., and DeGrace, J.R., 2019. Exploration and Mining in British Columbia, 2018: A summary. In: Provincial Overview of Exploration and Mining in British Columbia, 2018. British Columbia Ministry of Energy, Mines and Petroleum Resources, British Columbia Geological Survey, Information Circular 2019-01, pp. 1-37.

Cui, Y., Zhao, S., Fortin, G., Meredith-Jones, S., and Jones, L.D., 2018a. Development of MapPlace 2 geospatial web service to disseminate geoscience in British Columbia. In: Geological Fieldwork 2017, British Columbia Ministry of Energy, Mines and Petroleum Resources, British Columbia Geological Survey Paper 2018-1, pp. 183-195.

Cui, Y., Hickin, A.S., Schiarizza, P., Miller, D., Nixon, G.T., Nelson, J.L., and Ferri, F, 2018b. Methods to update the digital geology of British Columbia and synopses of recently integrated mapping programs. In: Geological Fieldwork 2017, British Columbia Ministry of Energy, Mines and Petroleum Resources, British Columbia Geological Survey Paper 2018-1, pp. 197-215.

Febbo, G.E., Friedman, R.M., Kennedy, L.A., and Nelson, J.L., 2019. U-Pb geochronology of the Mitchell deposit, northwestern British Columbia. British Columbia Ministry of Energy, Mines and Petroleum Resources, British Columbia Geological Survey GeoFile 2019-03, 8 p.

Ferbey, T., Plouffe, A., and Hickin, A.S., 2018. Geochemistry and mineralogy of subsurface till samples recovered from diamond drill hole R17-01, Rateria property (porphyry Cu±Mo), south-central British Columbia. British Columbia Ministry of Energy, Mines and Petroleum Resources, British Columbia Geological Survey GeoFile 2018-8, 15 p.

Han, T., and Rukhlov, A.S., 2017. Regional Geochemical Survey (RGS) data update and release using the newly developed RGS database, British Columbia British Columbia Ministry of Energy, Mines and Petroleum Resources, British Columbia Geological Survey GeoFile 2017-11, 7 p.

Han, T., Rukhlov, A.S., Naziri, M., and Moy, A., 2016. New British Columbia lithogeochemical database: Development and preliminary data release. British Columbia Ministry of Energy and Mines, British Columbia Geological Survey, GeoFile 2016-4, 6 p.

Han, T., Rukhlov, A.S., Riddell, J.M., and Ferbey, T., 2019. A skeleton data model for geochemical databases at the British Columbia Geological Survey. In: Geological Fieldwork 2018, British Columbia Ministry of Energy, Mines and Petroleum Resources, British Columbia Geological Survey Paper 2019-01, pp. 125-135.

Lett, R.E., 2018a. Compilation of geochemical data between Lillooet and French Bar Creek, south-central British Columbia. British Columbia Ministry of Energy, Mines and Petroleum Resources, British Columbia Geological Survey GeoFile 2018- 4, 42 p.

Lett, R.E., 2018b. Regional moss mat-sediment geochemical survey in the Porcher Island, Grenville Channel, and Dundas Island area, central British Columbia coast. British Columbia Ministry of Energy, Mines and Petroleum Resources, British Columbia Geological Survey GeoFile 2018-5, 32 p.

Lett, R.E., 2018c. Digital data release for a multimedia geochemical survey in the McLeod Lake map area (NTS 093J/5, 6, 12) central British Columbia. British Columbia Ministry of Energy, Mines and Petroleum Resources, British Columbia Geological Survey GeoFile 2018-7, 2 p.

Manor, J.M., Scoates, J.S., Wall, C.J., Nixon, G.T., Friedman, R.M., Amini, M., and Ames, D.E., 2017. Age of the Late Cretaceous ultramafic-hosted Giant Mascot Ni-Cu-PGE deposit, southern Canadian Cordillera: Integrating CA-ID-TIMS and LA-ICP-MS U-Pb geochronology and trace element geochemistry of zircon. Economic Geology, 112, 1395-1418.

Mihalynuk, M.G., Zagorevski, A., Logan, J.M., Friedman, R.M., and Johnston, S.T., 2019. Age constraints for rocks hosting massive sulphide mineralization at Rock and Roll and Granduc deposits between Iskut and Stewart, British Columbia. In: Geological Fieldwork 2018, British Columbia Ministry of Energy, Mines and Petroleum Resources, British Columbia Geological Survey Paper 2019-01, pp. 97-111.

Mihalynuk, M.G., Diakow, L.J., Friedman, R.M., and Logan, J.M., 2016. Chronology of southern Nicola arc stratigraphy and deformation. In: Geological Fieldwork 2015, British Columbia Ministry of Energy and Mines, British Columbia Geological Survey Paper 2016-1, pp. 31-63.

Milidragovic, D., and Grundy, R., 2019. Geochemistry and petrology of rocks in the Decar area, central British Columbia: Petrologically constrained subdivision of the Cache Creek complex. In: Geological Fieldwork 2018, British Columbia Ministry of Energy, Mines and Petroleum Resources, British Columbia Geological Survey Paper 2019-01, pp. 55-77.

Milidragovic, D., Grundy, R., and Schiarizza, P., 2018. Geology of the Decar area north of Trembleur Lake, NTS 93K/14. In: Geological Fieldwork 2017, British Columbia Ministry of Energy, Mines and Petroleum Resources, British Columbia Geological Survey Paper 2018-1, pp. 129-142.

Nelson, J.L., 2019. Iskut region geological compilation: Supporting data and working files. British Columbia Ministry of Energy, Mines and Petroleum Resources, British Columbia Geological Survey GeoFile 2019-02, 2 p.

Nelson, J.L., Waldron, J., van Straaten, B., Zagorevski, A., and Rees, C., 2018. Revised stratigraphy of the Hazelton Group in the Iskut River region, northwestern British Columbia. In: Geological Fieldwork 2017, British Columbia Ministry of Energy, Mines and Petroleum Resources, British Columbia Geological Survey Paper 2018-1, pp. 15-38.

Nixon, G.T., 2018. Geology of the Tulameen Alaskan-type ultramafic-mafic intrusion, British Columbia. British Columbia Ministry of Energy, Mines and Petroleum Resources, British Columbia Geological Survey Open File 2018-2, 1:20,000 scale.

Nixon, G.T., Scheel, J.E., Friedman, R.M., Wall, C.J., Gabites, J., Jackson-Brown, S., and Scoates, J.S., 2017. Staged emplacement of the Turnagain Alaskan-type ultramafic-mafic intrusion, British Columbia, Canada: implications for Ni-Cu-PGE mineralization and the origin of zoned complexes. Society for Geology Applied to Mineral Deposits, 14th Biennial Meeting, v. 2, 555-558.

Norris, J., and Fortin, G., 2019. Assessment report-sourced surface sediment geochemical database: Development and initial data release from the Interior Plateau. British Columbia Ministry of Energy, Mines and Petroleum Resources, British Columbia Geological Survey GeoFile 2019-04, 10 p.

Ootes, L., Castonguay, S., Friedman, R., Devine, F., and Simmonds, R., 2018. Testing the relationship between the Llewellyn fault, Tally-Ho shear zone, and gold mineralization in northwest British Columbia. In: Geological Fieldwork 2017, British Columbia Ministry of Energy, Mines and Petroleum Resources, British Columbia Geological Survey Paper 2018-1, pp. 67-81.

Ootes, L., Bergen, A.L., Milidragovic, D., Graham, B., Simmonds, R., 2019a. Preliminary geology of northern Hogem batholith, Quesnel terrane, north-central British Columbia. In: Geological Fieldwork 2018, British Columbia Ministry of Energy, Mines and Petroleum Resources British Columbia Geological Survey Paper 2019-01, pp. 31-53.

Ootes, L., Bergen, A.L., Milidragovic, D., and Graham, B., 2019b. Preliminary geology of Notch Peak and Ogden Creek (parts of NTS 094C/04 and 093N/13), northern Hogem batholith, Quesnel terrane, north-central British Columbia. British Columbia Ministry of Energy, Mines and Petroleum Resources, British Columbia Geological Survey Open File 2019-02, 1:50,000 scale.

Peltonen, P, Kontinen, A., Huhma, H., and Kuronen, U., 2008. Outokumpu revisited: New mineral deposit model for the mantle peridotite-associated Cu-Co-Zn-Ni-Ag-Au sulphide deposits, Ore Geology Reviews, 33, 559-617.

Plouffe, A., and Ferbey, T., 2018. Surficial geology of the Highland Valley Copper mine area (Parts of NTS 092I/06, 7, 10 and 11), British Columbia. British Columbia Ministry of Energy, Mines and Petroleum Resources, British Columbia Geological Survey, Geoscience Map 2018-01, 1:50,000 scale.

Preto, V.A., 1979. Geology of the Nicola Group between Merritt and Princeton. British Columbia Ministry of Energy, Mines and Petroleum Resources, British Columbia Geological Survey Bulletin 69, 90 p.

Rukhlov, A.S., Chudy, T.C., Arnold, H., and Miller, D., 2018a. Field trip guidebook to the Upper Fir carbonatite-hosted Ta-Nb deposit, Blue River area, east-central British Columbia. British Columbia Ministry of Energy, Mines and Petroleum Resources, British Columbia Geological Survey GeoFile 2018-6, 72 p.

Rukhlov, A.S., Mao, M., Spence, J., Creaser, R.A., Czech, E., and Gabites, J., 2018b. Mineral chemistry and isotopic systematics of carbonatites and related rocks from the Blue River area. Ministry of Energy, Mines and Petroleum Resources, British Columbia Geological Survey GeoFile 2018-1.

Schiarizza, P., 2019. Geology of the Nicola Group in the Bridge Lake-Quesnel River area, south-central British Columbia. In: Geological Fieldwork 2018, British Columbia Ministry of Energy, Mines and Petroleum Resources, British Columbia Geological Survey Paper 2019-01, pp. 15-30.

Simandl, G.J., Petrus, J.A., Matthew I., Leybourne, M.I., Paradis, S., and Akam, C., 2019. Characterization of primary fersmite from the Mount Brussilof magnesite deposit, southeastern British Columbia. In: Geological Fieldwork 2018, British Columbia Ministry of Energy, Mines and Petroleum Resources, British Columbia Geological Survey Paper 2019-01, pp. 113-123.

van Straaten, B.I., and Wearmouth, C., 2019. Geology of the Latham and Pallen Creek area, northwestern British Columbia: Distinguishing the Tsaybahe group, Stuhini Group, and Hazelton Group, and the onset of Triassic arc volcanism in northern Stikinia. In: Geological Fieldwork 2018, British Columbia Ministry of Energy, Mines and Petroleum Resources, British Columbia Geological Survey Paper 2019-01, pp. 79-96.

## In Memoriam

On November 20, 2018 Brian Grant, a former long-time member of the British Columbia Geological Survey, passed away peacefully surrounded by family. Brian first joined the Survey in 1986 as part the MINFILE group. He was later appointed head of the Scientific Review Office and then became Director of Regional Mapping and Economic Geology before leaving in 2008 to pursue interests in the private sector. Brian made an enormous contribution to the Survey during his time as editor by ensuring that all publications were of a high standard. He made the Survey and its employees look great! Brian's career in the mineral exploration and mining community spanned more than 50 years. After starting a degree in aerospace engineering at St. Francis Xavier University, Brian changed gears and entered the geology program at Memorial University in Newfoundland, where he completed his degree in 1974. He worked on many projects in North America, Africa, and South America, exploring for massive sulphides, gold, diamonds, tin, nickel, porphyries, uranium, coal, and industrial minerals. Between 2008 and 2012, Brian was President and Director of Goldbrook Ventures Inc. where he oversaw the exploration for Ni-Cu-PGE-bearing sulphides in the Raglan Belt of the Ungava Peninsula. Brian then took on advisory and consulting roles, serving on the board of several companies (Rockland Minerals Corp., Tasu Global Resources Inc., Masuparia Gold, Quadra Mining Corp.) and undertaking general contracting in the exploration community. Brian will be missed by his family, members of the British Columbia Geological Survey, and the exploration community.

# Geology of the Nicola Group in the Bridge Lake-Quesnel River area, south-central British Columbia

Paul Schiarizza[1, a]

[1] British Columbia Geological Survey, Ministry of Energy, Mines and Petroleum Resources, 300-865 Hornby Street, Vancouver, BC, V6Z 2G3

[a] corresponding author: Paul.Schiarizza@gov.bc.ca

Recommended citation: Schiarizza, P., 2019. Geology of the Nicola Group in the Bridge Lake-Quesnel River area, south-central British Columbia. In: Geological Fieldwork 2018, British Columbia Ministry of Energy, Mines and Petroleum Resources, British Columbia Geological Survey Paper 2019-01, pp. 15-30.

**Abstract**

The Nicola Group (Triassic) is the principal volcano-sedimentary component of the Quesnel arc terrane. In preliminary investigations to establish a regional stratigraphic framework for the Nicola Group, it was separated into four assemblages, which are refined here based on new work. Assemblage one is represented mainly by the Spanish Mountain unit (new informal name), exposed along the eastern margin of the Nicola belt and consisting of Middle Triassic siltstone, chert and argillite, with less common volcaniclastic sandstone and local pillowed basalt with N-MORB and E-MORB geochemical characteristics. Undated, but possibly correlative rocks in the south-central part of the Nicola belt include volcaniclastic sandstone, chert, pyroxene-phyric basalt and basalt breccia of the Wavey Lake unit (new informal name), which is locally overlain by early Carnian siltstone of the Meridian Lake unit (new informal name). Assemblage two (Carnian and early Norian), the most widespread subunit of the Nicola Group, contains volcanic sandstone and conglomerate, locally intercalated with pyroxene-phyric basalt and basalt breccia. Assemblage three is a relatively homogeneous succession of pyroxene-phyric basalt flows and related breccias and is considered Norian based on its stratigraphic position between assemblages two and four. Assemblage four (late Norian and Rhaetian) may be separated from older Nicola rocks by an unconformity or disconformity. It consists of red and maroon polymictic conglomerate with abundant hypabyssal and plutonic rock fragments, as well as red feldspathic sandstone and distinctive volcanic rocks that include analcime basalt and coarse, crowded plagioclase-phyric andesite.

The Nicola Group is flanked to the east by Middle and Upper Triassic slate, siltstone and quartz sandstone of the Slocan Group, part of a siliciclastic basin that formed east of, and coeval with, the Nicola arc. Two small fault-bounded inliers of Permian limestone and siltstone in the southern part of the Nicola belt are tentatively correlated with the Harper Ranch Group, which is therefore inferred to underlie the Nicola Group. Lower to Middle Jurassic polymictic conglomerate and sandstone of the Dragon Mountain succession overlie the Nicola Group and are the youngest stratified rocks in this part of Quesnel terrane. Upper Triassic to Lower Jurassic calcalkaline and alkaline plutonic rocks that cut the Nicola Group correlate with plutonic suites recognized regionally in Quesnel terrane, and include a latest Triassic monzodiorite suite that is coeval with assemblage four and hosts significant porphyry Cu-Au deposits.

**Keywords:** Nicola Group, Slocan Group, Quesnel terrane, Middle Triassic, Upper Triassic, volcanic arc, back-arc basin, basalt, basalt breccia, volcanic sandstone, Spanish Mountain unit, Wavey Lake unit, Meridian Lake unit

## 1. Introduction

The Nicola Group (Triassic) is the principal volcano-sedimentary component of the Mesozoic arc complex that is the defining feature of Quesnel terrane. Calcalkaline and alkaline intrusions in this arc complex host numerous porphyry Cu ±Au-Mo-Ag deposits, making it an important melallogenic belt and exploration target. In 2015, the British Columbia Geological Survey initiated a multi-year field-based program to establish a regional stratigraphic framework for the Nicola Group. This framework, combined with space-time-composition patterns of associated plutons, will contribute to a better understanding of the architecture of the arc, and improve the geologic framework within which to interpret the settings and controls of mineral occurrences.

Initial investigations in 2015 covered the entire width of Quesnel terrane in the Bridge Lake-Quesnel River area (Fig. 1), and established a preliminary stratigraphic framework for the Triassic rocks, comprising four assemblages in the

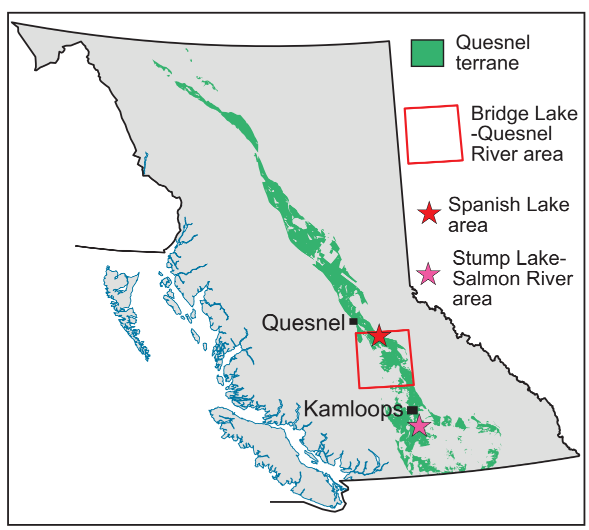


**Fig. 1.** Distribution of Quesnel terrane rocks in British Columbia and locations of areas studied from 2015 to 2018.

Nicola Group, and a separate assemblage to the east assigned to the Slocan Group (Schiarizza, 2016). In 2016, the eastern part of the Nicola Group and the adjacent Slocan Group were studied in the Stump Lake-Salmon River area, south of Kamloops (Schiarizza, 2017). Fieldwork in 2017 also focused on the eastern part of the Nicola Group and the adjacent Slocan Group, but in the Spanish Lake area (Fig. 1, Schiarizza, 2018). The 2018 field program included additional work in the Spanish Lake area, as well as studies at several other localities in the Bridge Lake-Quesnel River area, resulting in refinements and modifications to the stratigraphic scheme presented in Schiarizza (2016). This modified stratigraphic framework for the Nicola Group is presented here, along with descriptions of associated units, providing a summary of all Quesnel terrane map units in the Bridge Lake-Quesnel River area.

## 2. Overview of Quesnel terrane in southern British Columbia

Quesnel terrane (Quesnellia) was defined in the early 1980s, when the concept of tectonostratigraphic terranes was first applied to tectonic analysis of the North American Cordillera (Coney et al., 1980; Monger et al., 1982; Jones et al., 1983). It consists of upper Paleozoic and lower Mesozoic volcanic, sedimentary and plutonic rocks exposed west of pericratonic rocks and Slide Mountain terrane, and east of Cache Creek terrane (Monger et al., 1991; Wheeler et al., 1991). As with many other large terranes defined in the early days of terrane analysis, Quesnellia is not a simple or discreet tectonic entity. Instead it includes a number of different tectonic assemblages, with a variety of internal and external contact relationships.

Quesnel terrane contains mainly Triassic rocks, which record two tectonostratigraphic settings, a volcanic arc in the west, and a siliciclastic basin to the east. The volcanic arc is represented mainly by the Nicola Group (Middle and Upper Triassic), which forms a single linear belt that extends from the international boundary northward to, and beyond, Quesnel (Fig. 2). This belt also includes Late Triassic to Early Jurassic calcalkaline and alkaline arc intrusions, and Lower to Middle Jurassic arc-derived siliciclastic sedimentary rocks of the Ashcroft Formation and Dragon Mountain succession. Basement to the Nicola Group is not well exposed, but is locally represented by Permian sedimentary rocks of the Harper Ranch Group, one of the Paleozoic components of Quesnel terrane (Schiarizza et al., 2002; this study).

East of the Nicola arc, the siliciclastic basin is preserved as scattered Triassic remnants in an arcuate belt extending from Kootenay Lake northwest to beyond Quesnel Lake (Fig. 2). It is represented mainly by the Slocan Group (Little, 1960; Thompson et al., 2006), but also includes the Brooklyn Formation (Fyles, 1990), the Wallace Formation (Massey, 2010) and local occurrences of Triassic siliciclastic rocks near the eastern margin of the Nicola belt that were included in the Nicola Group by previous workers (Read and Okulitch, 1977; Ray and Dawson, 1994), but show no clear ties to the Nicola arc complex. Siltstone and slate predominate, but quartz sandstone, limestone and conglomerate are also present, as are local occurrences of calcalkaline arc volcanic rocks (Dostal et al., 2001; Massey, 2010). These Triassic rocks rest stratigraphically above a variety of units, including pericratonic rocks, Slide Mountain terrane, and Paleozoic units of Quesnel terrane, commonly across an angular unconformity (Read and Okulitch, 1977; Fyles, 1990; Thompson et al., 2006). They are overlain, mainly in the Nelson area (Fig. 2), by Lower Jurassic arc volcanic rocks of the Rossland Group (Höy and Dunne, 1997).

Paleozoic rocks assigned to Quesnel terrane include a large number of units that Monger et al. (1991) grouped into the oceanic Okanagan subterrane and the arc-like Harper Ranch subterrane (Fig. 2). The Okanagan subterrane, predominantly chert and basalt, might be part of Slide Mountain terrane (Monger et al., 1991). It crops out mainly as an east-west belt just north of the international boundary, where it is locally overlain by Triassic rocks of the Slocan basin across an angular unconformity (Read and Okulitch, 1977; Fyles, 1990).

The Harper Ranch subterrane is represented mainly by its namesake, the Harper Ranch Group, which in its type area northeast of Kamloops includes upper Paleozoic arc-derived volcaniclastic rocks and Carboniferous and Permian limestones (Smith, 1979; Beatty et al., 2006). Correlative rocks to the southeast include the Mount Roberts Formation (Little, 1982) and the Attwood Group (Fyles, 1990) which are exposed southwest of Nelson. These upper Paleozoic units are overlain by Triassic rocks of the Slocan basin, but Triassic rocks are locally missing, and parts of the Mount Roberts Formation and Harper Ranch Group are directly overlain by Lower Jurassic volcanic rocks of the Rossland Group (Fig. 2; Little, 1982; Acton et al., 2002; Beatty et al., 2006). Small inliers of Permian rocks in the Nicola Group in the southern part of the Bridge Lake-Quesnel River area suggest that parts of the Harper Ranch Group also underlie the Nicola arc (Schiarizza et al., 2002). A narrow fault-bounded belt of metamorphic rocks along the southwest margin of the Nicola Group, southwest of Princeton, may also be part of the Harper Ranch subterrane (Fig. 2), but its relationship to the Harper Ranch Group is unknown. These rocks comprise the Eastgate-Whipsaw metamorphic belt of Massey and Oliver (2010), and include arc-derived metasedimentary rocks intercalated with Lower Permian bimodal arc volcanic rocks (Oliver, 2011).

## 3. Setting of the Bridge Lake-Quesnel River area

The Bridge Lake-Quesnel River area is mainly in the Fraser Plateau, Quesnel Highland and Shuswap Highland physiographic provinces (Holland, 1976), and covers parts of the traditional territories of the Secwepemc, Esk'etemc, Tsilhqot'in, and Lhtako Dené First Nations. In this area, the Nicola Group forms a northwest-trending belt that is 30 to 70 km wide (Fig. 3). This belt also includes Upper Triassic to Lower Jurassic calcalkaline and alkaline arc intrusions, Lower to Middle Jurassic arc-derived siliciclastic sedimentary rocks of the Dragon Mountain succession, and in the south, two

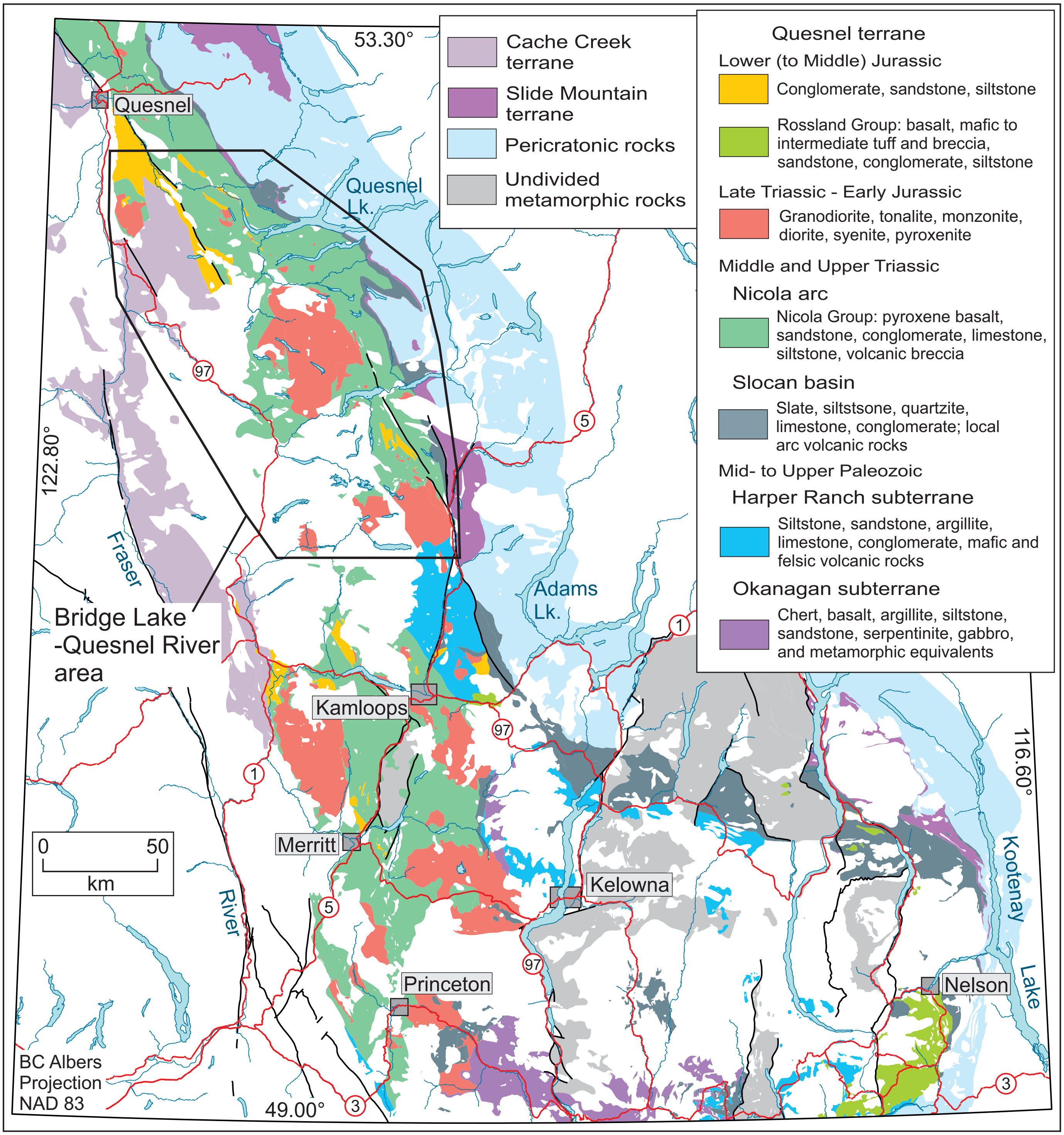


**Fig. 2.** Geology of south-central British Columbia highlighting the different components of Quesnel terrane. Upper Triassic-Lower Jurassic intrusions shown only where they cut the Nicola Group. Uncoloured areas mainly Middle Jurassic to Recent intrusive, volcanic and sedimentary rocks, but may include older rocks of uncertain correlation.

small fault-bounded inliers of Permian limestone and siltstone, tentatively correlated with the Harper Ranch Group.

The Nicola belt is flanked to the east by Triassic sedimentary rocks, mainly black phyllite, slate, and quartz sandstone, of the Slocan Group. Farther east are rocks of Slide Mountain terrane, including basalt, chert and gabbro of the Fennell Formation south of the Raft batholith, and a narrow belt of mafic schist, referred to as the Crooked amphibolite, to the north. East of, and structurally beneath Slide Mountain terrane are pericratonic rocks of Kootenay terrane, including Proterozoic and Paleozoic quartzites and pelitic schists (Snowshoe Group) locally cut by Devono-Mississippian granitic rocks (Quesnel Lake gneiss).

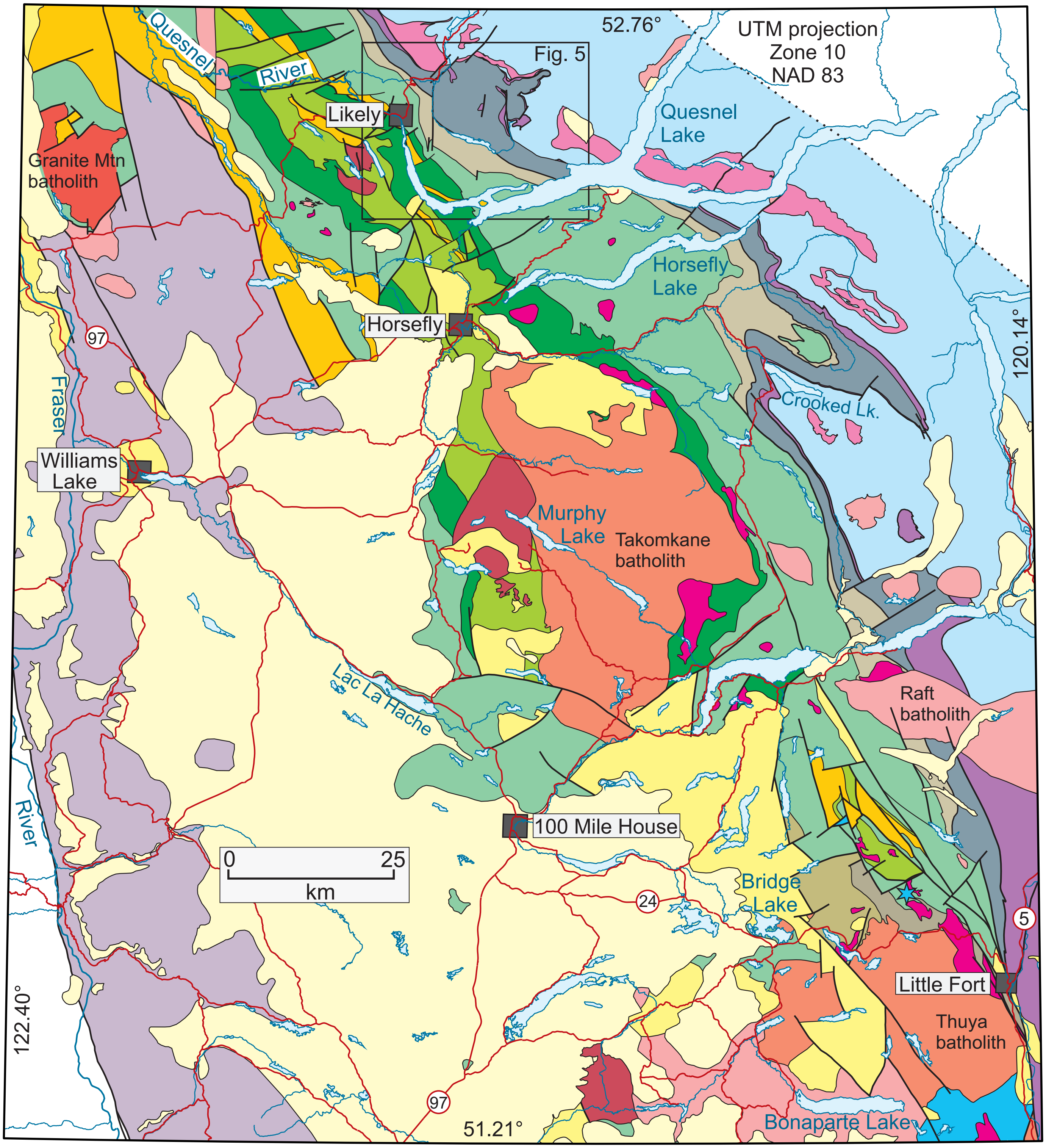


**Fig. 3a.** Geology of the Bridge Lake-Quesnel River area showing Nicola Group subdivisions from this study.

Cache Creek terrane, represented by late Paleozoic to early Mesozoic basalt, chert, limestone, siltstone and ultramafic rocks of the Cache Creek complex, is west of the Nicola belt and is generally interpreted as an accretionary complex genetically related to the subduction that generated the Nicola arc. Younger rocks found in the area include Middle Jurassic and Lower Cretaceous granitic intrusions, Eocene volcanic and sedimentary rocks, and flat-lying Neogene and Quaternary basalt.

The structural history of the area is protracted and complex. Early structures include an east-directed Permo-Triassic (McMullin et al., 1990) or Early Jurassic (Rees, 1987) thrust

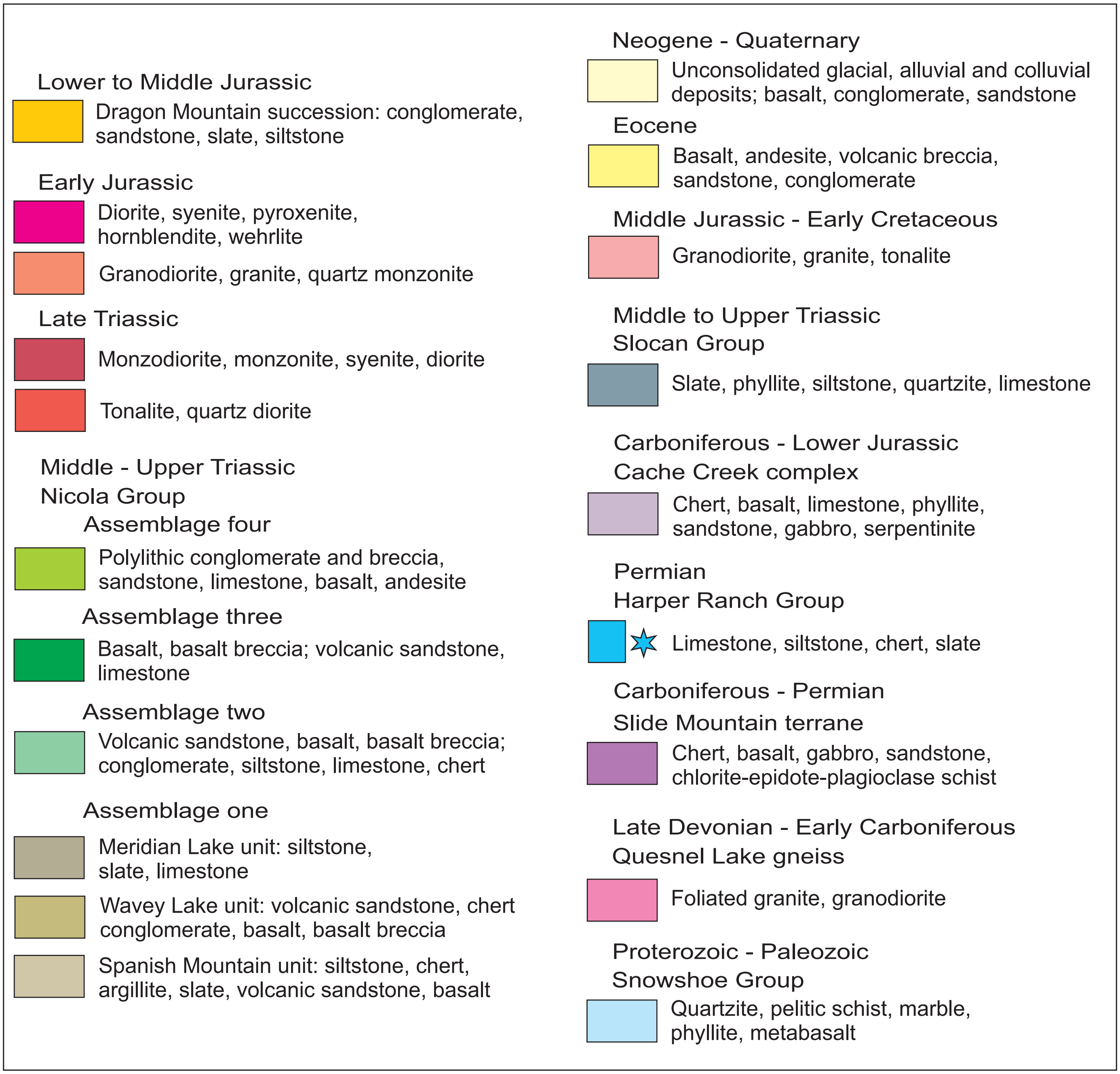


**Fig. 3b.** Legend for Figure 3a.

fault that separates Slide Mountain terrane from underlying pericratonic rocks, and an east-directed Early Jurassic thrust fault (Spanish thrust) that juxtaposes the Nicola Group above the Slocan Group (Struik, 1988). Subsequent contractional deformation and metamorphism that began in the early Middle Jurassic is reflected in polyphase mesoscopic structures in Kootenay terrane, Slide Mountain terrane, the Slocan Group, and eastern parts of the Nicola Group, as well as map-scale structures that fold these units and their mutual contacts (Campbell, 1971; Rees, 1987; Bloodgood, 1990; Fillipone and Ross, 1990). Equivalent structures are not well documented in the central part of the Nicola belt, but it is suspected that a regional syncline (Panteleyev et al., 1996), reflected in the distribution of the younger units of the Nicola Group (Fig. 3), formed at the same time. The youngest, and commonly most prominent structures in the region include sets of Eocene dextral strike-slip and extensional faults (Struik, 1993; Panteleyev et al., 1996; Schiarizza and Israel, 2001).

## 4. The Nicola Group

Schiarizza (2016) subdivided the Nicola Group in the Bridge Lake-Quesnel River area into four regional assemblages, and described how these assemblages related to Nicola subdivisions used in previous studies (Struik, 1983, 1988; Rees, 1987;

Bloodgood, 1990; Panteleyev et al., 1996; Schiarizza et al., 2013). These same four assemblages, with some modifications, are retained here (Fig. 4).

### 4.1. Assemblage one

Schiarizza (2016) defined assemblage one as a narrow belt of Middle Triassic rocks, predominantly siltstone and argillite, that forms the northeastern margin of the Nicola belt from Crooked Lake northward to beyond the Quesnel River (Fig. 3). Here, the definition is expanded to include these rocks and correlatives to the south (Spanish Mountain unit), and rocks that form the base of the Nicola Group east of Bridge Lake (Wavey Lake unit and Meridian Lake unit).

#### 4.1.1. Spanish Mountain unit (new informal name)

The Spanish Mountain unit includes rocks forming the northeast margin of the Nicola belt between Crooked Lake and the north boundary of the map area, as well as a narrow belt of similar rocks that forms the east margin of the Nicola belt farther south, on both sides of the Raft batholith (Figs. 3, 5). The northern belt was assigned to assemblage one by Schiarizza (2016), but the southern belt comprises rocks that were previously included in the Slocan Group.

The Spanish Mountain unit consists mainly of dark to medium grey siltstone, argillite, chert, and slate, but also includes feldspathic sandstone, basalt, and limestone. Chert, argillite, siltstone, and local quartzose siltstone commonly

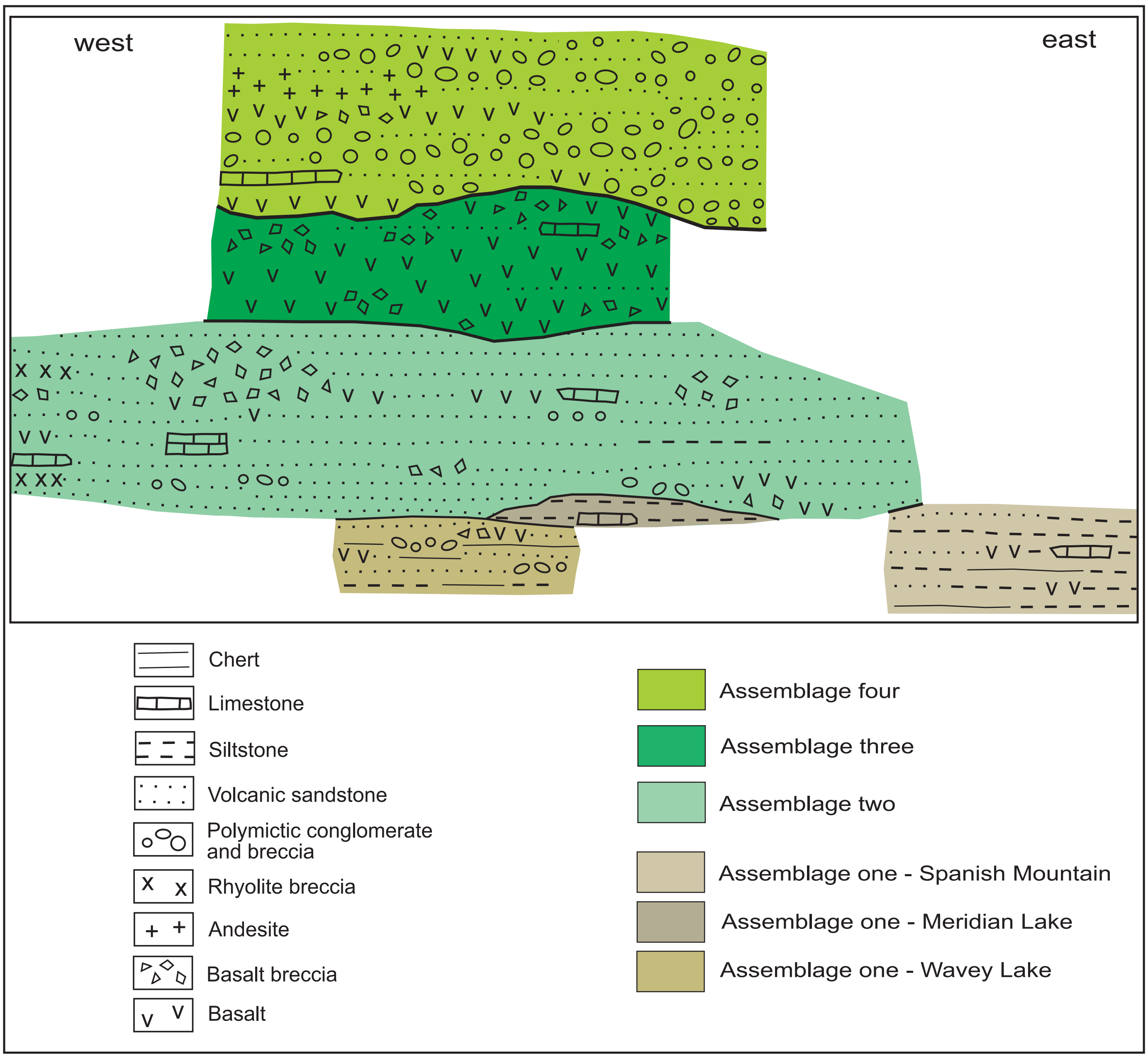


**Fig. 4.** Schematic summary of Nicola Group subdivisions in the Bridge Lake-Quesnel River area.

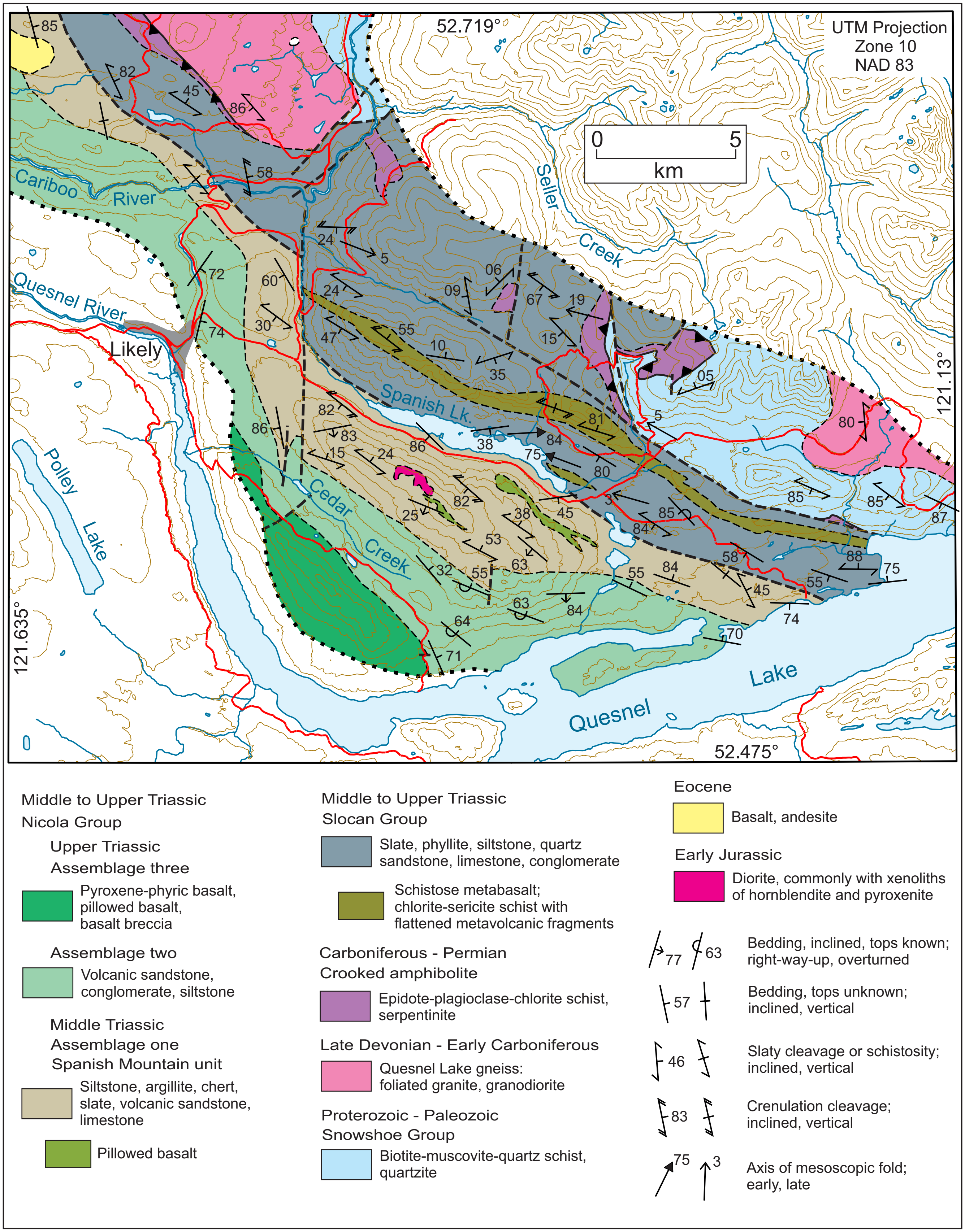


**Fig. 5.** Geology near Spanish Lake, in the northeast part of the Bridge Lake-Quesnel River study area. Geology based on fieldwork in 2015, 2017 and 2018, with information from Rees (1987) and Bloodgood (1990).

form thin (1-4 cm) lenticular beds separated by dark greenish -grey chloritic partings and/or thin interbeds of dark grey slate (Fig. 6). Siltstone and slaty siltstone also occur in sections of thin (1-10 cm) planar beds, and dark grey slate with lighter grey siltstone laminae occurs locally. Medium to dark grey limestone is rare, and forms layers or lenses, <2 m thick, intercalated with siltstone.

Green to grey, medium- to coarse-grained sandstone, very similar to the sandstone of assemblage two, occurs locally within the Spanish Mountain unit, as thin- to thick-bedded intervals intercalated with siltstone. Feldspar is the predominant constituent, and is accompanied by feldspathic lithic grains and altered mafic lithic and mineral grains. Volcanic quartz is a conspicuous component of some sandstone beds on the low ridge east of Likely (Fig. 5).

In the Spanish Lake area, two separate lenses of pillowed to massive basalt are mapped in the Spanish Mountain unit (Fig. 5). These lenses are lithologically distinct from the pyroxene-phyric arc basalts found in other parts of the Nicola Group, and display geochemical characteristics of normal mid-ocean ridge basalt (eastern lens, Logan and Bath, 2006) and enriched mid-ocean ridge basalt (western lens, this study, geochemical analysis in progress).

The Spanish Mountain unit is early Middle Triassic, at least in part, based on conodonts extracted from two different limestone lenses in the Spanish Lake area. One collection, from the northeast side of the assemblage on the north shore of Quesnel Lake is early-middle Anisian (Struik, 1988), and the other, from the central part of the unit 2 km south of the east end of Spanish Lake, is early Anisian (Panteleyev et al., 1996). Schiarizza (2016, 2018) suggested that a collection of late Ladinian to Carnian (Middle to Late Triassic) conodonts from the north shore of Quesnel Lake, about 3 km west-southwest of the Anisian locality (Struik, 1988) might also place constraints on the age of the Spanish Lake unit. However, fieldwork in 2018 shows that this collection is from Nicola assemblage two, several hundred metres south of the unexposed contact with the Spanish Mountain unit.

#### 4.1.2. Wavey Lake unit (new informal name)

The Wavey Lake unit is an undated succession exposed north of the Thuya batholith, east and north of Bridge Lake (Fig. 3). It was recognized as a unique part of the Nicola Group by Schiarizza et al. (2002) because of its significant chert content, and because its stratigraphic position beneath Carnian rocks of the Meridian Lake unit indicated that the volcanic rocks in the Wavey Lake unit are older than Nicola volcanic units to the east and northeast. It is included in assemblage one because of this relatively low stratigraphic position, and because assemblage one (Spanish Mountain unit) is the only other section in the area with significant amounts of chert.

The Wavey Lake unit contains abundant grey to green chert, which forms thin lenticular beds intercalated with slate, argillite and siltstone (Fig. 7). Chert-rich sections, up to 10 m thick, are intercalated with massive and thin- to medium-bedded, fine- to coarse-grained volcanic sandstone, which locally forms channels that cut into the chert. The Wavey Lake unit also includes pyroxene-phyric basalt flows, pyroxene porphyry breccias (Fig. 8), and polymictic pebble to cobble conglomerate units up to several 10s of m thick. The conglomerate contains subangular to rounded clasts of mainly laminated siltstone, cherty argillite, and argillite, but also includes fragments of chert, limestone, pyroxene-plagioclase-phyric basalt, and microdiorite.

The Wavey Lake unit is overlain to the northeast by volcanic sandstone of assemblage two or by siltstone of the Meridian Lake unit (Figs. 3 and 4). The base of the unit is not exposed because it is bounded on the southwest by a system of normal faults that juxtaposed it with Eocene volcanic rocks. Although undated, it is considered Middle Triassic or very early Upper Triassic, based on its stratigraphic position beneath the Meridian Lake unit.

**Fig. 6.** Bedded chert, Spanish Mountain unit, assemblage one of the Nicola Group, south of Spanish Lake.

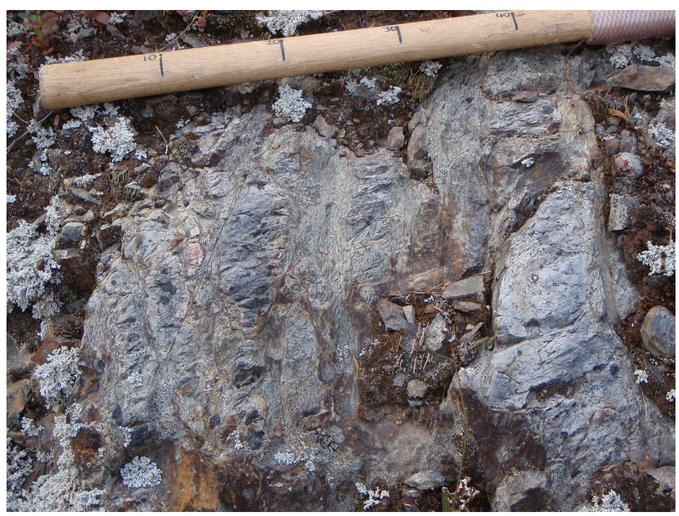

**Fig. 7.** Bedded chert, Wavey Lake unit, assemblage one of the Nicola Group, east of Bridge Lake.

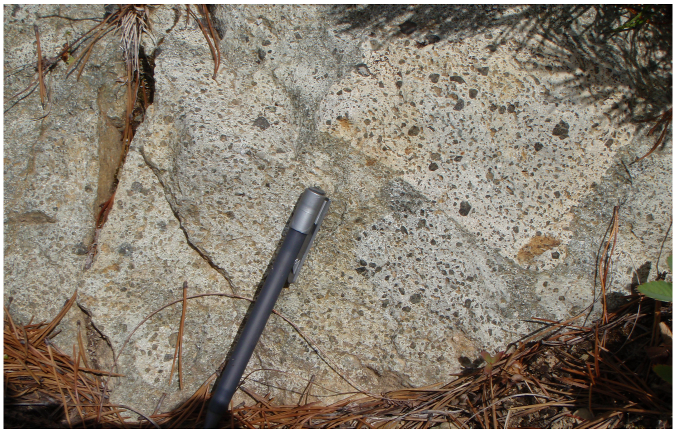

**Fig. 8.** Pyroxene porphyry breccia, Wavey Lake unit, assemblage one of the Nicola Group, northeast of Bridge Lake.

### 4.1.3. Meridian Lake unit (new informal name)

The Meridian Lake unit comprises siltstone that crops out on the north and northeast margins of the Thuya batholith (Fig. 3), where it is underlain by the Wavey Lake unit, and overlain by rocks of assemblage two. Schiarizza (2016) provisionally included it in the lower part of assemblage two, but noted that it is lithologically similar to the Slocan Group. Here, it is included in assemblage one because of its fine-grained nature and stratigraphic position beneath coarser grained volcanic sandstones and conglomerates that are typical of assemblage two.

The Meridian Lake unit consists mainly of rusty weathered, dark to medium grey, laminated to thinly bedded siltstone and slaty siltstone, locally with laminae and thin beds of light grey quartzose siltstone (Fig. 9), or thin interbeds of dark grey argillite and cherty argillite. Dark grey micritic limestone and limy argillite form local thin to thick beds intercalated with siltstone and argillite. One of these limestone beds yielded early Late Triassic (Carnian) conodonts, and another contains Middle or Late Triassic (late Ladinian to early Carnian) conodonts (Schiarizza et al., 2013).

**Fig. 9.** Thinly bedded light grey (quartzose) and dark grey siltstone, Meridian Lake unit, assemblage one of the Nicola Group, northwest of Little Fort.

The Meridian Lake unit is included in the Nicola Group (assemblage one) because it is both underlain and overlain by Nicola Group rocks (Wavey Lake unit and assemblage two). However, as noted by Schiarizza (2016), it is markedly similar to the Slocan Group in lithology and age. It may represent a tongue of Slocan Group-type rocks and an interfingering relationship between the Nicola Group and the Slocan Group.

### 4.2. Assemblage two

Assemblage two, predominantly volcanic sandstone and pyroxene-phyryic basalt and breccia, is the most widespread component of the Nicola Group in the study area (Fig. 3). The definition of the assemblage used here follows that originally proposed by Schiarizza (1016), but excludes the Wavey Lake and Meridian Lake units (here included in assemblage one), and a small area 20 km northeast of Bridge Lake (here inferred to be an outlier of assemblage four).

The predominant and characteristic lithology of assemblage two is grey to green, fine- to coarse-grained, commonly gritty, volcanogenic sandstone, consisting mainly of feldspar, pyroxene and volcanic lithic grains (Fig. 10). The sandstone is well bedded in places, but elsewhere forms massive units up to several 10s of m thick. In well-bedded sections, thin to thick sandstone beds commonly alternate with thin beds of green to grey siltstone or dark grey argillite, and locally display graded bedding, flame structures, and rip-up clasts. Pebble conglomerate and pebbly sandstone occur locally, as medium to very thick beds intercalated with sandstone. The pebbles are predominantly pyroxene-feldpar-phyric basalt, but some conglomerate units also contain limestone, siltstone, and sandstone clasts.

Basalt and basalt breccia are a common component of assemblage two, forming units up to several 100 m thick that occur at different stratigraphic levels and widespread geographic locations (Schiarizza, 2016). These volcanic units include pillowed and massive pyroxene-plagioclase-phyric basalt, but volcanic breccia (Fig. 11), locally intercalated with lenses and

**Fig. 10.** Parallel-stratified and massive gritty volcanic sandstone, assemblage two of the Nicola Group, east of the Takomkane batholith.

**Fig. 11.** Volcanic breccia with angular to subrounded pyroxene porphyry clasts in a sandy matrix with feldspar, pyroxene, and mafic lithic grains, assemblage two of the Nicola Group, southwest of Crooked Lake.

layers of dark green pyroxene-rich sandstone, is predominant. Most breccia units comprise angular to subangular fragments of pyroxene±plagioclase-phyric basalt within a gritty to sandy matrix of feldspar, pyroxene, and mafic lithic grains.

Felsic volcanic rocks are very rare in assemblage two, but rhyolite-clast volcanic breccias are in the Granite Mountain area (Schiarizza, 2014), and breccias with felsic volcanic clasts (Fig. 12) were also identified in 2018, in a small inlier 13 km south-southwest of 100 Mile House (Fig. 3). A third occurrence of felsic rocks is 23 km northwest of Little Fort, where massive and fragmental feldspar-phyric dacite forms a set of isolated outcrops in an area with mainly basalt and basalt breccia (Schiarizza and Israel, 2001; unit uTrNbf of Schiarizza et al., 2013).

Limestone is a very minor component of assemblage two, but thin intervals of dark grey limestone and silty limestone, up to a few m thick, occur locally. A thicker limestone unit forms an isolated ridge 10 km southeast of Lac La Hache (Schiarizza and Bligh, 2008), and a poorly exposed, but apparently substantial limestone interval occurs west of Antoine Lake, 14 km northwest of Horsefly (Logan et al., 2007a).

**Fig. 12.** Breccia with felsic volcanic fragments, assemblage two of the Nicola Group, 13 km south-southwest of 100 Mile House.

Conodonts and macrofossils from a few scattered localities in assemblage two (summarized by Schiarizza, 2016) indicate that it is Late Triassic, early Carnian to early Norian.

### 4.3. Assemblage three

Schiarizza (2016) described assemblage three as a succession of mafic volcanic flows and breccias that occur above assemblage two. As originally defined, the upper part of the unit included analcime basalt (Horsefly-Likely area), and hornblende-bearing basalt (north of the Quesnel River). However, subsequent work has shown that these basalts are intercalated with sedimentary rocks of assemblage four, within which they are now placed. As thus redefined, assemblage three is a relatively homogeneous succession of pyroxene-phyric basalt flows and related breccias. It lies between assemblage two and assemblage four, and crops out as two separate belts that define the limbs of a regional syncline (Fig. 3).

Assemblage three contains mainly dark green, locally grey or maroon, brownish-weathered, massive and pillowed basalts, typically with abundant pyroxene phenocrysts that are commonly up to 1 cm (Fig. 13). Plagioclase crystals, smaller and less abundant than pyroxene, are locally part of the phenocryst assemblage; olivine, replaced by iddingsite and other secondary minerals, is also local. Typically the groundmass is defined by an alteration assemblage of calcite, epidote and chlorite, but it may retain relict plagioclase laths and/or small clinopyroxene grains. Amygdules, filled with various combinations of calcite, epidote, chlorite and quartz, are common.

Breccia, consisting mainly or entirely of pyroxene-phyric basalt fragments, is a common, and locally predominant component of assemblage three. Some are flow breccias, but

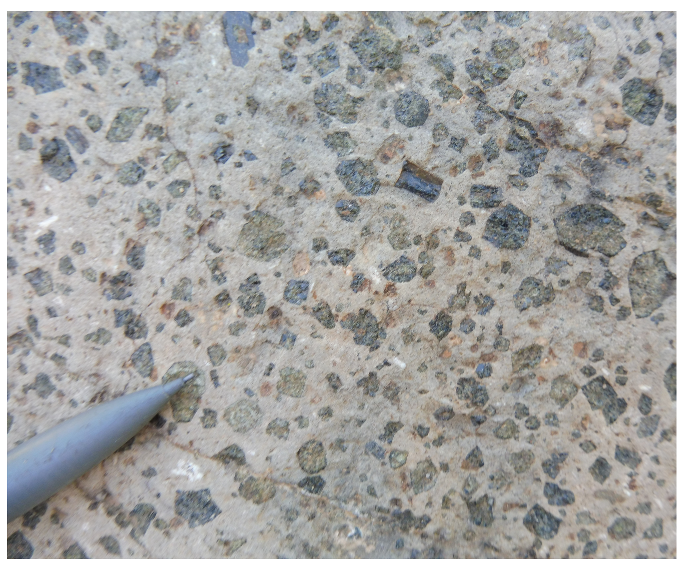

**Fig. 13.** Basalt with abundant coarse pyroxene phenocrysts, assemblage three of the Nicola Group, northeast side of Quesnel Lake south of Likely.

most are interpreted as locally derived epiclastic deposits. These form massive to weakly stratified units, up to several 10s of m thick, with poorly sorted basalt fragments supported by a sandy to gritty matrix with predominantly plagioclase, pyroxene and mafic lithic grains. These breccia units may include thin to thick beds of feldspar-pyroxene sandstone and gritty sandstone. Locally they are intercalated with narrow units of limestone, calcareous mudstone, and siltstone (Schiarizza, 2016).

Assemblage three is not well dated, but is inferred to be Norian, based on its stratigraphic position between assemblage two (Carnian and early Norian), and assemblage four (latest Triassic).

**4.4. Assemblage four**

Assemblage four is a lithologically distinct succession of conglomerates, sandstones and volcanic rocks forming the uppermost part of the Nicola Group, and possibly separated from older parts of the group by an unconformity or disconformity. Schiarizza (2016) noted that it was characterized by polymictic conglomerates containing abundant hypabyssal and plutonic clasts, a common red colour, and a volcanic suite that included a distinctive coarse, crowded plagioclase-phyric andesite. Here, the assemblage is expanded to also include analcime basalt and hornblende-bearing basalt (included in assemblage three by Schiarizza, 2016), making the volcanic component even more distinctive. As currently defined, assemblage four is exposed mainly as a single belt, in the core of the regional syncline, that extends from the north boundary of the study area to the west margin of the Takomkane batholith. As now shown in Figure 3, this belt does not extend as far south as portrayed by Schiarizza (2016) because rocks on the south flank of Mount Timothy are now known to be Eocene. A small outlier of assemblage four occurs 20 km northeast of Bridge Lake (Fig. 3), and consists of polymictic conglomerates and sandstones previously included in assemblage two (Schiarizza, 2016).

The predominant and most characteristic sedimentary rocks in assemblage four are polymictic conglomerates bearing a diverse clast population not seen in older parts of the Nicola Group (Fig. 14). They are commonly green or greenish-grey, but red to purple conglomerates occur throughout the section and are predominant at higher stratigraphic levels. Common clasts include: fine-grained, equigranular to weakly porphyritic feldspathic hypabyssal rocks; fine- to coarse-grained plutonic rocks, including gabbro, diorite, monzodiorite, monzonite, hornblendite, and pyroxenite; and mafic volcanic rocks containing variable proportions of feldspar, pyroxene and hornblende phenocrysts. Clasts are typically angular to subrounded, poorly sorted (from a few mm to 20 cm), and supported in a sandy feldspar-rich matrix, that may also include substantial hornblende and/or pyroxene grains. The conglomerates are commonly massive, but locally display weak stratification that may be accentuated by intercalations of sandstone and pebbly sandstone.

Medium- to coarse-grained, locally gritty, feldspathic sandstone is a common component of assemblage four, and is locally predominant in the upper part of the assemblage west of the Takomkane batholith (Schiarizza and Bligh, 2008; Schiarizza et al., 2009). The sandstones are mostly green to grey-green, but may be red or mottled red and green. They consist largely of feldspar (both plagioclase and pinkish grains that are K-spar and/or hematite-altered plagioclase), along with variably-altered mafic grains (hornblende and/or pyroxene) and fine-grained, chlorite-epidote-calcite-altered matrix. Thin to medium beds are locally well defined by distinct units of contrasting grain size, ranging from coarse, gritty sandstone to siltstone, but in some areas the sandstone is massive, or displays only vague laminations or indistinct platy to flaggy partings.

**Fig. 14.** Polymictic conglomerate with volcanic and plutonic clasts, assemblage four of the Nicola Group, northwest of Murphy Lake.

Grey limestone, locally at least several 10s of m thick, is intercalated with sandstone and conglomerate in the lower part of assemblage four west of Likely. It is exposed on both limbs of the regional syncline and on the southwest limb is traced, intermittently, for 6 km southeast from the Likely highway. Narrow lenses of skarn-altered limestone are intercalated with sandstone and conglomerate in the lower part of assemblage four also on the west side of the Takomkane batholith, south and southwest of Murphy Lake (Schiarizza and Bligh, 2008).

Volcanic rocks are a substantial part of assemblage four and include pyroxene-phyric basalt and basalt breccia not unlike volcanic units of assemblages two and three, as well as analcime basalt, hornblende-bearing basalt and plagioclase-phyryic andesite, found only in assemblage four. Analcime basalt is particularly prominent in the Horsefly-Likely area (Campbell, 1978; Panteleyev et al., 1996; Logan et al., 2007a). Analcime (Fig. 15) forms euhedral crystals in pyroxene±plagioclase±olivine-phyric basalt flows and related breccias that are intercalated with conglomerates and sandstones in the lower part of the assemblage, locally directly overlying assemblage three. Hornblende-pyroxene-plagioclase-phyric basalt along the northern boundary of the study area north of the Quesnel River (Panteleyev et al., 1996; Logan et al., 2007a), was not examined during this study,

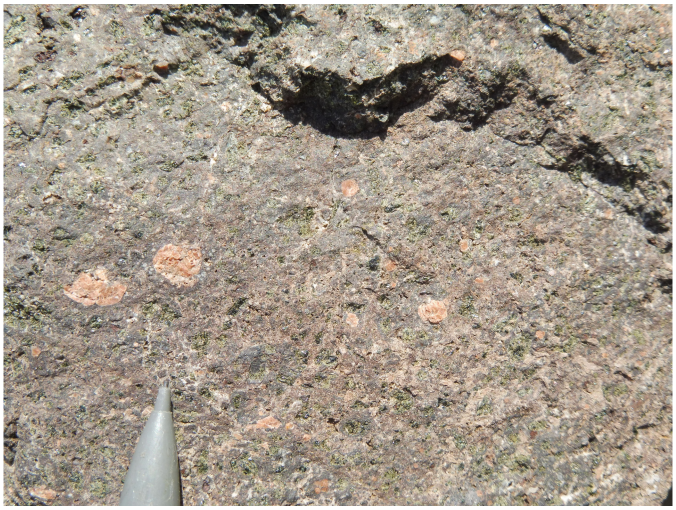

**Fig. 15.** Analcime-bearing pyroxene-phyric basalt, assemblage four of the Nicola Group, west of Likely.

but is tentatively included in assemblage four because it is associated with sedimentary rocks typical of this assemblage, and because hornblende-pyroxene-plagioclase-phyric basalt occurs in assemblage four in the Stump Lake-Salmon River area (Schiarizza, 2017). Coarse, crowded plagioclase-phyric andesite is a distinctive assemblage four volcanic rock along the west side of the Takomkane batholith, near its north end. It forms a single mappable unit (uTrNtp of Schiarizza et al., 2013), intercalated with conglomerate, sandstone, and pyroxene-phyric basalt, that has been traced for about 5 km. Schiarizza (2016) suggested that similar andesite exposed farther south, on the south flank of Mount Timothy, might also be part of assemblage four, but these rocks are now known to be Eocene (unpublished U-Pb zircon age of 50.84 ±0.04 Ma, Richard Friedman, The University of British Columbia), as originally mapped by Schiarizza and Bligh (2008) and Schiarizza et al. (2013).

Assemblage four is mainly or entirely Late Triassic because it rests above Norian rocks of assemblages two and three, and is locally cut by latest Triassic plutonic rocks (202-205 Ma; Logan et al., 2007b; Schiarizza et al, 2013). A very late Triassic age is confirmed by a U-Pb zircon date of 203.9 ±0.4 Ma from the plagioclase-phyric andesite that is part of the assemblage on the northwest margin of the Takomkane batholith (Schiarizza et al., 2013).

## 5. Other components of Quesnel terrane in the Bridge Lake-Quesnel River area

The Nicola Group in the Bridge Lake-Quesnel River area is spatially associated with several other Quesnel terrane units. These include: the Slocan Group (Triassic), east of the Nicola Group; rare exposures of Late Paleozoic rock (correlated with the Harper Ranch Group) inferred to underlie the Nicola Group; and Jurassic siliciclastic rocks (Dragon Mountain succession) stratigraphically above the Nicola Group. Plutonic rocks of Quesnel terrane include two Upper Triassic suites, coeval with the Nicola Group, and two Lower Jurassic suites.

### 5.1. Paleozoic rocks

Upper Paleozoic rocks, tentatively correlated with the Harper Ranch Group, outcrop on the south side of the Thuya batholith, east of Bonaparte Lake, and as two small fault-bounded inliers in the Nicola belt north of the batholith (Fig. 3). The rocks south of the Thuya batholith comprise undated siltstone, limestone and volcaniclastic sandstone that form the north end of a belt that extends southward into the type area of the Harper Ranch Group, east of Kamloops (Fig. 2; Smith, 1979; Beatty et al., 2006). The largest inlier in the Nicola belt north of the batholith forms a triangular fault block on the west slopes of Windy Mountain, 35 km northwest of Little Fort (Fig. 3). It includes fossiliferous limestone, limestone breccia with chert fragments, and laminated to massive chert intercalated with argillite and siltstone (Campbell and Tipper, 1971; Schiarizza et al., 2002). One fossil collection (brachiopods, corals and bryozoans) from this fault block is Permian, and another (fusulinids) is Early Permian (E.W. Bamber and C.A. Ross in Campbell and Tipper, 1971). In a second, smaller Paleozoic inlier, 20 km northwest of Little Fort (blue star on Fig. 3), are a few 10s of m of fossiliferous limestone with thin interbeds of dark grey argillite and chert (Schiarizza et al., 2002). The limestone contains Permian foraminifers and Early-Middle Permian conodonts (Schiarizza et al., 2013). External contacts are not exposed, but these Paleozoic rocks are apparently enclosed in Nicola assemblage two sandstones and conglomerates, a short distance from their contact with underlying Triassic siltstones of the Meridian Lake unit (assemblage one). The Paleozoic rocks might be a large olistolith or a small fault block.

Although exposure is limited, the lithologic attributes and fossil content of the Paleozoic rocks forming the two inliers north of the Thuya batholith suggest correlation with chert-rich carbonate rocks in the McGregor Creek succession (Lower-Middle Permian), which forms the upper unit of the Harper Ranch Group in its type area (Beatty et al., 2006). Stratigraphic contacts are not preserved, but the location of these inliers in the interior of the Nicola belt suggests that the Harper Ranch Group represents, at least in part, basement to the Nicola arc.

### 5.2. Slocan Group

The Slocan Group (Middle and Upper Triassic) forms a continuous belt that extends the full length of the Bridge Lake-Quesnel River area, and separates the Nicola Group to the west from Slide Mountain terrane and underlying pericratonic rocks to the east (Fig. 3). It consists mainly of dark grey to black phyllite, slate, and slaty siltstone, commonly with laminae and thin interbeds of lighter grey quartzose siltstone, and locally with thin to thick beds of quartzite and quartz-rich sandstone (Schiarizza et al., 2002; Schiarizza and Macauley, 2007; Schiarizza, 2018). Dark grey limestone occurs mainly as rare discontinuous lenses (1-2 m), but north of Little Fort, forms thin to thick beds intercalated with siltstone and slate for stratigraphic intervals approaching 100 m (Schiarizza et al. 2002).

Slocan Group volcanic rocks are only in the Spanish Lake area. Based on 2018 fieldwork, volcanic and volcaniclastic rocks shown as several separate lenses by Schiarizza (2018) are actually part of a single mappable unit, up to several 100 m thick, that can be traced for more than 20 km (Fig. 5). This unit includes coherent metabasalt and fragmental metavolcanic rock, as well as biotite-sericite-quartz schist that may have been derived from a fine-grained quartz-rich sedimentary protolith. The metabasalt is a pale to medium green, plagioclase-actinolite-biotite-chlorite (±epidote±calcite) schist that contains relict phenocrysts (1-2 mm) altered to actinolite-biotite-chlorite, and flattened amygdules (1-5 mm) of quartz±biotite. The fragmental rocks are mainly plagioclase-quartz-biotite-chlorite-sericite schists that contain variably flattened metabasalt clasts, but locally include ankerite-chlorite-sericite schists with granules of quartz and feldspar, and strongly flattened fragments of pale grey quartz-sericite schist. Metabasalt from the Slocan Group has geochemical characteristics of subduction-generated arc basalt, but is distinct from typical arc basalt of the Nicola Group to the west (Logan and Bath, 2006).

The age of the Slocan Group is constrained by conodont collections north of Little Fort, and in the Spanish Lake area, north of the west end of Quesnel Lake. Those near Little Fort are Middle and early Late Triassic (Anisian, Ladinian and early Carnian; Schiarizza et al., 2013), and the most diagnostic forms near Spanish Lake (Struik, 1988; Panteleyev et al., 1996) are Middle Triassic (late Anisian-early Ladinian, and Ladinian).

The Slocan Group is inferred to rest unconformably above the Crooked amphibolite of Slide Mountain terrane (Campbell, 1971; Rees, 1987; McMullin et al., 1990; Schiarizza, 2018), but the eastern contact of the group is, in many areas, marked by Jurassic and younger faults (Campbell and Tipper, 1971; Bloodgood, 1990; Schiarizza et al., 2013). The east-directed Spanish thrust (Early Jurassic) is inferred to mark the contact between the Slocan and Nicola groups (Struik, 1988; Bloodgood, 1990), but it too, is commonly overprinted by younger structures (Schiarizza et al., 2013; Schiarizza, 2018).

### 5.3. Dragon Mountain succession

Lower to Middle Jurassic siliciclastic rocks that overlie the Nicola Group and associated Late Triassic plutonic rocks are assigned to the Dragon Mountain succession, following Logan and Moynihan (2009). These rocks are exposed mainly in the northern part of the study area, but also occur in several fault panels northeast of Bridge Lake (Fig. 3; Windy Mountain succession of Schiarizza et al., 2013).

The Dragon Mountain succession consists mainly of interbedded conglomerate and sandstone. Conglomerate units are polymicitic and typically include quartz-bearing plutonic clasts (granite, granodiorite, tonalite), and a variety volcanic clasts derived from the underlying Nicola Group (Schiarizza et al., 2002; Logan and Moynihan, 2009; Schiarizza, 2015). Sandstone units may be very similar to Nicola sandstone (assemblage two), but commonly have a significant proportion of detrital quartz. Sandstone is locally interbedded with substantial amounts of siltstone and argillite. A distinctive facies exposed in the Granite Mountain area (Schiarizza, 2015) and along the Quesnel River north of the study area (Logan and Moynihan, 2009) consists of dark grey slate with laminae and thin interbeds of lighter grey siltstone, and local thin to medium beds of yellowish-brown-weathered quartz-rich sandstone.

Volcanic rocks are generally absent from the Dragon Mountain succession, but Logan and Moynihan (2009) reported that it includes rare pyroxene-phyryic basalt flows north of the study area, and Schiarizza et al. (2002) note that it hosts dikes of pyroxene porphyry in the area northeast of Bridge Lake. Early Jurassic dacitic tuff near the Mount Polley mine, west-southwest of Likely (U-Pb zircon age of 196.7 ±1.3 Ma; Logan et al., 2007b) is apparently part of the succession, but is within an enigmatic panel of rocks that apparently overlies the mineralized Mount Polley intrusive complex nonconformably, but is lithologically very similar to assemblage four of the Nicola Group (Logan et al., 2007a, b).

Macrofossils identified from a number of localities in the Dragon Mountain succession (Panteleyev et al., 1996; Peterson et al., 2004; Logan and Moynihan, 2009; Schiarizza et al., 2013) indicate that it is mainly Lower Jurassic (Sinemurian and Pliensbachian), but locally includes Middle Jurassic (Aalenian and possibly Bajocian) rocks. The composition of conglomerates and sandstones suggests derivation mainly from the Nicola Group and associated plutonic rocks (Panteleyev et al., 1996; Peterson et al., 2004; Logan and Moynihan, 2009). The outcrop distribution of the succession suggests that it may have accumulated, in part, in a number of linear fault-bounded sub-basins (Fig. 3).

### 5.4. Plutonic rocks

Plutonic rocks of Quesnel terrane are subdivided into two Late Triassic intrusive suites which are coeval with parts of the Nicola Group, and two Early Jurassic suites (Fig. 3). Here, and to the south, Quesnel plutons show a general pattern of alternating calcalkaline and alkaline belts, becoming progressively younger from west to east.

#### 5.4.1. Upper Triassic plutons

The oldest Quesnel plutonic rocks in the Bridge Lake-Quesnel River area are tonalites of the Granite Mountain batholith and adjacent Burgess Creek stock, which cut assemblage two of the Nicola Group in the northwest corner of the study area (Fig. 3), and have U-Pb zircon crystallization ages ranging from 215 to 223 Ma (Schiarizza, 2015; Mostaghimi, 2016). They are part of a suite of Late Triassic calcalkaline plutons cutting western exposures of the Nicola Group. South of the study area this suite includes the Guichon Creek batholith (210 Ma; Mortimer et al., 1990) and Allison pluton (223 Ma; Mihalynuk et al., 2016). The Granite Mountain and Guichon Creek batholiths host major calcalkaline porphyry Cu-Mo deposits.

A younger, latest Triassic intrusive suite includes alkaline plutons consisting of monzonite, monzodiorite, diorite and syenite (Fig. 3). This suite includes the Mount Polley intrusive complex and Bootjack Lake stock southwest of Likely (Logan et al., 2007a, b), the Spout Lake pluton and Peach Lake stocks near Murphy Lake (Schiarizza and Bligh, 2008), and the Rayfield River syenite pluton west of Bonaparte Lake (Logan and Schiarizza, 2014). U-Pb zircon ages are mainly 202-205 Ma (Mortensen et al., 1995; Logan et al., 2007b; Schiarizza et al, 2013), although the Rayfield River pluton may be slightly younger (ca. 200 Ma; Logan and Schiarizza, 2014). This linear belt of latest Triassic alkaline plutons continues southward to include the Iron Mask batholith near Kamloops and the Copper Mountain intrusions near Princeton (Schiarizza, 2014). This belt is remarkably well endowed with alkalic porphyry Cu-Au deposits, including the currently producing Mount Polley, New Afton and Copper Mountain mines.

**5.4.2. Lower Jurassic plutons**

The most prominent Lower Jurassic intrusions in the study area are calcalkaline rocks that form the Thuya and Takomkane batholiths (Fig. 3). They consist mainly of hornblende-biotite granodiorite and granite with U-Pb zircon ages ranging from 193 to 197 Ma, although an eastern border phase of the Takomkane batholith (granodiorite and quartz monzodiorite) ranges from 199 to 202 Ma (Schiarizza et al., 2013). These two batholiths are part of a linear belt of five large Early Jurassic calcalkaline batholiths, including the Wild Horse, Pennask and Bromley batholiths to the south, which extends for 300 km and cuts the central and eastern parts of the Nicola belt (Schiarizza, 2014). These batholiths locally host calcalkaline porphyry Cu-Mo deposits, including the past-producing Brenda Mine in the Pennask batholith, and the Woodjam SE zone in the northwestern part of the Takomkane batholith (Logan et al., 2011).

A variety of smaller Early Jurassic intrusions cut the central and eastern parts of the Nicola belt in the Bridge Lake-Quesnel River area (Fig. 3). Diorite, monzonite, quartz monzonite and syenite are most common, but this suite also includes ultramafic-mafic intrusions that are mainly gabbro, diorite, hornblendite and pyroxenite, locally with wehrlite and dunite (Panteleyev et al., 1996; Schiarizza et al., 2013). U-Pb zircon ages range from 196 to 184 Ma (Schiarizza et al., 2013). The youngest dated intrusion (184 Ma; Schiarizza et al., 2013) is an ultramafic-mafic body that cuts the Spanish Mountain unit of assemblage one on the north side of the Raft batholith (Fig. 3). Similar ages (185.6 to 187.3 Ma; Rhys et al., 2009) come from small diorite stocks and dikes, commonly with hornblendite and pyroxenite xenoliths, that cut the Spanish Mountain unit on the south side of Spanish Lake (Fig. 5).

**6. Summary**

With some modifications, the four-fold subdivision presented by Schiarizza (2016) provides a useful stratigraphic framework for the Nicola Group in the Bridge Lake-Quesnel River area. Assemblage one is represented mainly by Middle Triassic siltstone, chert and argillite, with less common volcaniclastic sandstone and local pillowed basalt (N-MORB and E-MORB), along the eastern margin of the Nicola belt (Spanish Mountain unit), but also includes rocks in the south-central part of the belt that were previously included in assemblage two. These include volcaniclastic sandstone, chert, pyroxene-phryic basalt and basalt breccia of the Wavey Lake unit, and overlying early Carnian siltstone of the Meridian Lake unit. Assemblage two (Late Triassic, Carnian and early Norian) is the most widespread component of the Nicola Group, and is mainly volcanic sandstone and conglomerate, locally intercalated with pyroxene-phyric basalt and basalt breccia. Assemblage three is above assemblage two, and is a relatively homogeneous succession of pyroxene-phyric basalt flows and related breccias that are similar to the volcanic rocks in the underlying assemblage. Assemblage four (late Norian and Rhaetian) forms the top of the Nicola Group, and may be separated from underlying rocks by an unconformity or disconformity. It includes red and maroon polymictic conglomerate with abundant hypabyssal and plutonic rock fragments, red feldspathic sandstone, and distinctive volcanic rocks that include analcime basalt and hornblende-bearing basalt (previously included in assemblage three), and coarse, crowded plagioclase-phyric andesite.

Assemblage one is significant in showing that the Nicola arc, represented mainly by Late Triassic rocks, was initiated during, or before, the Middle Triassic. This older part of the arc is not well understood, but includes an eastern back-arc basin represented by the Spanish Mountain unit. The main Late Triassic constructional phase of the Nicola arc is represented by assemblages two and three, which include abundant pyroxene-phyric basalt and related breccia, as well as volcanic sandstones and conglomerates derived from these volcanic rocks. Assemblage four reflects regional uplift and partial unroofing of the arc in the very late Triassic, with continuing volcanism that generated some distinctive volcanic products, including analcime basalt.

The Nicola Group was deposited above upper Paleozoic rocks of the Harper Ranch Group, at least in part, as indicated by two small Harper Ranch inliers in the southern part of the study area. Lower to Middle Jurassic polymictic conglomerate and sandstone of the Dragon Mountain succession, the youngest stratified rocks in this part of Quesnel terrane, overlie the Nicola Group unconformably, and were derived mainly from the Nicola Group and associated plutonic rocks. The four Late Triassic to Early Jurassic plutonic suites cutting the Nicola Group are distributed in a general pattern of alternating calcalkaline and alkaline belts, becoming progressively younger from west to east. The oldest calcalkaline suite includes Late Triassic tonalite of the Granite Mountain batholith, which hosts the Gibraltar porphyry Cu-Mo mine. A younger, latest Triassic alkaline suite, coeval with assemblage four of the Nicola Group, includes rocks that host the Mount Polley porphyry Cu-Au mine.

The Nicola Group is flanked to the east by Middle and Upper Triassic slate, siltstone and quartz sandstone of the Slocan Group, part of a siliciclastic basin that formed east of, and coeval with, the Nicola arc. The Meridian Lake unit may represent a tongue of Slocan Group that interfingers with the Nicola

Group, demonstrating proximity of the two groups during their formation. An additional link may be provided by the arc volcanic rocks intercalated with Middle Triassic sedimentary rocks of the Slocan Group. These may be part of an early stage of volcanism within the arc system, and westward migration to the main Late Triassic arc axis (Nicola Group) may have been linked to formation of the back-arc basin represented by the Spanish Mountain unit.

**Acknowledgments**

I thank Alex Avolio for his assistance and geological contributions during fieldwork, and Sharon and Skeed Borkowski, of Northern Lights Lodge, for providing excellent accommodation on Quesnel Lake. I also thank Fil Ferri for his field visit in August, and Lawrence Aspler for a thorough review that improved the paper.

**References cited**

Acton, S.L., Simony, P.S., and Heaman, L.M., 2002. Nature of the basement to Quesnel Terrane near Christina Lake, southeastern British Columbia. Canadian Journal of Earth Sciences, 39, 65-78.

Beatty, T.W., Orchard, M.J., and Mustard, P.S., 2006. Geology and tectonic history of the Quesnel terrane in the area of Kamloops, British Columbia. In: Colpron, M., and Nelson, J. (Eds.), Paleozoic evolution and metallogeny of pericratonic terranes at the ancient pacific margin of North America, Canadian and Alaskan cordillera, Geological Association of Canada, Special Paper 45, pp. 483-504.

Bloodgood, M.A., 1990. Geology of the Eureka Peak and Spanish Lake map areas, British Columbia. British Columbia Ministry of Energy, Mines and Petroleum Resources, British Columbia Geological Survey Paper 1990-3, 36 p.

Campbell, K.V., 1971. Metamorphic petrology and structural geology of the Crooked Lake area, Cariboo Mountains, British Columbia. Ph.D. thesis, The University of Washington, 192 p.

Campbell, R.B., 1978. Quesnel Lake, British Columbia. Geological Survey of Canada, Open File 574; scale 1: 125,000.

Campbell, R.B., and Tipper, H.W., 1971. Bonaparte Lake map area, British Columbia. Geological Survey of Canada, Memoir 363, 100 p.

Coney, P.J., Jones, D.L., and Monger, J.W.H., 1980. Cordilleran suspect terranes. Nature, 288, 329-333.

Dostal., J., Church, B.N., and Höy, T., 2001. Geological and geochemical evidence for variable magmatism and tectonics in the southern Canadian Cordillera: Paleozoic to Jurassic suites, Greenwood, southern British Columbia. Canadian Journal of Earth Sciences, 38, 75-90.

Fillipone, J.A., and Ross, J.V., 1990. Deformation of the western margin of the Omineca Belt near Crooked Lake, east-central British Columbia. Canadian Journal of Earth Sciences, 27, 414-425.

Fyles, J.T., 1990. Geology of the Greenwood-Grand Forks area, British Columbia, NTS 82E/1, 2. British Columbia Ministry of Energy, Mines and Petroleum Resources, British Columbia Geological Survey Open File 1990-25, 19 p.

Holland, S.S., 1976. Landforms of British Columbia, a physiographic outline. British Columbia Department of Mines and Petroleum Resources, British Columbia Geological Survey Bulletin 48, 138 p.

Höy, T., and Dunne, K.P.E., 1997. Early Jurassic Rossland Group, southern British Columbia: Part I - stratigraphy and tectonics. British Columbia Ministry of Employment and Investment, British Columbia Geological Survey Bulletin 102, 123 p.

Jones, D.L., Howell, D.G., Coney, P.J., and Monger, J.W.H., 1983. Recognition, character and analyses of tectonostratigraphic terranes in western North America. In: Hashimoto, M., and Uyeda, S. (Eds.), Accretion tectonics in the circum-Pacific regions, Terra, Tokyo, pp. 21-35.

Little, H.W., 1960. Nelson map-area, west half, British Columbia (82F W1/2). Geological Survey of Canada, Memoir 308, 205 p.

Little, H.W., 1982. Geology, Rossland - Trail map area, British Columbia. Geological Survey of Canada, Paper 79-26, 38 p.

Logan, J.M., and Bath, A.B., 2006. Geochemistry of Nicola Group basalt from the central Quesnel trough at the latitude of Mount Polley (NTS 093A/5, 6, 11, 12). In: Geological Fieldwork 2005, British Columbia Ministry of Energy and Mines, British Columbia Geological Survey Paper 2006-1, pp. 83-98.

Logan, J.M., and Moynihan, D.P., 2009. Geology and mineral occurrences of the Quesnel River map area, central British Columbia (NTS 093B/16). In: Geological Fieldwork 2008, British Columbia Ministry of Energy, Mines and Petroleum Resources, British Columbia Geological Survey Paper 2009-1, pp. 127-152.

Logan, J.M., and Schiarizza, P., 2014. The Rayfield River pluton, south-central British Columbia (NTS 92P/6): Geologic setting and copper mineralization. In: Geological Fieldwork 2013, British Columbia Ministry of Energy and Mines, British Columbia Geological Survey Paper 2014-1, pp. 15-27.

Logan, J.M., Bath, A., Mihalynuk, M. G., Rees, C.J., Ullrich, T.D., and Friedman, R., 2007a. Regional geology of the Mount Polley area, central British Columbia. British Columbia Ministry of Energy, Mines and Petroleum Resources, British Columbia Geological Survey Geoscience Map 2007-1; scale 1:50,000.

Logan, J.M., Mihalynuk, M.G., Ullrich, T., and Friedman, R.M., 2007b. U-Pb ages of intrusive rocks and $^{40}Ar/^{39}Ar$ plateau ages of copper-gold-silver mineralization associated with alkaline intrusive centres at Mount Polley and the Iron Mask batholith, southern and central British Columbia. In: Geological Fieldwork 2006, British Columbia Ministry of Energy, Mines and Petroleum Resources, British Columbia Geological Survey Paper 2007-1, pp. 93-116.

Logan, J.M., Mihalynuk, M.G., Friedman, R.M., and Creaser, R.A., 2011. Age constraints of mineralization at the Brenda and Woodjam Cu-Mo±Au porphyry deposits-an Early Jurassic calcalkaline event, south-central British Columbia. In: Geological Fieldwork 2010, British Columbia Ministry of Forests, Mines and Lands, British Columbia Geological Survey Paper 2011-1, pp. 129-143.

Massey, N.W.D., 2010. Boundary Project: Geochemistry of volcanic rocks of the Wallace Formation, Beaverdell area, south-central British Columbia (NTS 082E/06E, 07W, 10W, 11W). In: Geological Fieldwork 2009, British Columbia Ministry of Energy, Mines and Petroleum Resources, British Columbia Geological Survey Paper 2010-1, pp. 143-152.

Massey, N.W.D., and Oliver, S.L., 2010. Southern Nicola Project: Granite Creek area, southern British Columbia (parts of NTS 092H/07, 10). In: Geological Fieldwork 2009, British Columbia Ministry of Energy, Mines and Petroleum Resources, British Columbia Geological Survey Paper 2010-1, pp. 113-126.

McMullin, D.W.A., Greenwood, H.J., and Ross, J.V., 1990. Pebbles from Barkerville and Slide Mountain terranes in a Quesnel terrane conglomerate: evidence for pre-Jurassic deformation of the Barkerville and Slide Mountain terranes. Geology, 18, 962-965.

Mihalynuk, M.G., Diakow, L.J., Friedman, R.M., and Logan, J.M., 2016. Chronology of southern Nicola arc stratigraphy and deformation. In: Geological Fieldwork 2015, British Columbia Ministry of Energy and Mines, British Columbia Geological Survey Paper 2016-1, pp. 31-63.

Monger, J.W.H., Price, R.A., and Tempelman-Kluit, D.J., 1982. Tectonic accretion and the origin of the two major metamorphic and tectonic welts in the Canadian Cordillera. Geology, 10, 70-75.

Monger, J.W.H., Wheeler, J.O., Tipper, H.W., Gabrielse, H., Harms, T., Struik, L.C., Campbell, R.B., Dodds, C.J., Gehrels, G.E., and O'Brien, J., 1991. Upper Devonian to Middle Jurassic assemblages, Part B, Cordilleran Terranes. In: Gabrielse, H., and Yorath, C.J. (Eds.), Geology of the Cordilleran Orogen in Canada, Geological Survey of Canada, Geology of Canada, No. 4, pp. 281-327.

Mortensen, J.K., Ghosh, D.K., and Ferri, F., 1995. U-Pb geochronology of intrusive rocks associated with copper-gold porphyry deposits in the Canadian Cordillera. In: Schroeter, T.G. (Ed.), Porphyry Deposits of the Northwestern Cordillera of North America, Canadian Institute of Mining, Metallurgy and Petroleum, Special Volume 46, pp. 142-158.

Mortimer, N., van der Heyden, P., Armstrong, R.L., and Harakal, J., 1990. U-Pb and K-Ar dates related to timing of magmatism and deformation in the Cache Creek Terrane and Quesnellia, southern British Columbia. Canadian Journal of Earth Sciences, 27, 117-123.

Mostaghimi, N., 2016. Structural geology and timing of deformation at the Gibraltar copper-molybdenum porphyry deposit, south-central British Columbia. M.Sc. thesis, The University of British Columbia, 358 p.

Oliver, S.L., 2011. The Eastgate-Whipsaw metamorphic belt as Paleozoic underpinnings to the Nicola Group. M.Sc. thesis, the University of British Columbia, 101 p.

Panteleyev, A., Bailey, D.G., Bloodgood, M.A., and Hancock, K.D., 1996. Geology and mineral deposits of the Quesnel River-Horsefly map area, central Quesnel Trough, British Columbia. British Columbia Ministry of Employment and Investment, British Columbia Geological Survey Bulletin 97, 155 p.

Petersen, N.T., Smith, P.L., Mortensen, J.K., Creaser, R.A., and Tipper, H.W., 2004. Provenance of Jurassic sedimentary rocks of south-central Quesnellia, British Columbia: implications for paleogeography. Canadian Journal of Earth Sciences, 41, 103-125.

Ray, G.E., and Dawson, G.L., 1994. The geology and mineral deposits of the Hedley gold skarn district, southern British Columbia. British Columbia Ministry of Energy, Mines and Petroleum Resources, British Columbia Geological Survey Bulletin 87, 156 p.

Read, P.B., and Okulitch, A.V., 1977. The Triassic unconformity of south-central British Columbia. Canadian Journal of Earth Sciences, 14, 606-638.

Rees, C.J., 1987. The Intermontane - Omineca belt boundary in the Quesnel Lake area, east-central British Columbia: Tectonic implications based on geology, structure and paleomagnetism. Ph.D. thesis, Carleton University, 421 p.

Rhys, D.A., Mortensen, J.K., and Ross, K., 2009. Investigations of orogenic gold deposits in the Cariboo Gold District, east-central British Columbia (parts of NTS 093A, H): Progress report. In: Geoscience BC Summary of Activities 2008, Geoscience BC Report 2009-1, pp. 49-74.

Schiarizza, P., 2014. Geological setting of the Granite Mountain batholith, host to the Gibraltar Cu-Mo porphyry deposit, south-central British Columbia. In: Geological Fieldwork 2013, British Columbia Ministry of Energy and Mines, British Columbia Geological Survey Paper 2014-1, pp. 95-110.

Schiarizza, P., 2015. Geological setting of the Granite Mountain batholith, south-central British Columbia. In: Geological Fieldwork 2014, British Columbia Ministry of Energy and Mines, British Columbia Geological Survey Paper 2015-1, pp. 19-39.

Schiarizza, P., 2016. Toward a regional stratigraphic framework for the Nicola Group: Preliminary results from the Bridge Lake-Quesnel River area. In: Geological Fieldwork 2015, British Columbia Ministry of Energy and Mines, British Columbia Geological Survey Paper 2016-1, pp. 13-30.

Schiarizza, P., 2017. Ongoing stratigraphic studies in the Nicola Group: Stump Lake-Salmon River area, south-central British Columbia. In: Geological Fieldwork 2016, British Columbia Ministry of Energy and Mines, British Columbia Geological Survey Paper 2017-1, pp. 143-156.

Schiarizza, P., 2018. Geology of the Spanish Lake area, south-central British Columbia. In: Geological Fieldwork 2017, British Columbia Ministry of Energy, Mines and Petroleum Resources, British Columbia Geological Survey Paper 2018-1, pp. 17-33.

Schiarizza, P., and Bligh, J.S., 2008. Geology and mineral occurrences of the Timothy Lake area, south-central British Columbia (NTS 092P/14). In: Geological Fieldwork 2007, British Columbia Ministry of Energy, Mines and Petroleum Resources, British Columbia Geological Survey Paper 2008-1, pp. 191-211.

Schiarizza, P., and Israel, S., 2001. Geology and mineral occurrences of the Nehalliston Plateau, south-central British Columbia (92P/7, 8, 9, 10). In: Geological Fieldwork 2000, British Columbia Ministry of Energy and Mines, British Columbia Geological Survey Paper 2001-1, pp. 1-30.

Schiarizza, P., and Macauley, J., 2007. Geology and mineral occurrences of the Hendrix Lake area (NTS 093A/02), south-central British Columbia. In: Geological Fieldwork 2006, British Columbia Ministry of Energy, Mines and Petroleum Resources, British Columbia Geological Survey Paper 2007-1, pp. 179-202.

Schiarizza, P., Bell, K., and Bayliss, S., 2009. Geology and mineral occurrences of the Murphy Lake area, south-central British Columbia (NTS 093A/03). In: Geological Fieldwork 2008, British Columbia Ministry of Energy, Mines and Petroleum Resources, British Columbia Geological Survey Paper 2009-1, pp. 169-187.

Schiarizza, P., Heffernan, S., and Zuber, J., 2002. Geology of Quesnel and Slide Mountain terranes west of Clearwater, south-central British Columbia (92P/9, 10, 15, 16). In: Geological Fieldwork 2001, British Columbia Ministry of Energy and Mines, British Columbia Geological Survey Paper 2002-1, pp. 83-108.

Schiarizza, P., Israel, S., Heffernan, S., Boulton, A., Bligh, J., Bell, K., Bayliss, S., Macauley, J., Bluemel, B., Zuber, J., Friedman, R.M., Orchard, M.J., and Poulton, T.P., 2013. Bedrock geology between Thuya and Woodjam creeks, south-central British Columbia, NTS 92P/7, 8, 9, 10, 14, 15, 16; 93A/2, 3, 6. British Columbia Ministry of Energy, Mines and Natural Gas, British Columbia Geological Survey Open File 2013-05; 4 sheets, scale 1:100,000.

Smith, R.B., 1979. Geology of the Harper Ranch Group (Carboniferous-Permian) and Nicola Group (Upper Triassic) northeast of Kamloops, British Columbia. M.Sc. thesis, The University of British Columbia, 211 p.

Struik, L.C., 1983. Bedrock geology, Spanish Lake and adjoining areas, British Columbia. Geological Survey of Canada, Open File 920; scale 1:50,000.

Struik, L.C., 1988. Regional imbrication within Quesnel Terrane, central British Columbia, as suggested by conodont ages. Canadian Journal of Earth Sciences, 25, 1608-1617.

Struik, L.C., 1993. Intersecting intracontinental Tertiary transform fault systems in the North American Cordillera. Canadian Journal of Earth Sciences, 30, 1262-1274.

Thompson, R.I., Glombick, P., Erdmer, P., Heaman, L.M., Lemieux, Y., and Daughtry, K.L., 2006. Evolution of the ancestral Pacific margin, southern Canadian Cordillera: Insights from new geologic maps. In: Colpron, M., and Nelson, J. (Eds.), Paleozoic evolution and metallogeny of pericratonic terranes at the ancient Pacific margin of North America, Canadian and Alaskan cordillera, Geological Association of Canada, Special Paper 45, pp. 433-482.

Wheeler, J.O., Brookfield, A.J., Gabrielse, H., Monger, J.W.H., Tipper, H.W., and Woodsworth, G.J., 1991. Terrane map of the Canadian Cordillera. Geological Survey of Canada, Map 1713A; scale 1:2,000,000.

# Preliminary geology of northern Hogem batholith, Quesnel terrane, north-central British Columbia

Luke Ootes[1, a], Anika Bergen[1], Dejan Milidragovic[1], Ben Graham[1], and Reid Simmonds[1]

[1] British Columbia Geological Survey, Ministry of Energy, Mines and Petroleum Resources, Victoria, BC, V8W 9N3
[a] corresponding author: Luke.Ootes@gov.bc.ca

Recommended citation: Ootes, L., Bergen, A., Milidragovic, D., Graham, B., and Simmonds, R., 2019. Preliminary geology of northern Hogem batholith, Quesnel terrane, north-central British Columbia. In: Geological Fieldwork 2018, British Columbia Ministry of Energy, Mines and Petroleum Resources, British Columbia Geological Survey Paper 2019-01, pp. 31-53.

**Abstract**

New bedrock mapping in parts of NTS 94C/04 (Notch Peak) and 93N/13 (Ogden Creek) refines the distribution and relationships of plutonic rocks in northern Hogem batholith. We recognize four plutonic suites (from oldest to youngest): Thane Creek, Duckling Creek, Mesilinka, and Osilinka. The ages of these suites are relative and are based on crosscutting relationships and the presence or absence of tectonic fabrics. The eastern part of the study area is mostly underlain by diorite and lesser hornblendite of the Thane Creek suite. The diorites consistently have a weak to strong foliation, with locally developed mylonite. Relatively potassic monzodiorite to quartz monzodiorite phases are common and may have resulted from late magmatic or secondary alteration processes. Foliated tonalite and granodiorite to quartz monzonite are also included with the Thane Creek suite, but lack of alteration and mylonite indicate they post-date the hornblendite and diorite intrusions. The southern part of the study area is underlain by Duckling Creek suite syenite and monzonite, with enclaves of pyroxenite (ca. 180 Ma). These rocks lack quartz, are rich in K-feldspar (commonly zoned) and display local magmatic layering, which is accentuated by deformation. The western part of the study area is underlain by foliated granites assigned to the Mesilinka suite (Jurassic to Cretaceous?). These granites commonly contain xenoliths of Thane Creek suite rocks, typically at higher elevations, some of which were foliated before incorporation into the granite. In the central part of the study area, the Osilinka suite granite is characterized by its low content of mafic minerals (≤5%). The granite lacks a foliation, but displays local evidence of post-crystallization ductile deformation. The youngest rocks in the study area are small (<4 m wide) subhorizontal sheets and lesser dikes of intermediate feldspar porphyry and felsic quartz-feldspar porphyry that cut the Osilinka granite. Previously documented metallic mineralization is recorded in ca. 34 MINFILE occurrences. During bedrock mapping, 17 new mineral occurrences were discovered. Most are within the Thane Creek and Duckling Creek suites and consist mainly of disseminated chalcopyrite and malachite staining. New gold and copper-bearing quartz veins were also discovered, and crosscut Thane Creek diorite and Osilinka granite.

**Keywords:** Hogem batholith, Quesnel terrane, Jurassic, Cretaceous, copper and gold

## 1. Introduction

In 2018, the British Columbia Geological Survey initiated a three-year mapping project in an area of north-central British Columbia (Fig. 1). The project aims to better understand the bedrock and surficial geology of the area, which includes rocks of the Quesnel, Stikine, and Cache Creek terranes (Figs. 1, 2) and metallic mineralization associated with these rocks (e.g., Lorraine Cu-Au porphyry deposit; Devine et al., 2014). This report presents the preliminary results of 1:50,000-scale bedrock mapping from the first field season, which focussed on mafic to felsic plutonic rocks of northern Hogem batholith and younger intrusive suites. A full-scale map is presented elsewhere (Ootes et al., 2019).

## 2. Setting and previous work

The 2018 study area (Figs. 2-4) includes part of northern Hogem batholith. The batholith is bounded to the north and east by volcanic and sedimentary rocks of the Takla Group (Triassic) along fault and intrusive contacts. To the west, Hogem batholith and Takla Group, both within Quesnel terrane, are juxtaposed against Cache Creek (Late Paleozoic to Triassic) and Stikine (Triassic to Jurassic) terranes across the Pinchi and Ingenika dextral strike-slip faults (Fig. 2).

The regional geology was originally mapped by Armstrong (1948), Lord (1949), and Armstrong and Roots (1948, 1954; also see Roots, 1954), who assigned rocks now included in Hogem batholith, to the 'Omineca intrusions' (Jurassic to Cretaceous). The local study area was mapped by Armstrong (1946) and Armstrong and Roots (1948, 1954). Although Roots (1954) gave thorough descriptions of a wide variety of intrusive units, he grouped these units as 'undivided' on his maps. Garnett (1972, 1978) subdivided southern Hogem batholith and Woodsworth (1976) subdivided northern Hogem batholith. Mapping by Ferri et al. (2001) in the northeast corner of 94C/04, and in areas to the east and north, focussed on the Takla Group and left the Hogem batholith largely undivided. In the south-central part of the study area, Nelson et al. (2003) updated mapping near the Hawk quartz vein-hosted gold prospect. Schiarizza and Tan (2005 a, b) mapped north of the 2018 study area; on their map, Schiarizza and Tan (2005b) plotted preliminary isotopic ages for plutonic rocks at the northern tip of Hogem batholith. Devine et al. (2014) studied

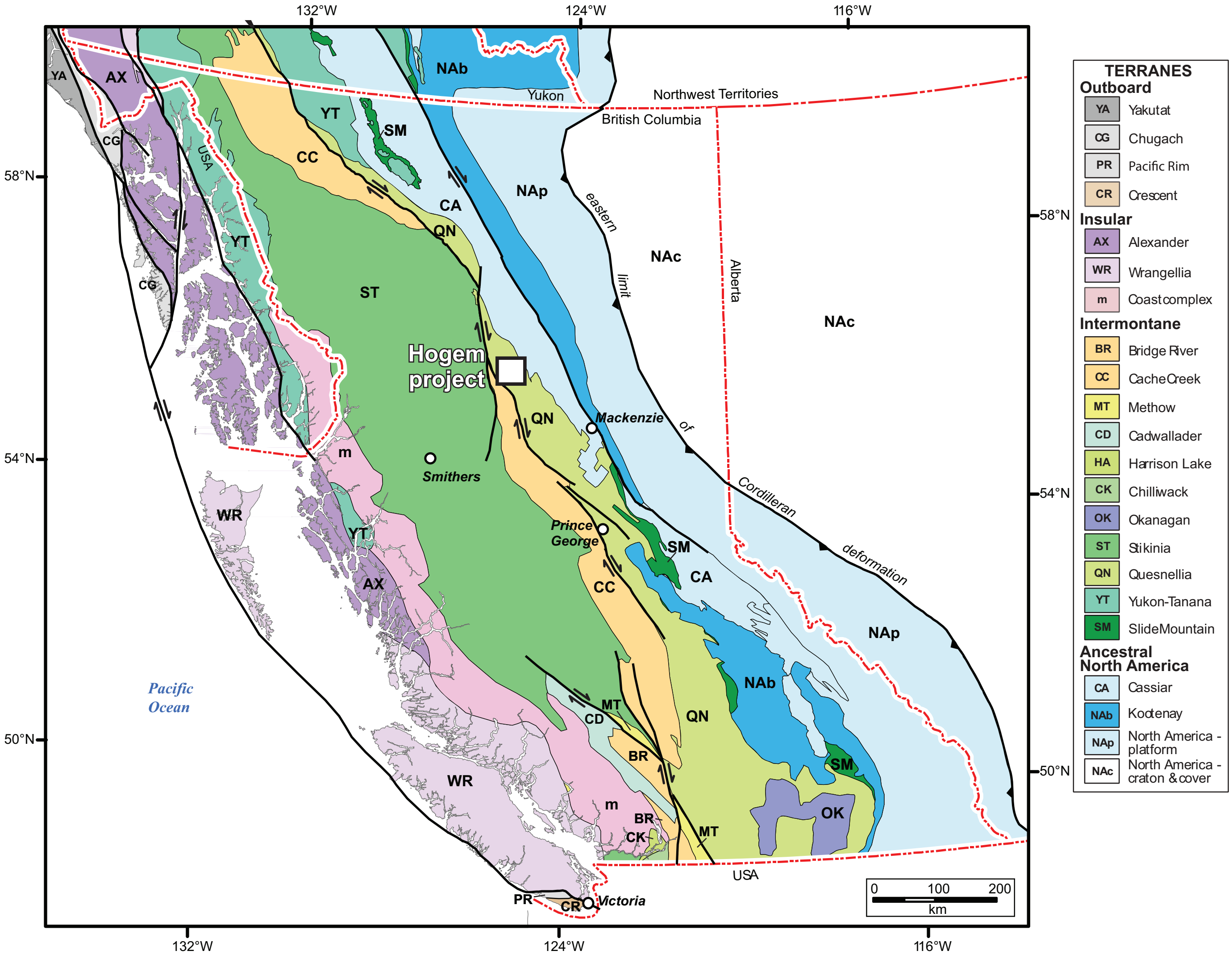


**Fig. 1.** Terrane map of British Columbia and neighbouring jurisdictions with location of study area. Modified after Nelson et al. (2013).

the Lorraine porphyry Cu-Au deposit, southeast of the 2018 map area and provided isotopic ages for the Duckling Creek suite. Recently, Madu and Ballantyne (2018) presented the results of an airborne geophysical survey flown with a line spacing of 250 m and a terrain-contouring elevation of 80 m. The survey included both radiometric (K, U, Th) and magnetic data collection (Fig. 3). Processed data and images of these data are available from GeoscienceBC (http://www.geosciencebc.com).

## 3. Bedrock geology

Mapping was conducted for two months in the summer of 2018 (Fig. 4; Ootes et al., 2019). Data were captured on tablets equipped with the Manifold (v.8.0) geographic information system, which also used georeferenced imagery, including aeromagnetic and radiometric maps from Madu and Ballantyne (2018). Each traversing pair carried a Terraplus KT-10 Magnetic Susceptibility Meter. About 10 discrete (non-scanning) measurements were acquired at each station (across an area up to 100 $m^2$) and the maximum, minimum, and mean were recorded (Fig. 5). Representative rock samples were collected and some prepared as polished thin sections (n=82). Thin section offcuts and a selection of other representative samples (n=65) were stained for K-feldspar. Results of samples collected for assay are presented below; geochemical and geochronological investigations are ongoing.

### 3.1. Lithologic units

The intrusive phases in northern Hogem batholith are organized into four suites (Fig. 4; Table 1), modified after Woodsworth (1976) and Woodsworth et al. (1991). The eastern and southwestern parts of the study area are underlain by diorite to monzodiorite and lesser hornblendite of the Thane Creek suite. In the west and southeast parts of the map area, the Thane Creek suite includes granodiorite, quartz monzodiorite, and tonalite. In the south-central part of the study area, the Duckling Creek suite comprises K-feldspar-rich syenite to monzonite. The Duckling Creek suite cuts the Thane Creek

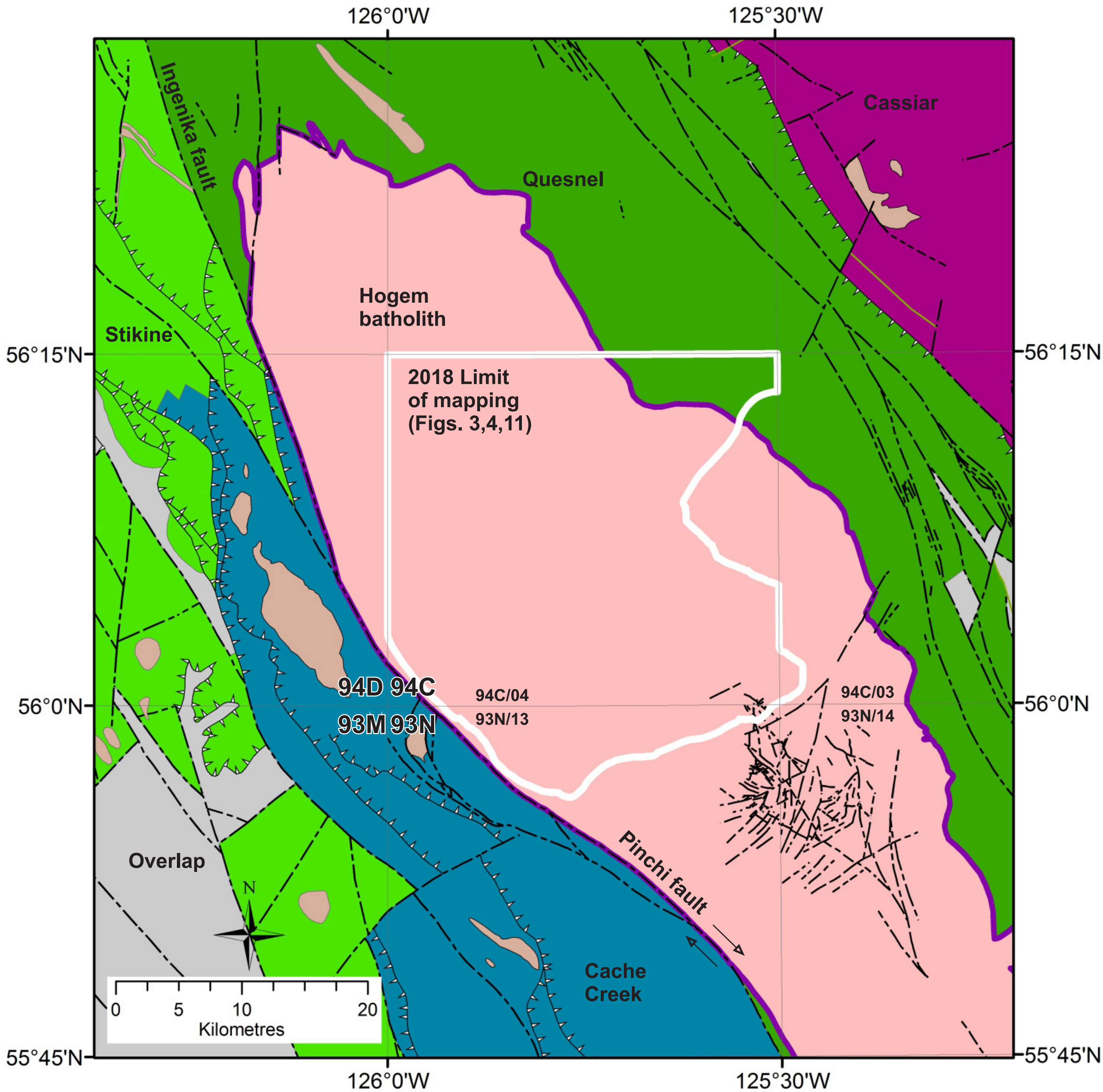


**Fig. 2.** Regional context of northern Hogem batholith and 2018 study area. Hogem batholith is in Quesnel terrane, which is separated from the Cache Creek and Stikine terranes by the Pinchi-Ingenika fault (dextral strike-slip). Thrust faults on the map have teeth on the hanging wall side; dashed lines are undifferentiated strike-slip and normal faults.

suite (Fig. 6). The western part of the study area is mainly underlain by Mesilinka suite granitic phases that cut the older Thane Creek suite (Fig. 6). In the central part of the study area is a unit of mafic-poor equigranular granite assigned to the Osilinka suite.

The only geochronological information directly from the study area is from K-Ar dating (Garnett, 1978; Woodsworth et al., 1991). Thus we rely on crosscutting relationships and the presence or absence of tectonic fabrics to establish relative ages of the suites. Uranium-lead zircon dates are available for selected units south and north of the study area (Fig. 6; Schiarizza and Tan, 2005b; Bath et al., 2014; Devine et al., 2014) and where appropriate these units are correlated to rocks in this study.

**Table 1.** Summary of plutonic map units, northern Hogem batholith.

| Suite | Unit Code | Rock type and texture | Deformation | Relative magnetism | Other features | Mineralogy of note |
|---|---|---|---|---|---|---|
| Porphyry sheets | | feldspar and quartz-feldspar porphyry | magmatic foliation (contact parallel) | low | fresh | |
| Osilinka | KHgg | equigranular granite | local shear zones | low | strongly jointed with local quartz veining | <5% biotite, altered to chlorite, local muscovite |
| Mesilinka | JHgg.or | K-feldspar porphyrytic granite | foliated | low, moderate when diorite xenoliths present | biotite foliation, local garnet and muscovite, abundant aplite and pegmatite dikes | allanite common |
| | JHgg.e | equigranular granite | foliated | low to moderate | K-feldspar phenocrysts up to 5 cm | allanite common |
| Duckling Creek | JHds | syenite to monzonite | magmatic layering and foliated | high | K-feldspar rich and quartz deficient, magmatic layering, zoned K-feldspar, and K-feldspar pegmatite common | sodic(?) amphibole and pyroxene, apatite and titanite common |
| | JHds | pyroxenite | magmatic layering and foliated | high to highest | Malachite staining common | contains biotite |
| Thane Creek | JHgt | tonalite | foliated | low | grey, lacks K-felspar, foliated | mostly plagioclase and quartz |
| | JHgd | granodiorite to quartz monzonite | foliated | moderate to high | contains quartz, variable amounts of biotite, and does not appear altered | pristine igneous mineralogy, magnetite and titanite common |
| | JHdd | diorite to quartz monzodiorite | foliated to locally mylonitic | low to high | equigranular hornblende-plagioclase bearing; locally moderately to extensively altered and locally strongly deformed, some malachite staining | extensive biotite and epidote, and little amphibole, coincide with K-feldspar-bearing phases, titanite, apatite, and magnetite common |
| | JHuhb | hornblendite | foliated | high to highest | black coarse-grained to pegmatitic; locally mingled with diorite, some malachite staining and disseminated chalcopyrite | coarse amphibole is overgrown by secondary amphibole and biotite, titanite, magnetite, and chalcopyrite common |

### 3.1.1. Thane Creek suite

#### 3.1.1.1. Hornblendite

Black to salt and pepper, medium-grained to pegmatitic hornblendite forms ≤100 m wide plutons (unit JHuhb) scattered through the diorite phases of the Thane Creek suite (Figs. 4-7; Table 1). Dark green amphibole crystals, with rare corroded clinopyroxene cores, predominate, and range from medium to coarse grained. Plagioclase, where present, is interstitial between amphibole and ranges from fine to coarse grained (Fig. 7a). Biotite, generally medium grained, is common in the hornblendites, in concentrations ranging from 0 to 20%. Accessory euhedral titanite and euhedral to subhedral crystals of apatite are also common. Magnetite abundance in hornblendite varies (mostly ≤5%), and these rocks have a strong magnetic signature (Fig. 5). Epidote is a secondary alteration phase in the hornblendite, and is generally ≤5% of the rock. Trace amounts of disseminated pyrite and chalcopyrite occur and, in a few small outcrops (~1 m$^2$), chalcopyrite comprises a few percent of the rock. Some of the sulphide-bearing rocks have local malachite or iron rust staining on weathered surfaces. The hornblendites are entirely within diorite (Fig. 4) and display both sharp and diffuse contacts, the latter indicating magma co-mingling (Fig. 7b). We interpret that the hornblendites are comagmatic with the diorite plutons and that they either represent crystal cumulates formed from a more primitive parental magma, or injections of a hydrous mafic to ultramafic magma into a predominantly dioritic chamber.

#### 3.1.1.2. Diorite to quartz monzodiorite

The eastern and southwestern parts of the study area are mostly underlain by green and white to black and white weathering, equigranular, medium- to coarse-grained diorite that is foliated to locally mylonitic (unit JHdd; Figs. 4-7). The diorite (Fig. 7c) consists mostly of plagioclase and hornblende, but locally transitions to units with more significant amounts of quartz and K-feldspar (quartz diorite, quartz monzodiorite, monzodiorite) and potentially gabbro. Accessory phases include clinopyroxene (as corroded cores to amphibole), euhedral to subhedral titanite, magnetite, and apatite. Epidote is locally common and interpreted as an alteration product

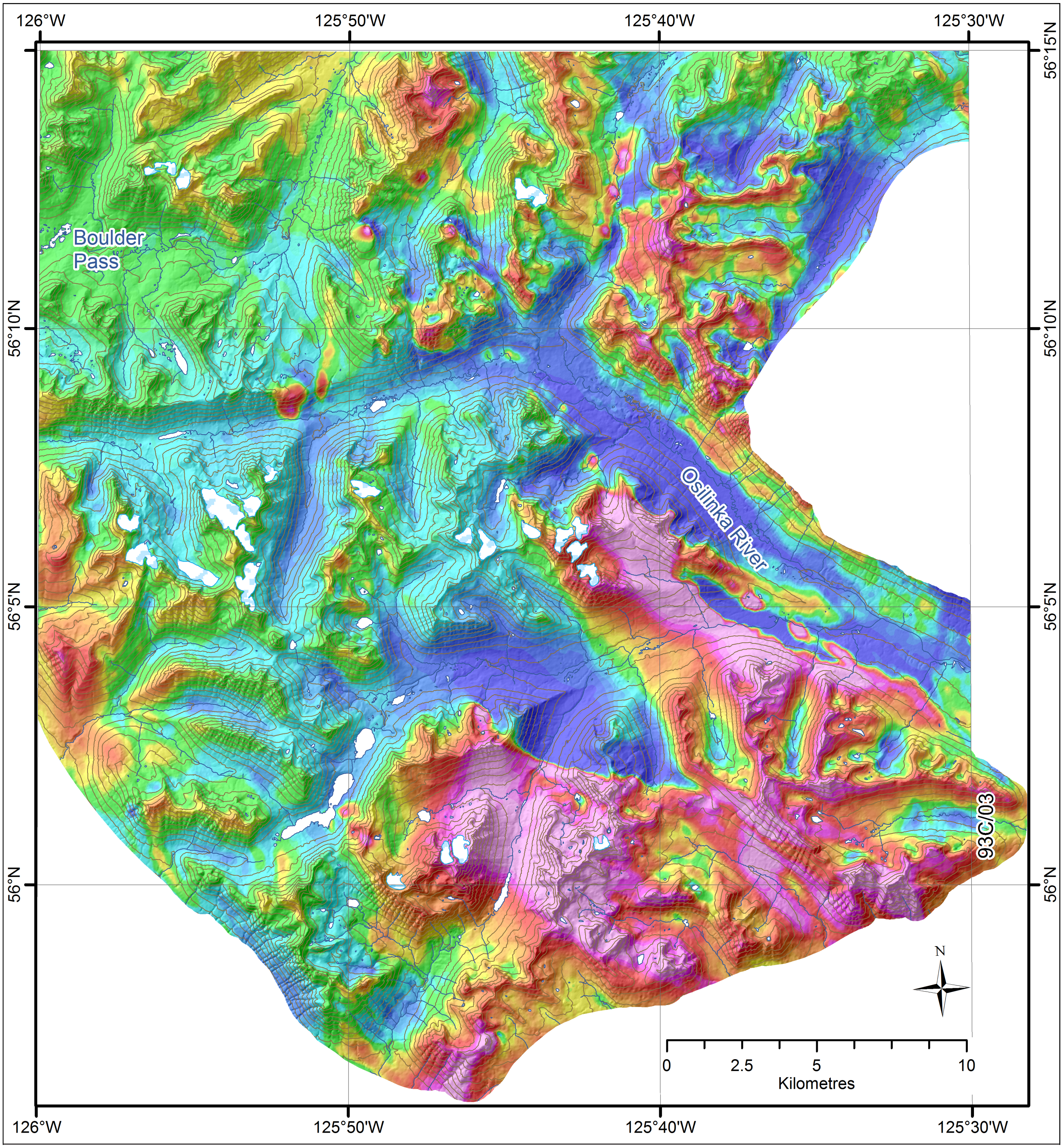


**Fig. 3. a)** Magnetic map of 2018 study area; warm colours (pink-white) correspond to high magnetism and cool colours (blue) correspond to low magnetism. From Madu and Ballantyne (2018).

(Table 1). The diorite locally contains biotite, in some cases in much greater abundance than amphibole, but it has not been resolved if the biotite is a primary magmatic or secondary metamorphic/alteration phase. The relatively potassic phases contain blotchy pink K-feldspar in the groundmass, which is locally accompanied by mint-green weathering (Fig. 7d). These zones correspond to biotite- and epidote-rich phases, where plagioclase has been altered to clay minerals, amphibole is rare, and titanite locally displays highly corroded grain boundaries. These features may indicate either late magmatic or secondary potassic alteration. Although our preliminarily interpretation favours secondary alteration for many potassic

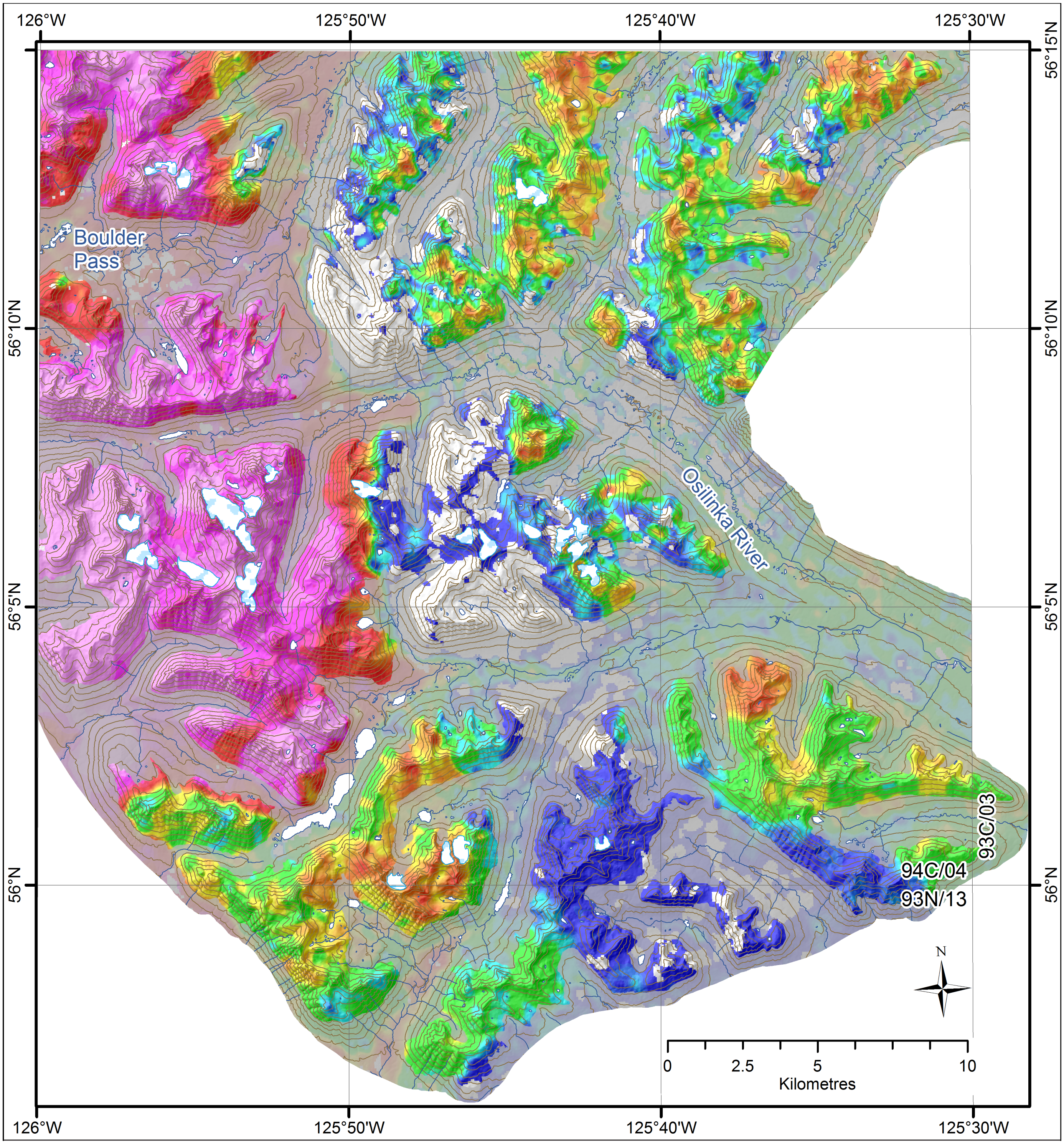


**Fig. 3. b)** Th/K map of 2018 study area; warm colours correspond to high Th/K and cool colours correspond to low Th/K. White zones are areas of no data. Grey overlay mask represents surficial cover. Draped on shaded relief map, contour intervals are 100 m. From Madu and Ballantyne (2018).

units, true magmatic monzodiorite may also be present. The diorite contains variable abundances of magnetite; this variation could be from magmatic fractionation, secondary alteration, or both. The magnetic variation is evident from magnetic susceptibility measurements (Fig. 5), which correlate with magnetic variations on airborne magnetic maps (Fig. 3a). Phase transitions from diorite to monzodiorite coincide with the variation of K on the radiometric maps (Fig. 3b).

The diorite crosscuts and comingles with the hornblendite (Fig. 7b). Where there is comingling (Fig. 7b), the rocks are texturally and compositionally heterogeneous in terms of amphibole, plagioclase, and magnetite concentrations. In some locations, the combined effects of mixing with enclaves, magmatic differentiation, and K-alteration, resulted in textural and compositional variations of a scale too small to map. The diorite locally contains xenoliths of layered fine-grained green rock, possibly derived from the Takla Group. The diorite is locally stained with malachite and rarely contains disseminated chalcopyrite (<1%).

Near its western margin, diorite is cut by Mesilinka suite equigranular granite and K-feldspar porphyritic granite (Fig. 4; Woodsworth, 1976). In the central part of the map area, diorite and, at one outcrop, hornblendite, are in sharp contact with crosscutting Osilinka suite equigranular granite (Fig. 4); rare xenoliths of diorite are in the granite.

Devine et al. (2014) described the Rhonda-Dorothy gabbro-diorite body, about 20 kilometres south of the study area, and documented a U-Pb zircon crystallization age of 200.9 ±0.2 Ma. Based on descriptions in Devine et al. (2014) we suggest that the Thane Creek and Rhonda-Dorothy bodies are equivalent. The Thane Creek diorite may be also be equivalent to diorite plutons that cut the Takla Group north of the Hogem batholith, for which Schiarizza and Tan (2005b) gave preliminary ages of 224 to 211 Ma. We tentatively regard the age of the Thane Creek diorite as ca. 200 Ma (Fig. 6).

#### 3.1.1.3. Tonalite

Tonalite (unit JHgt) outcrops in three areas near the western boundary of the study area (Figs. 4-7). It is equigranular, medium-grained, white to grey, with a moderate foliation. Quartz and plagioclase are accompanied by biotite, and accessory allanite. The rocks lack amphibole, K-feldspar, titanite, and magnetite (Table 1). In the northwest, tonalite is crosscut by fine-grained equigranular granite dikes and sheets that commonly contain garnet (Fig. 7e). Farther east, the tonalite is cut by granitic rocks of the Mesilinka suite (Figs. 4, 6). Tonalite xenoliths in the granites can contain secondary muscovite. The tonalite has a low to moderate magnetic signature (Fig. 5) and airborne radiometrics indicate low K, and moderate to high Th-U. The tonalite is interpreted to be younger than the Thane Creek diorite (Fig. 6) because the tonalite lacks alteration and, although foliated, it lacks strong deformation features such as mylonite. North of Hogem batholith, Schiarizza and Tan (2005b) mapped a tonalite body that cuts the Takla Group and gave a preliminary age estimate of ca. 174 Ma.

#### 3.1.1.4. Granodiorite to quartz monzonite

A unit that ranges from granodiorite to quartz monzodiorite to quartz monzonite (unit JHgd) outcrops in the northwest, southwest, and southeast parts of the study area (Fig. 4). These rocks are equigranular to weakly plagioclase porphyritic, and medium grained (Fig. 7f). They contain quartz (10-25%), weakly kinked biotite, which is locally more abundant than amphibole, and K-feldspar (20-30%) with well-developed crystal habit. Primary accessory phases include euhedral titanite and magnetite. Subrounded fine- to medium-grained xenoliths of intermediate composition are common (Fig. 7f). This unit has a moderate to strong magnetic expression (Fig. 5) and has Th>K>U (Fig. 3b).

These rocks are interpreted to be younger than the Thane Creek diorite (Fig. 6) because they lack hornblendite phases, potassic alteration, and strong deformation. This unit may be older than the Duckling Creek suite because it is locally cut by K-feldspar pegmatites, but other intrusive contacts have not been observed. In the southwest part of the study area, this unit forms outcrops near tonalite (Fig. 4), but intrusive relationships were not observed and their temporal relationships are unresolved (Fig. 6).

### 3.1.2. Duckling Creek suite

The south-southeast part of the study area is underlain by quartz-free, K-feldspar-rich rocks of the Duckling Creek suite (unit JHds; Figs. 4, 8), previously referred to as the Duckling Creek Syenite Complex (Woodsworth, 1976; Garnett, 1978; Nixon and Peatfield, 2003; Devine et al., 2014). The Duckling Creek suite is mostly syenite to monzonite, with lesser monzodiorite and local zones of biotite pyroxenite. These rocks are texturally heterogeneous (Fig. 8), ranging from equigranular to porphyritic to pegmatitic. Porphyrytic varieties contain K-feldspar phenocrysts (commonly zoned) in a groundmass of equigranular green amphibole and lesser plagioclase (possibly albite). They contain accessory subhedral to euhedral titanite and apatite, and variable amounts of magnetite with a subhedral to interstitial habit within amphibole-rich, polycrystalline aggregates. Rhythmic magmatic layering is common, with aligned K-feldspar phenocrysts that are further accentuated by deformation (Fig. 8c). Local pyroxenite enclaves, with dimensions in the scale of 10s of metres, are exposed mostly at higher elevations, where they are intruded by the more intermediate to felsic phases (Fig. 8a). The entire unit has moderate to strong magnetism (Fig. 5), with areas of highest magnetism spatially associated with exposed biotite pyroxenite. On the airborne radiometric map, the Duckling Creek suite has low Th/K (Fig. 3b), reflecting its K-rich character. The biotite pyroxenite zones are commonly stained with malachite and locally contain disseminated chalcopyrite.

South of the study area, Devine et al. (2014) identified three stages of the Duckling Creek suite and constrained their timing with U-Pb zircon ages: 1) biotite pyroxenite (ca. 182 to 178.5 Ma), which can contain base- and precious-metal mineralization and associated alteration (e.g., Lorraine Cu-Au deposit); 2) predominantly K-feldspar porphyritic syenite to monzonite (ca. 178.8 to 178.4 Ma); and 3) massive syenite and pegmatite (ca. 177 to 175 Ma). The older biotite pyroxenite (Fig. 7a) locally contains malachite staining and disseminated chalcopyrite and likely corresponds with Devine et al. (2014) stage 1. The more typical syenite to monzonite (Fig. 8) corresponds with Devine et al. (2014) stage 2.

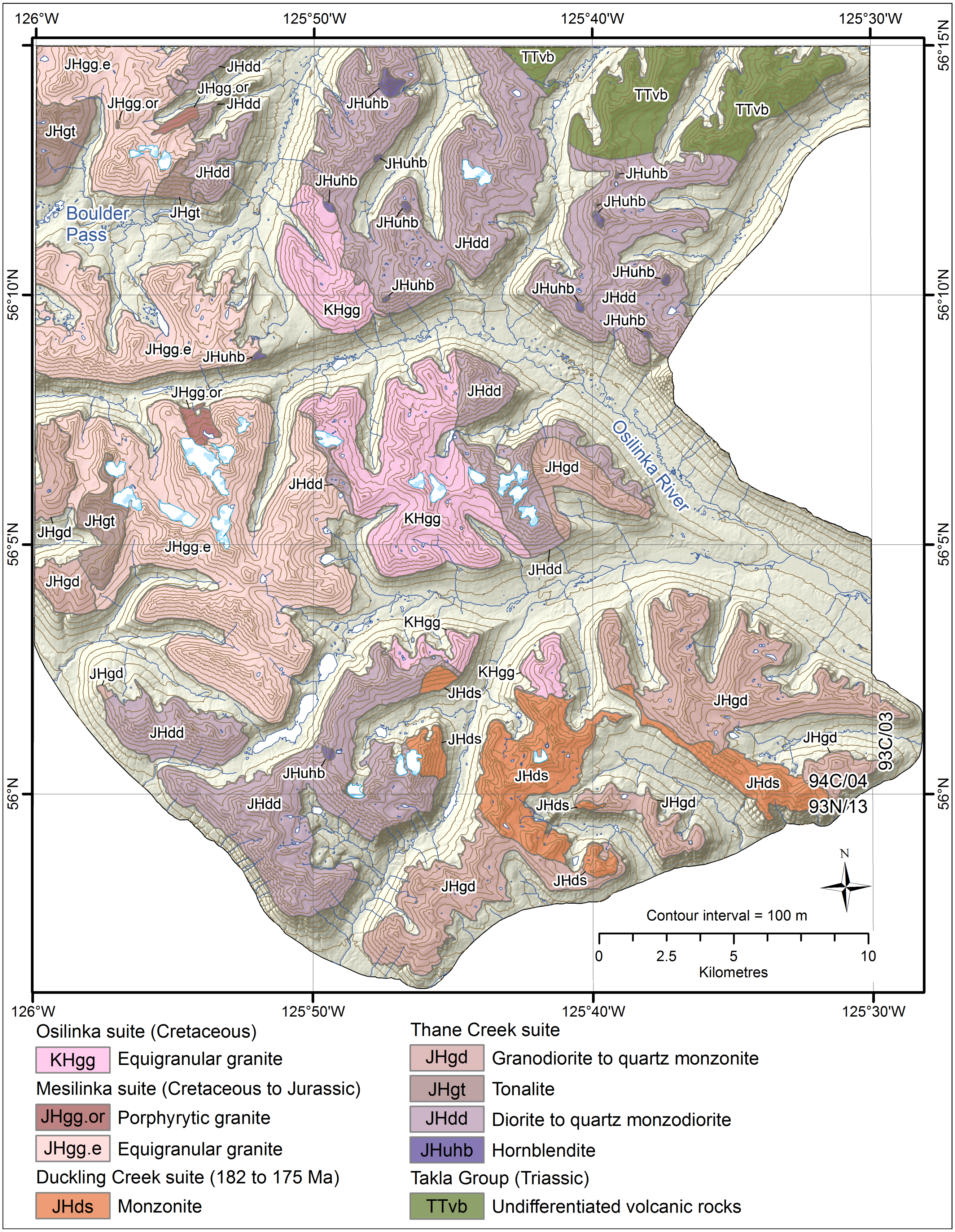


**Fig. 4. a)** Geology of northern Hogem batholith, generalized from Ootes et al. (2019). Intrusive suite names are modified from Woodsworth (1976). The Takla Group is from Ferri et al. (2001).

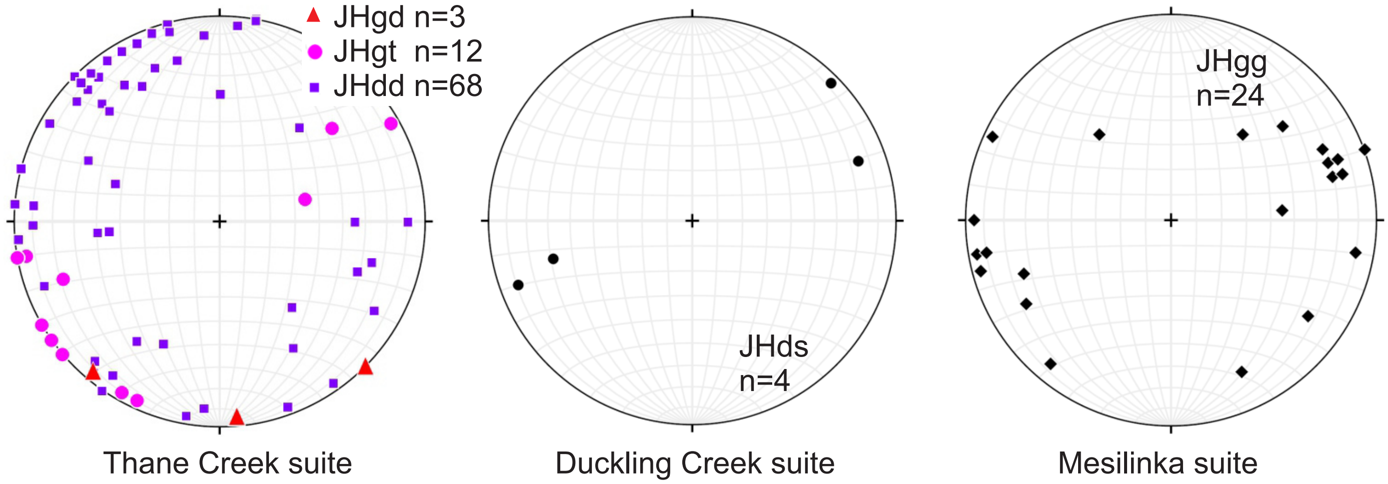


**Fig. 4. b)** Equal area lower hemisphere projections of poles to foliation planes for Thane Creek suite diorite (blue squares), tonalite (pink circles), and granodiorite (pink triangles), Duckling Creek suite rocks, and Mesilinka suite granites. Plots generated using Allmendinger software, available at http://www.geo.cornell.edu/geology/faculty/RWA/programs/stereonet.html.

### 3.1.3. Mesilinka suite

#### 3.1.3.1. Equigranular granite

Throughout the western part of the study area the predominant rock type is equigranular granite (unit JHgg.e; Figs. 4, 9a). The granite is medium grained, light pink to grey, and contains biotite (10-20%) that is kinked. Accessory phases include allanite, apatite, and zircon (Table 1). This granite contains a foliation defined by aligned biotite, which helps distinguish it from equigranular granite of the younger, biotite-deficient Osilinka suite (Fig. 4). The equigranular granite contains xenoliths of tonalite, which locally contain muscovite. Close to the xenoliths the granite contains garnet (Fig. 9a).

At higher elevations to the southwest (Fig. 4), the granite contains xenoliths of Thane Creek suite diorite, and has a relatively high magnetic expression. At lower elevations the granite is xenolith-free and has a low magnetic expression. The elevation-related appearance of diorite xenoliths may indicate that these are roof pendants, possibly indicating proximity to the top of the original magma chamber, whereas lower elevations represent the main granite body. We note that the magnetic signature in some areas appears to be topographically controlled, evident when the magnetic map is draped on elevation datum (Fig. 3a). This is best explained by erosion having variably incised this granitic body, leaving higher magnetic expressions that coincide with diorite xenoliths at higher elevations.

#### 3.1.3.2. Porphyritic granite

The youngest mappable Mesilinka phase is porphyritic granite with K-feldspar phenocrysts (≤5 cm long) in a medium- to coarse-grained equigranular groundmass (unit JHgg.or; Figs. 4 and 9b). The granite contains biotite, with accessory apatite, magnetite, allanite, and zircon (Table 1). It cuts the equigranular granite, and Thane Creek suite tonalite and diorite (Figs. 4, 6). The granite displays a foliation defined by aligned feldspar phenocrysts and biotite and this fabric crosscuts the intrusive contacts (Fig. 9c). The porphyritic granite has a low to medium aeromagnetic expression (Fig. 5). Both this unit and the equigranular granite have a high Th expression on airborne radiometric map, with Th >K (Fig. 3b). North of the study area, Schiarizza and Tan (2005b) reported a preliminary U-Pb zircon age of ca. 135 Ma from a Mesilinka granite.

### 3.1.4. Osilinka suite

The central part of the study area is underlain by equigranular granite (unit KHgg; Figs. 4, 10). Woodsworth (1976) mapped this unit as one of several ‘massive granodiorite plutons’ that he considered the youngest mappable units in northern Hogem batholith. These plutons were subsequently referred to as the Osilinka stocks by Woodsworth et al. (1991) and the Osilinka pluton by Nelson et al. (2003). The granite is medium grained and white, with a low mafic mineral content (<5%; Fig. 10). Plagioclase displays strong oscillatory zoning, and both feldspars typically have extensively corroded cores. This and the lack of a foliation distinguishes it from the biotite-bearing, foliated equigranular granite of the Mesilinka suite (Fig. 4). Compared to other intrusive suites in northern Hogem batholith, the granite is distinctly jointed. Some joints contain quartz veins and associated alteration haloes (locally muscovite-bearing) in the adjacent granite. The Osilinka suite mainly cuts the Thane Creek suite diorite but, in the southeast, it cuts Duckling Creek suite syenite. Along its western margin, the granite intruded the Mesilinka suite (Figs. 4, 6). The granite has a low magnetic expression and is characterized by K >Th (Figs. 3, 5). Schiarizza and Tan (2005b) reported a U-Pb titanite date of 134.0 ±1.2 Ma for an Osilinka stock at the north end of Hogem batholith, and a U-Pb zircon age of 136.6 ±0.7 Ma for a small stock north of the batholith.

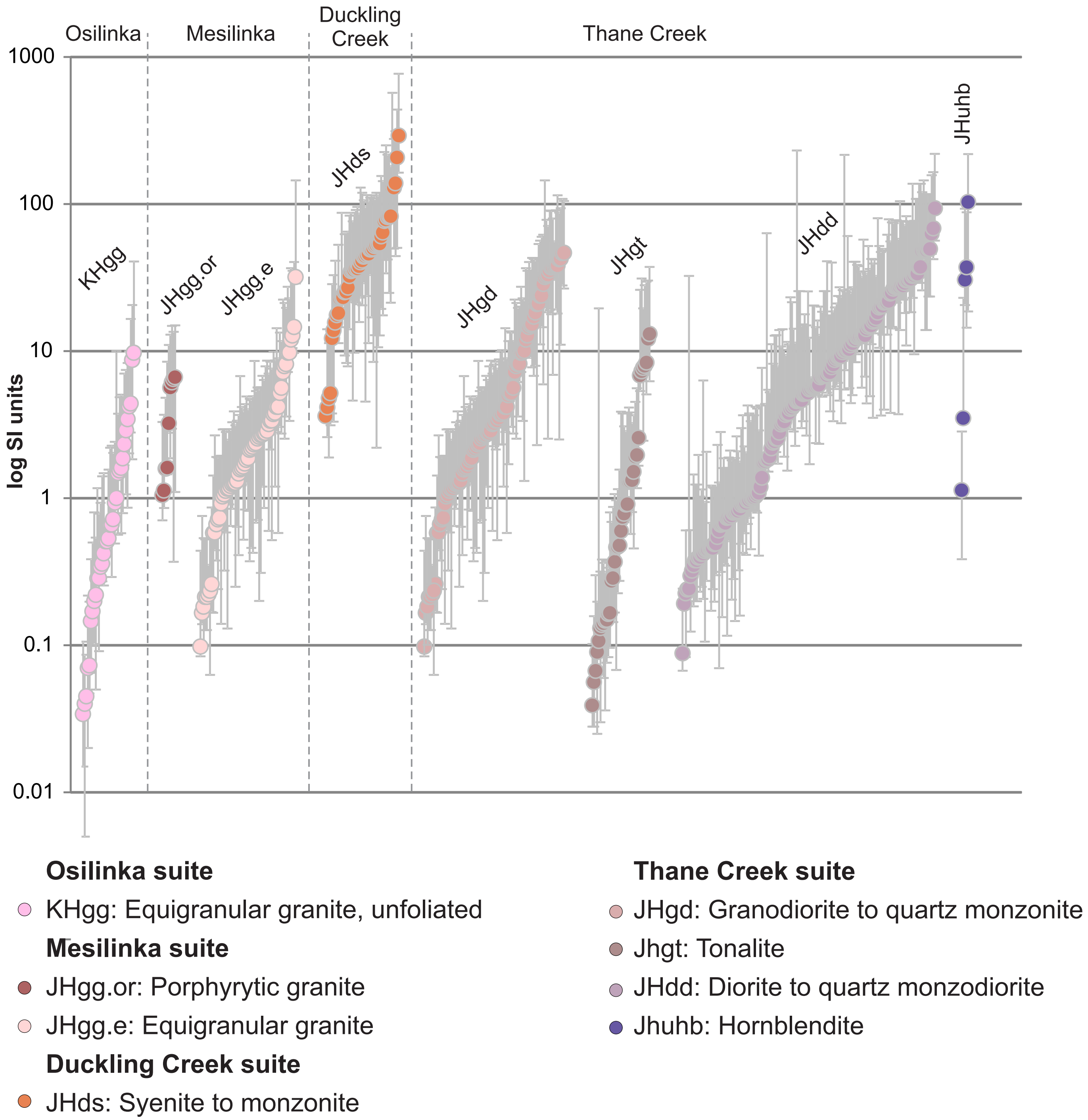


**Fig. 5.** Plot of magnetic susceptibility (logSI: International System of Units) for each of the intrusive suites. Each point represents the mean of ca. 10 measurements that were collected at each field station. Error bars represent the maximum and minimum measurements associated with each mean.

### 3.1.5. Porphyry sheets and dikes

Subhorizontal sheets and rare dikes of feldspar porphyry and quartz-feldspar porphyry cut equigranular granite of the Osilinka suite (Figs. 10c, d). The sheets are the youngest rock unit identified in the study area. They are <4 m wide and include at least two different subtypes characterized by: 1) plagioclase phenocrysts (≤4 cm) in a brown to dark green fine-grained intermediate groundmass; and 2) quartz (≤1 cm) and K-feldspar phenocrysts (≤2 cm; Fig. 10c), commonly densely packed, in a fine-grained white to light green felsic groundmass. Upper and lower contacts with the equigranular granite are common and are generally chilled and sheared. The sheets lack the jointing that is common in the equigranular granite.

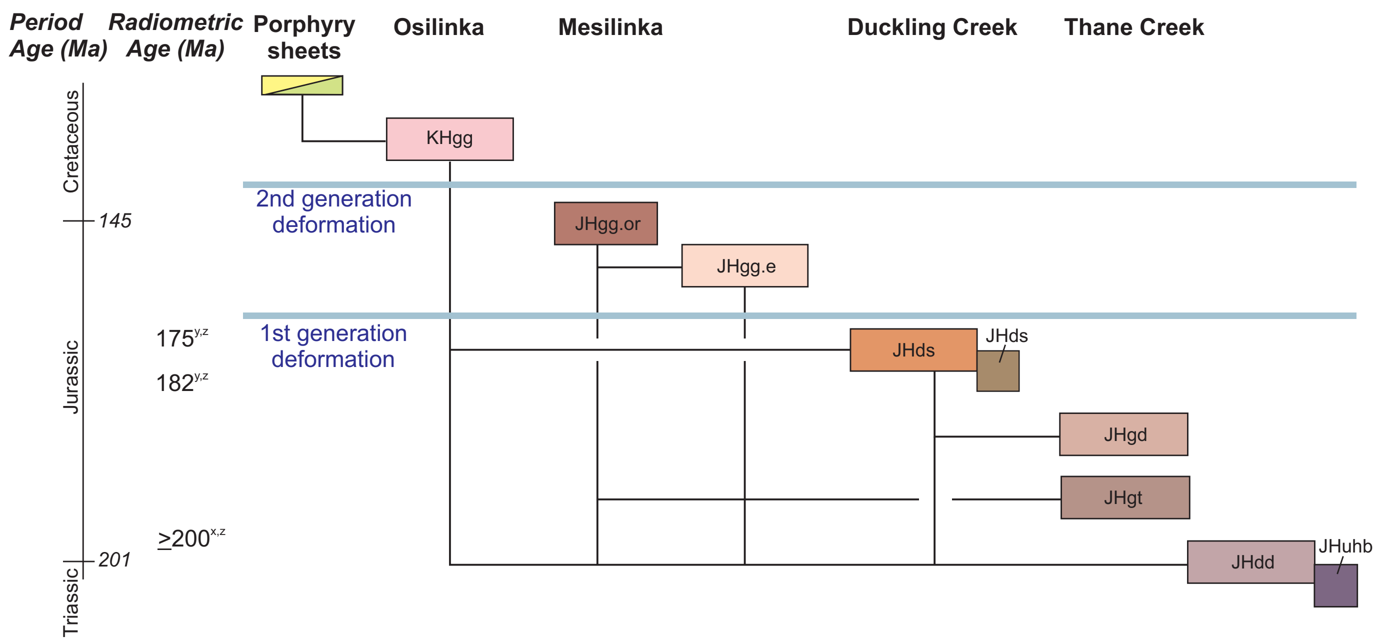


**Fig. 6.** Flow chart depicting the intrusive (thin black lines) and structural (thick blue lines) relationships of plutonic rocks in northern Hogem batholith. Observed crosscutting relationships are depicted by lines that connect units. Radiometric age data are from [x]Schiarizza and Tan (2005b), [y]Bath et al. (2014), and [z]Devine et al. (2014).

### 3.2. Structural observations

The diorite to quartz monzodiorite of the Thane Creek suite contains a weak to strong foliation (Fig. 4b), including local mylonite. The foliation is defined by the amphibole, plagioclase, and biotite. Within the diorite, flattened and aligned hornblendite enclaves and amphibole-biotite schlieren are primary magmatic features that were overprinted and accentuated by tectonic deformation. The hornblendite units do not contain a foliation, indicating that these bodies were likely more rigid than surrounding diorite during deformation, possibly due to coarse grain sizes. The tonalite and granodiorite to quartz monzodiorite units of the Thane Creek suite contain a weak to moderate foliation, typically defined by biotite and amphibole. The relationship of this fabric to the foliation in the diorite is unknown.

Syenite and monzonite of the Duckling Creek suite are weakly to strongly foliated (Fig. 4b), including local mylonite development. Similar fabrics are described from the oldest unit of the suite, south of the study area (Devine et al., 2014). The foliation is defined by coarse-grained K-feldspar with microlithons of medium-grained amphibole and lesser pyroxene and plagioclase or albite. Typically, the finer-grained mafic units appear more strongly deformed than the coarser-grained amphibole-poor rocks. Magmatic layering, in places rhythmic and graded, is a common feature in the monzonite and is interpreted to be a result of primary magmatic differentiation accentuated by ductile deformation (Fig. 8c).

Both porphyritic granite and equigranular granite of the Mesilinka suite have a moderate tectonic foliation (Fig. 4b), which cuts across intrusive contacts (Fig. 9c). In the northwest part of the study area, near the contact between the porphyritic granite and Thane Creek diorite and where outcrops are inaccessible, is talus with strongly deformed to mylonitic diorite. In the south-central part of the study area, the foliated equigranular granite contains xenoliths of diorite with an earlier formed, moderate to strong foliation, including local mylonite. Based on these observations, it appears that the Thane Creek diorite was deformed before, or possibly during, intrusion of the Mesilinka granite.

The Osilinka suite equigranular granite lacks a foliation, but does preserve evidence of post-crystallization ductile deformation. This evidence is, in part, within a two metre-wide intermediate dike that crosscuts the granite in the central part of the Osilinka suite (Fig. 4a). The granite lacks a fabric, whereas the dike contains a strong north striking foliation, and moderately north-plunging mineral lineations and boudins, and symmetric winged porphyroclasts. The relationship of this dike and porphyry dikes is unknown. Ductile deformation is also indicated by a weakly developed foliation in ≤20 cm wide alteration haloes adjacent to joints and quartz veins in the central part of the Osilinka suite. These alteration haloes likely resulted from fluid-rock interaction during quartz vein formation. The foliation in these haloes is perpendicular to the joints and veins and is gently folded, but the timing relationship between the joints and quartz vein and the foliation is unknown. These structures may be local, or may be the manifestation of regional deformation, with the paucity of mafic minerals accounting for the absence of a foliation in the granite itself.

The quartz-feldspar and feldspar porphyry sheets contain a contact-parallel foliation. This fabric is interpreted to be magmatic because it does not crosscut contacts, it does not occur in the equigranular granite, and it only developed close


**Fig. 7.** Representative outcrop photographs of Thane Creek suite. **a)** Coarse-grained hornblendite (Jhuhb) with pegmatitic phase of amphibole and plagioclase. **b)** Diffuse intrusive contact between hornblendite (dark) and diorite (green-grey). **c)** Equigranular, medium-grained diorite (Jhdd). **d)** Monzodiorite with subhedral pink K-feldspar crystals and mint green epidote-bearing groundmass. Mafic crystals retain the shape of amphibole but are mostly replaced by biotite, which is interpreted to record late- or post-magmatic potassic alteration. **e)** Tonalite (JHgt), crosscut by subhorizontal aplite sheet and older aplite dikelets. **f)** Equigranular quartz monzodiorite to granodiorite (JHgd) with subrounded intermediate xenoliths.

to the margins of the sheets, not in the cores. The fabrics that occur in the equigranular granite were not observed in the porphyry sheets.

## 4. Mineralization

The Lorraine Cu-Au porphyry deposit is 11 km southeast of this study and is hosted in rocks of the Duckling Creek suite (Garnett, 1978; Nixon and Peatfield, 2003; Bath et al., 2014,; Devine et al., 2014). There are no developed prospects within the study area, but ca. 34 mineral occurrences are documented in MINFILE (Fig. 11; Table 2). These can be considered as two end-member styles of mineralization. First, syngenetic

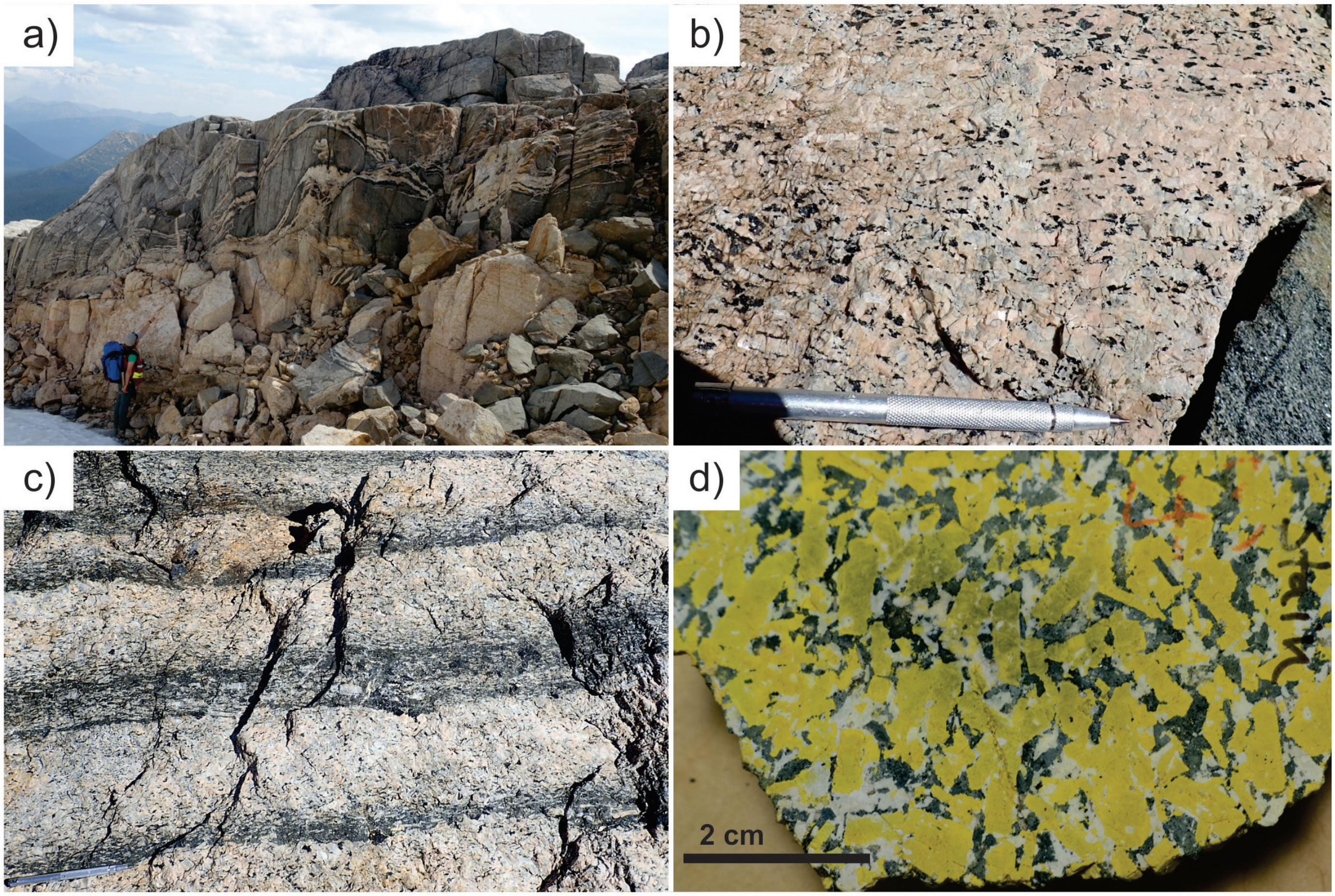


**Fig. 8.** Representative outcrop photographs of the Duckling Creek suite. **a)** Large pyroxenite enclaves in syenite. **b)** Coarse-grained syenite with K-feldspar and amphibole. **c)** Rhythmic magmatic layering that ranges from monzodiorite to syenite in composition. The layering is accentuated by a foliation, defined by alignment of the K-feldspar subparallel to the layers. **d)** Stained slab of monzonite showing coarse K-feldspar (yellow) and interstitial albite or plagioclase (white) and amphibole or pyroxene (black).

porphyry-style Cu (±Au, Ag, Mo; Fig. 11; Table 2), which is typically represented by malachite staining or disseminated chalcopyrite in the host rock. Most mineral showings of this type are in diorite and granodiorite of the Thane Creek suite and pyroxenite of the Duckling Creek suite, although one Mo-showing is related to the Osilinka granite (Fig. 11; Table 2). The second style includes epigenetic quartz veins with local concentrations of precious- and base-metals (Fig. 11; Table 2) that are relatively young as they cut the Osilinka granite (e.g., Hawk showing; Nelson et al., 2001).

While mapping, we collected grab samples with metallic mineralization from outcrops. These samples were sent to Activation Laboratories (Ancaster, Ontario) where they were crushed and pulped using mild steel (Code RX-1) and analyzed by a combination of instrumental neutron activation analysis (INAA) and acid dilution inductively coupled plasma-mass spectrometry (ICP-MS; Code 1H; Table 3). Two samples contained Cu values above detection limit of 10,000 ppm and were further analyzed by acid dilution inductively coupled plasma optical emission spectrometry (ICP-OES; Table 3).

The results document 17 new mineral occurrences, two of which are close to previously documented mineralization (Fig. 11; Tables 2 and 3). These occurrences conform to the same two end-member styles described above. Most are of the porphyry-style and comprise malachite staining and/or disseminated chalcopyrite. At location B (Fig. 11; Table 3) chalcopyrite occurs in veins and as disseminations in hornblendite of the Thane Creek suite, but most others are in Thane Creek diorite or granodiorite, or in pyroxenite of the Duckling Creek suite. The latter includes location L (Fig. 11; Table 3), which has malachite staining on a magnetite-cemented breccia zone in pyroxenite. Two of the new mineral occurrences are quartz vein-hosted. At location C (Fig. 11) mineralization is in a quartz vein (up to 15 cm wide) that pinches and swells, is exposed intermittently over ~100 m, and locally displays a malachite stain and disseminated chalcopyrite. At location E (Fig. 11) mineralization is in a poorly exposed subhorizontal 10 cm-wide quartz vein. Where exposed and in talus the quartz vein contains massive and disseminated pyrite, and carries minor amounts of Au, and elevated Mo (Table 3).

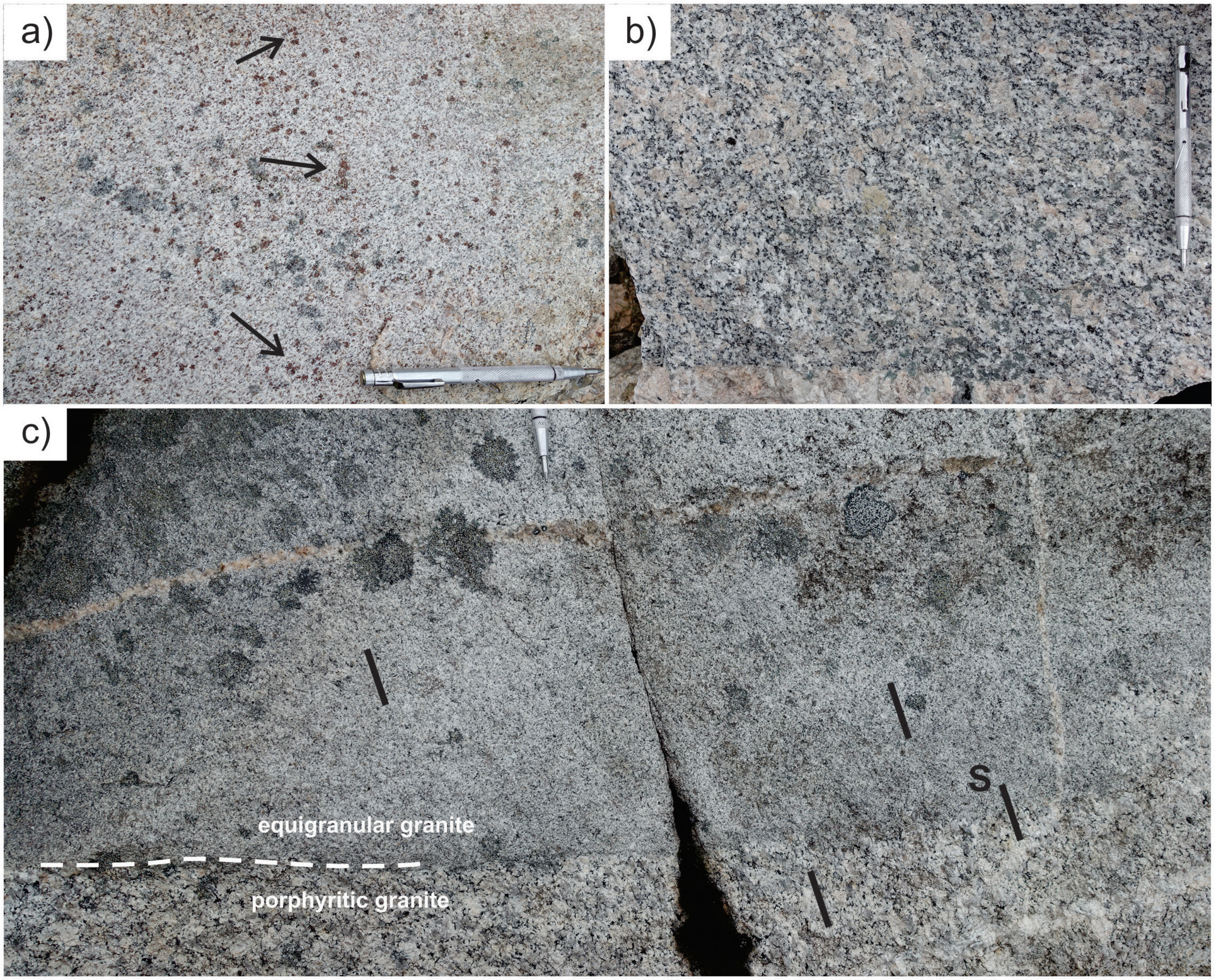


**Fig. 9.** Representative outcrop photographs of the Mesilinka suite**. a)** Equigranular granite, with red garnet (arrows). **b)** Porphyritic granite with K-feldspar phenocrysts. **c)** Intrusive contact where the porphyritic granite crosscuts the equigranular granite. The contact is cut by the foliation (S), demonstrating this fabric is tectonic, not magmatic.

## 5. Conclusions

New mapping has refined the subdivision and distribution of plutonic rocks in northern Hogem batholith. The eastern part of the study area is mostly underlain by diorite and lesser hornblendite of the Thane Creek suite. Quartz monzonite also occurs in the Thane Creek suite and may have formed as a result of magmatic differentiation, post-crystallization alteration processes, or both. The diorites consistently have a weak to strong foliation, with local mylonite. Tonalite and granodiorite to quartz monzonite are included in the Thane Creek suite, but appear to post-date the hornblendite and diorite intrusions. Syenite and monzonite, with local monzodiorite and biotite pyroxenite, underlie the southern part of the study area and are part of the Duckling Creek suite. Intrusive contacts with the Thane Creek diorites were not observed, but correlation with dated rocks to the south and north (Schiarizza and Tan, 2005b; Devine et al., 2014), suggests the Thane Creek suite is older (≥ 200 Ma) than the Duckling Creek suite (182 to 175 Ma).

The western part of the study area is underlain by granitic rocks of the Mesilinka suite. All Mesilinka suite rocks are deformed, with foliations that crosscut intrusive contacts. The youngest rocks are in the central part of the study area and consist of Osilinka suite granites, which contain low abundances of mafic minerals (≤5%). These granites lack a foliation, but display local evidence of post-crystallization ductile strain. The Osilinka granite is intruded by subhorizontal sheets and lesser dikes of intermediate feldspar porphyry and felsic quartz-feldspar porphyry, which are the youngest rocks in the study area.

Seventeen new mineral occurrences were discovered during mapping. These are mostly disseminated chalcopyrite and/or malachite staining in rocks of the Thane Creek and Duckling Creek suites, but also include quartz veins that crosscut the Thane Creek and Osilinka suites.

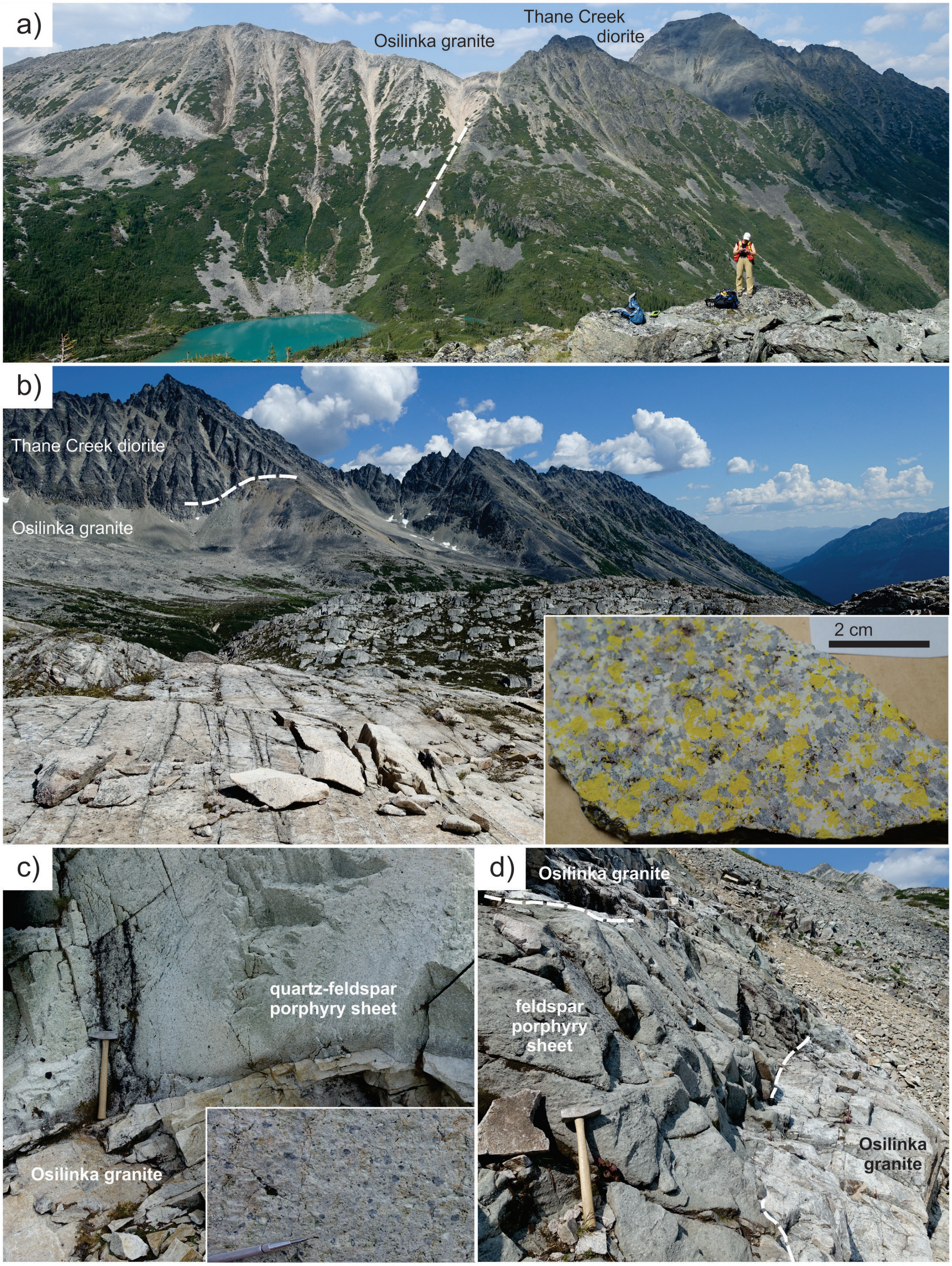


**Fig. 10.** Osilinka suite and porphyry sheets. **a)** Intrusive contact between the Osilinka granite and Thane Creek diorite. View is north. **b)** Foreground is Osilinka granite with joints (grey fractures) and background is intrusive contact with Thane Creek diorite. View is to the east. Inset is stained Oslinka granite showing K-feldspar (yellow) with quartz (grey), plagioclase (white) and low mafic mineral content. **c)** Subhorizontal quartz-feldspar porphyry sheet that cuts Osilinka granite. Inset shows quartz (blue-grey) and K-feldspar (white) phenocrysts in fine-grained groundmass. **d)** Subhorizontal intermediate feldspar porphyry sheet that cuts Osilinka granite.

**Table 2.** Mineral occurrences in the study area, extracted and modified from British Columbia Geological Survey MINFILE (https://www2.gov.bc.ca/gov/content/industry/mineral-exploration-mining/british-columbia-geological-survey/mineralinventory).

| Label | MINFILE | Name | Alias | Commodities | Deposit type | Status | UTM_X* | UTM_Y* |
|---|---|---|---|---|---|---|---|---|
| **1** | 094C 045 | HORNWAY CREEK | COPPER 1 | Cu | Alkalic porphyry | Showing | 321347 | 6233527 |
| **2** | 094C 098 | PAUL | MANIE | Mo | Porphyry | Showing | 323755 | 6232095 |
| **3** | 094C 011 | OS | | Cu | Alkalic porphyry | Showing | 325250 | 6228567 |
| **4** | 094C 010 | ET | CATHEDRAL | Cu | Alkalic porphyry | Showing | 326898 | 6234722 |
| **5** | 094C 016 | CHIEF THOMAS | THANE CREEK | Cu | Polymetallic veins | Showing | 330105 | 6232117 |
| **6** | 094C 046 | ETSCHITKA CREEK | COPPER 2 | Cu | Alkalic porphyry | Showing | 330433 | 6236901 |
| **7** | 094C 047 | MATETLO CREEK | COPPER 3 | Cu | Alkalic porphyry | Showing | 332209 | 6235593 |
| **8** | 094C 017 | ELIZABETH | | Au, Ag | Au-quartz veins | Showing | 331901 | 6233903 |
| **9** | 094C 117 | YETI | | Cu | Alkalic porphyry | Showing | 335263 | 6235227 |
| **10** | 094C 116 | BILL | MATE | Cu, Au | Alkalic porphyry | Showing | 335190 | 6233341 |
| **11** | 094C 115 | INTREPID | MATE | Cu | Alkalic porphyry | Showing | 335473 | 6232619 |
| **12** | 094C 188 | LAKE AREA (CATHEDRAL) | SADDLE | Cu | Alkalic porphyry | Showing | 335374 | 6231511 |
| **13** | 094C 018 | MATETLO | KAM | Cu | Alkalic porphyry | Prospect | 337907 | 6232216 |
| **14** | 094C 114 | KOALA | MATE | Cu | Alkalic porphyry | Showing | 338408 | 6232692 |
| **15** | 094C 113 | YAK | MATE | Cu | Alkalic porphyry | Showing | 338744 | 6232463 |
| **16** | 094C 118 | DRAGON | MATE | Cu, Au | Alkalic porphyry | Showing | 339143 | 6233438 |
| **17** | 094C 099 | MAT 1 | ROLLY | Ag, Cu, Pb, Zn, Au | Polymetallic veins | Prospect | 340305 | 6235468 |
| **18** | 094C 119 | TOUGH | | Cu | Alkalic porphyry | Showing | 343949 | 6236138 |
| **19** | 094C 174 | OSI | | Cu, Pt | Alkalic porphyry | Showing | 333708 | 6221450 |
| **20** | 094C 050 | HOGEM COPPER | OSILINKA RIVER | Cu | Porphyry | Showing | 331784 | 6221249 |
| **21** | 094C 051 | DETNI CREEK | OMINECA RIVER | Cu | Porphyry | Showing | 320429 | 6212794 |
| **22** | 094C 140 | HAWK (HSW) | HSW | Au, Cu | Au-quartz veins | Showing | 331457 | 6212471 |
| **23** | 094C 138 | HAWK (AD) | AD | Au, Cu, Pb, Zn, Ag | Au-quartz veins | Prospect | 333410 | 6213231 |
| **24** | 094C 171 | MEADOW | HAWK | Au, Ag, Cu | Au-quartz veins | Showing | 334000 | 6212160 |
| **25** | 094C 139 | HAWK (RADIO) | RADIO | Au, Cu, Ag | Au-quartz veins | Prospect | 333702 | 6211827 |
| **26** | 094C 063 | DOVE | HAW | Cu, Mo, Ag | Alkalic porphyry | Showing | 331505 | 6209715 |
| **27** | 093N 171 | HAW | HAWK | Cu | Alkalic porphyry | Showing | 331533 | 6207331 |
| **28** | 093N 249 | RAVEN | | Au, Cu | Alkalic porphyry | Showing | 333846 | 6206636 |
| **29** | 093N 176 | FLAME | OGK | Cu, Mo | Alkalic porphyry | Showing | 338000 | 6209032 |
| **30** | 093N 242 | SLIDE | JAN-TAM-MISTY | Cu, Au, Ag | Alkalic porphyry | Prospect | 341833 | 6208350 |
| **31** | 094C 097 | REM | AMP | Cu, Pb | Polymetallic veins | Showing | 345701 | 6211009 |
| **32** | 094C 077 | ND | | Cu | Alkalic porphyry | Showing | 342102 | 6210706 |
| **33** | 094C 170 | GOAT | TAM | Cu, Au, Ag | Alkalic porphyry | Showing | 338429 | 6211090 |
| **34** | 094C 177 | NOVA 5 | CAT MOUNTAIN | Cu | Alkalic porphyry | Showing | 339595 | 6214332 |

Label numbers correspond to Figure 11.

*UTM Zone 10, NAD 83

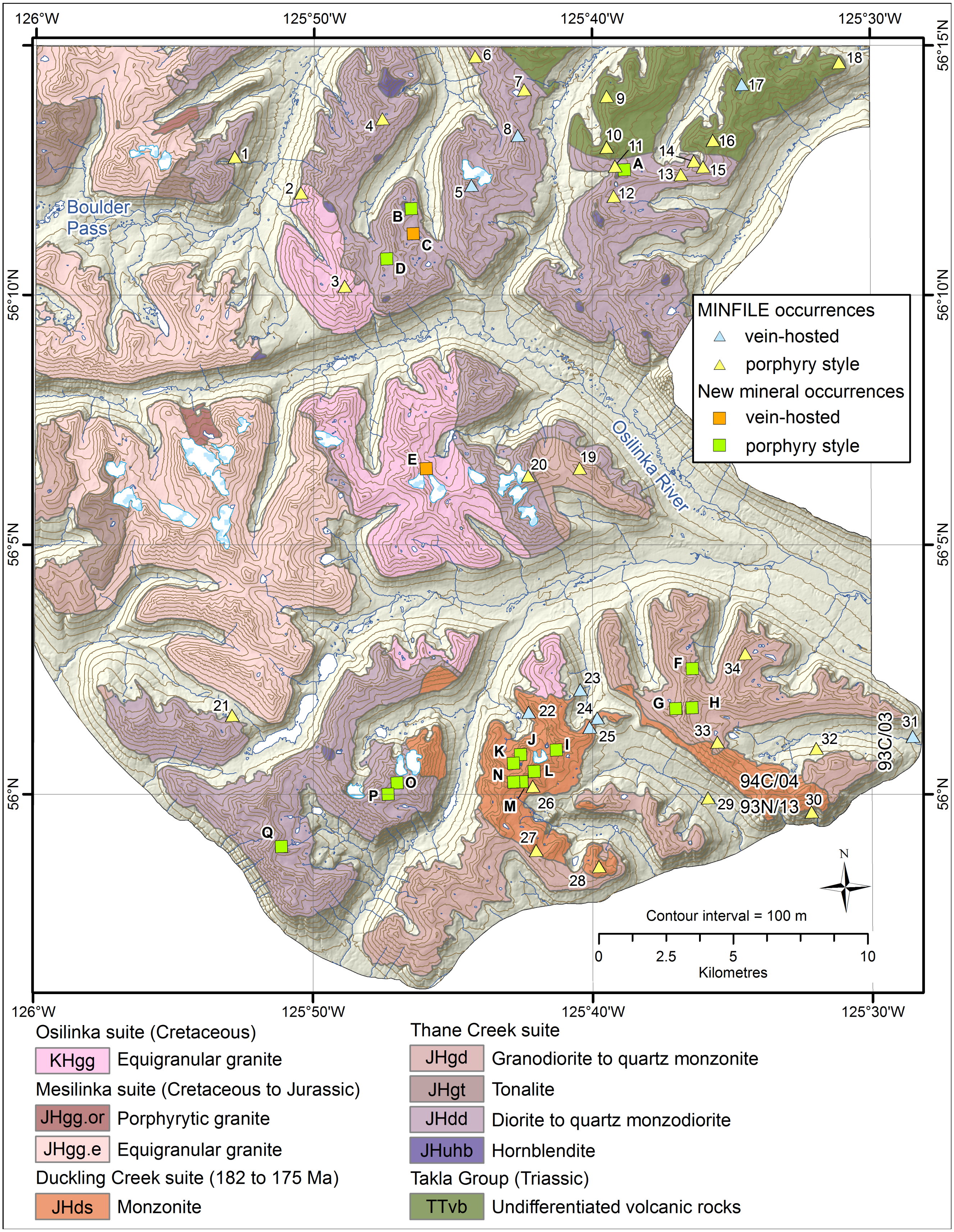


**Fig. 11.** Mineral occurrences in the study area. MINFILE occurrences are designated by numbers (see Table 2); newly mapped occurrences are designated by letters (see Table 3).

**Table 3.** Assay results from newly mapped mineral occurrences. Labels correspond to locations plotted on Figure 11; underlined values are considered of interest; *UTM zone 10, NAD 83; ^close to mineralization documented in MINFILE; **may contain lepidolite.

| Label | | A | B | C | D | E | E | E | F | G |
|---|---|---|---|---|---|---|---|---|---|---|
| station | | 18ab-6-3c | 18lo-6-2a | 18lo-7-2a | 18DMI-8-10 | 18lo-15-1b-1 | 18lo-15-1b-2 | 18lo-15-1b-3 | 18bg-31-1b | 18ab-26-4 |
| | | ^Known | New | New | New | New | New | New | New | New |
| MINFILE | | 094C 115 | | | | | | | | |
| Type | | porphyry | porphyry | vein | porphyry | vein | vein | vein | porphyry | porphyry |
| UTM_X* | | 335800 | 327819 | 327857 | 326835 | 327996 | 327996 | 327996 | 337594 | 336915 |
| UTM_Y* | | 6232472 | 6231338 | 6230407 | 6229511 | 6221663 | 6221663 | 6221663 | 6213838 | 6212379 |
| Au | ppb | 478 | 46 | 41 | 10 | 1600 | 3680 | 612 | 54 | 227 |
| Ag | ppm | 4.2 | 1.9 | 10.3 | 3.3 | 2.5 | 1.1 | 1.2 | 1.7 | 140 |
| Cu | ppm | 4430 | 3170 | > 10000 | 3860 | 12 | 10 | 5 | 5290 | 4340 |
| Cu | % | - | - | 1.28 | - | - | - | - | - | - |
| Cd | ppm | < 0.3 | 0.6 | 1.3 | 0.5 | < 0.3 | < 0.3 | < 0.3 | < 0.3 | 3.4 |
| Mo | ppm | 3 | < 1 | 1 | < 1 | 74 | 58 | 65 | < 1 | 32 |
| Pb | ppm | 11 | < 3 | < 3 | 4 | 13 | 6 | < 3 | < 3 | 480 |
| Ni | ppm | 18 | 31 | 8 | 11 | 2 | 4 | 3 | 9 | 3 |
| Zn | ppm | 63 | 115 | 43 | 79 | 10 | 13 | 7 | 43 | 387 |
| S | % | 0.02 | 3.96 | 0.75 | 0.19 | 5.45 | 4.49 | 4.19 | 0.11 | 0.44 |
| Al | % | 8.07 | 7.85 | 1.78 | 5.89 | 1.25 | 3.75 | 2.02 | 7.97 | 7.2 |
| As | ppm | 4.9 | 9.3 | 2.2 | 3 | 1.3 | 1.6 | 2.3 | 2 | 11.1 |
| Ba | ppm | 820 | 390 | 500 | 1050 | 390 | 660 | 550 | 1700 | 1680 |
| Be | ppm | 1 | < 1 | < 1 | < 1 | 1 | 4 | 2 | 1 | 1 |
| Bi | ppm | < 2 | < 2 | 11 | < 2 | 325 | 106 | 29 | < 2 | < 2 |
| Br | ppm | < 0.5 | < 0.5 | < 0.5 | < 0.5 | < 0.5 | < 0.5 | < 0.5 | < 0.5 | < 0.5 |
| Ca | % | 3.03 | 3.91 | 0.4 | 1.73 | 0.32 | 0.33 | 0.66 | 3.39 | 1.1 |
| Co | ppm | 22 | 51 | 11 | 21 | 7 | 8 | 5 | 19 | 10 |
| Cr | ppm | 4 | 31 | 104 | 4 | 3 | 91 | < 2 | < 2 | 40 |
| Cs | ppm | < 1 | < 1 | < 1 | < 1 | 1 | 3 | 2 | < 1 | < 1 |
| Eu | ppm | 1.2 | 0.6 | 1.1 | 0.3 | < 0.2 | < 0.2 | < 0.2 | 0.5 | < 0.2 |
| Fe | % | 6.77 | 11.7 | 3.21 | 4.24 | 5.02 | 4.58 | 4.27 | 3.91 | 2.93 |
| Hf | ppm | 13 | < 1 | < 1 | < 1 | < 1 | < 1 | < 1 | 4 | 3 |
| Hg | ppm | < 1 | < 1 | < 1 | < 1 | < 1 | < 1 | < 1 | < 1 | < 1 |
| Ir | ppb | < 5 | < 5 | < 5 | < 5 | < 5 | < 5 | < 5 | < 5 | < 5 |
| K | % | 3.63 | 0.28 | 0.5 | 1.25 | 0.8 | 1.78 | 1.34 | 2.31 | 4.69 |
| Li | ppm | 11 | 6 | 4 | 12 | 4 | 7 | 6 | 9 | 7 |
| Mg | % | 1.5 | 3.38 | 0.6 | 1.4 | 0.05 | 0.11 | 0.07 | 1.07 | 0.44 |
| Mn | ppm | 897 | 978 | 545 | 775 | 115 | 254 | 138 | 768 | 380 |
| Na | % | 1.92 | 2.31 | 0.1 | 1.86 | 0.04 | 0.31 | 0.05 | 2.86 | 2.02 |
| P | % | 0.189 | 0.266 | 0.03 | 0.096 | 0.001 | 0.004 | 0.001 | 0.101 | 0.04 |
| Rb | ppm | 72 | < 15 | < 15 | < 15 | 35 | 115 | 93 | 69 | 128 |
| Sb | ppm | 1.4 | 0.3 | 0.3 | 1 | < 0.1 | < 0.1 | < 0.1 | 0.4 | 192 |
| Sc | ppm | 15.7 | 24.7 | 2.7 | 9.9 | 0.6 | 0.8 | 0.8 | 9.2 | 2.5 |
| Se | ppm | < 3 | < 3 | < 3 | < 3 | < 3 | < 3 | < 3 | < 3 | < 3 |
| Sr | ppm | 508 | 388 | 29 | 289 | 27 | 56 | 46 | 762 | 101 |
| Ta | ppm | < 0.5 | < 0.5 | < 0.5 | < 0.5 | < 0.5 | < 0.5 | < 0.5 | < 0.5 | < 0.5 |
| Ti | % | 0.18 | 0.44 | 0.07 | 0.23 | 0.01 | 0.03 | 0.02 | 0.26 | 0.14 |
| Th | ppm | 4 | < 0.2 | 1.5 | < 0.2 | 0.2 | 0.3 | < 0.2 | 3.5 | 6.6 |
| U | ppm | 11.5 | < 0.5 | < 0.5 | < 0.5 | < 0.5 | < 0.5 | < 0.5 | 2.8 | 5.1 |
| V | ppm | 66 | 206 | 62 | 102 | 49 | 59 | 66 | 114 | 61 |
| W | ppm | < 1 | < 1 | 2 | < 1 | 13 | 61 | 164 | < 1 | 16 |
| Y | ppm | 26 | 14 | 5 | 9 | < 1 | < 1 | < 1 | 11 | 4 |
| La | ppm | 20.1 | 6.2 | 21 | 5.3 | 0.7 | 0.8 | < 0.5 | 14.6 | 11.6 |
| Ce | ppm | 48 | 14 | 40 | 14 | < 3 | < 3 | < 3 | 22 | 17 |
| Nd | ppm | 17 | 15 | 17 | < 5 | < 5 | < 5 | < 5 | 10 | < 5 |
| Sm | ppm | 3.7 | 2.7 | 4 | 1.5 | < 0.1 | < 0.1 | 0.1 | 2.5 | 1 |
| Sn | % | < 0.02 | < 0.02 | < 0.02 | < 0.02 | < 0.02 | < 0.02 | < 0.02 | < 0.02 | < 0.02 |
| Tb | ppm | < 0.5 | < 0.5 | < 0.5 | < 0.5 | < 0.5 | < 0.5 | < 0.5 | < 0.5 | < 0.5 |
| Yb | ppm | 2.2 | 1.4 | 0.5 | 0.9 | < 0.2 | < 0.2 | < 0.2 | 1.1 | 0.5 |
| Lu | ppm | 0.26 | 0.05 | 0.05 | < 0.05 | < 0.05 | < 0.05 | < 0.05 | 0.1 | < 0.05 |
| Mass | g | 34.7 | 34.8 | 32 | 33.7 | 32.2 | 32.5 | 32.9 | 30 | 31 |

**Table 3.** Continued.

| Label | | **H**** | **I** | **J** | **K** | **L** | M | **N** | **O** | **P** |
|---|---|---|---|---|---|---|---|---|---|---|
| station | | 18ab-24-11 | 18lo-24-5a | 18ab-17-2 | 18ab-18-10b | 18lo-25-2c | 18bg-28-2 | 18ab-16-9 | 18ab-23-8 | 18ab-22-7 |
| MINFILE | | New | New | New | New | New | ^Known 094C 063 | New | New | New |
| Type | | porphyry | porphyry | porphyry | porphyry | porphyry | porphyry | porphyry | porphyry | porphyry |
| UTM_X* | | 337530 | 332420 | 331080 | 330806 | 331567 | 331098 | 330783 | 326452 | 326100 |
| UTM_Y* | | 6212386 | 6211021 | 6210906 | 6210596 | 6210259 | 6209887 | 6209894 | 6210031 | 6209630 |
| Au | ppb | 774 | 72 | 73 | 466 | 718 | 300 | 186 | 58 | 119 |
| Ag | ppm | 7.8 | 1.7 | 1.8 | 4.3 | 3.1 | 5.7 | 2.1 | 3.3 | 9.2 |
| Cu | ppm | 19 | 1910 | 2150 | 5660 | > 10000 | 6800 | 2620 | 3610 | 3720 |
| Cu | % | - | - | - | - | 1.53 | - | - | - | - |
| Cd | ppm | 2.7 | < 0.3 | < 0.3 | 0.5 | 1.1 | 0.6 | < 0.3 | 0.4 | < 0.3 |
| Mo | ppm | 2 | < 1 | < 1 | < 1 | 2 | < 1 | < 1 | 5 | 1 |
| Pb | ppm | 149 | 4 | 6 | 8 | 9 | 6 | < 3 | 5 | 22 |
| Ni | ppm | 6 | 5 | 5 | 8 | 26 | 11 | 15 | 9 | 3 |
| Zn | ppm | 285 | 102 | 75 | 69 | 216 | 129 | 193 | 106 | 7 |
| S | % | 1.42 | 0.02 | 0.01 | 0.17 | 0.94 | 0.04 | 0.06 | 0.21 | 0.24 |
| Al | % | 7.97 | 10.1 | 9.48 | 8.96 | 7.59 | 3.78 | 4.88 | 9.19 | 0.25 |
| As | ppm | 2.3 | 2.5 | 1.8 | < 0.5 | 1.1 | 2 | 2.3 | 1 | 1.9 |
| Ba | ppm | 940 | 1740 | 3130 | 3310 | 2600 | 730 | 1120 | 1080 | 200 |
| Be | ppm | 1 | 2 | 1 | < 1 | < 1 | 3 | 2 | 1 | < 1 |
| Bi | ppm | < 2 | < 2 | < 2 | < 2 | < 2 | 6 | < 2 | < 2 | 17 |
| Br | ppm | < 0.5 | < 0.5 | < 0.5 | < 0.5 | < 0.5 | < 0.5 | < 0.5 | < 0.5 | < 0.5 |
| Ca | % | 4.98 | 1.78 | 2.44 | 3.42 | 1.17 | 13.7 | 9.34 | 3.18 | 0.06 |
| Co | ppm | 14 | 14 | 19 | 14 | 60 | 43 | 53 | 37 | 4 |
| Cr | ppm | 40 | 3 | 8 | 23 | 24 | 26 | 31 | 6 | < 2 |
| Cs | ppm | < 1 | < 1 | < 1 | < 1 | < 1 | < 1 | < 1 | 2 | < 1 |
| Eu | ppm | 0.4 | < 0.2 | < 0.2 | < 0.2 | 0.4 | 3.2 | 2.8 | < 0.2 | < 0.2 |
| Fe | % | 3.27 | 3.56 | 4.14 | 3.79 | 8.03 | 7.49 | 12.9 | 5.56 | 1.41 |
| Hf | ppm | 3 | 4 | 3 | 1 | 2 | 2 | 4 | 4 | < 1 |
| Hg | ppm | < 1 | < 1 | < 1 | < 1 | < 1 | < 1 | < 1 | < 1 | < 1 |
| Ir | ppb | < 5 | < 5 | < 5 | < 5 | < 5 | < 5 | < 5 | < 5 | < 5 |
| K | % | 4.47 | 6.19 | 5.96 | 4.64 | 5.79 | 1.43 | 1.55 | 1.76 | 0.04 |
| Li | ppm | 5 | 9 | 7 | 2 | 8 | 11 | 14 | 12 | < 1 |
| Mg | % | 0.29 | 0.63 | 0.66 | 0.76 | 1.35 | 3.71 | 3.33 | 1.66 | 0.03 |
| Mn | ppm | 1060 | 1130 | 916 | 924 | 1240 | 2930 | 2780 | 956 | 63 |
| Na | % | 0.17 | 2.34 | 2.15 | 2.71 | 1.54 | 1.19 | 1.72 | 3.4 | 0.12 |
| P | % | 0.102 | 0.074 | 0.074 | 0.12 | 0.264 | 1.52 | 0.327 | 0.096 | 0.008 |
| Rb | ppm | 199 | 110 | 149 | 88 | 185 | < 15 | 34 | < 15 | < 15 |
| Sb | ppm | 2.4 | < 0.1 | 0.2 | < 0.1 | < 0.1 | < 0.1 | < 0.1 | < 0.1 | < 0.1 |
| Sc | ppm | 6.7 | 4.6 | 5.7 | 5.6 | 2.6 | 30.8 | 27.6 | 10.9 | < 0.1 |
| Se | ppm | < 3 | < 3 | < 3 | < 3 | < 3 | < 3 | < 3 | < 3 | 10 |
| Sr | ppm | 105 | 1900 | 4160 | 3920 | 1230 | 708 | 990 | 659 | 12 |
| Ta | ppm | < 0.5 | < 0.5 | < 0.5 | < 0.5 | < 0.5 | < 0.5 | < 0.5 | < 0.5 | < 0.5 |
| Ti | % | 0.26 | 0.24 | 0.19 | 0.25 | 0.33 | 0.02 | 0.26 | 0.39 | 0.01 |
| Th | ppm | 3.2 | 4 | 2.1 | 1.8 | 3.7 | 6 | 2.2 | 1.3 | < 0.2 |
| U | ppm | 3.8 | 0.9 | < 0.5 | < 0.5 | 1.7 | < 0.5 | 1 | < 0.5 | < 0.5 |
| V | ppm | 108 | 155 | 120 | 192 | 295 | 324 | 317 | 147 | 8 |
| W | ppm | 34 | < 1 | < 1 | < 1 | < 1 | < 1 | < 1 | < 1 | < 1 |
| Y | ppm | 8 | 8 | 11 | 13 | 13 | 60 | 38 | 10 | < 1 |
| La | ppm | 13.7 | 8.4 | 8.2 | 13.9 | 16.5 | 100 | 33.5 | 12.6 | 1.3 |
| Ce | ppm | 23 | 17 | 18 | 29 | 29 | 151 | 63 | 18 | < 3 |
| Nd | ppm | 11 | < 5 | 9 | 8 | 11 | 50 | 23 | 8 | < 5 |
| Sm | ppm | 2.2 | 1.5 | 2.3 | 2.8 | 2.5 | 12 | 7.7 | 1.7 | < 0.1 |
| Sn | % | < 0.02 | < 0.02 | < 0.02 | < 0.02 | < 0.02 | < 0.02 | < 0.02 | < 0.02 | < 0.02 |
| Tb | ppm | < 0.5 | < 0.5 | < 0.5 | < 0.5 | < 0.5 | 2.1 | 1.4 | < 0.5 | < 0.5 |
| Yb | ppm | 0.9 | 0.9 | 1.1 | 1.1 | 1 | 4.4 | 3.2 | 1 | < 0.2 |
| Lu | ppm | 0.1 | < 0.05 | 0.07 | 0.07 | 0.07 | 0.28 | 0.15 | < 0.05 | < 0.05 |
| Mass | g | 30 | 37.4 | 34.7 | 30.2 | 33.1 | 38.3 | 37.3 | 32.4 | 36.7 |

**Table 3.** Continued.

| Label | | Q | | | | | | | | |
|---|---|---|---|---|---|---|---|---|---|---|
| station | | 18bg-26-2b | 18ab-23-7 | 18ab-26-9 | 18ab-6-3a | 18bg-19-2 | 18bg-25-2b | 18bg-25-7 | 18bg-27-7 | 18bg-29-8a |
| MINFILE | | New | | | | | | | | |
| Type | | porphyry | | | | | | | | |
| UTM_X* | | 322055 | 326536 | 336101 | 335800 | 324553 | 322661 | 321909 | 338051 | 329741 |
| UTM_Y* | | 6207840 | 6209997 | 6212567 | 6232472 | 6220350 | 6208033 | 6209181 | 6212345 | 6206600 |
| Au | ppb | 232 | 7 | 27 | < 2 | 6 | 7 | 2 | 249 | < 2 |
| Ag | ppm | 5.8 | 0.3 | 0.8 | 0.4 | 4 | 0.4 | < 0.3 | 1.5 | < 0.3 |
| Cu | ppm | 3580 | 716 | 11 | 178 | 114 | 86 | 21 | 43 | 238 |
| Cu | % | - | - | - | - | - | - | - | - | - |
| Cd | ppm | 0.4 | < 0.3 | < 0.3 | < 0.3 | < 0.3 | < 0.3 | < 0.3 | 0.5 | < 0.3 |
| Mo | ppm | 1 | 4 | 21 | < 1 | 9 | 2 | < 1 | 3 | < 1 |
| Pb | ppm | 14 | < 3 | 16 | < 3 | 1200 | < 3 | < 3 | 16 | < 3 |
| Ni | ppm | 6 | 3 | 5 | 16 | 4 | 5 | 2 | 3 | 8 |
| Zn | ppm | 12 | 5 | 6 | 54 | 13 | 21 | 5 | 15 | 62 |
| S | % | 0.41 | 0.02 | 0.03 | 0.1 | 0.25 | 0.44 | 0.03 | 0.21 | 0.04 |
| Al | % | 1.55 | 1 | 0.65 | 7.14 | 4.63 | 2.86 | 0.24 | 4.05 | 8.71 |
| As | ppm | 5.1 | 2.6 | 2.1 | 2.5 | 4.3 | 1.5 | 3 | 1.5 | < 0.5 |
| Ba | ppm | < 50 | < 50 | 240 | 610 | 2810 | 790 | 930 | 740 | 2120 |
| Be | ppm | < 1 | < 1 | < 1 | 1 | 2 | < 1 | < 1 | < 1 | 1 |
| Bi | ppm | < 2 | < 2 | < 2 | < 2 | 11 | < 2 | < 2 | < 2 | < 2 |
| Br | ppm | < 0.5 | < 0.5 | < 0.5 | < 0.5 | < 0.5 | < 0.5 | < 0.5 | < 0.5 | < 0.5 |
| Ca | % | 0.32 | 1.32 | 0.46 | 7 | 0.49 | 0.28 | 0.5 | 0.14 | 2.29 |
| Co | ppm | 9 | 2 | 2 | 21 | < 1 | 15 | < 1 | 5 | 14 |
| Cr | ppm | 119 | 124 | 162 | 26 | < 2 | 3 | < 2 | 85 | 28 |
| Cs | ppm | < 1 | < 1 | < 1 | 6 | < 1 | < 1 | < 1 | < 1 | < 1 |
| Eu | ppm | < 0.2 | < 0.2 | < 0.2 | 1.1 | < 0.2 | < 0.2 | < 0.2 | < 0.2 | < 0.2 |
| Fe | % | 2.06 | 1.27 | 0.62 | 7.59 | 0.74 | 2.38 | 0.51 | 1.23 | 3.73 |
| Hf | ppm | < 1 | < 1 | < 1 | 30 | 1 | < 1 | < 1 | < 1 | 4 |
| Hg | ppm | < 1 | < 1 | < 1 | < 1 | < 1 | < 1 | < 1 | < 1 | < 1 |
| Ir | ppb | < 5 | < 5 | < 5 | < 5 | < 5 | < 5 | < 5 | < 5 | < 5 |
| K | % | 0.07 | 0.03 | 0.59 | 2.05 | 1.03 | 0.98 | 0.06 | 4.36 | 2.47 |
| Li | ppm | < 1 | < 1 | 3 | 6 | 16 | 3 | < 1 | 2 | 15 |
| Mg | % | 0.1 | < 0.01 | 0.05 | 0.74 | 0.06 | 0.38 | 0.03 | 0.02 | 1.26 |
| Mn | ppm | 161 | 248 | 270 | 1120 | 238 | 416 | 158 | 169 | 797 |
| Na | % | 1.01 | 0.03 | 0.06 | 2.05 | 2.25 | 0.36 | 0.12 | 0.15 | 2.97 |
| P | % | 0.009 | 0.005 | 0.005 | 0.255 | 0.008 | 0.035 | 0.003 | 0.02 | 0.108 |
| Rb | ppm | < 15 | < 15 | < 15 | 60 | < 15 | 26 | < 15 | 109 | 98 |
| Sb | ppm | 0.3 | 0.2 | 2 | 2.4 | 0.2 | < 0.1 | < 0.1 | 0.3 | 0.1 |
| Sc | ppm | 3 | 0.8 | 0.3 | 33.7 | 1.3 | 6.1 | 0.2 | 1.6 | 8.9 |
| Se | ppm | < 3 | < 3 | < 3 | < 3 | < 3 | < 3 | < 3 | < 3 | < 3 |
| Sr | ppm | 50 | 201 | 45 | 144 | 889 | 43 | 66 | 70 | 510 |
| Ta | ppm | < 0.5 | < 0.5 | < 0.5 | < 0.5 | < 0.5 | < 0.5 | < 0.5 | < 0.5 | < 0.5 |
| Ti | % | 0.08 | 0.02 | 0.02 | 0.43 | 0.04 | 0.14 | 0.01 | 0.09 | 0.28 |
| Th | ppm | < 0.2 | < 0.2 | 0.2 | 1.6 | < 0.2 | < 0.2 | 1.5 | 2.3 | 4.8 |
| U | ppm | < 0.5 | < 0.5 | 0.6 | 1.5 | < 0.5 | 0.6 | < 0.5 | < 0.5 | 2.7 |
| V | ppm | 65 | 46 | 5 | 254 | 21 | 99 | 4 | 21 | 115 |
| W | ppm | < 1 | < 1 | < 1 | 8 | 8 | 15 | < 1 | 16 | < 1 |
| Y | ppm | 2 | 1 | 2 | 24 | 2 | 3 | < 1 | 2 | 12 |
| La | ppm | 1.2 | 0.6 | 2 | 17.9 | 1.4 | 2 | 3.5 | 7.7 | 13.4 |
| Ce | ppm | < 3 | < 3 | 3 | 45 | < 3 | 4 | 6 | 12 | 20 |
| Nd | ppm | < 5 | < 5 | < 5 | 8 | < 5 | < 5 | < 5 | < 5 | 9 |
| Sm | ppm | 0.1 | < 0.1 | 0.3 | 4.4 | 0.2 | 0.3 | 0.2 | 0.8 | 2.4 |
| Sn | % | < 0.02 | < 0.02 | < 0.02 | < 0.02 | < 0.02 | 0.03 | < 0.02 | < 0.02 | < 0.02 |
| Tb | ppm | < 0.5 | < 0.5 | < 0.5 | < 0.5 | < 0.5 | < 0.5 | < 0.5 | < 0.5 | < 0.5 |
| Yb | ppm | < 0.2 | < 0.2 | < 0.2 | 3 | < 0.2 | 0.4 | < 0.2 | 0.3 | 1.4 |
| Lu | ppm | < 0.05 | < 0.05 | < 0.05 | 0.24 | < 0.05 | < 0.05 | < 0.05 | < 0.05 | 0.1 |
| Mass | g | 33.1 | 32.8 | 32.4 | 32.3 | 31.7 | 34.4 | 33.9 | 30.3 | 30.6 |

**Table 3.** Continued.

| Label | | | | | | | | | | |
|---|---|---|---|---|---|---|---|---|---|---|
| station | | 18DMI-6-5c | 18DMI-8-9 | 18lo-10-1c | 18 lo-11-4 | 18lo-16-3 | 18lo-18-6 | 18lo-19-3e | 18lo-3-3 | 18lo-4-3 |
| MINFILE | | | | | | | | | | |
| Type | | | | | | | | | | |
| UTM_X* | | 326795 | 326970 | 327036 | 318473 | 328230 | 329386 | 327259 | 327818 | 328406 |
| UTM_Y* | | 6229078 | 6229561 | 6235679 | 6234670 | 6222501 | 6219042 | 6210680 | 6230415 | 6229794 |
| Au | ppb | < 2 | 4 | 5 | < 2 | 7 | 37 | 11 | 18 | 8 |
| Ag | ppm | < 0.3 | < 0.3 | 3.4 | < 0.3 | < 0.3 | 0.8 | < 0.3 | < 0.3 | < 0.3 |
| Cu | ppm | 2 | 67 | 725 | 18 | 11 | 441 | 25 | 75 | 87 |
| Cu | % | - | - | - | - | - | - | - | - | - |
| Cd | ppm | < 0.3 | < 0.3 | < 0.3 | < 0.3 | < 0.3 | < 0.3 | < 0.3 | < 0.3 | < 0.3 |
| Mo | ppm | < 1 | 24 | 7 | 1 | 19 | 5 | < 1 | < 1 | 19 |
| Pb | ppm | < 3 | < 3 | < 3 | < 3 | < 3 | 3 | 25 | < 3 | < 3 |
| Ni | ppm | 5 | 4 | 6 | 4 | 3 | 5 | 4 | 6 | 8 |
| Zn | ppm | 10 | 2 | 15 | 2 | 3 | 21 | 140 | 25 | 52 |
| S | % | < 0.01 | 0.18 | 0.2 | 0.29 | 0.94 | 1.75 | 0.33 | 0.42 | 0.21 |
| Al | % | 0.27 | 0.51 | 5.46 | 0.78 | 2.4 | 0.2 | 7.39 | 1.1 | 7.77 |
| As | ppm | < 0.5 | < 0.5 | 3.5 | 2.4 | 1.1 | 6.6 | 1.5 | 1.4 | 3.8 |
| Ba | ppm | < 50 | 70 | 1120 | 230 | 510 | < 50 | 1720 | 220 | 210 |
| Be | ppm | < 1 | < 1 | < 1 | < 1 | 1 | < 1 | < 1 | < 1 | < 1 |
| Bi | ppm | < 2 | < 2 | 31 | < 2 | 13 | 12 | < 2 | < 2 | < 2 |
| Br | ppm | < 0.5 | < 0.5 | < 0.5 | < 0.5 | < 0.5 | < 0.5 | < 0.5 | < 0.5 | < 0.5 |
| Ca | % | 0.24 | 0.32 | 1.7 | 0.05 | 0.03 | < 0.01 | 2.85 | 0.39 | 7.68 |
| Co | ppm | 2 | 4 | 51 | 2 | < 1 | 5 | 12 | 14 | 13 |
| Cr | ppm | 8 | 124 | 87 | 112 | 105 | 87 | < 2 | 116 | 5 |
| Cs | ppm | < 1 | < 1 | 2 | 1 | 2 | < 1 | 2 | < 1 | < 1 |
| Eu | ppm | < 0.2 | < 0.2 | < 0.2 | < 0.2 | < 0.2 | 1 | < 0.2 | < 0.2 | 0.9 |
| Fe | % | 0.67 | 1.75 | 2.68 | 0.8 | 2.63 | 8.83 | 3.05 | 2.26 | 6.83 |
| Hf | ppm | < 1 | < 1 | < 1 | < 1 | < 1 | < 1 | 4 | < 1 | < 1 |
| Hg | ppm | < 1 | < 1 | < 1 | < 1 | < 1 | < 1 | < 1 | < 1 | < 1 |
| Ir | ppb | < 5 | < 5 | < 5 | < 5 | < 5 | < 5 | < 5 | < 5 | < 5 |
| K | % | < 0.01 | 0.08 | 1.48 | 0.54 | 1.41 | 0.06 | 2.58 | 0.16 | 0.24 |
| Li | ppm | 2 | < 1 | 3 | 5 | 3 | 1 | 7 | 4 | 5 |
| Mg | % | 0.24 | 0.02 | 0.35 | 0.01 | 0.02 | < 0.01 | 0.83 | 0.54 | 1.29 |
| Mn | ppm | 152 | 96 | 215 | 59 | 115 | 18000 | 1050 | 390 | 1070 |
| Na | % | 0.02 | 0.15 | 0.74 | 0.17 | 0.5 | 0.02 | 2.73 | 0.12 | 1.88 |
| P | % | 0.001 | 0.007 | 0.172 | 0.004 | 0.003 | 0.002 | 0.077 | 0.013 | 0.121 |
| Rb | ppm | < 15 | < 15 | < 15 | < 15 | 81 | < 15 | 30 | < 15 | < 15 |
| Sb | ppm | 0.1 | 0.3 | < 0.1 | 0.4 | 0.1 | 0.1 | 0.4 | 0.2 | 1.1 |
| Sc | ppm | 0.9 | 1.1 | 2.2 | 0.4 | 0.5 | 0.2 | 5.4 | 1.5 | 12 |
| Se | ppm | < 3 | < 3 | < 3 | < 3 | < 3 | < 3 | < 3 | < 3 | < 3 |
| Sr | ppm | 6 | 97 | 300 | 33 | 50 | 21 | 457 | 28 | 1470 |
| Ta | ppm | < 0.5 | < 0.5 | < 0.5 | < 0.5 | < 0.5 | < 0.5 | < 0.5 | < 0.5 | < 0.5 |
| Ti | % | < 0.01 | 0.02 | 0.07 | 0.06 | 0.01 | < 0.01 | 0.23 | 0.04 | 0.34 |
| Th | ppm | < 0.2 | < 0.2 | < 0.2 | 0.6 | < 0.2 | < 0.2 | 1.1 | 0.3 | 1 |
| U | ppm | < 0.5 | < 0.5 | < 0.5 | 1.4 | < 0.5 | < 0.5 | < 0.5 | < 0.5 | 0.9 |
| V | ppm | 16 | 21 | 53 | 4 | 8 | < 2 | 86 | 31 | 228 |
| W | ppm | < 1 | < 1 | 1 | 4 | 4 | 72 | 7 | < 1 | < 1 |
| Y | ppm | < 1 | < 1 | 3 | 1 | < 1 | 4 | 4 | 2 | 9 |
| La | ppm | < 0.5 | 0.5 | 4.7 | 0.9 | < 0.5 | 8.3 | 7.6 | 2.6 | 8.8 |
| Ce | ppm | < 3 | < 3 | 7 | < 3 | < 3 | 12 | 12 | 5 | 15 |
| Nd | ppm | < 5 | < 5 | < 5 | < 5 | < 5 | < 5 | < 5 | < 5 | 7 |
| Sm | ppm | < 0.1 | 0.1 | 1 | < 0.1 | < 0.1 | 0.6 | 1 | 0.5 | 1.8 |
| Sn | % | < 0.02 | < 0.02 | < 0.02 | < 0.02 | < 0.02 | < 0.02 | 0.04 | < 0.02 | < 0.02 |
| Tb | ppm | < 0.5 | < 0.5 | < 0.5 | < 0.5 | < 0.5 | < 0.5 | < 0.5 | < 0.5 | < 0.5 |
| Yb | ppm | < 0.2 | < 0.2 | < 0.2 | < 0.2 | < 0.2 | 0.4 | 0.7 | < 0.2 | 0.9 |
| Lu | ppm | < 0.05 | < 0.05 | < 0.05 | < 0.05 | < 0.05 | < 0.05 | < 0.05 | < 0.05 | < 0.05 |
| Mass | g | 36.4 | 34.8 | 31.7 | 32.6 | 31.3 | 31.5 | 31.7 | 32.9 | 35.3 |

**Table 3.** Continued.

| Label station | | 18lo-5-5 | 18lo-5-5b | 18lo-6-2c | 18lo-7-2b | 18ab-24-2 | Analysis Method | Detection Limit |
|---|---|---|---|---|---|---|---|---|
| MINFILE | | | | | | | | |
| Type | | | | | | | | |
| UTM_X* | | 330919 | 330919 | 327819 | 327857 | 337895 | | |
| UTM_Y* | | 6233783 | 6233783 | 6231338 | 6230407 | 6211421 | | |
| Au | ppb | 15 | 11 | < 2 | 13 | < 2 | INAA | 2 |
| Ag | ppm | 0.5 | 0.7 | < 0.3 | 0.8 | < 0.3 | MULT INAA / TD-ICP | 0.3 |
| Cu | ppm | 45 | 46 | 397 | 288 | 16 | TD-ICP | 1 |
| Cu | % | - | - | - | - | - | 4Acid ICPOES | 0.001 |
| Cd | ppm | < 0.3 | < 0.3 | < 0.3 | < 0.3 | < 0.3 | TD-ICP | 0.3 |
| Mo | ppm | 5 | 4 | < 1 | 2 | < 1 | TD-ICP | 1 |
| Pb | ppm | 72 | 112 | 4 | < 3 | < 3 | TD-ICP | 3 |
| Ni | ppm | 3 | 4 | 32 | 5 | 6 | MULT INAA / TD-ICP | 1 |
| Zn | ppm | 8 | 7 | 124 | 10 | 7 | MULT INAA / TD-ICP | 1 |
| S | % | 3.53 | 5.28 | 0.52 | 0.1 | < 0.01 | TD-ICP | 0.01 |
| Al | % | 1.69 | 1.91 | 5.21 | 0.56 | 0.95 | TD-ICP | 0.01 |
| As | ppm | 16.4 | 26.4 | 2 | 3.3 | < 0.5 | INAA | 0.5 |
| Ba | ppm | 350 | 390 | 610 | 190 | 180 | INAA | 50 |
| Be | ppm | < 1 | < 1 | < 1 | < 1 | < 1 | TD-ICP | 1 |
| Bi | ppm | 298 | 480 | < 2 | < 2 | < 2 | TD-ICP | 2 |
| Br | ppm | < 0.5 | < 0.5 | < 0.5 | < 0.5 | < 0.5 | INAA | 0.5 |
| Ca | % | 0.46 | 0.37 | 6.49 | 0.12 | 0.5 | TD-ICP | 0.01 |
| Co | ppm | 11 | 9 | 69 | 10 | 3 | INAA | 1 |
| Cr | ppm | 3 | 4 | 25 | 125 | 148 | INAA | 2 |
| Cs | ppm | < 1 | < 1 | 6 | < 1 | < 1 | INAA | 1 |
| Eu | ppm | < 0.2 | < 0.2 | 1.5 | < 0.2 | < 0.2 | INAA | 0.2 |
| Fe | % | 5.36 | 5.41 | 11.8 | 1.6 | 0.86 | INAA | 0.01 |
| Hf | ppm | < 1 | < 1 | 2 | < 1 | < 1 | INAA | 1 |
| Hg | ppm | < 1 | < 1 | < 1 | < 1 | < 1 | INAA | 1 |
| Ir | ppb | < 5 | < 5 | < 5 | < 5 | < 5 | INAA | 5 |
| K | % | 0.74 | 0.87 | 1.94 | 0.16 | 0.23 | TD-ICP | 0.01 |
| Li | ppm | 2 | < 1 | 19 | 1 | 6 | TD-ICP | 1 |
| Mg | % | 0.25 | 0.08 | 5.58 | 0.18 | 0.16 | TD-ICP | 0.01 |
| Mn | ppm | 1500 | 1130 | 1230 | 156 | 356 | TD-ICP | 1 |
| Na | % | 0.04 | 0.04 | 0.49 | 0.04 | 0.28 | INAA | 0.01 |
| P | % | 0.027 | 0.016 | 0.011 | 0.006 | 0.015 | TD-ICP | 0.001 |
| Rb | ppm | 30 | 33 | 19 | < 15 | < 15 | INAA | 15 |
| Sb | ppm | 0.1 | 0.2 | < 0.1 | 0.3 | 0.1 | INAA | 0.1 |
| Sc | ppm | 2.7 | 1.5 | 55.8 | 1.1 | 1.1 | INAA | 0.1 |
| Se | ppm | < 3 | < 3 | < 3 | < 3 | < 3 | INAA | 3 |
| Sr | ppm | 16 | 12 | 323 | 8 | 101 | TD-ICP | 1 |
| Ta | ppm | < 0.5 | < 0.5 | < 0.5 | < 0.5 | < 0.5 | INAA | 0.5 |
| Ti | % | 0.08 | 0.06 | 0.4 | 0.02 | 0.05 | TD-ICP | 0.01 |
| Th | ppm | 1 | 1.7 | < 0.2 | < 0.2 | 1.6 | INAA | 0.2 |
| U | ppm | < 0.5 | < 0.5 | < 0.5 | < 0.5 | < 0.5 | INAA | 0.5 |
| V | ppm | 36 | 25 | 350 | 22 | 15 | TD-ICP | 2 |
| W | ppm | 11 | 9 | < 1 | < 1 | < 1 | INAA | 1 |
| Y | ppm | 9 | 2 | 27 | < 1 | 2 | TD-ICP | 1 |
| La | ppm | 3.7 | 4.8 | 5.3 | 0.6 | 3.1 | INAA | 0.5 |
| Ce | ppm | 6 | 7 | 19 | < 3 | 4 | INAA | 3 |
| Nd | ppm | < 5 | < 5 | < 5 | < 5 | < 5 | INAA | 5 |
| Sm | ppm | 0.7 | 0.7 | 4.2 | 0.2 | 0.3 | INAA | 0.1 |
| Sn | % | < 0.02 | < 0.02 | < 0.02 | < 0.02 | < 0.02 | INAA | 0.02 |
| Tb | ppm | < 0.5 | < 0.5 | < 0.5 | < 0.5 | < 0.5 | INAA | 0.5 |
| Yb | ppm | 0.8 | 0.2 | 2.5 | < 0.2 | < 0.2 | INAA | 0.2 |
| Lu | ppm | 0.05 | < 0.05 | 0.07 | < 0.05 | < 0.05 | INAA | 0.05 |
| Mass | g | 33.7 | 32.8 | 36.3 | 31.2 | 31.1 | INAA | |

**Acknowledgments**

Field assistance was from Gaby Jones, Silken Rauhala, and Dylan Spence. A field visit and discussions with Fil Ferri helped improve our understanding of the study area. We thank Silver King helicopters for air support and Cassiar Geoscience for expediting services. Reviews by F. Devine and P. Schiarizza helped improve the clarity of the manuscript.

**References cited**

Armstrong, J.E., 1946. Aiken Lake (south half), British Columbia. Geological Survey of Canada, Paper 46-11, scale 1 inch:2 miles.

Armstrong, J.E., 1948. Fort St. James, British Columbia. Geological Survey of Canada, A Series Map 907A, scale 1 inch:4 miles.

Armstrong, J.E., and Roots, E.F., 1948. Aiken Lake map-area, British Columbia. Geological Survey of Canada, Paper 48-5, 46 p.

Armstrong, J.E., and Roots, E.F., 1954. Aiken Lake, Cassiar District, British Columbia. Geological Survey of Canada, A Series Map 1030A, scale 1 inch:4 miles.

Bath, A.B., Cooke, D.R., Friedman, R.M., Faure, K., Kamenetsky, V.S., Tosdal, R.M., and Berry, R.F., 2014. Mineralization, U-Pb geochronology, stable isotope geochemistry of the Lower Main Zone of the Lorraine deposit, north-central British Columbia: A replacement-style alkalic Cu-Au porphyry. Economic Geology, 109, 979-1004.

Devine, F.A.M., Chamberlain, C.M., Davies, A.G.S., Friedman, R., and Baxter, P., 2014. Geology and district-scale setting of tilted alkalic porphyry Cu-Au mineralization at the Lorraine deposit, British Columbia. Economic Geology, 109, 939-977.

Ferri, F., Dudka, S.F., Rees, C.J., Meldrum, D.G., and Willson, M.J., 2001. Geology of the Uslika Lake Area, north-central B.C. (NTS 94C/2, 3 & 4). British Columbia Ministry of Energy and Mines, British Columbia Geological Survey Geoscience Map 2001-04, scale 1:50,000.

Garnett, J.A., 1972, Preliminary geological map of part of Hogem batholith, Duckling Creek area (parts of NTS 93N/13, 14; 94C/3, 4). British Columbia Ministry of Energy, Mines and Petroleum Resources, British Columbia Geological Survey Preliminary Map 09.

Garnett, J.A., 1978. Geology and mineral occurrences of the southern Hogem batholith. British Columbia Ministry of Energy, Mines and Petroleum Resources, British Columbia Geological Survey Bulletin 70, 75 p.

Lord, C.S., 1949. McConnell Creek, Cassiar District, British Columbia. Geological Survey of Canada, A Series Map 962A, scale 1 inch:4 miles.

Madu, B.E., and Ballantyne, T., 2018. Search project: Phase III activities in north-central British Columbia (Phase III, covering NTS 094C, D, E, F, 093M, N). Geoscience BC Summary of Activities 2017: Minerals and Mining, Geoscience BC, Report 2018-1, pp. 1-6.

Nelson, J., Carmichael, B., and Gray, M., 2003. Innovative gold targets in the Pinchi Fault/Hogem batholith area: The Hawk and Axelgold properties, central British Columbia (94C/4, 94N/13). In: Geological Fieldwork 2002, British Columbia Ministry of Energy and Mines, British Columbia Geological Survey Paper 2003-1, pp. 97-114.

Nelson, J.L., Colpron, M., and Israel, S., 2013. The Cordillera of British Columbia, Yukon, and Alaska: Tectonics and metallogeny. In: Colpron, M., Bissing, T., Rusk, B.G., and Thompson, J.F.H., (Eds.), Tectonics, Metallogeny, and Discovery: The North American Cordillera and similar accretionary settings. Society of Economic Geologists, Special Publication 17, pp. 53-109.

Nixon, G.T., and Peatfield, G.R., 2003. Geological setting of the Lorraine Cu-Au porphyry deposit, Duckling Creek Syenite Complex, north-central British Columbia. British Columbia Ministry of Energy and Mines, British Columbia Geological Survey Open File 2003-4, 24 p.

Ootes, L., Bergen, A.L., Milidragovic, D., and Graham, B., 2019. Preliminary geology of Notch Peak and Ogden Creek (parts of NTS 094C/04 and 093N/13), northern Hogem batholith, Quesnel terrane, north-central British Columbia. British Columbia Ministry of Energy, Mines and Petroleum Resources, British Columbia Geological Survey Open File 2019-02, scale 1:50,000.

Roots, E.F., 1954. Geology and mineral deposits of Aiken Lake map-area, British Columbia. Geological Survey of Canada, Memoir 274, 246 p.

Schiarizza, P., and Tan, S.H., 2005a. Geology and mineral occurrences of the Quesnel terrane between the Mesilinka River and Wrede Creek (NTS 94D/8, 9), north-central British Columbia. In: Geological Fieldwork 2004, British Columbia Ministry of Energy and Mines, British Columbia Geological Survey Paper 2005-1, pp. 109-130.

Schiarizza, P., and Tan, S.H., 2005b. Geology of the Johanson Lake area, parts of NTS 94D/8 and 9. British Columbia Ministry of Energy and Mines, British Columbia Geological Survey Open File 2005-4; scale 1:50,000.

Woodsworth, G.J., 1976. Plutonic rocks of McConnell Creek (94 D west half) and Aiken Lake (94 C east half) map-areas, British Columbia. Geological Survey of Canada, Paper 76-1A, pp. 69-73.

Woodsworth, G.J., Anderson, R.G., and Armstrong, R.L., 1991. Plutonic regimes, Chapter 15. In: Gabrielse, H., and Yorath, C.J. (Eds.), Geology of the Cordilleran Orogen in Canada, Geological Survey of Canada, Geology of Canada, no. 4, pp. 491-531.

# Geochemistry and petrology of rocks in the Decar area, central British Columbia: Petrologically constrained subdivision of the Cache Creek complex

Dejan Milidragovic[1, a] and Ryan Grundy[1, 2]

[1] British Columbia Geological Survey, Ministry of Energy, Mines and Petroleum Resources, Victoria, BC, V8W 9N3
[2] School of Earth and Ocean Sciences, University of Victoria, Victoria, BC, V8W 3P6
[a] corresponding author: Dejan.Milidragovic@gov.bc.ca

Recommended citation: Milidragovic, D., and Grundy, R., 2019. Geochemistry and petrology of rocks in the Decar area, central British Columbia: Petrologically constrained subdivision of the Cache Creek complex. In: Geological Fieldwork 2018, British Columbia Ministry of Energy, Mines and Petroleum Resources, British Columbia Geological Survey Paper 2019-01, pp. 55-77.

**Abstract**

Upper Paleozoic to Lower Jurassic deformed rocks of the Cache Creek terrane in the Decar area, central British Columbia, include a central region of variably serpentinized or carbonate-altered ultramafic rocks (Trembleur ultramafite) that is bounded to the northeast and southwest by greenschist facies- to amphibolite facies volcano-sedimentary rocks. The predominant olivine-orthopyroxene-spinel (harzburgitic) mineralogy, and major and trace element geochemical composition of the least-altered ultramafic rocks suggest that they are remnants of a highly melt-depleted (F ~0.15-0.30) lithospheric mantle. The relatively high $SiO_2$ concentrations and high modal abundance of orthopyroxene in the harzburgite indicate later metasomatism, probably in a supra-subduction setting. Based on immobile and incompatible trace element abundances, we identify four geochemical suites of volcanic and shallow intrusive rocks in the Decar area. The Sowchea succession (Upper Pennsylvanian to Lower Jurassic) contains both the high-Ti alkaline and enriched to depleted tholeiitic suites, the Rubyrock igneous complex (Lower Permian to Upper Triassic) contains the HFSE-depleted suite, and local unnamed, undeformed mafic intrusions that appear to postdate assembly of the Cache Creek complex are of the calc-alkaline suite. The geochemistry of samples from the Decar area provides evidence that rocks of the Cache Creek complex consist of two fundamentally different tectono-stratigraphic assemblages. Volcanic and intrusive rocks, limestone, chert, and argillite of the Sowchea succession were likely deposited in an oceanic plateau setting. They resided on a lower plate before being juxtaposed against an upper plate consisting of the Trembleur ultramafite and overlying supracrustal rocks of the Rubyrock igneous complex.

**Keywords:** Cache Creek terrane, Decar, Trembleur ultramafite, Rubyrock igneous complex, Sowchea succession, Sitlika assemblage

## 1. Introduction

The Cache Creek terrane is a northwest-trending belt of oceanic rocks that extends for ca. 1500 km along strike in central British Columbia (Fig. 1; Monger, 1977; Nelson et al., 2013). It contains structurally imbricated and variably deformed and metamorphosed: 1) lithospheric mantle; and 2) Paleozoic to Mesozoic mafic plutonic rocks and oceanic supracrustal rocks (Monger, 1977; English and Johnston, 2005; Nelson et al., 2013; McGoldrick et al., 2017, 2018). The structural style and varied lithology of the Cache Creek terrane is widely regarded to record tectonic juxtaposition of rocks formed in disparate tectonic environments, including subduction-related fore-arc and mantle plume-related oceanic seamount and/or plateau settings (Mihalynuk et al., 1994; Struik et al., 2001; Tardy et al., 2001; Lapierre et al., 2003; English and Johnston, 2005; English et al., 2010). However, recent petrological studies in the northern part of the Cache Creek terrane offer a different perspective. McGoldrick et al. (2017) found that geochemical compositions indicate a close genetic relationship between most volcanic and intrusive rocks from northern Cache Creek terrane and adjacent ophiolite massifs, with both having evolved on the upper plate in a supra-subduction zone setting. They also found that rocks with geochemical signatures

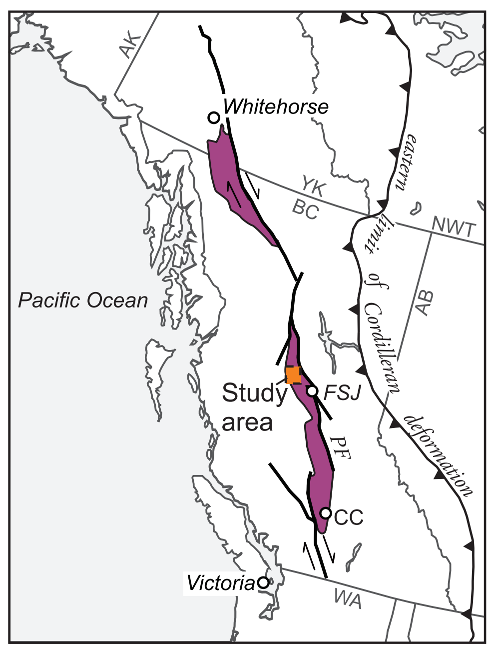


**Fig. 1.** Location of the study area and distribution of Cache Creek terrane (purple) in the Canadian Cordillera. Abbreviations: FSJ – town of Fort St. James; CC: village of Cache Creek; PF – Pinchi fault.

typical of intraplate oceanic basalts and related magmas (e.g., Pearce, 2008) are volumetrically minor (McGoldrick et al., 2017), casting doubt on the proposition of Tardy et al. (2001) and Lapierre et al. (2003) that Cache Creek terrane originated mainly as a fragmented oceanic plateau.

In this paper, we investigate the geochemistry of mantle, volcanic, and intrusive rocks from the southern segment of the Cache Creek terrane in the Decar area, approximately 100 km northwest of Fort St. James in central British Columbia (Fig. 1). We analyzed variably serpentinized and carbonate-altered rocks of the Trembleur ultramafite (Armstrong, 1949; Elliott, 1975; Paterson, 1977; Schiarizza and MacIntyre, 1998; MacIntyre and Schiarizza, 1999; Struik et al., 2001) and two supracrustal units: the Sowchea volcano-sedimentary succession (Upper Pennsylvanian to Lower Jurassic; Struik et al., 2001; Struik et al., 2007; previously assigned to the North Arm succession, Permo-Triassic, Schiarizza and MacIntyre, 1998; MacIntyre and Schiarizza, 1999) and the Rubyrock igneous complex (Lower Permian to Upper Triassic; MacIntyre and Schiarizza, 1999; Struik et al., 2001). Similar to data from northern Cache Creek terrane, our geochemical results highlight a supra-subduction zone component in the south. Our data also serve as a tool to assign outcrops to specific lithostratigraphic units that are difficult to distinguish in the field.

## 2. Geological setting

The Cache Creek terrane contains extensive sections of carbonate rocks, ribbon chert, argillite, coarse siliciclastic rocks, and mafic to intermediate volcanic and intrusive rocks (Monger, 1975; Mihalynuk et al., 1999; Struik et al., 2001; English et al., 2010). These rocks are temporally bracketed by Late Devonian-Middle Mississippian conodonts in northwestern British Columbia (Golding et al., 2016) and Early Jurassic radiolaria in southern Yukon (Cordey et al., 1991; Golding et al., 2016). The Cache Creek terrane collided with Stikinia by ca. 172 Ma, as indicated by the age of blueschist facies metamorphism of oceanic supracrustal rocks and the oldest post-kinematic plutons in northwestern British Columbia (Mihalynuk et al., 2004). Recent analysis of conodont collections demonstrates a significant time-dependant variation along the length of the terrane during the Pennsylvanian to Late Triassic (Golding, 2018). This finding suggests that different segments of the Cache Creek terrane were mobile relative to one another during much of the terrane's history and casts doubt on the widely accepted hypothesis of a far-travelled Cache Creek terrane that evolved in the Tethyan paleographic realm and crossed the Panthalassan ocean (Monger and Ross, 1971; Orchard et al., 2001; Nelson et al., 2013). A key feature of the Cache Creek terrane is the widespread occurrence of ultramafic rocks, interpreted as tectonic slivers that originally formed the lithospheric mantle beneath the Cache Creek ocean (Struik et al., 2001; Lapierre et al., 2003; English and Johnston, 2005; Canil et al., 2006; English et al., 2010; McGoldrick et al., 2017, 2018).

Currently, the tectonostratigraphic framework for the Cache Creek terrane in central British Columbia includes three structurally disrupted components (MacIntyre and Schiarizza, 1999; Schiarizza and MacIntyre, 1999; Struik et al., 2001, 2007): 1) the Cache Creek complex, which contains ultramafic rocks considered mantle tectonites (Trembleur ultramafite), fine-grained, strongly deformed siliciclastic metasedimentary and less abundant volcanic rocks interpreted as accretionary complex deposits (Sowchea succession), and several predominantly carbonate rock units (Pope, Copley, and Kloch Lake successions; Struik et al., 2001); 2) the Sitlika assemblage, which is found structurally beneath ophiolitic rocks of the Cache Creek complex in the western part of the terrane, and comprises a Permo-Triassic predominantly volcanic unit interpreted as an intra-oceanic arc complex (Schiarizza and Massey, 2010) and an unconformably overlying Upper Triassic to Lower Jurassic siliciclastic succession; and 3) the Tezzeron succession, an Upper Triassic to Lower Jurassic siliciclastic unit along the eastern edge of the terrane, adjacent to the Quesnel terrane.

## 3. Geology of the Decar area

The central part of the Decar area is underlain by ultramafic and mafic rocks (Fig. 2) interpreted as relicts of a dismembered ophiolitic sequence (e.g., Boudier and Nicolas, 1985). The ophiolitic rocks include variably altered harzburgite, and lesser dunite and pyroxenite of the Trembleur ultramafite (cf., Struik et al., 2001), and greenschist- to amphibolite-facies mafic to ultramafic, altered and variably deformed intrusive and volcanic rocks of the Rubyrock igneous complex (MacIntyre and Schiarizza, 1999; Struik et al., 2001; Milidragovic et al., 2018a). The Rubyrock igneous complex is structurally interleaved with the western part of the Trembleur ultramafite and is widely regarded (Schiarizza and MacIntyre, 1999; Struik et al., 2001; Britten, 2017) as the crustal portion of the ophiolite. Locally, fine-grained dikes of saussuritized hornblende gabbro, which are geochemically correlative with the rocks of the Rubyrock igneous complex (see section 5.3.2.), cut the Trembleur ultramafite. A tonalite lens from the Rubyrock igneous complex yielded a U-Pb zircon crystallization age of 257 ±5 Ma (Late Permian; Struik et al., 2001; Struik et al., 2007). This age is indistinguishable from a 258 +10/-1 Ma U-Pb zircon age of a rhyolite in the lower volcanic unit of the Sitlika assemblage, approximately 75 km north-northeast of the study area (Childe and Schiarizza, 1997; Schiarizza and Massey, 2010), and overlaps within error the maximum age (ca. 254-242 Ma) of Kutcho assemblage volcano-sedimentary rocks in the northern segment of the Cache Creek terrane (Childe and Thompson, 1997; Schiarizza, 2012). The Trembleur ultramafite is weakly to strongly altered to either serpentinite or listwanite (magnesite±serpentine±talc±quartz; Hansen et al., 2005). We assign the basalt-chert unit on the northeast flank of the Trembleur ultramafite to the Sowchea succession which, as defined by Struik et al. (2001; 2007), is a unit of Upper Pennsylvanian-Lower Jurassic fine-grained siliceous sedimentary rocks (cherty argillite and slate to muddy chert), with lesser limestone, greywacke, basalt,

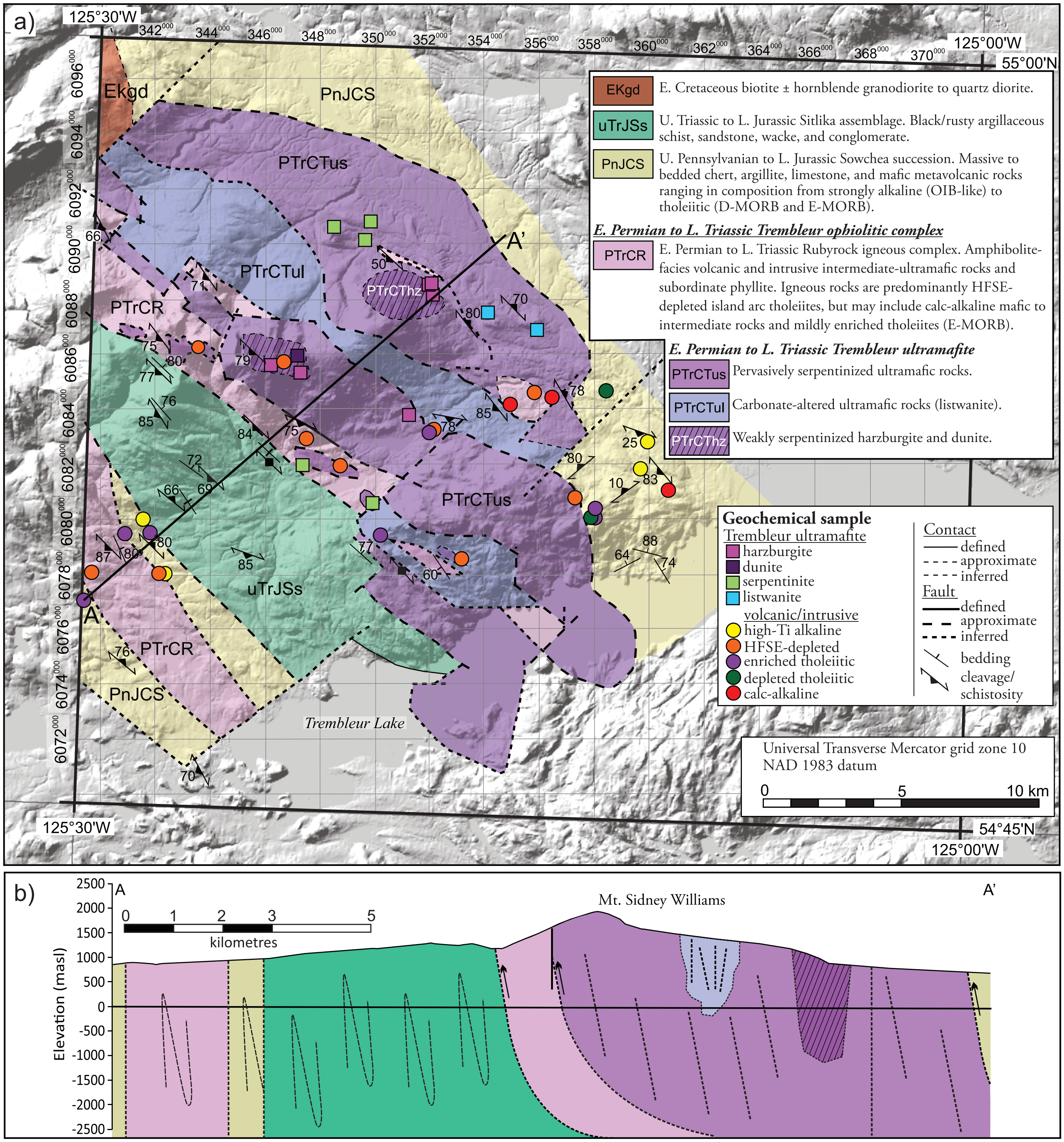


**Fig. 2. a)** Preliminary geology of the Decar area showing the location of samples discussed in this geochemical study. Modified from MacIntyre and Schiarizza (1999), Struik et al. (2007), and Milidragovic et al. (2018a). The hillshade terrain resource information management (TRIM) digital elevation model (DEM) base map has 25 m grid spacing. **b)** Schematic cross section (A-A') of the Decar area. Location of section is shown in Fig. 2a. Fault geometry at depth is speculative; fold pattern is ornamental.

andesite, and conglomerate containing intraformational siltstone clasts. This unit was formerly included in the North Arm succession of suspected ophiolite affinity by Schiarizza and MacIntyre (1999) and MacIntyre and Schiarizza (1999). Immediately southwest of the ultramafic rocks are siliciclastic rocks of the upper part of Sitlika assemblage (Upper Triassic-Lower Jurassic; Schiarizza and MacIntyre, 1998; MacIntyre and Schiarizza, 1999). Farther southwest are two panels of sedimentary and volcanic rocks that we consider part of the Sowchea succession, based on their geochemistry (see section 5.3.) and similar field appearance to rocks exposed in the northeast. Previously, these rocks, specifically a unit of mafic sills and dikes with abundant screens of basalt and chert that were interpreted as transitional between the Rubyrock complex and the North Arm succession, were included in the Rubyrock igneous complex (Schiarizza and MacIntyre, 1999; MacIntyre and Schiarizza, 1999). These Sowchea succession panels are separated by a panel of Rubyrock igneous complex rocks that we identify on the basis of geochemical data presented below (see section 5.3.2.).

The Decar area is characterized by a prominent subvertical northwest-southeast trending fabric (Fig. 2) that is consistent with northeast-southwest directed shortening (Milidragovic et al., 2018a) along northeast-dipping thrust faults (Schiarizza and MacIntyre, 1998). Shortening was also likely accompanied by significant strike-slip motion, both parallel and perpendicular to the regional fabric (Britten et al., 2017), further complicating the regional structure (Fig. 2). On the surface, observed and inferred fault contacts are subvertical and extensive drilling of the Trembleur ultramafite by FPX Nickel Corp. suggests that the ultramafic rocks extend to a minimum depth of 550 m (Voordouw and Simpson, 2018). The geometry and attitude of thrust faults at depth is unknown.

## 4. Analytical techniques and data quality

A total of 45 samples collected during the 2017 field season were selected for geochemical analysis at Geoscience Laboratories, Sudbury, ON. These samples span the range of rock types described by Milidragovic et al. (2018a) and include both ultramafic rocks (Table 1) and mafic- to intermediate volcanic and intrusive rocks (Table 2). The samples were prepared at the BCGS rock preparation facility before submission to Geoscience Laboratories. Before crushing in a steel jaw-crusher, obvious alteration and veins were removed from fist-sized rock samples using a diamond-studded lapidary saw. Following crushing, aliquots of each sample, weighing 30-50 g and comprising coarse (0.2-1.0 cm) rock chips and fragments, were pulverized to sub-100 µm particles using a stainless steel piston apparatus.

The samples were pulverized in an agate mill at Geoscience Laboratories. Major element oxides and selected trace element concentrations were determined using X-ray Fluorescence (XRF); trace elements were analyzed using Inductively Coupled Plasma-Mass Spectrometry (ICP-MS) following closed vessel multi-acid dissolution. Variably altered ultramafic samples were analyzed for total $CO_2$ and S concentrations, and a subset of serpentinite and relatively unaltered harzburgite was analyzed for platinum group element (PGE) concentrations by Ni-S fire assay.

The uncertainty in measurement, at a 95% confidence interval, is ≤5% relative for most major element oxides whose abundance exceeds the quantification limit (defined as 3.3 times the detection limit; Fig. 3a). The relative uncertainty in measurement of $P_2O_5$ ranges between 10-30% for rocks in which the absolute abundance of $P_2O_5$ is <0.1 wt.%. The relative uncertainty in Co, Cu, Ni, V, and Zn as determined by XRF is typically ≤20% at a 95% confidence interval.

Most trace element concentrations determined by ICP-MS on duplicate, in-house standard, and certified reference samples show good agreement (≤15% relative) with the expected values at a 95% confidence interval (Fig. 3b). However, the trace element concentrations of sample ZE15-DM-01A are up to 30% higher than those determined by high resolution-ICP-MS (HR-ICP-MS; Milidragovic et al., 2018b), suggesting that the relative uncertainty in trace element concentrations determined by ICP-MS is ≤30%. The relative uncertainty in measurement of the PGE is <10%, based on the analysis of one certified reference sample and one duplicate (Fig. 3c).

## 5. Petrology and geochemistry

### 5.1. Petrology of the Trembleur ultramafite

The least-altered rocks of the Trembleur ultramafite (LOI ≤10 wt.%) are spinel harzburgite with coarse or protogranular texture (Mercier and Nicholas, 1974; Harte, 1977). Partly serpentinized olivine is ≥3 mm across, displays kink bands and/or undulose extinction, and has curvilinear grain boundaries (Fig. 4a). Electron microprobe analysis of olivine from the Trembleur ultramafite (Grundy, 2018) demonstrated limited compositional variability (Fo=0.90-0.91; Ni=3170 ±780 ppm). Orthopyroxene (~2-5 mm) is subhedral to anhedral and commonly contains exsolution lamellae of clinopyroxene, some of which have been deformed. Bastite alteration rims around orthopyroxene vary in thickness, but correlate broadly with the degree of serpentinization. Pervasive replacement of orthopyroxene by bastite is typically also accompanied by secondary black spinel. Rare subhedral clinopyroxene grains (<1 mm; Fig. 4b) commonly contain cleavage-parallel exsolution of thin, closely spaced (<10 µm) laminae of secondary spinel. Primary spinel is characteristically irregular (Fig. 4a), with a vermicular, interstitial habit and commonly displays holly-leaf texture in orthopyroxene porphyroclasts. Primary spinel is medium brown to dark red with Cr-numbers $((Cr/(Cr+Fe^{3+}+Al))$ between 0.22 and 0.30 and Mg-numbers $(Mg/(Mg+Fe^{2+})$ between 0.69 and 0.73 (Grundy, 2018). Secondary black magnetite haloes around primary spinel are in all samples. Sulphide occurs in trace quantities as small (<50 µm) subhedral crystals.

The peridotitic rocks of the Trembleur ultramafite were altered to either serpentinite or listwanite (magnesite±serpentine±talc ±quartz; Hansen et al., 2005; Figs. 4c and d). Progressive hydration (LOI=10-14 wt.%) of harzburgite resulted in the replacement of olivine by serpentine±brucite±magnetite, and formation of microscopic awaruite ($Ni_3Fe$; Britten, 2017; Milidragovic et al., 2018). Trace amounts of heazlewoodite ($Ni_3S_2$), pentlandite ($(Fe,Ni_9)S_8$), cobalt-pentlandite, millerite (NiFe), and wairauite (CoFe) occur in the serpentinites of the Decar area (Figs. 4e-f; C. Lawley, pers. comm., 2018). Ultramafic rocks in the south-central and eastern portion of the

**Table 1.** Major and trace element composition of the Trembleur ultramafite.

| Sample | | DMI17-5-9 | DMI17-5-10 | DMI17-9-3 | DMI17-9-7A | DMI17-9-11 | DMI17-16-3C | RGR17-16-6 |
|---|---|---|---|---|---|---|---|---|
| Lithology | | harzburgite | harzburgite | harzburgite | harzburgite | dunite | harzburgite | harzburgite |
| Easting | | 352040 | 351934 | 347289 | 346215 | 347175 | 352085 | 351229 |
| Northing | | 6088686 | 6088643 | 6085450 | 6085724 | 6086068 | 6088282 | 6083981 |
| Major elements (wt.%) | | | | | | | | |
| $SiO_2$ | *0.04* | 39.40 | 39.74 | 40.47 | 41.64 | 37.3 | 38.32 | 39.83 |
| $TiO_2$ | *0.001* | 0.02 | 0.01 | 0.01 | 0.02 | 0.01 | 0.01 | 0.01 |
| $Al_2O_3$ | *0.02* | 1.03 | 0.79 | 1.34 | 1.23 | 0.06 | 0.48 | 0.56 |
| $Fe_2O_3$(T) | *0.01* | 8.18 | 7.97 | 8.43 | 8.45 | 7.61 | 7.89 | 7.95 |
| MnO | *0.02* | 0.121 | 0.111 | 0.119 | 0.135 | 0.109 | 0.114 | 0.117 |
| MgO | *0.01* | 40.21 | 40.81 | 39.51 | 38.71 | 46.37 | 40.66 | 41.65 |
| CaO | *0.006* | 1.819 | 1.286 | 1.345 | 2.614 | 0.053 | 0.51 | 1.724 |
| $Na_2O$ | *0.02* | <0.02 | <0.02 | <0.02 | <0.02 | <0.02 | <0.02 | <0.02 |
| $K_2O$ | *0.01* | 0.01 | 0.01 | 0.01 | 0.01 | 0.01 | 0.01 | 0.01 |
| $P_2O_5$ | *0.002* | 0.002 | <0.002 | 0.003 | 0.003 | 0.002 | 0.002 | 0.002 |
| $Cr_2O_3$ | *0.002* | 0.426 | 0.367 | 0.453 | 0.381 | 0.375 | 0.366 | 0.400 |
| LOI | - | 8.51 | 8.93 | 7.29 | 5.41 | 7.08 | 10.28 | 7.61 |
| $CO_2$ | *0.023* | 0.142 | 0.160 | 0.303 | 0.274 | 0.321 | 0.234 | 0.209 |
| S | *0.003* | 0.008 | 0.009 | 0.02 | 0.005 | 0.012 | 0.009 | 0.005 |
| Total | *0.01* | 99.68 | 99.98 | 99.01 | 98.55 | 98.94 | 98.66 | 99.82 |
| Trace elements (ppm) | | | | | | | | |
| Ni[a] | *9* | 2238 | 2386 | 2315 | 2198 | 2870 | 2318 | 2369 |
| V[a] | *8* | 41 | 40 | 51 | 51 | 12 | 31 | 37 |
| Co[a] | *12* | 110 | 108 | 116 | 117 | 128 | 115 | 112 |
| Cu | *1.4* | 11.3 | 15.2 | 20.1 | 18.9 | <1.4 | 3.3 | 8.6 |
| Zn | *1.8* | 67.7 | 63.2 | 76.1 | 70.3 | 49.2 | 47.1 | 47.2 |
| Cd | *0.013* | 0.022 | 0.024 | 0.027 | 0.013 | <0.013 | 0.013 | 0.016 |
| Sc | *1.1* | 11 | 10 | 13 | 13 | 3 | 9 | 10 |
| Ga | *0.04* | 1.01 | 0.89 | 1.36 | 1.07 | 0.21 | 0.57 | 0.50 |
| Li | *0.4* | 0.7 | 0.4 | 1.8 | 1.7 | 1 | 1.5 | 0.7 |
| Be | *0.04* | 0.08 | 0.08 | 0.07 | 0.12 | 0.07 | 0.07 | 0.08 |
| Mo | *0.08* | 0.13 | 0.15 | 0.16 | 0.47 | 0.18 | 0.13 | 0.11 |
| In | *0.0018* | 0.0076 | 0.0071 | 0.008 | 0.009 | 0.0047 | 0.0045 | 0.0059 |
| Sn | *0.16* | <0.16 | <0.16 | <0.16 | 0.29 | <0.16 | <0.16 | <0.16 |
| Sb | *0.04* | <0.04 | <0.04 | 0.37 | 0.05 | 0.07 | <0.04 | <0.04 |
| W | *0.05* | <0.05 | <0.05 | 0.18 | 0.08 | 0.06 | <0.05 | 0.05 |
| Tl | *0.002* | <0.002 | 0.002 | 0.002 | 0.002 | <0.002 | 0.002 | <0.002 |
| Pb | *0.18* | <0.18 | <0.18 | <0.18 | 0.26 | <0.18 | <0.18 | <0.18 |
| Bi | *0.47* | <0.47 | <0.47 | <0.47 | <0.47 | <0.47 | <0.47 | <0.47 |
| Cs | *0.013* | <0.013 | <0.013 | 0.036 | <0.013 | <0.013 | <0.013 | <0.013 |
| Rb | *0.11* | <0.11 | 0.13 | 0.22 | 0.12 | <0.11 | 0.17 | 0.11 |
| Ba | *0.8* | <0.8 | <0.8 | 0.8 | 1.0 | <0.8 | <0.8 | <0.8 |
| Sr | *0.6* | <0.6 | 0.6 | 1.0 | <0.6 | <0.6 | <0.6 | <0.6 |
| Nb | *0.028* | 0.052 | 0.049 | 0.102 | 0.046 | 0.035 | 0.056 | 0.063 |
| Zr | *6* | <6 | 7 | <6 | <6 | <6 | <6 | <6 |
| Y | *0.05* | 0.39 | 0.24 | 0.41 | 0.58 | <0.05 | 0.08 | 0.08 |
| Th | *0.018* | <0.018 | <0.018 | <0.018 | <0.018 | <0.018 | <0.018 | <0.018 |
| U | *0.011* | <0.011 | <0.011 | <0.011 | 0.15 | <0.011 | <0.011 | <0.011 |
| Ta | *0.007* | 0.011 | 0.016 | 0.012 | 0.025 | 0.033 | <0.007 | <0.007 |
| La | *0.1* | <0.1 | <0.1 | 0.1 | 0.1 | <0.1 | <0.1 | <0.1 |
| Ce | *0.12* | <0.12 | <0.12 | 0.13 | <0.12 | <0.12 | <0.12 | <0.12 |
| Pr | *0.014* | <0.014 | <0.014 | <0.014 | 0.014 | <0.014 | <0.014 | <0.014 |
| Nd | *0.06* | <0.06 | 0.06 | <0.06 | <0.06 | <0.06 | <0.06 | <0.06 |
| Sm | *0.026* | <0.026 | <0.026 | <0.026 | <0.026 | <0.026 | <0.026 | <0.026 |
| Hf | *0.14* | <0.14 | 0.16 | <0.14 | <0.14 | <0.14 | <0.14 | <0.14 |
| Eu | *0.0031* | 0.0061 | 0.0049 | 0.0045 | 0.0062 | <0.0031 | 0.0031 | <0.0031 |
| Gd | *0.009* | 0.028 | 0.019 | 0.020 | 0.035 | <0.009 | <0.009 | <0.009 |
| Tb | *0.0023* | 0.006 | 0.004 | 0.006 | 0.008 | <0.0023 | <0.0023 | <0.0023 |
| Dy | *0.009* | 0.057 | 0.033 | 0.052 | 0.076 | <0.009 | 0.01 | <0.009 |
| Ho | *0.0025* | 0.015 | 0.008 | 0.015 | 0.019 | <0.0025 | 0.004 | 0.003 |
| Er | *0.007* | 0.050 | 0.034 | 0.053 | 0.072 | <0.007 | 0.015 | 0.013 |
| Tm | *0.0019* | 0.010 | 0.006 | 0.012 | 0.013 | <0.0019 | 0.003 | 0.003 |
| Yb | *0.009* | 0.072 | 0.049 | 0.081 | 0.095 | 0.01 | 0.024 | 0.03 |
| Lu | *0.002* | 0.012 | 0.009 | 0.014 | 0.016 | 0.003 | 0.004 | 0.005 |
| Au + PGE (ppb) | | | | | | | | |
| Au[b] | *0.4* | - | 1.5 | - | 1.3 | - | 1.0 | 1.1 |
| Ir[b] | *0.01* | - | 3.34 | - | 3.77 | - | 3.36 | 3.52 |
| Pd[b] | *0.12* | - | 6.51 | - | 6.82 | - | 6.43 | 8.28 |
| Pt[b] | *0.17* | - | 7.10 | - | 7.48 | - | 6.40 | 6.88 |
| Rh[b] | *0.04* | - | 1.20 | - | 1.33 | - | 1.14 | 1.20 |
| Ru[b] | *0.08* | - | 6.38 | - | 7.09 | - | 6.29 | 6.17 |

**Table 1.** Continued.

| Sample | DMI17-4-5 | DMI17-10-1 | DMI17-10-2 | DMI17-10-4 | DMI17-14-1A | DMI17-5-5 | DMI17-15-6 |
|---|---|---|---|---|---|---|---|
| Lithology | serpentinite | serpentinite | serpentinite | serpentinite | serpentinite | listwanite | listwanite |
| Easting | 349909 | 349832 | 349628 | 348503 | 347369 | 354084 | 355867 |
| Northing | 6080711 | 6090937 | 6090266 | 6090743 | 6082090 | 6087633 | 6087002 |
| Major elements (wt.%) | | | | | | | |
| $SiO_2$ | 38.05 | 38.84 | 38.02 | 38.49 | 41.16 | 32.25 | 25.43 |
| $TiO_2$ | 0.01 | 0.01 | 0.03 | 0.02 | 0.03 | 0.01 | 0.01 |
| $Al_2O_3$ | 0.3 | 0.72 | 1.36 | 0.91 | 1.21 | 0.49 | 0.49 |
| $Fe_2O_3$(T) | 7.27 | 7.64 | 9.51 | 8.47 | 7.43 | 2.98 | 5.88 |
| MnO | 0.123 | 0.121 | 0.239 | 0.127 | 0.082 | 0.072 | 0.074 |
| MgO | 39.95 | 40.40 | 35.29 | 38.38 | 36.86 | 29.92 | 30.93 |
| CaO | 0.022 | 0.992 | 2.864 | 0.532 | 0.105 | 0.236 | 0.427 |
| $Na_2O$ | <0.02 | | <0.02 | <0.02 | <0.02 | <0.02 | <0.02 |
| $K_2O$ | 0.01 | 0.01 | 0.01 | 0.01 | 0.02 | 0.01 | 0.11 |
| $P_2O_5$ | 0.007 | 0.002 | 0.002 | 0.002 | 0.007 | 0.002 | 0.002 |
| $Cr_2O_3$ | 0.343 | 0.4 | 0.329 | 0.407 | 0.381 | 0.170 | 0.263 |
| LOI | 13.5 | 10.64 | 11.46 | 11.79 | 11.94 | 34.14 | 36.22 |
| $CO_2$ | 2.609 | 1.649 | 0.818 | 0.408 | - | 34.10 | 36.19 |
| S | 0.091 | 0.009 | 0.024 | 0.009 | - | <0.003 | 0.029 |
| Total | 99.54 | 99.73 | 99.09 | 99.09 | 99.21 | 100.23 | 99.80 |
| Trace elements (ppm) | | | | | | | |
| Ni[a] | 2341 | 2464 | 1988 | 2346 | 2266 | 1140 | 1683 |
| V[a] | 19 | 37 | 56 | 36 | 45 | 16 | 24 |
| Co[a] | 109 | 114 | 122 | 111 | 104 | 49 | 84 |
| Cu | 7.5 | 16.7 | 22.1 | 14.6 | 17.3 | 3.2 | 26.2 |
| Zn | 48.9 | 56.1 | 75.8 | 60.6 | 41.4 | 36 | 47.1 |
| Cd | <0.013 | <0.013 | 0.021 | 0.015 | 0.014 | 0.014 | 0.018 |
| Sc | 8 | 9 | 15 | 10 | 13 | 5 | 7 |
| Ga | 0.88 | 0.61 | 1.00 | 0.99 | 1.12 | 0.63 | 0.67 |
| Li | 0.4 | 0.9 | 0.5 | 0.8 | 0.6 | 3.9 | 1.9 |
| Be | 0.1 | 0.07 | 0.10 | 0.09 | 0.11 | 0.13 | 0.12 |
| Mo | 0.28 | 0.13 | 0.13 | 0.21 | 0.09 | 0.15 | 0.26 |
| In | 0.0064 | 0.0067 | 0.0114 | 0.0076 | 0.008 | 0.0036 | 0.0042 |
| Sn | <0.16 | <0.16 | <0.16 | <0.16 | <0.16 | <0.16 | <0.16 |
| Sb | >28 | <0.04 | 0.11 | <0.04 | 1.34 | 1.46 | 1.21 |
| W | 9.72 | <0.05 | 0.08 | <0.05 | 0.23 | 0.93 | 0.59 |
| Tl | <0.002 | <0.002 | <0.002 | <0.002 | 0.004 | 0.004 | 0.022 |
| Pb | 0.32 | <0.18 | 0.34 | <0.18 | 0.54 | <0.18 | 0.38 |
| Bi | <0.47 | <0.47 | <0.47 | <0.47 | <0.47 | <0.47 | <0.47 |
| Cs | 0.137 | 0.015 | <0.013 | <0.013 | 0.022 | 0.131 | 0.552 |
| Rb | 0.18 | <0.11 | 0.11 | <0.11 | 0.32 | 0.29 | 2.75 |
| Ba | <0.8 | <0.8 | <0.8 | 1.7 | 7.4 | 1.2 | 3.6 |
| Sr | 1.1 | <0.6 | <0.6 | 1.8 | 5.6 | 2.1 | 2.3 |
| Nb | 0.045 | <0.028 | <0.028 | <0.028 | 0.213 | 0.117 | 0.051 |
| Zr | <6 | <6 | <6 | <6 | <6 | <6 | <6 |
| Y | 0.09 | 0.3 | 1.06 | 0.3 | 0.76 | 0.12 | 0.11 |
| Th | <0.018 | <0.018 | <0.018 | <0.018 | <0.018 | 0.027 | <0.018 |
| U | 0.02 | <0.011 | <0.011 | <0.011 | 0.02 | <0.011 | <0.011 |
| Ta | <0.007 | <0.007 | <0.007 | <0.007 | <0.007 | <0.007 | <0.007 |
| La | <0.1 | <0.1 | <0.1 | <0.1 | 0.30 | 0.1 | <0.1 |
| Ce | <0.12 | <0.12 | <0.12 | <0.12 | 0.61 | 0.20 | <0.12 |
| Pr | <0.014 | <0.014 | <0.014 | <0.014 | 0.071 | 0.019 | <0.014 |
| Nd | <0.06 | <0.06 | <0.06 | <0.06 | 0.31 | 0.06 | <0.06 |
| Sm | <0.026 | <0.026 | 0.03 | <0.026 | 0.073 | <0.026 | <0.026 |
| Hf | <0.14 | <0.14 | <0.14 | <0.14 | <0.14 | <0.14 | <0.14 |
| Eu | 0.005 | 0.005 | 0.015 | 0.004 | 0.036 | 0.004 | 0.004 |
| Gd | <0.009 | 0.015 | 0.080 | 0.015 | 0.085 | 0.013 | 0.012 |
| Tb | <0.0023 | 0.005 | 0.018 | 0.004 | 0.016 | <0.0023 | <0.0023 |
| Dy | 0.015 | 0.036 | 0.16 | 0.038 | 0.126 | 0.021 | 0.018 |
| Ho | 0.003 | 0.011 | 0.040 | 0.011 | 0.030 | 0.004 | 0.005 |
| Er | 0.012 | 0.044 | 0.135 | 0.045 | 0.095 | 0.017 | 0.019 |
| Tm | 0.003 | 0.008 | 0.024 | 0.008 | 0.016 | 0.004 | 0.004 |
| Yb | 0.023 | 0.061 | 0.177 | 0.054 | 0.106 | 0.024 | 0.026 |
| Lu | 0.004 | 0.012 | 0.029 | 0.010 | 0.017 | 0.005 | 0.006 |
| Au + PGE (ppb) | | | | | | | |
| Au[b] | 2.7 | 1.0 | 2.1 | 1.2 | - | - | - |
| Ir[b] | 3.95 | 3.38 | 2.76 | 4.17 | - | - | - |
| Pd[b] | 3.68 | 10.27 | 5.51 | 5.16 | - | - | - |
| Pt[b] | 6.43 | 7.8 | 5.89 | 7.01 | - | - | - |
| Rh[b] | 1.21 | 1.29 | 0.96 | 1.26 | - | - | - |
| Ru[b] | 6.49 | 6.47 | 5.23 | 7.31 | - | - | - |

Trace elements were analyzed by ICP-MS unless reported otherwise. [a] analyzed by XRF; [b] analyzed by Ni-S fire assay. Numbers in the first column (italics) are detection limits for individual elements. UTM coordinates for sample locations are based on Zone 10 North American datum 1983 (NAD83).

**Table 2.** Major and trace element composition of volcanic and shallow intrusive rocks.

| ***Suite*** | | ***HFSE-depleted tholeiitic*** | | | | | | |
|---|---|---|---|---|---|---|---|---|
| Sample | | 98PSC-33-9-1 | DMI17-3-8 | DMI17-9-8 | DMI17-7-8 | DMI17-7-11 | DMI17-3-3 | DMI17-3-5 |
| Lithology | | gabbro | gabbro | gabbro | fragmental | fragmental | fragmental | basalt |
| Easting | | 343618 | 348735 | 346730 | 355776 | 357261 | 342151 | 339701 |
| Northing | | 6086409 | 6082069 | 6085645 | 6084729 | 6080910 | 6078164 | 6078209 |
| Unit | | Rubyrock | Rubyrock | Rubyrock | Rubyrock | Rubyrock | Rubyrock | Rubyrock |
| *Former unit | | - | - | - | - | - | Sowchea | - |
| Major elements (wt.%) | | | | | | | | |
| $SiO_2$ | *0.04* | 43.26 | 42.66 | 48.48 | 51.14 | 47.63 | 49.10 | 49.41 |
| $TiO_2$ | *0.001* | 1.28 | 1.78 | 1.82 | 1.01 | 1.07 | 1.41 | 1.00 |
| $Al_2O_3$ | *0.02* | 13.70 | 17.58 | 13.94 | 14.44 | 15.49 | 14.94 | 13.96 |
| $Fe_2O_3$(T) | *0.01* | 13.46 | 11.30 | 13.38 | 9.61 | 10.28 | 11.16 | 11.12 |
| MnO | *0.02* | 0.21 | 0.15 | 0.21 | 0.18 | 0.19 | 0.18 | 0.19 |
| MgO | *0.01* | 10.92 | 5.02 | 6.34 | 5.99 | 7.04 | 5.78 | 6.00 |
| CaO | *0.006* | 12.58 | 19.35 | 9.31 | 10.58 | 7.89 | 9.82 | 10.95 |
| $Na_2O$ | *0.02* | 1.61 | 0.28 | 3.78 | 2.54 | 3.79 | 3.86 | 2.94 |
| $K_2O$ | *0.01* | 0.30 | 0.06 | 0.26 | 0.34 | 0.65 | 0.08 | 1.09 |
| $P_2O_5$ | *0.002* | 0.13 | 0.14 | 0.15 | 0.09 | 0.09 | 0.13 | 0.14 |
| $Cr_2O_3$ | *0.002* | 0.06 | 0.01 | 0.01 | 0.03 | 0.04 | 0.02 | 0.02 |
| LOI | - | 2.13 | 1.88 | 2.03 | 3.17 | 5.18 | 2.63 | 2.55 |
| Total | *0.01* | 99.66 | 100.21 | 99.71 | 99.12 | 99.36 | 99.12 | 99.38 |
| Trace elements (ppm) | | | | | | | | |
| Ni[a] | *9* | 161 | 37 | 32 | 73 | 85 | 75 | 41 |
| V[a] | *8* | 362 | 350 | 379 | 255 | 291 | 310 | 265 |
| Co[a] | *12* | 48 | 35 | 47 | 37 | 34 | 36 | 50 |
| Cu | *1.4* | 27 | 62 | 53 | 36 | 35 | 21 | 40 |
| Zn | *1.8* | 109 | 96 | 106 | 97 | 91 | 86 | 89 |
| Cd | *0.013* | 0.14 | 0.28 | 0.16 | 0.18 | 0.094 | 0.12 | 0.21 |
| Sc | *1.1* | 54 | 40 | 41 | 35 | 40 | 39 | 52 |
| Ga | *0.04* | 17 | 21 | 19 | 18 | 20 | 19 | 15 |
| Li | *0.4* | 8 | 1 | 9 | 8 | 13 | 9 | 14 |
| Be | *0.04* | 0.38 | 0.41 | 0.56 | 0.44 | 0.38 | 0.55 | 0.46 |
| Mo | *0.08* | 0.31 | 0.53 | 0.36 | 0.33 | 1.09 | 0.35 | 0.17 |
| In | *0.0018* | 0.083 | 0.084 | 0.092 | 0.056 | 0.066 | 0.078 | 0.064 |
| Sn | *0.16* | 0.67 | 0.69 | 1.03 | 0.81 | 0.87 | 0.89 | 0.48 |
| Sb | *0.04* | <0.04 | 0.5 | 0.05 | 0.75 | 0.46 | 0.16 | 0.17 |
| W | *0.05* | 0.07 | 0.34 | 0.08 | 0.21 | 0.29 | 0.16 | 0.1 |
| Tl | *0.002* | 0.028 | 0.008 | 0.052 | 0.071 | 0.106 | 0.003 | 0.052 |
| Pb | *0.18* | 0.3 | 1.02 | 0.53 | 0.92 | 1.91 | 0.5 | 0.31 |
| Bi | *0.47* | <0.47 | <0.47 | <0.47 | <0.47 | <0.47 | <0.47 | <0.47 |
| Cs | *0.013* | 0.11 | 0.06 | 1.29 | 0.13 | 0.19 | 0.04 | 0.64 |
| Rb | *0.11* | 2.8 | 0.6 | 6.1 | 7.1 | 12.3 | 0.5 | 24.2 |
| Ba | *0.8* | 16 | 22 | 28 | 52 | 198 | 23 | 36 |
| Sr | *0.6* | 66 | 54 | 143 | 72 | 122 | 269 | 112 |
| Nb | *0.028* | 1.0 | 1.9 | 1.6 | 0.9 | 1.3 | 2.0 | 2.2 |
| Zr | *6* | 53 | 106 | 109 | 66 | 70 | 95 | 59 |
| Y | *0.05* | 30.6 | 38.5 | 40.8 | 23.7 | 29.0 | 32.9 | 31.6 |
| Th | *0.018* | 0.17 | 0.16 | 0.16 | 0.10 | 0.14 | 0.23 | 0.16 |
| U | *0.011* | 0.17 | 0.08 | 0.07 | 0.08 | 0.13 | 0.10 | 0.26 |
| Ta | *0.007* | 0.07 | 0.13 | 0.11 | 0.06 | 0.09 | 0.13 | 0.14 |
| La | *0.1* | 3.10 | 4.10 | 3.80 | 2.00 | 2.40 | 3.90 | 3.30 |
| Ce | *0.12* | 9.41 | 12.43 | 12.37 | 6.58 | 7.41 | 11.38 | 7.61 |
| Pr | *0.014* | 1.71 | 2.26 | 2.19 | 1.21 | 1.34 | 1.99 | 1.47 |
| Nd | *0.06* | 9.26 | 12.23 | 12.01 | 6.84 | 7.69 | 10.28 | 7.80 |
| Sm | *0.026* | 3.27 | 4.22 | 4.34 | 2.46 | 2.77 | 3.48 | 2.81 |
| Hf | *0.14* | 1.75 | 2.98 | 3.15 | 1.87 | 1.92 | 2.55 | 1.61 |
| Eu | *0.0031* | 1.18 | 1.71 | 1.52 | 0.960 | 1.07 | 1.37 | 1.02 |
| Gd | *0.009* | 4.40 | 5.65 | 5.88 | 3.49 | 3.95 | 4.83 | 4.06 |
| Tb | *0.0023* | 0.783 | 0.992 | 1.030 | 0.610 | 0.677 | 0.835 | 0.740 |
| Dy | *0.009* | 5.38 | 6.76 | 7.17 | 4.18 | 4.79 | 5.65 | 5.13 |
| Ho | *0.0025* | 1.14 | 1.46 | 1.53 | 0.87 | 1.02 | 1.20 | 1.12 |
| Er | *0.007* | 3.36 | 4.37 | 4.58 | 2.65 | 3.09 | 3.57 | 3.31 |
| Tm | *0.0019* | 0.493 | 0.630 | 0.661 | 0.382 | 0.452 | 0.512 | 0.476 |
| Yb | *0.009* | 3.27 | 4.09 | 4.34 | 2.51 | 2.92 | 3.39 | 3.11 |
| Lu | *0.002* | 0.493 | 0.619 | 0.655 | 0.381 | 0.449 | 0.496 | 0.464 |

**Table 2.** Continued.

| Suite | *HFSE-depleted tholeiitic* | | | *High-Ti alkaline* | | | |
|---|---|---|---|---|---|---|---|
| Sample | DMI17-4-16 | DMI17-14-9 | DMI17-5-2 | DMI17-3-4 | DMI17-2-12 | DMI17-8-4 | DMI17-8-5 |
| Lithology | gabbro | basalt | fragmental | basalt | basalt | basalt | basalt |
| Easting | 353146 | 347506 | 352136 | 342367 | 341575 | 359890 | 359636 |
| Northing | 6078686 | 6083053 | 6083383 | 6078155 | 6080135 | 6082947 | 6081964 |
| Unit | Rubyrock | Rubyrock | Rubyrock | Sowchea | Sowchea | Sowchea | Sowchea |
| *Former unit | Sowchea | - | - | - | - | - | - |
| Major elements (wt.%) | | | | | | | |
| $SiO_2$ | 42.12 | 45.30 | 49.11 | 45.88 | 32.85 | 38.04 | 55.59 |
| $TiO_2$ | 0.29 | 1.32 | 1.27 | 2.83 | 3.68 | 2.09 | 1.41 |
| $Al_2O_3$ | 18.45 | 15.42 | 13.36 | 14.49 | 17.23 | 14.3 | 18.07 |
| $Fe_2O_3$(T) | 6.59 | 12.66 | 15.29 | 12.4 | 13.49 | 13.45 | 6.55 |
| MnO | 0.14 | 0.21 | 0.27 | 0.16 | 0.18 | 0.11 | 0.14 |
| MgO | 9.38 | 7.76 | 5.77 | 6.14 | 5.38 | 5.67 | 3.17 |
| CaO | 17.90 | 12.16 | 7.82 | 9.36 | 14.62 | 4.56 | 1.99 |
| $Na_2O$ | 0.26 | 1.61 | 3.36 | 2.95 | 1.32 | 2.47 | 5.67 |
| $K_2O$ | 0.28 | 0.75 | 0.41 | 0.6 | 0.62 | 1.62 | 1.89 |
| $P_2O_5$ | 0.02 | 0.09 | 0.11 | 0.59 | 0.96 | 0.37 | 0.75 |
| $Cr_2O_3$ | 0.13 | 0.02 | 0.00 | 0.02 | 0.01 | 0.03 | 0.09 |
| LOI | 3.95 | 2.52 | 2.69 | 3.3 | 9.24 | 16.76 | 3.93 |
| Total | 99.51 | 99.87 | 99.48 | 98.74 | 99.62 | 99.56 | 99.36 |
| Trace elements (ppm) | | | | | | | |
| Ni[a] | 149 | 54 | 35 | 79 | 99 | 90 | 19 |
| V[a] | 161 | 392 | 474 | 196 | 232 | 141 | 131 |
| Co[a] | 41 | 51 | 52 | 37 | 42 | 42 | 13 |
| Cu | 128 | 276 | 237 | 53 | 7 | 56 | 53 |
| Zn | 38 | 110 | 121 | 115 | 163 | 219 | 89 |
| Cd | 0.16 | 0.47 | 0.07 | 0.17 | 0.30 | 0.08 | 0.03 |
| Sc | 40 | 47 | 56 | 21 | 23 | 22 | 43 |
| Ga | 15 | 20 | 18 | 24 | 31 | 16 | 16 |
| Li | 16 | 12 | 9 | 21 | 48 | 34 | 20 |
| Be | 0.22 | 0.50 | 0.33 | 1.06 | 0.89 | 0.82 | 1.12 |
| Mo | 0.27 | 0.2 | 0.17 | 2.08 | 0.94 | 0.13 | 1.01 |
| In | 0.028 | 0.109 | 0.096 | 0.088 | 0.109 | 0.044 | 0.059 |
| Sn | <0.16 | 1.06 | 0.70 | 2.28 | 2.43 | 0.84 | 1.14 |
| Sb | 1.29 | 0.87 | 0.16 | 0.41 | 0.72 | 0.84 | 0.39 |
| W | 0.16 | 0.24 | 0.10 | 0.4 | 0.81 | 5.95 | 0.87 |
| Tl | 0.026 | 0.107 | 0.063 | 0.121 | 0.067 | 0.349 | 0.35 |
| Pb | 1.33 | 1.83 | 0.58 | 2.06 | 6.02 | 1.74 | 1.34 |
| Bi | <0.47 | <0.47 | <0.47 | <0.47 | <0.47 | <0.47 | <0.47 |
| Cs | 0.04 | 0.18 | 0.96 | 0.56 | 0.30 | 1.62 | 1.13 |
| Rb | 4.3 | 12.3 | 8.7 | 15.3 | 12.5 | 41.4 | 38.2 |
| Ba | 56 | 351 | 66 | 79 | 461 | 881 | 906 |
| Sr | 206 | 405 | 219 | 240 | 409 | 193 | 66 |
| Nb | 0.4 | 1.1 | 1.0 | 49.9 | 41.6 | 29.5 | 29.7 |
| Zr | 10 | 47 | 71 | 292 | 314 | 169 | 118 |
| Y | 7.56 | 32.72 | 42.2 | 33.58 | 35.77 | 20.97 | 33.37 |
| Th | 0.04 | 0.02 | 0.111 | 4.526 | 2.175 | 2.03 | 2.575 |
| U | 0.01 | 0.02 | 0.03 | 1.45 | 0.54 | 0.47 | 0.59 |
| Ta | 0.02 | 0.07 | 0.06 | 3.14 | 2.67 | 1.54 | 1.85 |
| La | 0.80 | 1.50 | 1.50 | 37.60 | 33.70 | 11.90 | 17.30 |
| Ce | 1.74 | 6.11 | 4.83 | 82.3 | 75.84 | 24.33 | 27.22 |
| Pr | 0.34 | 1.28 | 0.98 | 10.32 | 10.38 | 3.46 | 4.23 |
| Nd | 1.74 | 7.62 | 6.02 | 42.49 | 45.52 | 15.83 | 17.53 |
| Sm | 0.75 | 3.03 | 2.83 | 9.07 | 10.30 | 3.80 | 3.99 |
| Hf | 0.33 | 1.52 | 2.11 | 6.68 | 7.52 | 3.98 | 2.72 |
| Eu | 0.417 | 1.213 | 1.115 | 2.78 | 3.53 | 1.19 | 1.29 |
| Gd | 1.11 | 4.44 | 4.85 | 8.27 | 9.49 | 3.97 | 4.36 |
| Tb | 0.200 | 0.799 | 0.938 | 1.19 | 1.34 | 0.584 | 0.713 |
| Dy | 1.33 | 5.53 | 6.89 | 6.87 | 7.62 | 3.59 | 4.71 |
| Ho | 0.29 | 1.18 | 1.56 | 1.24 | 1.33 | 0.74 | 0.99 |
| Er | 0.83 | 3.595 | 4.90 | 3.27 | 3.39 | 2.29 | 2.97 |
| Tm | 0.117 | 0.524 | 0.728 | 0.428 | 0.429 | 0.323 | 0.425 |
| Yb | 0.75 | 3.45 | 4.89 | 2.63 | 2.58 | 2.13 | 2.74 |
| Lu | 0.110 | 0.524 | 0.742 | 0.368 | 0.345 | 0.328 | 0.419 |

**Table 2.** Continued.

| Suite | *Enriched tholeiitic* | | | | | | |
|---|---|---|---|---|---|---|---|
| Sample | DMI17-2-9 | DMI17-2-15 | DMI17-4-10 | DMI17-18-5 | DMI17-5-1A | DMI17-1-2 | DMI17-1-7 |
| Lithology | basalt | basalt | fragmental | basalt | fragmental | basalt | basalt |
| Easting | 341827 | 339417 | 350198 | 340913 | 351965 | 358000 | 357993 |
| Northing | 6079643 | 6077194 | 6079547 | 6079612 | 6083272 | 6080523 | 6080182 |
| Unit | Sowchea | Sowchea | Rubyrock? | Sowchea | Rubyrock? | Sowchea | Sowchea |
| *Former unit | - | Rubyrock | Trembleur | - | Rubyrock | - | - |
| Major elements (wt.%) | | | | | | | |
| $SiO_2$ | 49.89 | 49.28 | 45.7 | 54.33 | 49.59 | 50.98 | 57.12 |
| $TiO_2$ | 1.12 | 1.37 | 1.90 | 0.64 | 0.56 | 0.52 | 0.40 |
| $Al_2O_3$ | 13.35 | 13.9 | 14.35 | 11.49 | 18.55 | 14.59 | 12.43 |
| $Fe_2O_3$(T) | 12.49 | 12.16 | 12.55 | 9.13 | 9.39 | 8.49 | 5.74 |
| MnO | 0.19 | 0.21 | 0.22 | 0.16 | 0.17 | 0.16 | 0.10 |
| MgO | 6.51 | 6.58 | 6.03 | 8.43 | 5.19 | 8.40 | 6.97 |
| CaO | 9.72 | 9.11 | 10.53 | 8.90 | 7.95 | 6.20 | 9.81 |
| $Na_2O$ | 3.27 | 3.38 | 3.14 | 3.33 | 4.47 | 2.09 | 3.96 |
| $K_2O$ | 0.25 | 0.16 | 0.07 | 0.54 | 0.41 | 3.39 | 0.08 |
| $P_2O_5$ | 0.11 | 0.12 | 0.22 | 0.05 | 0.13 | 0.08 | 0.04 |
| $Cr_2O_3$ | 0.02 | 0.01 | 0.01 | 0.13 | 0.01 | 0.03 | 0.01 |
| LOI | 2.03 | 3.02 | 5.36 | 1.85 | 3.12 | 4.33 | 2.38 |
| Total | 98.96 | 99.28 | 100.07 | 99.01 | 99.56 | 99.41 | 99.04 |
| Trace elements (ppm) | | | | | | | |
| Ni[a] | 60 | 36 | 32 | 244 | 53 | 72 | 115 |
| V[a] | 331 | 317 | 318 | 225 | 125 | 206 | 98 |
| Co[a] | 46 | 55 | 44 | 44 | 33 | 39 | 30 |
| Cu | 90 | 102 | 16 | 217 | 79 | 139 | 58 |
| Zn | 99 | 96 | 92 | 65 | 74 | 66 | 50 |
| Cd | 0.11 | 0.09 | 0.16 | 0.11 | 0.07 | 0.15 | 0.18 |
| Sc | 48 | 57 | 45 | 39 | 28 | 36 | 21 |
| Ga | 15 | 15 | 20 | 11 | 15 | 14 | 11 |
| Li | 11 | 10 | 15 | 7 | 13 | 16 | 3 |
| Be | 0.4 | 0.58 | 1.05 | 0.66 | 0.32 | 0.44 | 0.16 |
| Mo | 0.09 | 0.2 | 0.44 | 0.36 | 0.18 | <0.08 | 0.09 |
| In | 0.075 | 0.081 | 0.077 | 0.054 | 0.049 | 0.055 | 0.025 |
| Sn | 0.74 | 0.74 | 1.29 | 0.60 | 0.36 | 0.31 | 0.33 |
| Sb | 0.64 | 0.22 | 0.3 | 1.11 | 0.22 | 0.34 | 0.18 |
| W | 0.31 | 0.19 | 0.17 | 0.25 | 0.14 | 0.30 | 0.10 |
| Tl | 0.016 | 0.015 | 0.009 | 0.055 | 0.058 | 0.686 | 0.007 |
| Pb | 0.79 | 0.52 | 0.76 | 1.99 | 0.45 | 0.18 | 0.58 |
| Bi | <0.47 | <0.47 | <0.47 | <0.47 | <0.47 | <0.47 | <0.47 |
| Cs | 0.05 | 0.06 | 0.04 | 0.22 | 0.12 | 1.50 | 0.02 |
| Rb | 3.2 | 2.2 | 1.0 | 9.6 | 7.4 | 66.0 | 0.8 |
| Ba | 45 | 45 | 12 | 214 | 176 | 1302 | 32 |
| Sr | 188 | 61 | 114 | 88 | 90 | 32 | 101 |
| Nb | 4.0 | 3.9 | 10.8 | 2.5 | 4.2 | 2.4 | 3.0 |
| Zr | 75 | 85 | 163 | 38 | 47 | 32 | 48 |
| Y | 30.24 | 33.64 | 33.23 | 16.54 | 15.91 | 15.24 | 11.14 |
| Th | 0.288 | 0.29 | 0.861 | 0.187 | 0.218 | 0.147 | 0.617 |
| U | 0.34 | 0.10 | 0.48 | 0.04 | 0.08 | 0.05 | 0.82 |
| Ta | 0.26 | 0.25 | 0.70 | 0.16 | 0.23 | 0.14 | 0.21 |
| La | 4.20 | 3.90 | 11.30 | 2.00 | 3.40 | 1.60 | 4.60 |
| Ce | 10.59 | 10.82 | 27.31 | 4.77 | 7.84 | 3.94 | 7.79 |
| Pr | 1.68 | 1.76 | 3.95 | 0.78 | 1.13 | 0.70 | 1.29 |
| Nd | 8.44 | 9.13 | 18.02 | 3.91 | 4.99 | 3.55 | 5.31 |
| Sm | 2.85 | 3.24 | 4.92 | 1.39 | 1.41 | 1.23 | 1.44 |
| Hf | 2.00 | 2.25 | 3.85 | 1.06 | 1.20 | 0.87 | 1.29 |
| Eu | 1.12 | 1.21 | 1.61 | 0.530 | 0.578 | 0.467 | 0.503 |
| Gd | 3.92 | 4.57 | 5.64 | 2.04 | 1.85 | 1.85 | 1.71 |
| Tb | 0.724 | 0.823 | 0.930 | 0.376 | 0.339 | 0.347 | 0.306 |
| Dy | 5.09 | 5.77 | 6.05 | 2.64 | 2.48 | 2.55 | 2.14 |
| Ho | 1.12 | 1.24 | 1.23 | 0.58 | 0.56 | 0.58 | 0.45 |
| Er | 3.43 | 3.72 | 3.63 | 1.82 | 1.78 | 1.80 | 1.35 |
| Tm | 0.503 | 0.545 | 0.515 | 0.278 | 0.278 | 0.277 | 0.199 |
| Yb | 3.32 | 3.56 | 3.39 | 1.90 | 1.92 | 1.87 | 1.30 |
| Lu | 0.503 | 0.538 | 0.503 | 0.292 | 0.311 | 0.293 | 0.202 |

**Table 2.** Continued.

| Suite | *Depleted tholeiitic* | | *Calc-alkaline* | | |
|---|---|---|---|---|---|
| Sample | DMI17-15-7 | DMI17-1-5 | DMI17-8-11 | DMI17-15-3 | DMI17-7-6 |
| Lithology | gabbro | ol. cpxite. | gabbro | qz. diorite | hornblendite |
| Easting | 358303 | 357841 | 360652 | 356417 | 354903 |
| Northing | 6084840 | 6080196 | 6081188 | 6084553 | 6084296 |
| Unit | Sowchea | Sowchea | Late intrusion | Late intrusion | Late intrusion |
| *Former unit | - | - | Sowchea (S'01) | Rubyrock (S'01) | Rubyrock (S'01) |
| Major elements (wt.%) | | | | | |
| $SiO_2$ | 49.32 | 42.70 | 46.55 | 62.55 | 43.51 |
| $TiO_2$ | 0.58 | 0.44 | 0.78 | 0.34 | 0.70 |
| $Al_2O_3$ | 15.75 | 8.80 | 12.55 | 15.40 | 11.62 |
| $Fe_2O_3$(T) | 9.41 | 11.46 | 7.52 | 2.93 | 9.57 |
| MnO | 0.16 | 0.21 | 0.14 | 0.07 | 0.17 |
| MgO | 7.16 | 19.50 | 10.47 | 1.01 | 17.76 |
| CaO | 10.38 | 8.55 | 10.36 | 3.54 | 8.93 |
| $Na_2O$ | 3.28 | 0.09 | 3.10 | 8.74 | 1.20 |
| $K_2O$ | 0.05 | 0.26 | 0.85 | 0.29 | 0.51 |
| $P_2O_5$ | 0.05 | 0.04 | 0.15 | 0.16 | 0.15 |
| $Cr_2O_3$ | 0.04 | 0.37 | 0.09 | <0.002 | 0.15 |
| LOI | 3.07 | 6.25 | 6.63 | 3.41 | 4.69 |
| Total | 99.25 | 98.66 | 99.21 | 98.45 | 99.00 |
| Trace elements (ppm) | | | | | |
| Ni[a] | 62 | 921 | 223 | <9 | 575 |
| V[a] | 240 | 192 | 200 | 44 | 170 |
| Co[a] | 37 | 104 | 40 | <12 | 66 |
| Cu | 29 | 86 | 9 | 16 | 15 |
| Zn | 67 | 105 | 55 | 26 | 80 |
| Cd | 0.08 | 0.24 | 0.05 | 0.30 | 0.08 |
| Sc | 50 | 39 | 38 | 7 | 25 |
| Ga | 14 | 9 | 13 | 15 | 12 |
| Li | 8 | 57 | 41 | 1 | 24 |
| Be | 0.19 | 0.28 | 1.59 | 1.17 | 0.90 |
| Mo | 0.12 | 0.1 | 0.1 | <0.08 | 0.45 |
| In | 0.052 | 0.043 | 0.042 | 0.013 | 0.043 |
| Sn | 0.34 | <0.16 | 0.55 | 0.64 | 0.29 |
| Sb | 0.46 | 1.99 | 0.61 | 0.33 | 0.29 |
| W | 0.21 | 0.05 | 0.36 | 6.87 | 0.23 |
| Tl | 0.003 | 0.029 | 0.169 | 0.020 | 0.043 |
| Pb | 0.40 | 0.18 | 1.29 | 5.79 | 0.45 |
| Bi | <0.47 | <0.47 | <0.47 | 0.61 | <0.47 |
| Cs | 0.02 | 0.18 | 1.08 | 0.05 | 0.35 |
| Rb | 0.5 | 4.1 | 21.8 | 3.0 | 7.8 |
| Ba | 21 | 91 | 217 | 203 | 320 |
| Sr | 47 | 7 | 482 | 480 | 104 |
| Nb | 1.1 | 1.0 | 7.0 | 2.0 | 4.9 |
| Zr | 32 | 21 | 63 | 89 | 63 |
| Y | 20.31 | 13.7 | 16.74 | 11.11 | 14.07 |
| Th | 0.094 | 0.075 | 1.268 | 0.955 | 0.5 |
| U | 0.03 | 0.11 | 0.58 | 0.59 | 0.22 |
| Ta | 0.06 | 0.06 | 0.32 | 0.11 | 0.28 |
| La | 1.20 | 1.10 | 29.60 | 7.00 | 7.60 |
| Ce | 3.06 | 2.52 | 75.81 | 16.78 | 18.22 |
| Pr | 0.57 | 0.45 | 10.47 | 2.31 | 2.57 |
| Nd | 3.16 | 2.35 | 39.50 | 9.97 | 11.28 |
| Sm | 1.40 | 0.97 | 5.44 | 2.12 | 2.56 |
| Hf | 0.94 | 0.63 | 1.74 | 2.57 | 1.59 |
| Eu | 0.565 | 0.342 | 1.332 | 0.661 | 0.827 |
| Gd | 2.28 | 1.57 | 3.76 | 1.88 | 2.61 |
| Tb | 0.455 | 0.309 | 0.541 | 0.290 | 0.407 |
| Dy | 3.31 | 2.32 | 3.24 | 1.85 | 2.69 |
| Ho | 0.76 | 0.53 | 0.64 | 0.38 | 0.53 |
| Er | 2.357 | 1.655 | 1.78 | 1.15 | 1.54 |
| Tm | 0.351 | 0.251 | 0.250 | 0.170 | 0.216 |
| Yb | 2.37 | 1.76 | 1.65 | 1.18 | 1.39 |
| Lu | 0.363 | 0.274 | 0.243 | 0.182 | 0.211 |

Trace elements were analyzed by ICP-MS unless reported otherwise. [a] analyzed by XRF. Numbers in first column (italics) are detection limits for individual elements. UTM coordinates for sample locations are based on Zone 10 North American datum 1983 (NAD83).

*Former stratigraphic rock unit assignment as used by Struik et al. (2007) is given for rock samples that were reassigned to different units based on their geochemistry.

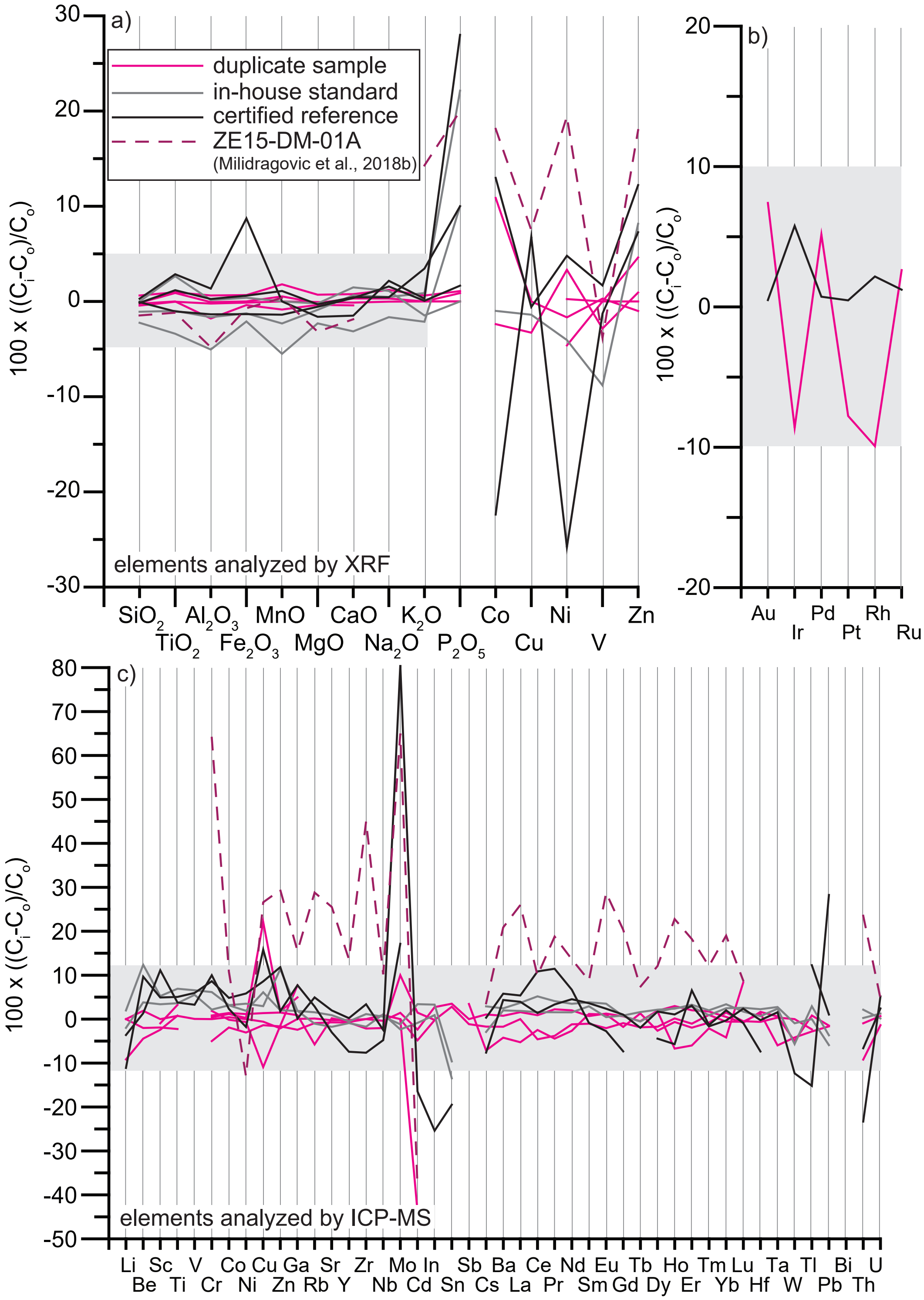


**Fig. 3.** Diagrams showing the relative uncertainty (in %) in elemental concentrations of samples analyzed in this study. Relative uncertainty is defined as the difference between the measured and reference value for an element, normalized to the reference value. **a)** Major element oxides and selected trace element concentrations determined by XRF. **b)** Gold and platinum group element (PGE) concentrations determined by Ni-S fire assay. **c)** Trace element concentrations determined by ICP-MS.

study area (Fig. 2) are extensively $CO_2$-altered ($CO_2$ >30 wt.%). Different extents of carbonation have resulted in significant mineralogical variability among listwanite samples (Hansen et al., 2005).

### 5.2. Geochemistry of the Trembleur ultramafite

The major element chemistry (Table 1) of the relatively unaltered (5.4-10.3 wt.% LOI) Trembleur ultramafite samples ($SiO_2$=40.8-44.4 wt.%, MgO=43.4-50.7 wt.%, Ni=2200-

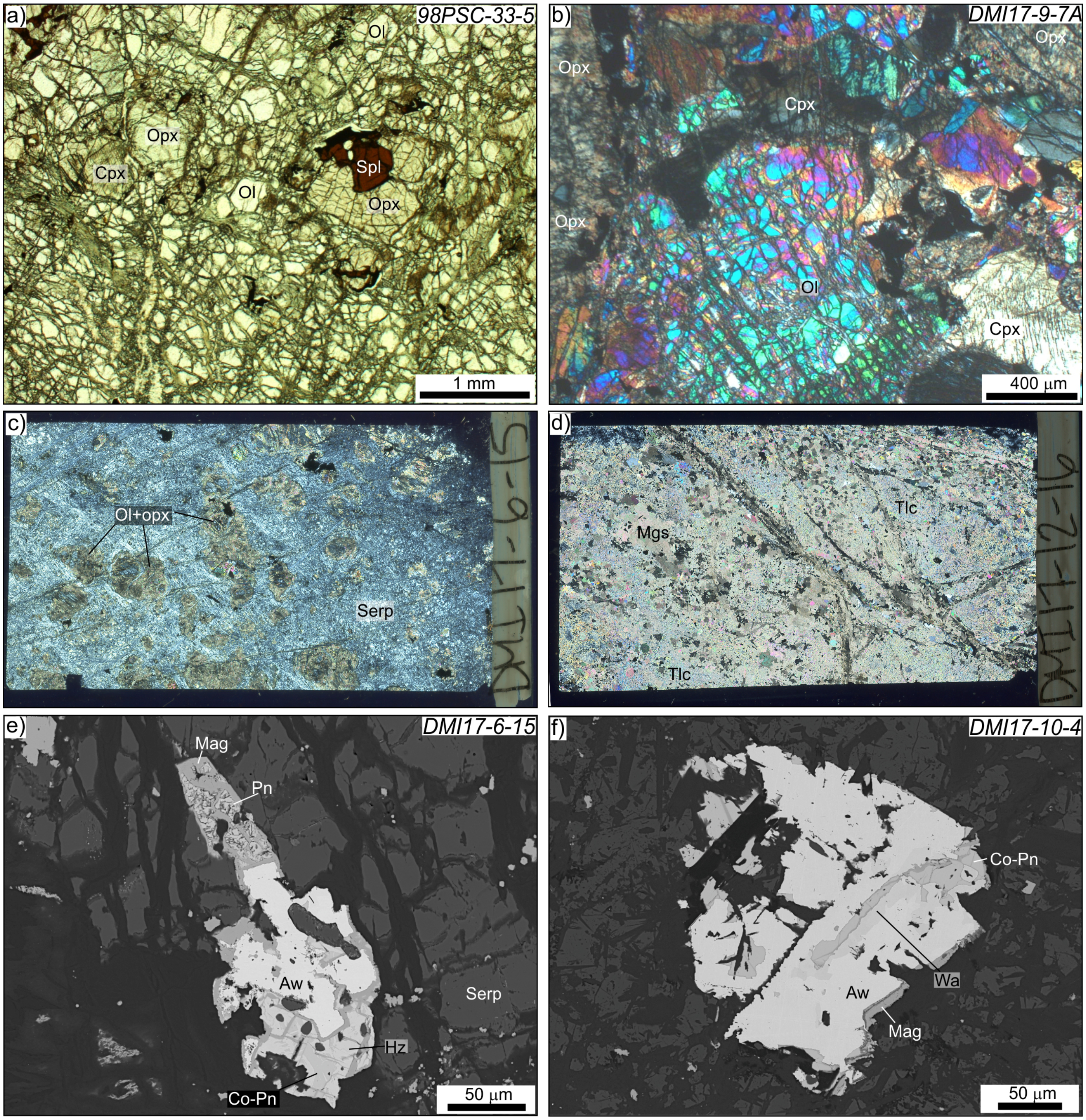


**Fig. 4.** Representative petrographic images of variably altered Trembleur ultramafite samples from the Decar area. **a)** Plane-polarized light photomicrograph of spinel harzburgite 98PSC-33-5. **b)** Cross-polarized light photomicrograph of spinel harzburgite DMI17-9-7A. **c)** Cross-polarized light scan of serpentinite DMI17-6-15 thin section. Light brown 'enclaves' in grey massive serpentine are composed of bastite-altered orthopyroxene that has been partly replaced by metamorphic olivine. **d)** Cross-polarized light scan of magnesite-talc listwanite DMI17-12-16 thin section. **e)** Backscattered electron (BSE) image of a composite grain of magnetite (Mag) – pentlandite (Pn) – cobalt-pentlandite (Co-Pn) – heazlewoodite (Hz) – awaruite (Aw) from serpentinite DMI17-6-15. **f)** BSE image of composite magnetite (Mag) – cobalt-pentlandite (Co-Pn) – wairauite (Wa) – awaruite (Aw) from serpentinite DMI17-10-4.

2900 ppm LOI-free) is consistent with a mineralogy of mainly olivine and orthopyroxene (Figs. 4a-b). Measured LOI contents are consistent with a high degree of serpentinization (40-80%), assuming an $H_2O$ content of anhydrous depleted mantle of 0.116 wt.% (Salters and Strackle, 2004) and $H_2O$ ~13% wt.% in pure serpentine (e.g., Carlson and Miller, 2003). Samples of harzburgite have a limited range of $SiO_2$ (43.4-45.0 wt.%), MgO (41.8-46.3 wt.%) and $FeO^{TOT}$ (7.8-8.3 wt.%), which distinguish them from dunite ($SiO_2$ <41 wt.%, MgO >50 wt.%, $FeO^{TOT}$ <7.5 wt.%; Figs. 5a-c). Contents of $Al_2O_3$ (0.6–1.5 wt.%; Fig. 4d) and CaO (0.6-2.8 wt.%) in harzburgite are higher than in dunite, but they are lower than those of the Earth's upper mantle source of mid-ocean ridge basalts (e.g., DM of Salters and Stracke, 2004 or DMM of Workman and Hart, 2005). Measured LOI contents are higher in pervasively serpentinized rocks (>10 wt.%) and carbonate-altered rocks (listwanite; >34 wt.%) compared to relatively unaltered peridotites. In contrast to listwanite ($CO_2$ >34-36 wt.%), serpentinite contains relatively minor $CO_2$ (0.1-2.6 wt.%). Major element abundances of listwanite and serpentinite, normalized to LOI-free compositions, show significant scatter (Figs. 5a-c), but do not differ systematically from less altered peridotite.

Except for the most mobile trace elements (large ion lithophile elements or LILE, Pb, Sr), the ultramafic rocks of the Decar area have low incompatible trace element abundances (<0.3 x PM; primitive mantle of Palme and O'Neill, 2003; Fig. 6a). Middle and heavy rare earth element (MREE and HREE, respectively) abundances, normalized to primitive mantle, show increasing depletion with decreasing atomic number. Limited light REE (LREE) results suggest enrichment of LREE relative to MREE in the Trembleur ultramafite as evidenced by the broadly U-shaped trace element profiles of the analyzed samples (Fig. 6a). There are no systematic differences in trace element contents between the relatively unaltered and serpentinized ultramafic samples (Fig. 6b). This is in contrast to listwanite samples, which display a general depletion in absolute trace element concentrations relative to their harzburgitic protolith, a likely consequence of dilution through carbonate metasomatism.

The abundances of Au and PGE in selected harzburgites and serpentinites of the Trembleur ultramafite (Fig. 6c) are low (~0.005-0.02 x CI-chondrite; Palme and O'Neill, 2003), but within the estimated range of abundances in the Earth's depleted upper mantle (Salters and Stracke, 2004). Overall, the iridium-group PGE that were analyzed (Ir, Ru) are not fractionated from the palladium-group PGE (Rh, Pt, Pd).

### 5.3. Volcanic and shallow intrusive rocks

The volcanic and shallow intrusive rocks of the Decar area have undergone variable deformation and greenschist- to amphibolite-facies metamorphism and recrystallization (Figs. 7, 8). Although primary volcanic structures, such as carbonate or epidote-filled amygdules, are locally recognizable in the field, obscured primary mineralogy and igneous textures are an impediment to petrographic classification and lithostratigraphic unit assignment.

We classify volcanic rocks of the Decar area according to their immobile element concentrations (Fig. 9), following an approach commonly used in petrological investigations of Archean rocks (e.g., Jensen, 1976; Maurice et al., 2003). We define four main geochemical suites (Table 2): 1) high-Ti alkaline; 2) HFSE-depleted; 3) depleted to enriched tholeiitic; and 4) calc-alkaline. Specifying the suite of some samples is ambiguous because magmatic signatures are modified by alteration and crystal accumulation. For example, samples DMI17-4-10 and DMI17-1-7 are classified as enriched tholeiites based on their extended trace element profiles (Table 2, Fig. 10), although their elevated Th/Yb and Nb/Yb ratios (Fig. 11), suggest a calc-alkaline affinity. Similarly, we classified the coarse-grained sample DMI17-1-5, which is inferred to be a metamorphosed (olivine) clinopyroxenite on the basis of relict clinopyroxene and CaO and MgO-rich composition, as a depleted tholeiite (Fig. 11). However, because of the strong incompatibility of HFSE in clinopyroxene relative to HREE (e.g., Francis and Minarik, 2008), clinopyroxene accumulation lowers the Nb/Yb ratios of resulting cumulate rocks relative to their parental magmas, resulting in a more depleted apparent character. Some of these suites indicate mutually incompatible tectonic settings (e.g., high-Ti alkaline suite and HFSE-depleted suite) and the existence of significant crustal structures. The distribution of volcanic rocks, thus, helps define the position of faults that may mark tectonic boundaries. Furthermore, the suites we define may permit limited regional correlation within the Cache Creek terrane as more geochemical data become available.

#### 5.3.1. High-Ti alkaline suite

High-Ti alkaline samples collected from areas we mapped as Sowchea succession, both east and west of the Trembleur ultramafite (Fig. 2), have variable, but high overall, $TiO_2$ concentrations (1.5 to 4.1 wt.%; Table 2), which distinguish them from other volcanic suites in the Decar area. The samples have moderate to high LOI (3.3-16.8 wt.%), highly variable $SiO_2$ (36.9-58.7 wt.%, reported on anhydrous, LOI-free basis), and less variable MgO (3.3-7.0 wt.%), and $Al_2O_3$ (15.4-19.1 wt.%). The measured range of $SiO_2$ in the high-Ti alkaline samples spans the compositional spectrum between foidite and trachyandesite. However, classification using immobile elements Zr, Ti, Nb, and Y (Fig. 9a; Pearce, 1996), suggests that all four high-Ti alkaline samples are strongly altered and derived from an alkaline basalt protolith. The defining features of the high-Ti alkaline basalts of the Decar area are the highly fractionated REE profiles ($Ce/Yb_{MORB}$=4-13, where subscript MORB denotes normalization relative to MORB concentrations of Sun and McDonough, 1989), absolute HREE abundances that are below those of MORB, and enrichment of Nb-Ta relative to the similarly compatible LREE ($Nb/La_{MORB}$=1.3-2.7; Fig. 10a). The trace element patterns of the high-Ti alkaline basalts overlap those of the Type 2 alkalic basalts of Lapierre et al. (2003), and the Type 3 mafic volcanic rocks from the western belt of the Sitlika assemblage (Schiarizza and Massey, 2010). On the Th/Yb vs. Nb/Yb diagram of Pearce (2008; Fig. 11), alkaline basalts of the Decar area plot within the mantle array, near the average ocean island basalt (OIB) composition (Sun and McDonough, 1989).

#### 5.3.2. HFSE-depleted tholeiitic suite

HFSE-depleted suite samples represent rocks mapped as part of the Rubyrock igneous complex by Struik et al. (2007) and

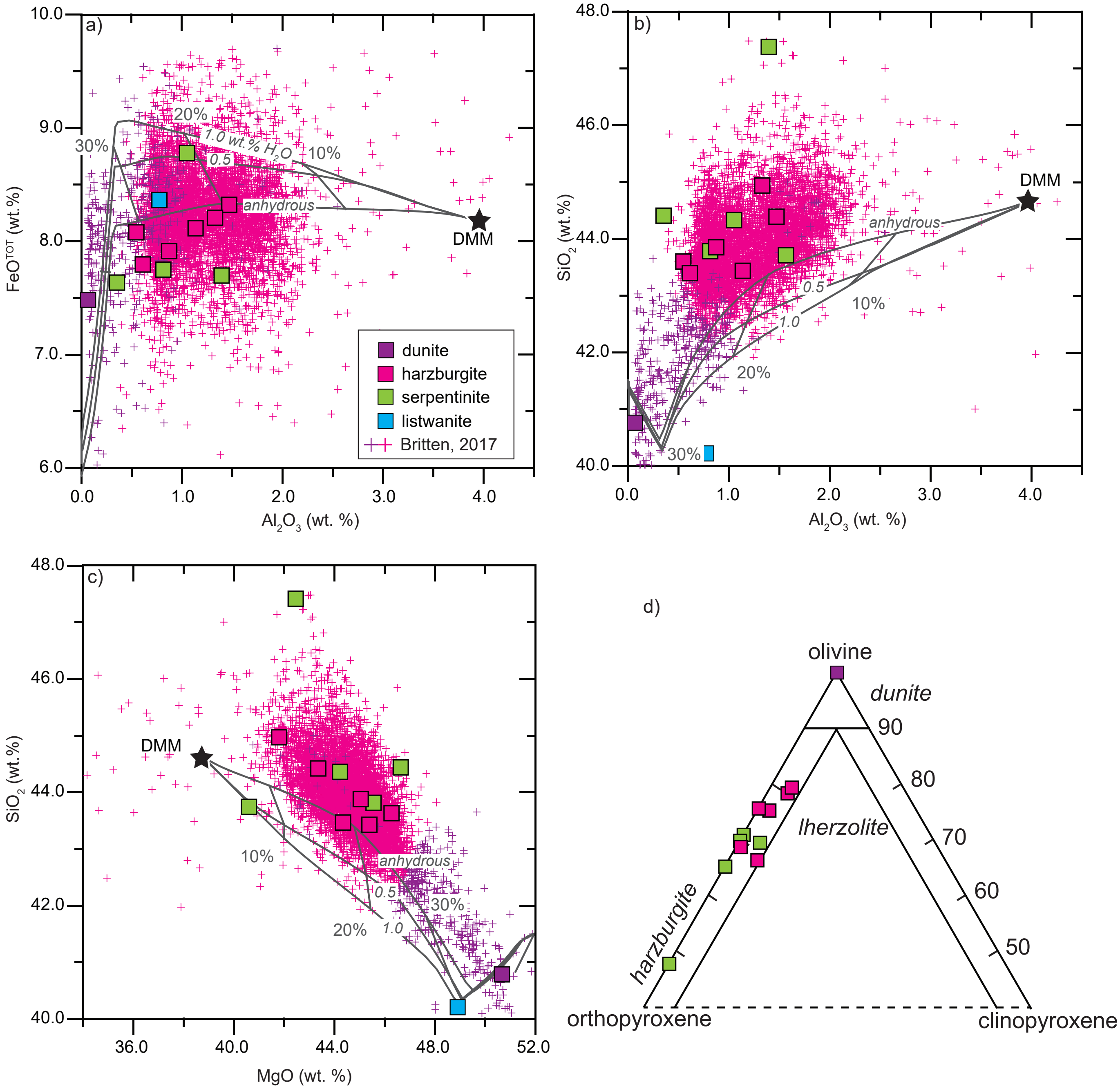


**Fig. 5.** Whole rock chemistry of Trembleur peridotites. **a)** FeO$^{TOT}$ vs. $Al_2O_3$. **b)** $SiO_2$ vs. $Al_2O_3$. **c)** $SiO_2$ vs. MgO. Also shown are the calculated compositions of residual peridotite formed by 10-30% batch melting of relatively oxidized ($\Delta$log $fO_2$=FMQ+1) depleted MORB mantle (DMM; Workman and Hart, 2005) with variable initial water contents (anhydrous, 0.5, and 1.0 wt.%). **d)** Normative (wt.%) olivine-orthopyroxene-clinopyroxene plot of the relatively unaltered and serpentinized ultramafic rocks from the Decar area.

Milidragovic et al. (2018a), a gabbro that cuts the Trembleur ultramafite, and rocks previously mapped by Struik et al. (2007) as Sowchea succession on both east and west sides of the Trembleur ultramafite (Fig. 2). These rocks have moderate LOI contents (1.9-5.2 wt.%; Table 2) and variable $SiO_2$ (43.9-53.9 wt.%;), MgO (5.2-11.4 wt.%), and $Al_2O_3$ (14.0-19.4 wt.%), suggesting a combination of alteration-related mobility and accumulation-differentiation processes. The measured range of $SiO_2$ in the HFSE-depleted samples spans the compositional spectrum from picro-basalt to basaltic andesite on the total alkali-silica classification diagram (TAS diagram; LeMaitre, 2005). However, on the Zr/$TiO_2$ vs. Nb/Y classification diagram (Fig. 9a; Pearce, 1996) the rocks of the HFSE-depleted suite have uniformly basaltic, subalkaline compositions, indicating significant mobility of major elements during metamorphism. On Jensen's (1976) immobile major element classification plot

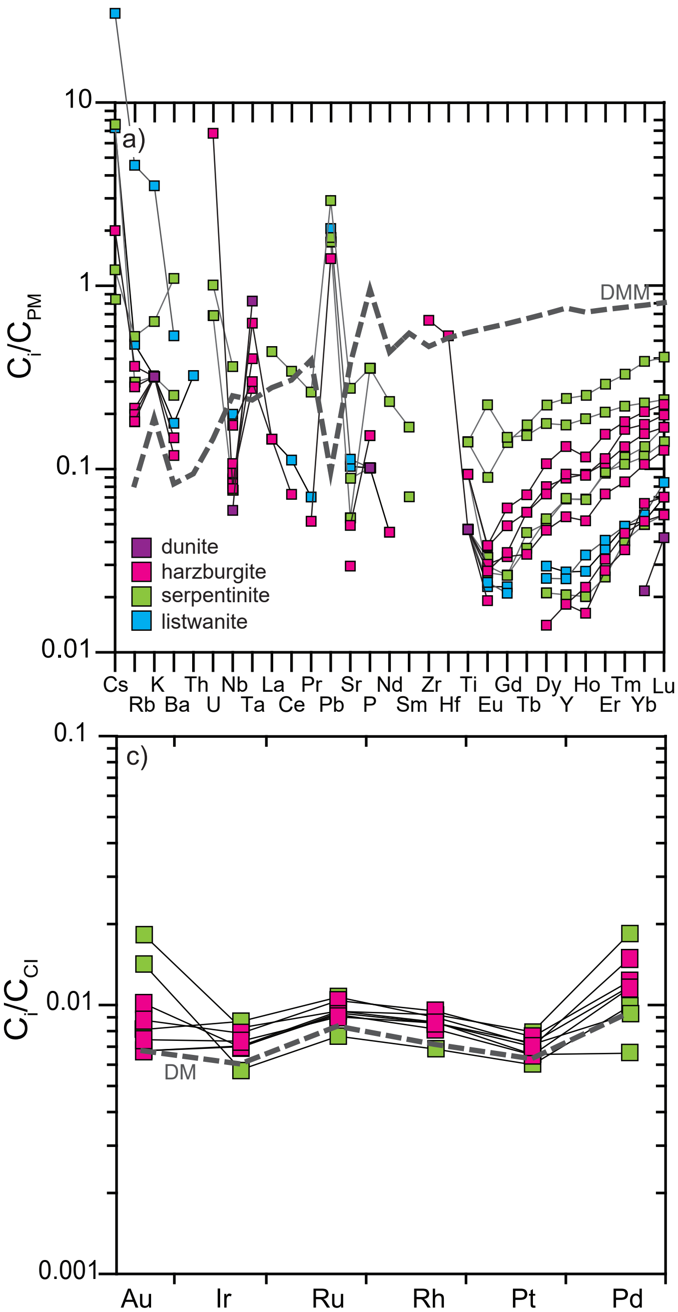


**Fig. 6.** Trace element systematics of the Trembleur ultramafite in the Decar area. **a)** Primitive mantle-normalized incompatible trace element profiles. Normalizing values from Palme and O'Neill, (2003). Composition of Depleted MORB mantle (DMM; Workman and Hart, 2005) is shown for reference. **b)** Incompatible trace element concentrations of the Trembleur ultramafic rocks normalized to harzburgite DMI17-5-10. **c)** PGE concentrations in select harzburgites and serpentinites from the Decar area normalized to chondritic (CI) abundances (Palme and O'Neill, 2003). The estimated concentrations of PGE in the depleted upper mantle (DM) are from Salters and Stracke (2004).

for subalkaline volcanic rocks (Fig. 9b), all but one HFSE-depleted sample have a tholeiitic affinity.

The HFSE-depleted suite is defined by unfractionated to mildly LREE-depleted MORB-normalized (Sun and McDonough, 1989) trace element patterns coupled with pronounced relative depletions in HFSE (Nb, Ta±Zr, and Hf), and relative enrichments in Th and U (Fig. 10b). Except for one sample, the HFSE-depleted suite has absolute HREE element abundances that are 0.8-1.5 times those of MORB. Although HFSE-depleted tholeiitic basalts were not explicitly identified by Tardy et al. (2001) and Lapierre et al. (2003), our examination of their results reveals that at least four samples (01PG-64, 99CC1, 99CC2; PG96-14), previously classified as N-MORB and collected north of the town of Cache Creek and from the Pinchi fault near Fort St. James, have HFSE-depleted tholeiitic trace element profiles. On the Th/Yb vs. Nb/Yb diagram (Fig. 11; Pearce, 2008) HFSE-depleted volcanic rocks plot within or slightly above the mantle array and indicate a mantle source that was depleted relative to that of N-MORB.

### 5.3.3. Depleted to enriched tholeiitic suite

This suite includes a spectrum of altered (LOI=1.9-6.3 wt.%) mafic ($SiO_2$=46.7-59.4; MgO=5.4-21.3 wt.%; $Al_2O_3$=9.6-19.4 wt.%) rocks with generally low $TiO_2$ contents (0.4-2.0 wt.%) and weakly to moderately fractionated trace element patterns. Importantly, these rocks lack the marked depletions


a)
b)
c)
d)
e)
chert lenses
f)


**Fig. 7.** Field photographs of volcanic and intrusive rocks from the Decar area. **a)** Rusty weathering, veined high-Ti alkaline basalt from the undivided Sowchea succession (Struik et al., 2007) in the southeastern corner of the study area. Sample locality: DMI17-8-4. Rusty colour is due to weathering of cubic pyrite crystals. **b)** Steeply dipping schistosity (upper right to lower left) in an aphanitic, HFSE-depleted tholeiitic basalt, formerly assigned to the greenstone unit of the Sowchea succession in the southwest part of the study area (Struik et al., 2007). Sample locality: DMI17-3-3. **c)** Highly altered (chlorite, carbonate, sericite), and heterogeneously brecciated HFSE-depleted tholeiitic basalt at a small exposure of volcanic rock in the southern portion of Trembleur ultramafite formerly assigned to the Sowchea succession by Struik et al. (2007). Sample locality: DMI17-4-16. **d)** Aphanitic enriched tholeiitic basalt assigned to the greenstone unit of the Sowchea succession in the southwest part of the study area. Sample locality: DMI17-2-9. **e)** Strongly altered and pyrite-rich, aphanitic, enriched tholeiitic basalt with lenses of chert; greenstone unit of the Sowchea succession in the southwest part of the study area (Struik et al., 2007). Sample locality: DMI17-18-5. **f)** Massive, homogeneous plagioclase and clinopyroxene-phyric depleted tholeiitic gabbro from the undivided Sowchea succession (Struik et al., 2007) in the southeastern corner of the study area. Sample locality: DMI17-15-7. **g)** Massive, homogeneous calc-alkaline feldspathic hornblendite from a panel of Rubyrock igneous complex in the eastern part of the study area. Sample locality:DMI17-7-6. **h)** Rusty weathering coarse-grained massive calc-alkaline plagioclase-phyric gabbro intruding chert of the Sowchea succession in the southeastern corner of the study area. Sample: DMI17-8-11.

in HFSE that characterize the HFSE-depleted tholeiitic suite. Our samples came mainly from volcanic units we mapped as undivided sedimentary rocks and greenstones of the Sowchea succession, although one sample (DMI17-5-1A) was collected from an outcrop previously assigned (MacIntyre and Schiarizza, 1999; Struik et al., 2007) to the Rubyrock igneous complex and one sample (DMI17-4-10) was from an outcrop previously mapped (MacIntyre and Schiarizza, 1999; Struik et al., 2007) as Trembleur ultramafite (Table 2, Fig. 2). The large compositional range of samples included in this suite is attributed in part to the effects of crystal accumulation (e.g., DMI17-1-5; Fig. 9b), but is also interpreted to reflect differences in magma chemistry arising from mantle source composition and/or melting dynamics. As in the case of high-Ti alkaline and HFSE-depleted tholeiitic suites, classification based on the TAS diagram indicates a wide compositional range of tholeiitic rocks that spans the fields of basalt to andesite. However, immobile trace element concentrations, suggest that at least some of this variability is due to alteration and metamorphism, and that the tholeiitic samples derive from a subalkaline basalt protolith with tholeiitic affinity (Fig. 9). In contrast to the alkaline basalts, tholeiitic basalts show relatively flat MORB-normalized HREE profiles ($Gd/Yb_{MORB}$=0.7-1.4; Fig. 10c), and display both enrichment and depletion in LREE relative to HREE (Ce/Yb=0.5-3.3). The trace element patterns of the relatively enriched tholeiitic samples show overlap with the Type 3 basalts of Lapierre et al. (2003), albeit at a greater range of absolute concentrations (Fig. 10c). Moreover, the depleted to enriched tholeiitic basalts from the Decar area are broadly similar to the mildly depleted to mildly enriched Type 1 tholeiitic basalts and andesites from the eastern belt of the Sitlika assemblage (Schiarizza and MacIntyre, 2010). The tholeiitic samples plot within the mantle array (Fig. 11) and they have Nb/Yb ratios that are intermediate between those of N-MORB and E-MORB (Sun and McDonough, 1989).

### 5.3.4. Calc-alkaline suite

The three coarse-grained intrusive samples of the calc-alkaline suite have moderate LOI (3.4-6.6 wt.%), variable $SiO_2$ (46.6-66.0 wt.%) and MgO (1.1-19.0 wt.%), and less variable $Al_2O_3$ (12.4-16.3 wt.%). The samples have characteristically low $TiO_2$ contents (0.4-0.9 wt.%). The samples were collected from small outcrops of the Rubyrock igneous complex and the Sowchea succession (Fig. 2). All three outcrops lack the pervasive deformation fabrics typical of the other three volcanic suites, possibly indicating intrusion after the deformation that resulted in the predominant steeply dipping northwest-striking structural trends. When plotted on the $Zr/TiO_2$ vs. Nb/Y classification diagram (Fig. 9a) the calc-alkaline samples have basaltic to andesitic compositions. Two of the samples have accumulated amphibole±clinopyroxene and consequently plot on the right hand half of the Jansen classification plot (Fig. 9b).

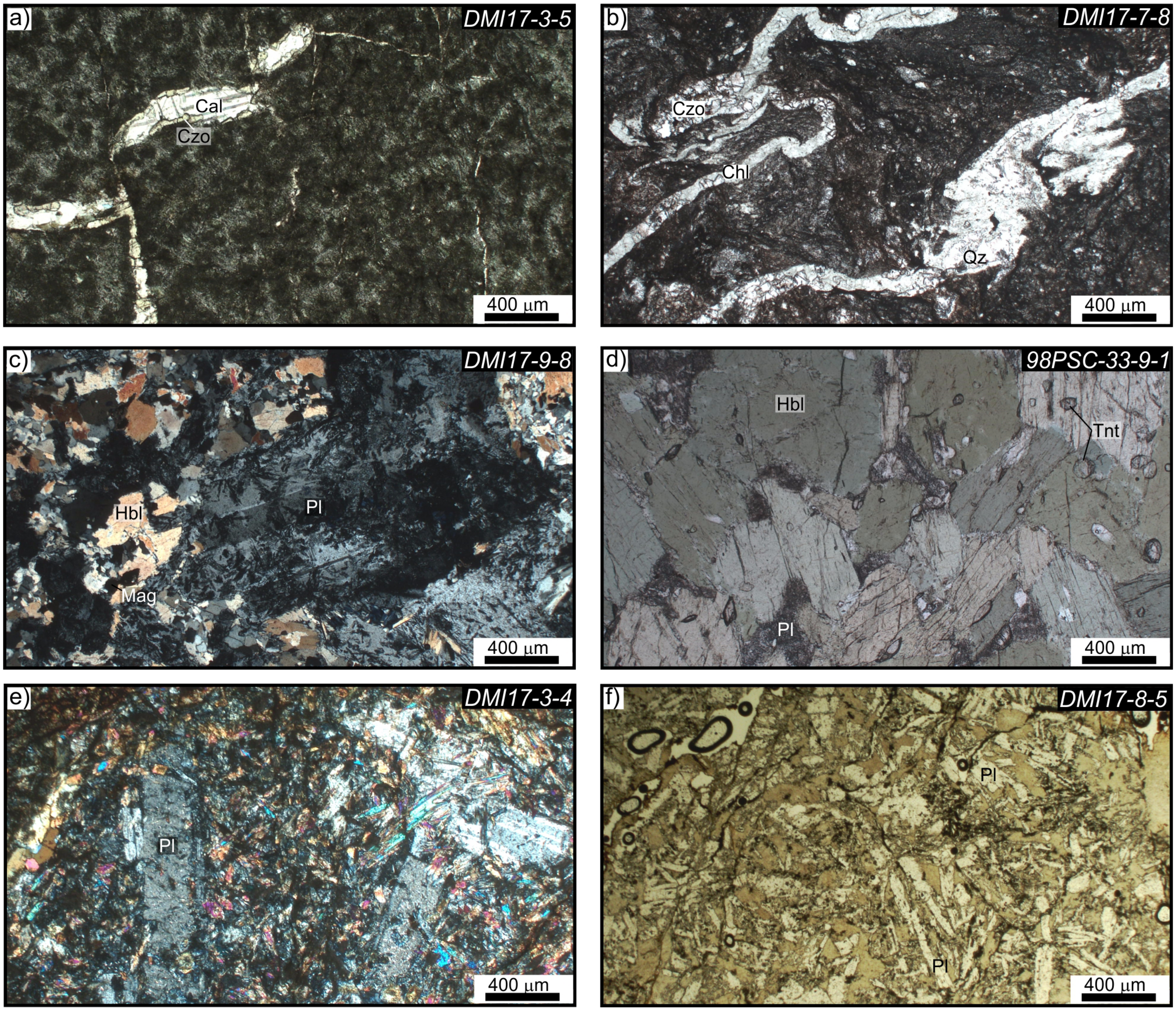


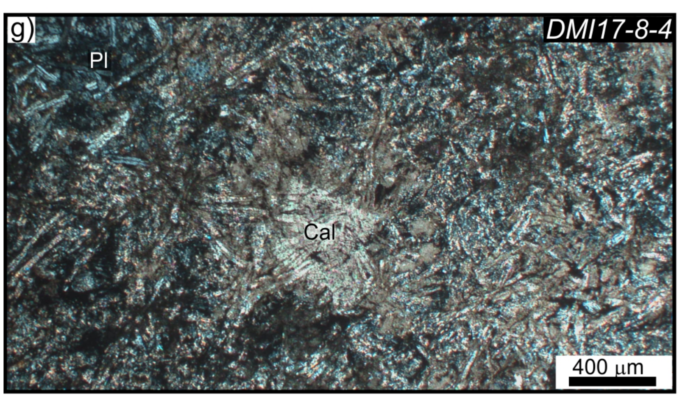


**Fig. 8.** Representative petrographic images of volcanic and shallow intrusive rocks from the Decar area. **a)** Strongly altered, aphanitic HFSE-depleted tholeiitic basalt with calcite-epidote stringers and veinlets. Sample collected from rocks formerly assigned to the Sowchea succession in the southwest part of the study area (Struik et al., 2007). **b)** Deformed, strongly altered and possibly fragmental, aphanitic HFSE-depleted tholeiitic basalt with folded calcite-epidote-chlorite-quartz veinlets. Sample collected from a panel of Rubyrock igneous complex in the eastern part of the study area. **c)** Cross-polarized light photomicrograph of a medium-grained HFSE-depleted tholeiitic metagabbro with partly saussuritized primary plagioclase. The metagabbro cross-cuts harzburgite of the Trembleur ultramafite in the central part of the study area. **d)** Medium-grained, homogeneous, completely recrystallized HFSE-depleted tholeiitic metagabbro collected from a panel of Rubyrock igneous complex on the west side of the Trembleur ultramafite. **e)** Fine-grained, plagioclase-phyric high-Ti alkaline basalt from the greenstone unit of the Sowchea succession in the southwest part of the study area. **f)** Medium to coarse-grained, plagioclase-phyric high-Ti alkaline volcanic breccia from the undivided Sowchea succession in the southeastern corner of the study area. **g)** Highly altered (carbonate), plagioclase-phyric high-Ti alkaline basalt from the undivided Sowchea succession in the southeastern corner of the study area. Unless otherwise specified, all photomicrographs are in plane-polarized light.

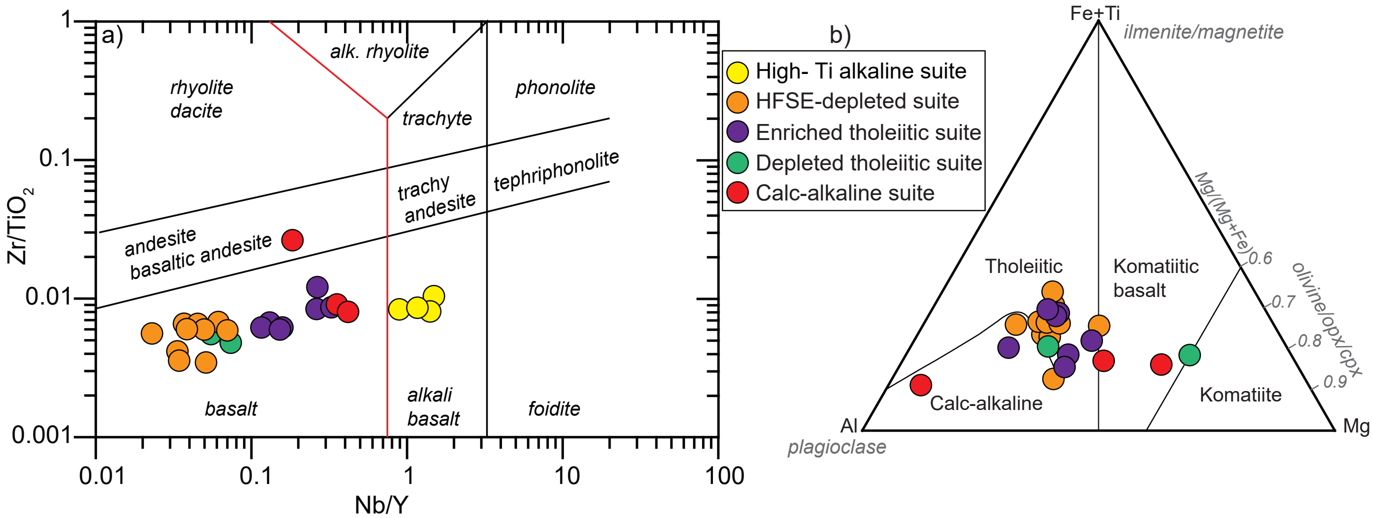


**Fig. 9.** Classification plots for volcanic and shallow intrusive rocks. **a)** $Zr/TiO_2$ vs. Nb/Y classification plot for volcanic rocks after Pearce (1996). The red line divides subalkaline from alkaline rocks. **b)** Ternary cation classification plot for subalkaline volcanic rocks after Jensen (1976). Rocks plotting on the right hand side of the triangle are inferred to have accumulated ferromagnesian minerals and are not considered komatiitic.

However, the strongly fractionated trace element patterns and moderate to strong HFSE depletions of all three samples suggest a calc-alkaline magmatic affinity (Fig. 10d).

## 6. Discussion

### 6.1. Petrogenesis of the Trembleur ultramafite

The large depletion of $Al_2O_3$ and CaO relative to depleted upper mantle suggests that the harzburgites of the Decar area are residual mantle rocks formed through significant extraction of basaltic melt. Isobaric batch melting models, performed using alphaMELTS (version 1.8; Ghiorso et al., 2002; Smith and Asimow, 2005) on a relatively oxidized ($DlogfO_2$=FMQ+1) depleted mantle source (DMM; Workman and Hart, 2005) at 1 GPa suggest that the harzburgites represent residues after ~15-30% melt extraction (Figs. 5a-c). This estimate is higher than the estimation of Grundy (2018) who, using REE concentrations in clinopyroxene and Cr-numbers of spinel (after Hellebrand et al., 2001), suggested that the extent of melting recorded by harzburgites of the Trembleur ultramafite in the Decar area is ~10-15%. This discrepancy in the estimated degree of melting cannot be attributed to the effects of serpentinization because $Al_2O_3$ is typically immobile during serpentine alteration of peridotite, and harzburgite compositions plotted in Fig. 5 have been corrected for LOI to anhydrous compositions. Furthermore, melt depletion degree estimates that are based on spinel (Hellebrand et al., 2001) and clinopyroxene (Warren, 2016) compositions are highly sensitive to the imposed melting mechanism (batch vs. fractional). Thus at a spinel Cr-number of 0.22 (cf., Grundy, 2018), fractional melting yields a significantly lower melting estimate (~10%) than the batch melting model (~15%). At a spinel Cr-number of 0.3, the discrepancy in melt depletion extent between fractional (~12%) and batch melting (~27%) models is even larger. Although there is no consensus on the melting mechanism affecting the Trembleur ultramafite, the relatively high degree of depletion implied by low modal and normative abundance of clinopyroxene (Fig. 4d) coupled with the strong depletion of the relatively immobile and incompatible HREE (Fig. 5a) argues against a predominantly fractional melting model.

The relatively low $FeO^{TOT}$ contents of harzburgite samples (<8.3 wt.%) may be explained by melting of dry depleted mantle (Fig. 5a). These samples, as well as the much larger dataset of peridotites from the Decar area reported by Britten (2017; n=5670), have elevated $SiO_2$ concentrations that significantly exceed the modeled residual compositions (Figs. 5b-c), regardless of the assumed $H_2O$ content or oxygen fugacity. A systematic enrichment in $SiO_2$ was also observed in spinel-bearing harzburgite and dunite xenoliths from Kamchatka and Bismarck arcs by Bénard et al. (2017). The $SiO_2$-enrichment of the peridotite xenoliths from the western Pacific, as well as the high modal orthopyroxene abundance in mantle xenoliths from volcanic arcs (Parkinson and Pearce, 1998; Ionov, 2010) in general, were interpreted by Bénard et al. (2017) to be a defining feature of sub-arc mantle attributable to metasomatism of refractory mantle by slab-derived fluids and/or melts. Accordingly, the relatively high $SiO_2$ concentration and high modal proportion of orthopyroxene (17-30%) in harzburgites of the Decar area are interpreted to reflect a silica-enriched refractory mantle source. Given the apparent prevalence of such mantle under modern-day arcs, we propose that the Trembleur ultramafite developed in a supra-subduction zone setting.

### 6.2. Lithostratigraphic reassignment of outcrops in the Decar area using the geochemistry of volcanic suites

The geochemical data presented herein can be used to assign outcrops to lithostratigraphic units that are otherwise difficult to distinguish in the field. Two samples in the southwestern part

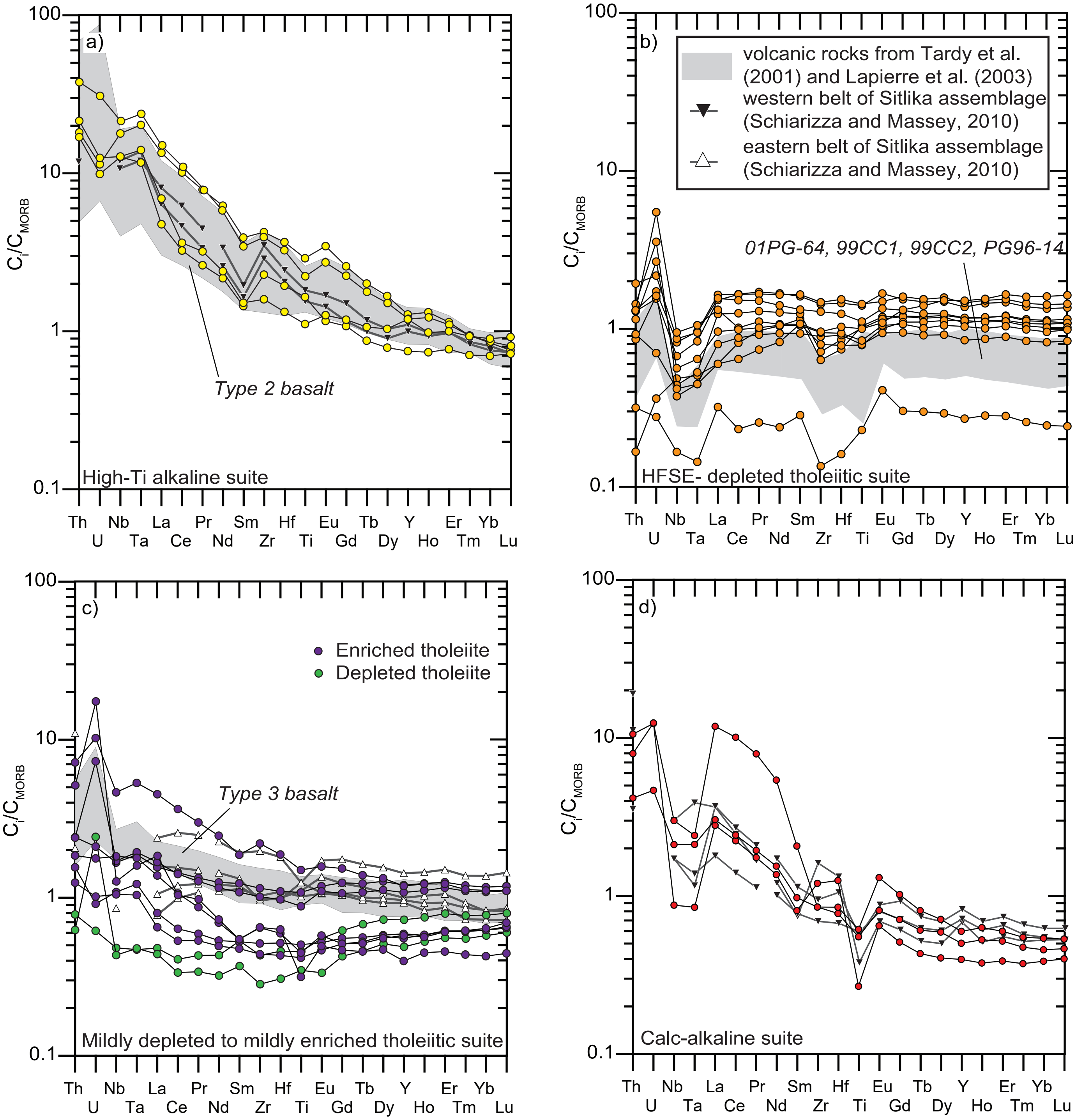


**Fig. 10.** MORB-normalized trace element patterns of the volcanic and shallow intrusive rocks from the Decar area. Normalization values from Sun and McDonough (1989). **a)** High-Ti alkaline suite compared to the Type 2 alkaline basalts from the Cache Creek terrane in central British Columbia (Lapierre et al., 2003) and Type 3 mafic volcanic rocks from the western belt of the Sitlika assemblage (Schiarizza and Massey, 2010). **b)** HFSE-depleted tholeiitic suite. Also shown is the compositional range of HFSE-depleted samples assigned to Type 1 N-MORB suite by Lapierre et al. (2003). **c)** Mildly depleted and mildly enriched tholeiitic suite. Shown for comparison are the Type 3 oceanic plateau basalts of Lapierre et al., 2003 and the Type 1 volcanics from the eastern belt of the Sitlika assemblage (Schiarizza and Massey, 2010). **d)** Calc-alkaline suite. Type 2 volcanic rocks from the western belt of the Sitlika assemblage (Schiarizza and Massey, 2010) are shown for comparison.

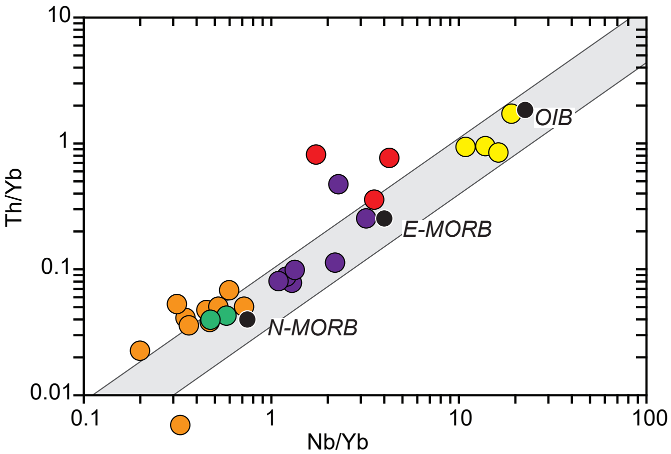


**Fig. 11.** Plot of Th/Yb vs. Nb/Yb after Pearce (2008), showing the wide compositional range of volcanic and shallow intrusive rocks of the Decar area and superimposed on the MORB-OIB array (grey field). The average compositions of N-MORB, E-MORB, and OIB are from Sun and McDonough (1989). Symbols as in Fig. 9.

of the Decar area (DMI17-3-3 and DMI17-3-5), which display HFSE-depleted tholeiitic suite geochemistry (Fig. 2; Table 2), redefine the geometry of the panel of rocks previously mapped as the Rubyrock igneous complex by Struik et al. (2007). A sample of schistose aphanitic metabasalt on the western edge of the study area (sample DMI17-2-15) is distinguished from the aforementioned samples by its enriched tholeiitic geochemical signature and indicates a previously unmapped (MacIntyre and Schiarizza, 1999; Struik et al., 2007) panel of volcanic rocks that lack a subduction signature in the westernmost part of the Decar area. Consequently, this panel is assigned to the Sowchea succession, necessitating a fault that separates the two geochemically distinct volcanic units.

### 6.3. Tectonic significance

Previous interpretations from the southern segment of the Cache Creek terrane (Tardy et al., 2001; Lapierre et al., 2003) emphasized the prevalence of volcanic rocks with alkaline to mildly depleted tholeiitic trace element patterns and argued that most volcanic rocks of the Cache Creek complex erupted in an oceanic plateau setting and were mantle plume derived. Our Sowchea succession data, which indicate an alkaline to mildly LREE-enriched to mildly LREE-depleted tholeiitic geochemistry (Figs. 2, 9-11), largely support this interpretation. However, our data also contradict this interpretation by identifying an HFSE-depleted volcanic component typical of island arc tholeiite (IAT) magmas in the Rubyrock igneous complex (Figs. 9-10). We conclude that the Cache Creek terrane in central British Columbia is not merely a tectonic amalgamation of mantle plume-related oceanic plateau rocks and suggest that, based on our results, the contrasting geochemical signatures in the southern segment of the Cache Creek terrane (e.g., Type 2 and 3 volcanic rocks, western belt of Sitlika assemblage of Schiarizza and MacIntyre, 2010) warrant re-evaluation. Our results support the conclusion of McGoldrick et al. (2017) who interpreted that supracrustal volcanic and plutonic rocks in the northern segment of the Cache Creek terrane mainly represent the product of an intraoceanic arc, with only a minor intraplate oceanic component.

The IAT crustal affinity of the Rubyrock igneous complex and the anomalous $SiO_2$ enrichment of the adjacent mantle harzburgite (Trembleur ultramafite) are consistent with the view that the two units represent crustal and mantle segments of a dismembered supra-subduction ophiolitic complex (Schiarizza and MacIntyre, 1999; Struik et al., 2001; Britten, 2017). This supra-subduction zone setting is incompatible with the intraoceanic (OIB-E-MORB-N-MORB, Fig. 11) basalt geochemistry of volcanic rocks in the Sowchea succession. The oceanic plateau affinity of the volcanic rocks and associated carbonate rocks, cherts, and argillites of the Sowchea succession suggests that these rocks formed in an unrelated tectonic setting and that they were likely sliced off the subducting 'Cache Creek ocean' during its Jurassic closure (Nelson et al., 2013). Therefore, we propose that the term 'Cache Creek complex' be restricted to include only those lower plate rocks that lack a supra-subduction zone signature (cf., Struik et al., 2001). Future work will evaluate links between units formed on the upper plate of the convergent margin such as the Trembleur ultramafite and Rubyrock igneous complex in the Decar area, and the Kutcho-Sitlika-Venables arc (Permo-Triassic, e.g., Logan and Mihalynuk, 2014) farther north in the Cache Creek terrane.

### 7. Summary

The geochemistry of variably serpentinized and carbonate-altered mantle tectonite and greenschist- to amphibolite-facies mafic to intermediate igneous rocks from the Decar area in central British Columbia provide new evidence of two distinct tectono-stratigraphic assemblages in the Cache Creek complex. Volcanic and intrusive rocks with alkaline to mildly LREE-depleted tholeiitic chemistry and associated limestone, chert, and argillite comprising the Sowchea succession (Upper Pennsylvanian to Lower Jurassic) may have been deposited in an oceanic plateau setting (Tardy et al., 2001; Struik et al., 2001; Lapierre et al., 2003) and resided on the lower plate during the Jurassic closure of the Cache Creek ocean. In contrast, the high-$SiO_2$ refractory mantle peridotite of the Trembleur ultramafite and the overlying supracrustal rocks with a predominant island arc tholeiite component originated in an upper plate, suprasubduction zone setting. These tectono-stratigraphic packages were likely juxtaposed and interleaved during the collision between the Cache Creek terrane and Stikinia in the Late Jurassic (Struik et al., 2001; English and Johnston, 2005).

### Acknowledgments

We thank Tl'azt'en Nation and Chief Bev John for hospitality and FPX Nickel Corp. and Ron Britten for sharing their geochemical and geophysical data with us. Alan King (Geoscience North) is thanked for processing the aeromagnetic

survey data provided by FPX Nickel Corp. We thank A. Zagorevski and J. Scoates for their helpful and constructive reviews.

## References cited

Armstrong, J.E., 1949. Fort St. James map-area, Cassiar and Coast Districts, British Columbia. Geological Survey of Canada, Memoir 252. 210 p.

Bénard, A., Arculus, R.J., Nebel, O., Ionov, D.A., and McAlpine, S.R.B., 2017. Silica-enriched mantle sources of subalkaline picrite-boninite-andesite island arc magmas. Geochimica et Cosmochimica Acta, 199, 287-303.

Boudier, F., and Nicolas, A., 1985. Harzburgite and lherzolite subtypes in ophiolitic and oceanic environments. Earth and Planetary Science Letters, 76, 84-92.

Britten, R., 2017. Regional metallogeny and genesis of a new deposit type-disseminated awaruite ($Ni_3Fe$) mineralization hosted in the Cache Creek terrane. Economic Geology, 112, 517-550.

Canil, D., Johnston, S.T., and Mihalynuk, M., 2006. Mantle redox in Cordilleran ophiolites as a record of oxygen fugacity during partial melting and the lifetime of mantle lithosphere. Earth and Planetary Science Letters, 248, 91-102.

Carlson, R.L., and Miller, D.J., 2003. Mantle wedge water contents estimated from seismic velocities in partially serpentinized peridotites. Geophysical Research Letters, 30, 1250-1253.

Childe, F.C., and Schiarizza, P., 1997. U-Pb geochronology, geochemistry and Nd isotopic systematics of the Sitlika assemblage, central British Columbia. In: Geological Fieldwork 1996, British Columbia Ministry of Energy, Mines and Petroleum Resources, Paper 1997-1, pp. 69-77.

Childe, F.C., and Thompson, J.F.H., 1997. Geological setting, U-Pb geochronology, and radiogenic isotopic characteristics of the Permo-Triassic Kutcho assemblage, north-central British Columbia. Canadian Journal of Earth Sciences, 34, 1310-1324.

Cordey, F., Gordey, S.P., and Orchard, M.J., 1991. New biostratigraphic data from the northern Cache Creek terrane, Teslin map area, southern Yukon. In: Current research part E. Geological Survey of Canada, pp. 67-76.

Elliot, A.J.M., 1975. Geology and metamorphism of the Mitchell Mountains ultramafite, Fort St. James map area, British Columbia. Unpublished M.Sc. thesis, The University of British Columbia, Vancouver, B.C., 129 p.

English, J.M., and Johnston, S.T., 2005. Collisional orogenesis in the northern Canadian Cordillera: Implications for Cordilleran crustal structure, ophiolite emplacement, continental growth, and the terrane hypothesis. Earth and Planetary Science Letters, 232, 333-344.

English, J.M., Mihalynuk, M.G., and Johnston, S.T., 2010. Geochemistry of the northern Cache Creek terrane and implications for accretionary processes in the Canadian Cordillera. Canadian Journal of Earth Sciences, 47, 13-34.

Francis, D., and Minarik, W., 2008. Aluminum-dependent trace element partitioning in clinopyroxene. Contributions to Minaralogy and Petrology, 156, 439-451.

Ghiorso, M. S., Hirschmann, M.M., Reiners, P.W., and Kress, V.C., 2002. The pMELTS: A revision of MELTS for improved calculation of phase relations and major element partitioning related to partial melting of the mantle to 3GPa. Geochemistry, Geophysics, Geosystems, 3, 1030. doi: 10.1029/2001GC000217.

Golding, M.L., 2018. Heterogeneity of conodont faunas in the Cache Creek Terrane, Canada; significance for tectonic reconstructions of the North American Cordillera. Palaeogeography, Palaeoclimatology, Palaeoecology, 506, 208-216.

Golding, M.L., Orchard, M.J., and Zagorevski, A., 2016. Microfossils from the Cache Creek Complex in northern British Columbia and southern Yukon. Geological Survey of Canada, Open File 8033, 25 p.

Grundy, R., 2018. Melting and cooling histories of two upper mantle massifs in the Cache Creek Terrane, central British Columbia. Unpublished B.Sc. Thesis, University of Victoria, 60 p.

Hansen, L.D., Dipple, G.M., Gordon, T.M., and Kellett, D.A., 2005. Carbonated serpentinite (listwanite) at Atlin, British Columbia: a geological analogue to carbon dioxide sequestration. Canadian Mineralogist, 43, 225-239.

Harte, B., 1977. Rock nomenclature with particular relation to deformation and recrystallisation textures in olivine-bearing xenoliths. Geology, 85, 279-288.

Hellebrand, E., Snow, J.E., Dick, H.J.B., and Hofmann, A.W., 2001. Coupled major and trace elements as indicators of melting in mid-ocean ridge peridotites. Nature, 410, 677-681.

Ionov, D.A., 2010. Petrology of mantle wedge lithosphere: new data on supra-subduction zone peridotite xenoliths from the andesitic Avacha volcano, Kamchatka. Journal of Petrology, 51, 327-361.

Jensen, L.S., 1976. A new cation plot for classifying subalkalic volcanic rocks. Ontario Ministry of Natural Resources, Division of Mines, Miscellaneous Paper 66, 22 p.

Lapierre, H., Bosch, D., Tardy, M., and Struik, L.C., 2003. Late Paleozoic and Triassic plume-derived magmas in the Canadian Cordillera played a key role in continental crust growth. Chemical Geology, 201, 55-89.

LeMaitre, R.W., 2005. Igneous Rocks: A Classification and Glossary of Terms. In: R.W. LeMaitre (Ed.), Recommendations of the International Union of Geological Sciences Subcommission on the Systematics of Igneous Rocks (2nd edition). Cambridge University Press, 236 p.

Logan, J.M., and Mihalynuk, M.G., 2014. Tectonic controls on early Mesozoic paired alkaline porphyry deposit belts (Cu-Au±Ag-Pt-Pd-Mo) within the Canadian Cordillera. Economic Geology, 109, 827-858.

MacIntyre, D.M., and Schiarizza, P., 1999. Bedrock geology, Cunningham Lake (93K/11, 12, 13, 14). British Columbia Ministry of Energy and Mines, British Columbia Geological Survey Open File 1999-11; scale 1:100,000.

McGoldrick, S., Zagorevski, A., and Canil, D., 2017. Geochemistry of volcanic and plutonic rocks from the Nahlin ophiolite with implications for a Permo-Triassic arc in the Cache Creek terrane, northwestern British Columbia. Canadian Journal of Earth Sciences, 54, 1214-1227.

McGoldrick, S., Canil, D., and Zagorevski, A., 2018. Contrasting thermal histories for segments of mantle lithosphere in the Nahlin ophiolite, British Columbia, Canada. Contributions to Mineralogy and Petrology, 173:25, 17 p.

Maurice, C., Francis, D., and Madore, L., 2003. Constraints on early Archean crustal extraction and tholeiitic-komatiitic volcanism in greenstone belts of the Northern Superior Province. Canadian Journal of Earth Sciences, 40, 431-445.

Mercier, J.C.C., and Nicolas, A., 1975. Textures and fabrics of upper-mantle peridotites as illustrated by xenoliths from basalts. Journal of Petrology, 16, 454-487.

Milidragovic, D., Grundy, R., and Schiarizza, P., 2018a. Geology of the Decar area north of Trembleur Lake, NTS 93K/14. In: Geological Fieldwork 2017, British Columbia Ministry of Energy, Mines and Petroleum Resources, British Columbia Geological Survey Paper 2018-1, pp. 129-142.

Milidragovic, D., Zagorevski, A., Weis, D., Joyce, N., and Chapman, J.B., 2018b. Picrite "intelligence" from the Middle-Late Triassic Stikine arc: Composition of mantle wedge asthenosphere. Lithos, 308-309, 446-461.

Monger, J.W.H., 1975. Upper Paleozoic rocks of the Atlin terrane, northwestern British Columbia and south-central Yukon. Geological Survey of Canada, Paper 74-47, 63 p.

Monger, J.W.H., 1977. Upper Paleozoic rocks of the western Canadian Cordillera and their bearing on Cordilleran evolution. Canadian Journal of Earth Sciences, 14, 1832-1859.
Monger, J.W.H., and Ross, C.A., 1971. Distribution of fusulinaceans in the western Canadian Cordillera. Canadian Journal of Earth Sciences, 8, 259-278.
Mihalynuk, M.G., Nelson, J.L., and Diakow, L.J., 1994. Cache Creek terrane entrapment: Oroclinal paradox within the Canadian Cordillera. Tectonics, 13, 575-595.
Nelson, J.L., Colpron, M., and Israel, S., 2013. The Cordillera of British Columbia, Yukon, and Alaska: Tectonics and metallogeny. In: Colpron, M., Bissing, T., Rusk, B.G., and Thompson, J.F.H., (Eds.), Tectonics, Metallogeny, and Discovery: The North American Cordillera and Similar Accretionary Settings. Society of Economic Geologists, Special Publication 17, pp. 53-109.
Orchard, M.J., Cordey, F., Rui, L., Bamber, E.W., Mamet, B., Struik, L.C., Sano, H., and Taylor, H.J., 2001. Biostratigraphic and biogeographic constraints on the Carboniferous to Jurassic Cache Creek terrane in central British Columbia. Canadian Journal of Earth Sciences, 38, 551-578.
Palme, H., and O'Neill, H.St.C., 2003. Cosmochemical estimates of mantle composition. In: Holland, H.D., Turekian, K.K., and Davis, A.M. (Eds.), Treatise on Geochemistry, Vol. 2. Elsevier, Amsterdam, The Netherlands, pp. 1-38.
Parkinson I.J., and Pearce J.A., 1998. Peridotites from the Izu-Bonin-Mariana forearc (ODP leg 125): evidence for mantle melting and melt-mantle interaction in a supra-subduction zone setting. Journal of Petrology, 39, 1577-1618.
Paterson, I.A., 1977. The geology and evolution of the Pinchi Fault Zone at Pinchi Lake, central British Columbia. Canadian Journal of Earth Sciences, 14, 1324-1342.
Pearce, J.A., 1996. A user's guide to basalt discrimination diagrams. In: Wyman D.A., (Ed.), Trace Element Geochemistry of Volcanic Rocks: Applications for Massive Sulphide Exploration. Geological Association of Canada, Short Course Notes, 12, pp. 79-113.
Pearce, J.A., 2008. Geochemical fingerprinting of oceanic basalts with applications to ophiolite classification and the search for Archean oceanic crust. Lithos, 100, 14-48.
Salters, V.J., and Stracke, A., 2004. Composition of the depleted mantle. Geochemistry, Geophysics, geosystems, 5, Q05B07, doi:10.1029/2003GC000597.
Schiarizza, P., 2012. Geology of the Kutcho Assemblage between the Kehlechoa and Tucho Rivers, Northern British Columbia (NTS 104I/01, 02). In: Geological Fieldwork 2011, British Columbia Ministry of Energy and Mines, British Columbia Geological Survey Paper 2012-1, pp. 75-98.
Schiarizza, P., and MacIntyre, D.G., 1999. Geology of the Babine Lake-Takla Lake area, central British Columbia (93K/11, 12, 13, 14; 93N/3, 4, 5, 6). In: Geological Fieldwork 1998, British Columbia Ministry of Energy and Mines, British Columbia Geological Survey Paper 1999-1, pp. 33-68.
Schiarizza, P., and Massey, N.W.D., 2010. Geochemistry of volcanic and plutonic rocks of the Sitlika assemblage, Takla Lake area, central British Columbia (NTS 093N/04, 05, 12, 13). In: Geological Fieldwork 2009, British Columbia Ministry of Energy, Mines and Petroleum Resources, British Columbia Geological Survey Paper 2010-1, pp. 55-67.
Smith, P.M., and Asimow, P.D., 2005. Adiabat_1ph: A new public front- end to the MELTS, pMELTS, and pHMELTS models. Geochemistry, Geophysics, Geosystems, 6, Q02004, doi:10.1029/2004GC000816.
Struik, L., Schiarizza, P., Orchard, M., Cordey, F., Sano, H., MacIntyre, D.G., Lapierre, H., and Tardy, M., 2001. Imbricate architecture of the upper Paleozoic to Jurassic oceanic Cache Creek terrane, central British Columbia. Canadian Journal of Earth Sciences, 38, 495-514.
Struik, L.C., MacIntyre, D.G., and Williams, S.P., 2007. Nechako NATMAP project: A digital suite of geoscience information for central British Columbia. Geological Survey of Canada Open File 5623.
Sun, S., and McDonough, W.F., 1989. Chemical and isotopic systematics of oceanic basalts: implications for mantle composition and processes. In: Saunders, A.D., and Norry, M.J. (Eds.), Magmatism in the Ocean Basins, Geological Society of London, Special Publication 42, 313-345.
Tardy, M., Lapierre, H., Struik, L.C., Bosch, D., and Brunet, P., 2001. The influence of mantle plume in the genesis of the Cache Creek oceanic igneous rocks: implications for the geodynamic evolution of the inner accreted terranes of the Canadian Cordillera. Canadian Journal of Earth Sciences, 38, 515-534.
Voordouw, R.J., and Simpson, R.G., 2018. 2018 technical (N.I. 43-101) report on the Decar nickel-iron alloy property. Independent technical report, 81 p. https://fpxnickel.com/wp-content/uploads/2018/04/2018_Decar_NI43101.pdf (Last accessed Dec.4th, 2018).
Warren, J.M., 2016. Global variation in abyssal peridotite compositions. Lithos, 248-251, 193-219.
Workman, R.K., and Hart, S.R., 2005. Major and trace element composition of the depleted MORB mantle (DMM). Earth and Planetary Science Letters, 231, 53-72.

# Geology of the Latham and Pallen Creek area, northwestern British Columbia: Distinguishing the Tsaybahe group, Stuhini Group, and Hazelton Group, and the onset of Triassic arc volcanism in northern Stikinia

Bram I. van Straaten[1, a] and Curran Wearmouth[1]

[1] British Columbia Geological Survey, Ministry of Energy, Mines and Petroleum Resources, Victoria, BC, V8W 9N3
[a] corresponding author: Bram.vanStraaten@gov.bc.ca

Recommended citation: van Straaten, B.I., and Wearmouth, C., 2019. Geology of the Latham and Pallen Creek area, northwestern British Columbia: Distinguishing the Tsaybahe group, Stuhini Group, and Hazelton Group, and the onset of Triassic arc volcanism in northern Stikinia. In: Geological Fieldwork 2018, British Columbia Ministry of Energy, Mines and Petroleum Resources, British Columbia Geological Survey Paper 2019-01, pp. 79-96.

**Abstract**

The oldest units in the Latham Creek and Pallen Creek area are penetratively deformed meta-sedimentary and volcanic rocks and limestones of the Stikine assemblage (upper Paleozoic). These rocks are overlain (likely unconformably) by a volcano-sedimentary sequence informally referred to as the Tsaybahe group (Lower-Middle Triassic), which is succeeded by the Stuhini Group (Upper Triassic). We subdivide the Tsaybahe group into a sedimentary unit of fine-grained siliciclastic rocks and minor chert, and a volcanic unit of monomictic tuff breccia with plagioclase-augite-phyric volcanic clasts. Tsaybahe volcanic rocks appear texturally similar to the overlying Stuhini Group, but are separated based on their stratigraphic position atop of the Stikine assemblage, rare Middle Triassic biostratigraphic ages, low magnetic susceptibility, and low response on regional aeromagnetic surveys. Stuhini Group volcanic rocks include massive monomictic tuff breccia and lapilli-tuff with augite-plagioclase-phyric volcanic clasts, have a high magnetic susceptibility, and display a high and variable response on regional aeromagnetic surveys. Triassic and older stratified rocks are cut by Late Triassic stocks and plutons ranging from ultramafic to gabbro, hornblende-rich quartz diorite and hornblende quartz monzonite in composition. Triassic units generally lack penetrative tectonic fabrics and are deformed into map-scale open folds. An outlier of volcano-sedimentary rocks assigned to the upper part of the Hazelton Group is inferred to unconformably overlie the Triassic rocks. The succession (~500 m thick) includes two sedimentary units that are overlain by a maroon volcanic unit, which is capped by a felsic volcanic unit. Based on lithological and stratigraphic criteria, the sedimentary units are assigned to the Spatsizi Formation and the volcanic units to the Horn Mountain Formation. Three Middle Jurassic plutons are exposed in the area, ranging in composition from biotite-hornblende quartz diorite to biotite monzogranite. Developed within or adjacent to these plutons are zones of alteration and mineralization containing locally elevated copper, gold, silver and/or molybdenum in fractures, veins, skarns, and gossans.

Augite-phyric mafic volcanic units in each of the Tsaybahe group, Stuhini Group, and Horn Mountain Formation, although temporally distinct, are texturally similar. Compared to widespread exposures of mafic volcanic rocks of the Stuhini Group in northern Stikinia, occurrences of the Tsaybahe group and its correlatives are rare. However, owing to a lack of age constraints, we consider that Tsaybahe group exposures may have been included in the Stuhini Group and suggest that the unit is more extensive than currently recognized. The Tsaybahe group may represent nascent Middle Triassic arc volcanism before widespread Upper Triassic Stuhini arc activity.

**Keywords:** Stikine assemblage, Tsaybahe group, Stuhini Group, Spatsizi Formation, Horn Mountain Formation, Hazelton Group, Latham Creek pluton, Cake Hill pluton, Three Sisters pluton, Pallen Creek pluton, Tanzilla pluton, Hotailuh batholith, Paleozoic, Permian, Triassic, Jurassic, Stikine terrane.

## 1. Introduction

Mapping near Dease Lake (Figs. 1, 2) has highlighted temporally distinct, but texturally similar augite-phyric mafic volcanic units in each of the Tsaybahe group (Lower-Middle Triassic; Read, 1983; 1984), Stuhini Group (Upper Triassic; Logan et al., 2012a) and Horn Mountain Formation (Lower to Middle Jurassic; van Straaten and Nelson, 2016; van Straaten and Gibson, 2017; van Straaten and Bichlmaier, 2018a). Continuing as part of a multi-year program, two field teams spent six weeks mapping at a 1:20,000 scale in the Latham Creek and Pallen Creek area, south of Dease Lake (Fig. 2; NTS 104J/01 and parts of 104I/04, 05; 104J/08). Because access was limited by wildfires, the geology of the south central and southwestern parts of the study area (Fig. 2) is interpreted from previous mapping by Read (1983; 1984) and Gabrielse (1998), and an aeromagnetic survey by Aeroquest Airborne (2012).

Our study confirms the presence of Read's (1984) Tsaybahe group (Lower-Middle Triassic). It can be distinguished from younger units based on its stratigraphic position, presence of a lithologically characteristic sedimentary unit, presence of Lower-Middle Triassic microfossils (Read, 1983; 1984; Gabrielse, 1998; Golding et al., 2017), and low magnetic susceptibility values and a low response on Aeroquest Airborne's (2012) aeromagnetic survey. We use these criteria to

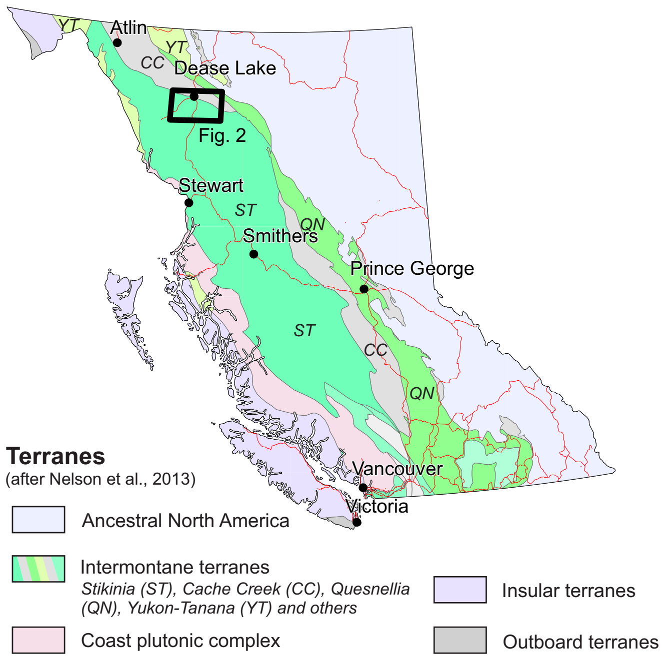


**Fig. 1.** Location of study area, modified after Nelson et al. (2013).

reinterpret Triassic stratigraphic assignments in the study area and consider if the Tsaybahe group and its equivalents are more extensive in northern Stikinia than previously appreciated.

## 2. Geological setting

The study area is in the Intermontane belt of the Canadian Cordillera, near the northeastern margin of the Stikine terrane (Stikinia; Fig. 1). Stikinia is a multi-episodic volcanic island arc terrane that accreted to ancestral North America during the Middle Jurassic (Nelson and Mihalynuk, 1993; Mihalynuk et al., 1994; Evenchick et al., 2007; Nelson et al., 2013). Volcanic and sedimentary rocks of the Stikine assemblage (Devonian to Permian), basement to Stikinia, are overlain by volcanic and related sedimentary rocks of the Stuhini Group (Triassic) and the Hazelton Group (Lower to Middle Jurassic; Tipper and Richards, 1976; Marsden and Thorkelson, 1992). Also in the Intermontane belt, the Quesnel terrane (Quesnellia) is a volcanic island arc with a similar Devonian to Early Jurassic history. The two volcanic arcs are separated by the Cache Creek terrane (Fig. 1), an accretionary complex of oceanic crustal rocks, primitive arc ophiolites, pelagic rocks, carbonate rocks, and blueschists. The northeastern margin of Stikinia and adjacent Cache Creek terrane are covered by Lower Jurassic siliciclastic rocks of the Whitehorse trough (Colpron et al., 2015). Accretion of Stikinia to the Cache Creek terrane, Quesnellia, and ancestral North America is recorded by deposition of Bowser Lake Group siliciclastic rocks (Middle Jurassic) in a foreland basin atop Stikinia (Evenchick et al., 2007). Combined, Stikinia and Quesnellia host most of the porphyry copper deposits in the Canadian Cordillera (Logan and Mihalynuk, 2014).

## 3. Lithostratigraphic units

In the study area, Paleozoic to Middle Jurassic lithostratigraphic units of Stikinia are overlain by Cretaceous and younger overlap units (Figs. 2, 3; Table 1). The oldest rocks are part of the Stikine assemblage (Devonian-Permian). These basement rocks are overlain by three temporally distinct, but texturally similar, augite-phyric mafic volcanic and related sedimentary successions. The oldest succession, informally referred to as the Tsaybahe group by Read (1984), is Early-Middle Triassic, and is recognized only locally in northern Stikinia. The second succession comprises Late Triassic mafic volcanic and sedimentary rocks of the Stuhini Group. These rocks are widespread throughout northern Stikinia. In the northwestern part of the map area is an outlier of sedimentary and volcanic rocks of the Spatsizi and Horn Mountain formations (upper part of the Hazelton Group) as defined by van Straaten and Nelson (2016), van Straaten and Gibson (2017) and van Straaten and Bichlmaier (2018a).

Within the study area, low magnetic susceptibility values (Fig. 4) and a low response on Aeroquest Airborne's (2012) aeromagnetic survey characterize all Triassic rocks lying immediately above the Stikine assemblage, all units containing accurately located Lower-Middle Triassic fossil collections (Read, 1983; Read, 1984; Gabrielse, 1998; Golding et al., 2017) and all Triassic fine-grained sedimentary rock units. In contrast, high magnetic susceptibility values and a high and variable aeromagnetic response characterize stratigraphically higher Triassic strata that contain rare Upper Triassic conodonts (Read, 1984; Gabrielse, 1998; Logan et al., 2012b; Golding et al., 2017). We used this observation to reinterpret Triassic stratigraphic assignments east of the Plateau fault (Fig. 2).

In the following we use classifications for sedimentary rocks from Hallsworth and Knox, (1999) and for igneous rocks from Gillespie and Styles (1999).

### 3.1. Stikinia

#### 3.1.1. Stikine assemblage (Devonian-Permian)

Stikine assemblage rocks are exposed in the northwestern and southeastern parts of the map area (Fig. 2); observations presented herein are based mainly on work in the northwestern part. We recognize a meta-sedimentary unit (DPS*s*), a volcanic unit (DPS*v*) and a limestone unit (DPS*ls*; Table 1). These units are folded and generally show a well-developed phyllitic foliation. Although way-up indicators were not observed, the limestone unit seems to overlie the meta-sedimentary unit (see Section 5.1.). The volcanic unit forms a lens in the meta-sedimentary unit (Figs. 2, 3). Contacts between units are not exposed. Direct age constraints are only available for the limestone unit; it contains Early-Middle Permian fossils (Table 1).

#### 3.1.2. Tsaybahe group (Lower-Middle Triassic)

Based on mapping near the Stikine River that overlaps with our study area (Fig. 2b), Read (1984) introduced the Tsaybahe group as an informal name for a section of Lower-Middle

**Table 1.** Summary of volcano-sedimentary units on Stikinia, excluding overlap assemblages. Mineral abbreviations after Kretz (1983).

| Age | Unit | | Description |
|---|---|---|---|
| Lower-Middle Jurassic | upper part of Hazelton Gp. | Horn Mnt. Fm. | **Middle felsic volcanic rocks (lmJHM*Mvf*).** Massive to locally crudely stratified felsic tuff, lapilli-tuff and minor tuff breccia; matrix-supported to lesser clast-supported. Generally contains angular to very angular light-coloured aphanitic to Pl-phyric volcanic clasts, rare flow-banded clasts, very rare quartz-phyric and spherulitic clasts. Unit includes lesser coherent Pl-phyric, commonly flow-banded, rhyolitic rock with 5-20% subhedral equant to lath-shaped Pl (0.3-1.5 mm). Fairly resistant, light-medium grey weathering. |
| | | | **Middle maroon volcanic rocks (lmJHM*Mv*).** Generally crudely stratified maroon volcanic breccia, tuff breccia, lapillistone, lapilli-tuff and tuff; matrix- to clast-supported. Contains generally subangular volcanic clasts with 20% euhedral lath-shaped to equant Pl (1-3 mm) and 15% euhedral equant Aug (1-3 mm), typically set in a Pl and Aug crystal and fine ash matrix. Aug-Pl and Pl-phyric coherent rocks; may represent flows or subvolcanic intrusions. Local monomictic clast-supported volcanic breccia with a matrix-deficient open framework (likely flow-margin autobreccia). One internally laminated limestone bed observed. Resistant, dark grey to maroonish weathering. |
| | | Spatsizi Fm. | **Volcaniclastic sandstone (lmJSP*sv*).** Medium- to very thickly bedded, medium-grained (lesser fine-, rare coarse-grained) volcaniclastic feldspathic arenite with angular and lesser euhedral Pl and Aug grains. Interstratified with siltstone and fine-grained feldspathic wacke. Lesser medium-grained calcareous feldspathic arenite. Minor crystal tuff with subordinate Aug-Pl-phyric volcanic clasts. Very rare limestone and volcaniclastic feldspathic arenite with limestone pebbles. Fairly recessive, light-medium grey weathering. |
| | | | **Sedimentary rocks (lmJSP*s*).** Laminated to thinly bedded siltstone, very fine- to medium-grained sandstone. Strongly silicified with abundant disseminated pyrite. Grades upward to interbedded volcaniclastic siltstone, volcaniclastic sandstone, tuff, crystal tuff, and lesser lapilli-tuff with abundant euhedral Pl, minor altered mafic crystals and up to 15% aphanitic to Pl-phyric grey to green volcanic clasts. Fairly recessive, rusty weathering. |
| Upper Triassic | Stuhini Gp. | | **Volcanic rocks (uTrST*vm*).** Monomictic tuff breccia, lapilli-tuff, lesser volcanic breccia and lapillistone; massive to very rarely crudely thin to very thick bedded, clast- to matrix-supported. Subangular clasts contain 20-50% euhedral platy Pl (aspect ratio 1:4:4, 0.2-2 mm) and 15-40% euhedral equant Aug (0.5-3 mm) and 0-10% round to irregular-shaped amygdules (0.5-3 mm) set in a Pl and Aug crystal and fine ash matrix. Aug-Pl-phyric coherent rocks contain 15-30% subhedral equant Aug (0.5-3.0 mm) and 15-30% subhedral equant Pl (0.3-2 mm), and may represent subvolcanic intrusions or flows. Mean magnetic susceptibility $23 \times 10^{-3}$ SI units. Resistant, dark grey weathering. Contains early Carnian conodonts (Read, 1984; Golding et al., 2017). |
| | | | **Sedimentary rocks (uTrST*sv*).** Laminated to medium-bedded interstratified fine- to medium-grained (lesser very fine-, rare coarse-grained) volcaniclastic feldspathic arenite, lesser feldspathic wacke and siltstone. Sandstone is generally planar- to cross- to trough cross-stratified, poorly sorted, and contains 80% angular to subangular Pl, 20% equant mafic grains. Moderately recessive, dark grey to orangey grey weathering. Contains late Carnian conodonts in adjacent map area to the north (Logan et al., 2012b; Golding et al., 2017). |
| Lower-Middle Triassic | Tsaybahe gp. | | **Volcanic rocks (lmTrT*vm*).** Massive monomictic tuff breccia and lesser lapilli-tuff; clast- to matrix-supported. Contains subangular to subround, lesser angular and minor irregular-shaped volcanic clasts with 15-35% euhedral rectangular Pl (0.2-1.5 mm), 15-32% euhedral equant Aug (0.5-7 mm) and commonly 10-20% round-ovoid amygdules (0.5-2.5 mm) in an Aug and Pl crystal and fine ash matrix. Mean magnetic susceptibility $0.88 \times 10^{-3}$ SI units. Resistant, dark grey weathering. |
| | | | **Sedimentary rocks (lmTrT*s*).** Laminated to thinly-bedded interstratified dark grey argillite, siliceous argillite, siltstone, dark-medium grey, greenish grey very fine- to fine-grained (rare medium-grained) sandstone and minor dark grey, black, green chert. Sandstone is generally planar- to ripple cross-stratified, contains predominantly Pl and lesser mafic grains, and varies from feldspathic arenite, feldspathic wacke to lesser lithic arenite. Commonly cut by Pl-Aug-phyric sills and dikes. Recessive, dark grey to locally rusty weathering. Contains Early-Middle Triassic fossils (Read, 1983; 1984; Gabrielse, 1998; Golding et al., 2017). |
| Devonian-Permian | Stikine assemblage | | **Limestone (DPS*ls*).** Pale, medium to dark grey and rare rusty orange laminated lime mudstone and thin to medium bedded fossiliferous wackestone and packstone. Planar, wavey planar to lensoidal stratified. Commonly interstratified with medium to dark grey chert laminae, cherty limestone laminae and chert beds. Commonly foliated, with 0.5-1 mm pressure solution cleavage and local boudinaged chert beds. Locally slightly fetid. Resistant, light grey to yellowish-grey weathering. Contains Early-Middle Permian and Artinskian-Kungurian fossils (Read, 1983; Gabrielse, 1998; Logan et al., 2012b; Golding et al., 2017). |
| | | | **Volcanic rocks (DPS*v*).** Grey, greenish grey to maroon tuff, crystal tuff and lapillistone. Contains 3-60% euhedral Pl (0.1-4 mm), up to 5% altered mafic crystals (0.5 mm), and 2-70% pale greenish grey, maroon, brick red, medium to dark grey and medium green aphanitic to microphenocrystic volcanic clasts (0.1-15 mm). Generally has a well-developed phyllitic foliation. Fairly recessive, grey weathering. |
| | | | **Meta-sedimentary rocks (DPS*s*).** Pale, medium to dark grey, minor pale to medium green, rare orange, rare maroonish, very fine- to fine-grained (rare medium-grained) meta-sandstone and phyllite. Minor meta-volcaniclastic sandstone or tuff with euhedral Pl grains and dark green possible mafic grains. Rare medium grey laminated to massive recrystallized limestone beds or boudins. Generally has a well-developed phyllitic foliation. Rare dark grey to black argillite, siliceous argillite, siltstone and chert. Recessive, grey weathering. |

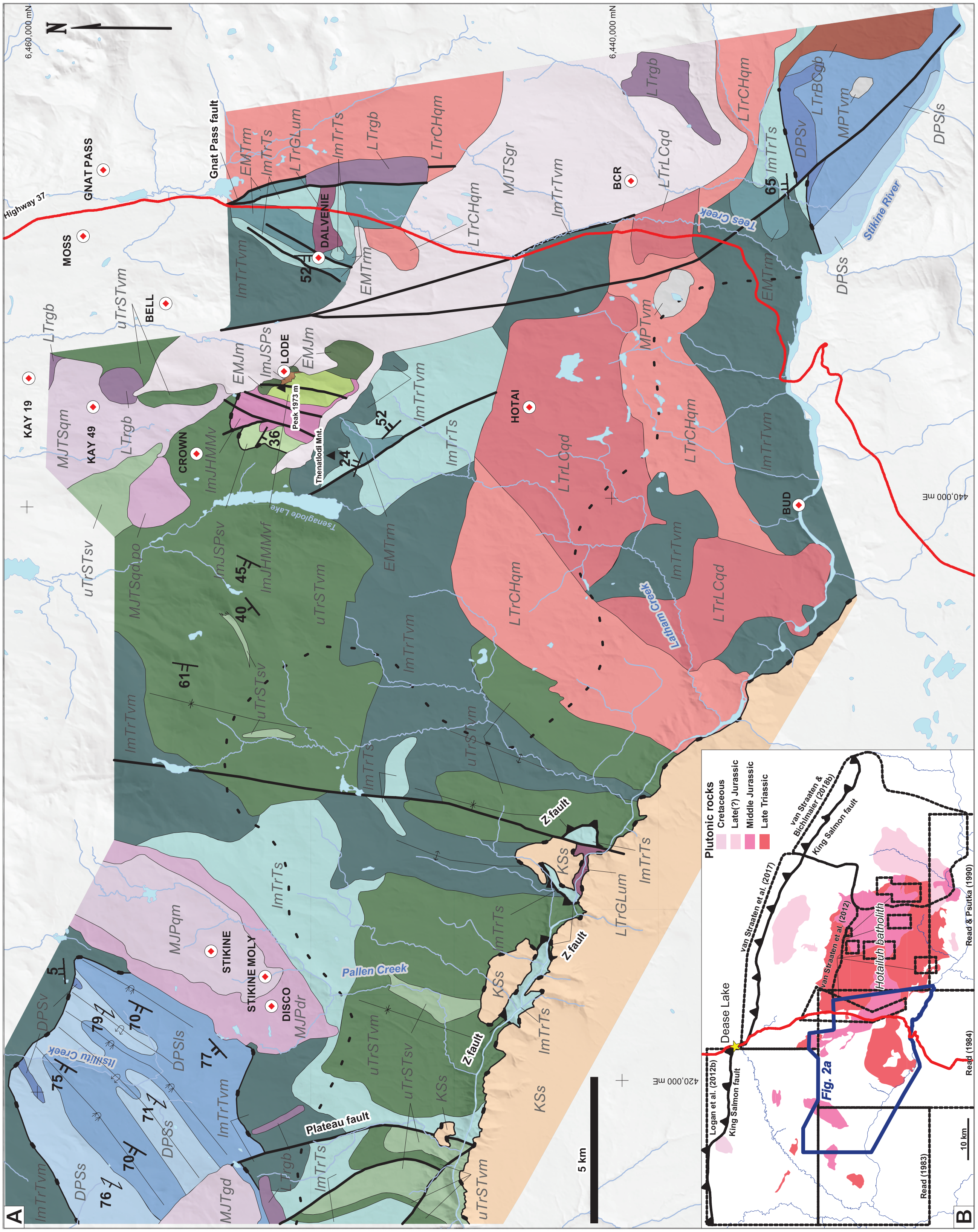


**Fig. 2. a)** Generalized geology of the Latham Creek and Pallen Creek area, incorporating data from Read (1983, 1984), Gabrielse (1998) and Logan et al. (2012b). The study area is mainly below treeline, with only 5-15% outcrop; exposure is better in alpine areas (~50%). **b)** Location of the Latham Creek and Pallen Creek area in the context of previous mapping in the Dease Lake region.

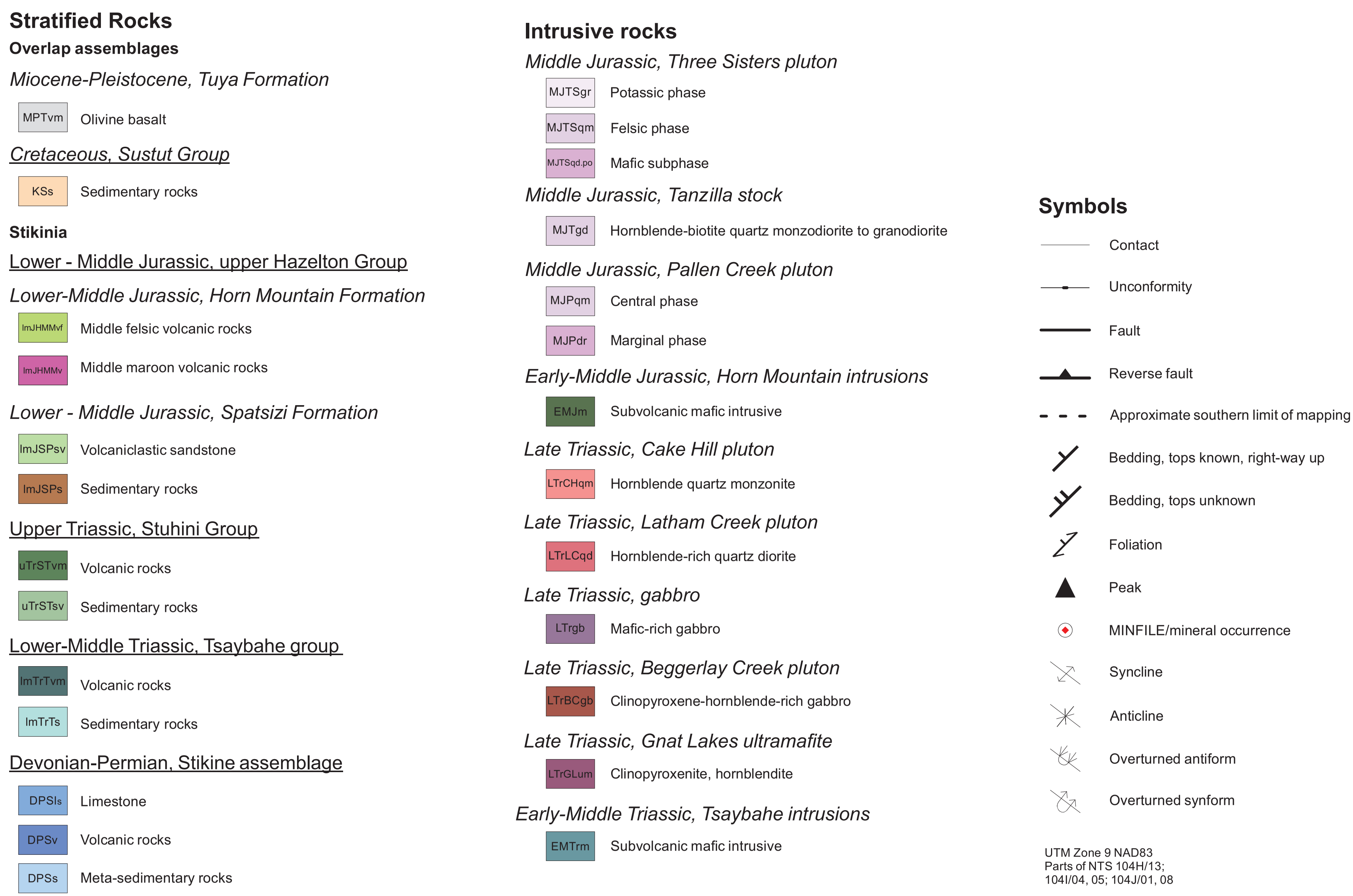


**Fig. 2.** Continued.

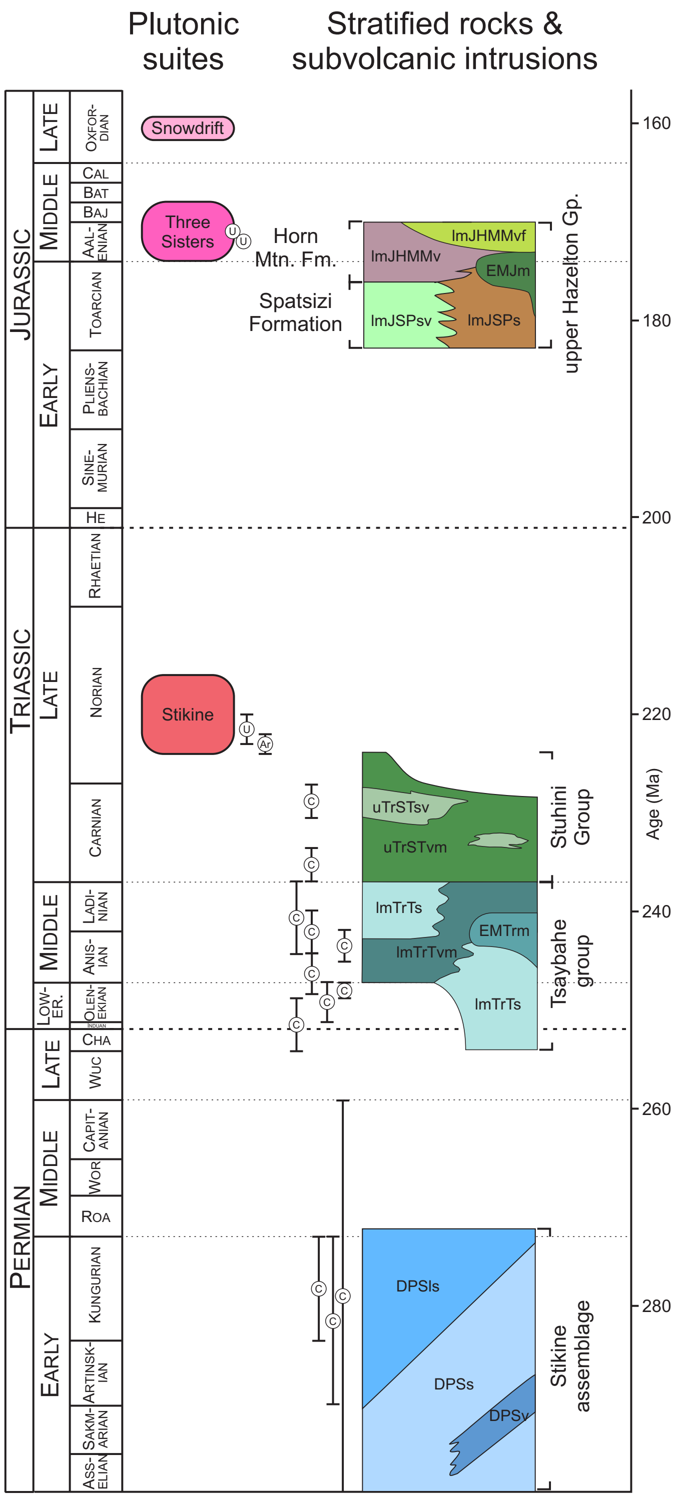


**Fig. 3.** Schematic stratigraphic and plutonic relationships for Permian to Jurassic rocks in the map area. References for geochronological and biostratigraphic age constraints listed in Tables 1 and 2. Chronostratigraphic ages from Cohen et al. (2013, updated August 2018).

Triassic sedimentary and mafic volcanic rocks. He subdivided the group into four units (basal sedimentary, lower volcanic, middle sedimentary, upper volcanic), and interpreted that they underlie most of the current study area. Both sedimentary units yielded Middle (and rare Lower) Triassic conodonts (Read, 1983; 1984). The lower and upper volcanic units comprise texturally similar mafic volcanic rocks (Read, 1983; 1984). Based on the difficulty of separating Read's lower and upper volcanic units on a regional scale, particularly where intervening sedimentary rocks are not exposed, Gabrielse (1998) discontinued the use of Tsaybahe group. Instead Gabrielse (1998) assigned all of Read's units to the Stuhini Group, which he mapped as undivided Triassic. In this study we retain the Tsaybahe group to include all Early to Middle Triassic volcano-sedimentary rocks, and subdivide it into a volcanic unit and a sedimentary unit (Table 1). Following Gabrielse (1998), we generally include Read's (1983; 1984) upper volcanic unit in the Stuhini Group (Table 1), but based on studies throughout northern Stikinia (e.g., Souther, 1971; Logan and Koyanagi, 1994; Brown et al., 1996; Mihalynuk, 1999) we consider that the Stuhini Group formed entirely in the Late Triassic.

The Tsaybahe group sedimentary unit we mapped (lmTrT*s*, Table 1) comprises fine-grained siliciclastic rocks (Fig. 5) and minor chert. It includes Read's (1983; 1984) basal sedimentary unit and most exposures of his middle sedimentary unit. It can generally be distinguished from Stuhini Group sedimentary rocks (Table 1) based on the presence of minor chert and a greater abundance of argillite, siltstone, and fine-grained sandstone relative to medium- to coarse-grained volcaniclastic sandstone. The Tsaybahe group volcanic unit (lmTrT*vm*, Table 1) contains massive monomictic tuff breccia with plagioclase-augite-phyric volcanic clasts. It appears texturally similar to Stuhini Group volcanic rocks, but has magnetic susceptibility values that are more than one order of magnitude lower (Fig. 4). It includes occurrences of Read's (1983; 1984) lower and upper volcanic unit displaying a low magnetic susceptibility and a low response on aeromagnetic surveys.

Contacts between the Tsaybahe group and underlying Stikine assemblage are not exposed, but the lack of widespread tight, north-northeast trending folds and accompanying phyllitic foliation in Triassic and younger rocks (see Section 5.2.), bedding in basal Tsaybahe units that dips away from Stikine assemblage exposures (Fig. 2; Read, 1983; 1984; Logan et al., 2012b; this study) and an apparent ca. 20 m.y. gap in biostratigraphic ages (Fig. 3) suggest an unconformable relationship. We note significant lateral variation in the character of basal Tsaybahe strata; Stikine assemblage rocks in the west of the map area are overlain by Tsaybahe volcanic rocks, whereas in the east they are overlain by Tsaybahe sedimentary rocks (Fig. 2; Read, 1983; 1984; Logan et al., 2012b; this study). The contact between the Tsaybahe sedimentary and volcanic unit is exposed immediately south of Thenatlodi Mountain, where interbedded siliceous argillite and fine sandstone are conformably overlain by lapillistone with plagioclase-augite-phyric volcanic and minor chert clasts.

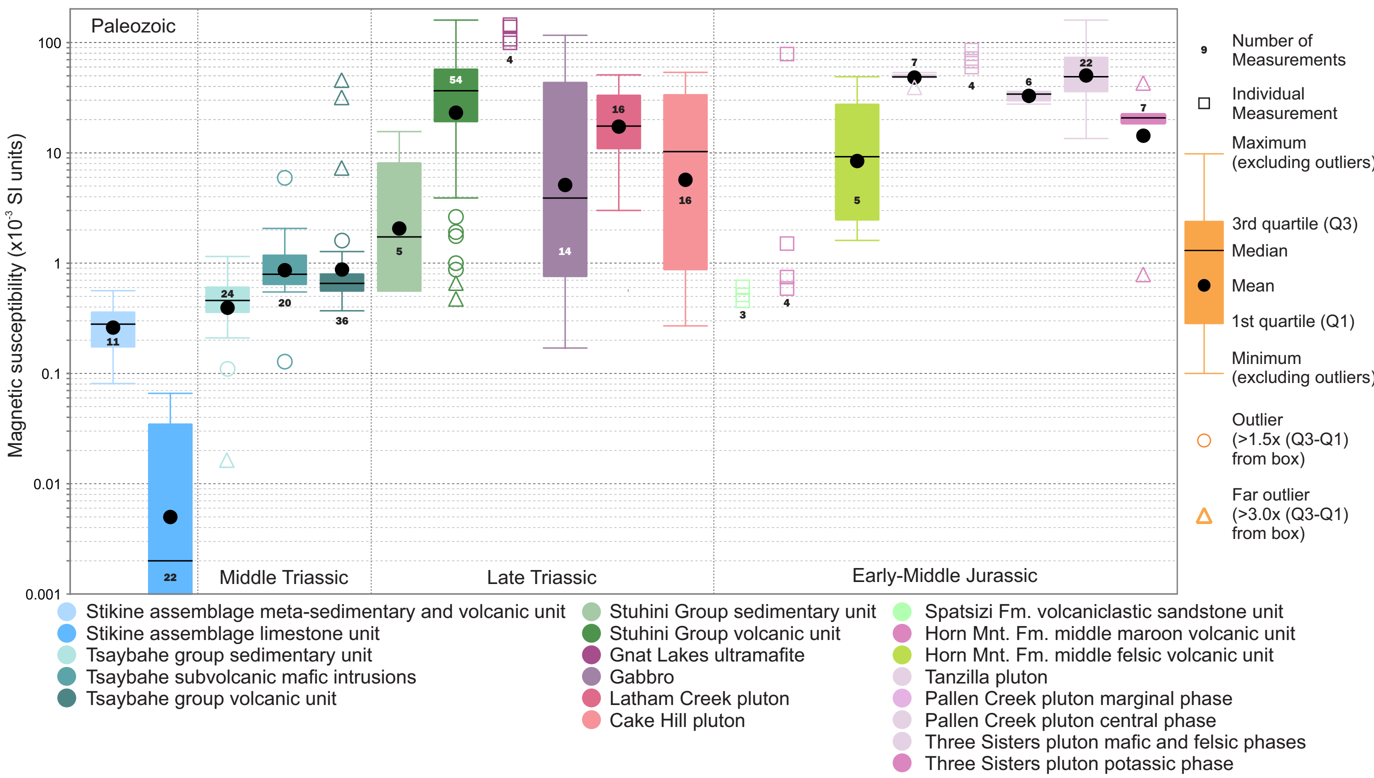


**Fig. 4.** Box and whisker plots showing magnetic susceptibility values for stratified and intrusive units, ordered from old (left) to young (right). Each magnetic susceptibility value represents the average of ten measurements at one field station. Where less than five data points per unit, individual measurements are shown.

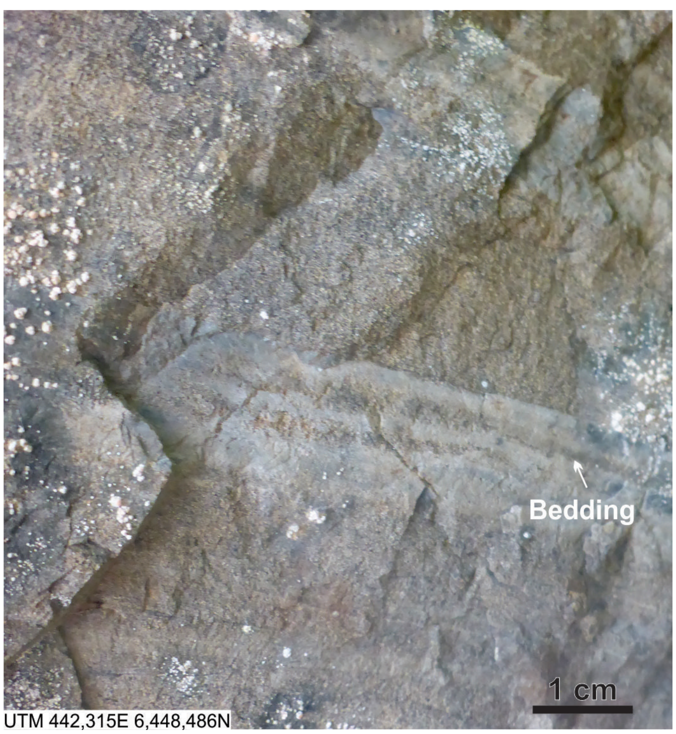


**Fig. 5.** Tsaybahe Group sedimentary unit (lmTrTs). Interstratified fine-grained sandstone and siliceous argillite.

### 3.1.3. Stuhini Group (Upper Triassic)

The Stuhini Group crops out in the southwestern, central and northwestern parts of the map area (Fig. 2) and comprises volcanic and minor sedimentary rocks. The volcanic unit contains massive monomictic tuff breccia and lapilli-tuff with augite-plagioclase-phyric volcanic clasts (uTrST*vm*, Table 1; Fig. 6). It locally includes significant proportions of augite-plagioclase-phyric coherent rocks that may represent subvolcanic intrusions or flows. The unit has high magnetic susceptibility values (Fig. 4) and returned one early Carnian conodont collection (Read, 1984; Gabrielse, 1998; revised by Golding et al., 2017). A sedimentary unit, mostly fine- to medium-grained volcaniclastic feldspathic arenite (uTrSTsv, Table 1), forms <140 m-thick intervals within the Stuhini volcanic unit in the centre of the map area. Due to a lack of exposures we were unable to observe the contact between the Tsaybahe and Stuhini groups.

### 3.1.4. Upper part of the Hazelton Group (Lower-Middle Jurassic)

Peak 1979 m and the surrounding high ground expose maroon volcanic and felsic volcanic rocks that are distinct from surrounding Triassic rocks (Fig. 2). Read (1984) assigned the sequence to the Toodoggone volcanics (Lower Jurassic), whereas Gabrielse (1998) interpreted them as an undifferentiated Triassic-Jurassic volcanic unit. We recognize two lower sedimentary and two upper volcanic units, and expand the areal extent of Jurassic rocks. We assign the sedimentary units to the Spatsizi Formation and the volcanic units to the Horn Mountain Formation (both late Early to Middle Jurassic and in the upper part of the Hazelton Group), based

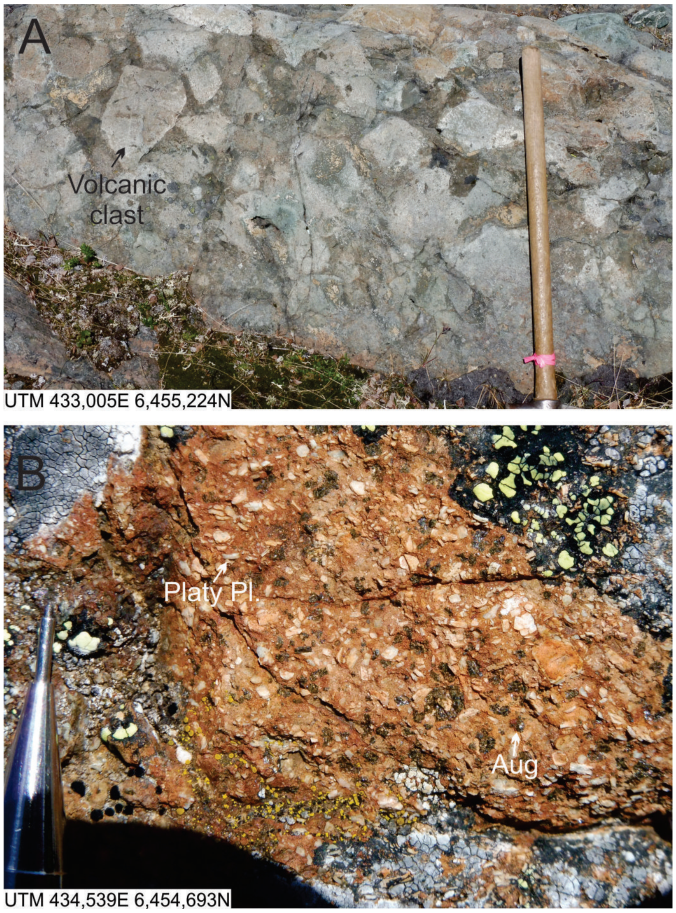


**Fig. 6.** Stuhini Group volcanic unit (uTrSTvm). **a)** Volcanic breccia with clast-supported subangular augite-plagioclase-phyric volcanic clasts. **b)** Close-up of volcanic clast with platy plagioclase and augite phenocrysts.

on similarities to rocks on the northern to eastern margin of the Hotailuh batholith as described by van Straaten and Nelson (2016), van Straaten and Gibson (2017) and van Straaten and Bichlmaier (2018a). The change in character of sedimentary rocks from west to east, and absence of one of the volcanic units in a stratigraphic section in the northeast may be related to syn-depositional north-trending faults (Section 5.3.). Based on mapping north and east of the Hotailuh batholith, we assume that the Stuhini Group and Hazelton Group in the map area are separated by an unconformity. Locally, the contact between these rocks is cut by the Three Sisters pluton (Middle Jurassic, see Section 4.4.).

### 3.1.4.1. Spatsizi Formation

We recognize two Spatsizi Formation sedimentary units. Exposed in the cirque east of Peak 1979 m (Fig. 2) is a unit of interstratified siltstone and very fine- to medium-grained sandstone (lmJSP*s*, Table 1). It grades conformably up to Horn Mountain Formation felsic volcanic rocks (Fig. 7). It is similar to a discontinuous 48 km-long belt of Spatsizi Formation sedimentary rocks along the northern to northeastern margin of the Hotailuh batholith described by van Straaten and Nelson

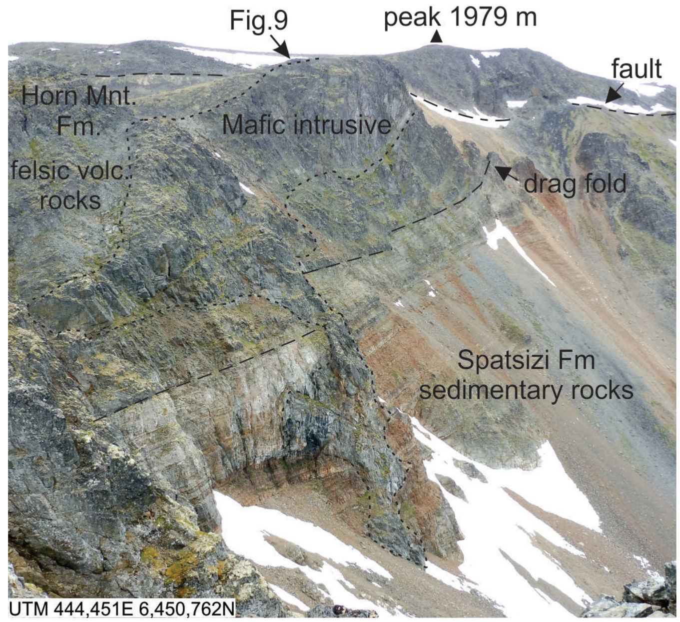


**Fig. 7.** Hazelton Group volcano-sedimentary rocks. Stratified rusty weathering Spatsizi Formation sedimentary rocks (lmJSP*s*) overlain by Horn Mountain Formation middle felsic volcanic unit (lmJHM*Mvf*); both units are cut by mafic intrusive (EMJ*m*). Megascopic drag fold suggests east-side-down normal movement along north-trending fault. View to west.

(2016), van Straaten and Gibson (2017) and van Straaten and Bichlmaier (2018a).

About 1-2 km west of Peak 1979 m is a unit of medium-grained volcaniclastic feldspathic arenite (lmJSP*sv*, Table 1; Fig. 2) that was previously interpreted as Middle Triassic (Read, 1984). We reinterpret these rocks as Spatsizi Formation because: 1) they resemble Spatsizi Formation rocks on the northern margin of the Hotailuh batholith, 2) they appear to grade upward into maroon volcanic rocks interpreted as Horn Mountain Formation, and 3) they contain limestone beds that are similar to those within Horn Mountain middle maroon volcanic rocks, and both limestone beds failed to yield conodonts (Read, 1984). Two sandstone samples from this unit were processed for U-Pb geochronology but yielded no zircons (Iverson et al., 2012).

### 3.1.4.2. Horn Mountain Formation

We subdivide the Jurassic volcanic rocks near Peak 1979 m into a maroon volcanic unit and an overlying felsic volcanic unit (Fig. 2). The first unit includes crudely stratified maroon volcanic breccia, flows, tuff breccia, lapillistone, lapilli-tuff and tuff; coherent rocks and volcanic clasts are augite-plagioclase-phyric (lmJHM*Mv*, Table 1; Fig. 8). The unit is similar to an 80 km-long belt of Horn Mountain maroon volcanic rocks along the northern to eastern margin of the Hotailuh batholith.

The second volcanic unit comprises felsic tuff, lapilli-tuff, and minor tuff breccia with light-coloured, aphanitic to plagioclase-phyric volcanic clasts (lmJHM*Mvf*, Table 1; Fig. 9). Although we correlate this unit with felsic rocks in


**Fig. 8.** Horn Mountain Formation middle maroon volcanic unit (lmJHM*Mv*). Interstratified cream coarse crystal tuff and maroon tuff.


**Fig. 9.** Horn Mountain Formation middle felsic volcanic unit (lmJHM*Mvf*); lapilli-tuff with angular cream-coloured plagioclase-phyric to aphyric felsic clasts.

the Horn Mountain middle maroon volcanic unit (late Early to Middle Jurassic) exposed east of the Hotailuh batholith (van Straaten and Bichlmaier, 2018a), it could also be equivalent to the Horn Mountain upper felsic volcanic unit (Middle Jurassic) of van Straaten and Nelson (2016), van Straaten and Gibson (2017) and van Straaten and Bichlmaier (2018a). West and south of Peak 1979 m, maroon volcanic rocks appear to be stratigraphically overlain by felsic volcanic rocks (Fig. 2). In the cirque east of Peak 1979, the sedimentary unit of the Spatsizi Formation grades directly to the felsic volcanic unit of the Horn Mountain Formation without intervening maroon volcanic rocks (Fig. 7).

The Hazelton Group in the present map area differs from exposures along the northern to eastern margin of the Hotailuh batholith. First, the exposed stratigraphic thickness (<0.5 km) is significantly less than farther east, where the section is up to 6.4 km thick. Second, units display abrupt lateral facies and thickness changes in contrast to farther east where units display significant lateral continuity. Third, the lower volcanic unit of the Horn Mountain Formation is absent in the present map area.

### 3.2. Overlap units

#### 3.2.1. Sustut Group (Cretaceous)

Sedimentary rocks of the Sustut Group (Cretaceous) unconformably overlie Stikinia rocks along the Stikine River (Fig. 2). The Sustut Group includes feldspathic and lithic sandstone (locally muscovite-bearing), siltstone, shale, carbonaceous shale, chert clast-bearing pebble to lesser cobble conglomerate and thin zeolitized tuff beds (Read, 1983; 1984).

#### 3.2.2. Tuya Formation (Miocene-Pleistocene)

Several 0.2-1.7 km-wide olivine basalt volcanic centres were mapped by Read (1983; 1984) and Gabrielse (1998) in the southeastern part of the study area.

## 4. Intrusive units

Plutonic rocks in the map area can be grouped with the Stikine plutonic suite (Late Triassic) and Three Sisters plutonic suite (Middle Jurassic). We recognize two subvolcanic intrusive units, one related to Tsaybahe group volcanic rocks (Early-Middle Triassic) and another related to Horn Mountain volcanic rocks (Early-Middle Jurassic; Fig. 3; Table 2).

### 4.1. Early-Middle Triassic subvolcanic intrusions

Plagioclase-augite- to augite-phyric sills, dikes, and subvolcanic intrusive complexes (EMTr*m*, Table 2; Fig. 10) up to 1-3 km$^2$ in size are exposed in the eastern part of the map area (Fig. 2). Mafic intrusions cut, and include xenoliths of, Tsaybahe group sedimentary rocks (lmTrT*s*, Table 1). The intrusions have low magnetic susceptibility values (Fig. 4) and are texturally and mineralogically similar to clasts in the Tsaybahe volcanic unit (lmTrT*vm*). Thus we consider them as feeder dikes.

### 4.2. Late Triassic plutonic rocks

We recognize four Late Triassic plutonic units in the map area: the Gnat Lakes ultramafite, an unnamed gabbro unit,

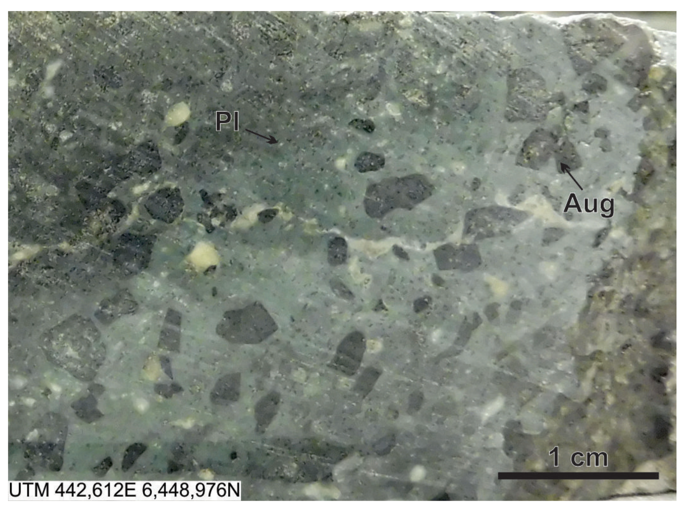


**Fig. 10.** Subvolcanic Tsaybahe mafic intrusive (EMTr*m*) with euhedral augite and dispersed fine stubby plagioclase; striae are saw cut marks.

**Table 2.** Summary of intrusive units. Mineral abbreviations after Kretz (1983).

| Age | Phase | Description | Relationships to adjacent units | Geochronology |
|---|---|---|---|---|
| Middle Jurassic | Three Sisters pluton | **Potassic phase (MJTS*gr*).** Bt-Hbl Qtz monzonite to Bt (-bearing) monzogranite. Massive, equigranular (1-4 mm) to Bt, Pl and/or Kfs porphyritic (3-5 mm). Contains 25-70% equant Kfs, 25-40% equant Pl, 5-25% Qtz, 5-25% mafic minerals, up to 4% Mag and fine-grained xenoliths. Moderately recessive, light grey to pinkish weathering. | Cuts Tsaybahe group volcanic rocks, Stuhini Group volcanic rocks, Horn Mountain middle maroon volcanic rocks. Adjacent Spatsizi Formation sedimentary unit (lmJSP*s*) displays features of contact metamorphism. | U-Pb zircon: 171±1 Ma[4] |
| | | **Felsic phase (MJTS*qm*).** Hbl-Bt to Bt-Hbl Qtz monzodiorite. Massive, equigranular (0.2-3.5 mm). Contains 35-60% equant Pl, 10-35% equant Kfs, 5-20% Hbl, 4-20% Bt, 3-20% Qtz, and up to 4% Mag. Resistant, weathers pink to cream. | | |
| | | **Mafic phase (MJTS*qd*).** Bt-Cpx-Hbl Qtz diorite. Massive, equigranular (0.5-3 mm). Contains 55-75% euhedral blocky to rectangular Pl, 20-30% green altered mafic minerals (predominantly Hbl, with possible Cpx and Bt), 0-20% anhedral Qtz, 0-15% possible Kfs. Resistant, weathers light grey to greenish grey.<br>**(MJTS*qd.po*).** Bt-bearing Hbl-Cpx diorite with 60-70% platy Pl (0.3-7 mm), 30-40% equant mafic minerals (0.2-1.5 mm) and possibly 2-5% Bt. Resistant, orange to tan weathering. | | |
| | Pallen Creek pluton | **Central phase (MJP*qm*).** Bt to Hbl-Bt Qtz monzonite, lesser Qtz monzodiorite, rare Bt monzogranite. Massive, Kfs porphyritic (4-10 mm) to equigranular (1-3 mm), and contains trace Mag. Moderately recessive, weathers grey to pinkish. | Apophyses cut Pallen Creek marginal phase. | U-Pb zircon: 172±1 Ma[2] |
| | | **Marginal phase (MJP*dr*).** Hbl-Bt, Bt-Hbl to Hbl-rich diorite, Qtz diorite and lesser Qtz monzodiorite. Massive to rarely foliated, equigranular (0.5-2 mm) to rarely Bt-Hbl porphyritic (5-10 mm). Contains 42-55% blocky to rectangular Pl (0.5-1.5 mm), 10-50% rectangular Hbl (0.5-2 mm), 0-20% green altered Bt (1-3 mm), 3-10% Qtz (0.5-1 mm), 0-20% Kfs and trace Mag. Locally contains Bt Hbl-rich microdiorite xenoliths. Moderately recessive, pinkish cream to orange cream weathering. | Dike cuts Stikine assemblage limestone unit. Includes xenoliths of Tsaybahe group volcanic unit. Adjacent Tsaybahe group volcanic unit and Stikine assemblage limestone unit display features of contact metamorphism. | |
| | Tanzilla pluton | **Tanzilla pluton (MJT*gd*).** Bt-bearing Hbl-rich to Hbl Bt-rich Qtz monzodiorite and Bt-Hbl to Bt Hbl-rich granodiorite. Massive, equigranular (0.5-2 mm). Contains 35-65% rectangular Pl, 10-30% elongate to rectangular Hbl, 5-30% equant Bt, 10-20% Qtz and 5-10% blocky Kfs. Resistant, white to grey blue with some pinkish weathering. | Adjacent Stikine assemblage limestone unit displays features of contact metamorphism. | K-Ar Hbl: 171±14 Ma[6]<br>K-Ar Bt: 188±4 Ma[6] |

**Table 2.** Continued.

| Age | Phase | Description | Relationships to adjacent units | Geochronology |
|---|---|---|---|---|
| Early-Middle Jurassic | Horn Mountain-related subvolcanic intrusions | **Platy Pl porphyry (EMJ*m.po*).** Aug-Plag-phyric dikes. Contains 35% platy Pl (0.5-1 cm) and 20% Aug (1-4 mm) in a pale grey groundmass. | Cuts Gnat Lakes ultramafite, Tsaybahe group sedimentary unit and mafic intrusive unit (EMTr*m*). | |
| | | **Mafic intrusive (EMJ*m*).** Aug-Pl-phyric to Pl-phyric coherent rocks interpreted as sills, dikes and intrusions. Contains 25-40% rectangular to lath-shaped Pl (0.1-2 mm) and 0-20% equant to hexagonal Aug (0.5-10 mm). Resistant, dark grey weathering. | Cuts Spatsizi Fm. sedimentary unit and Horn Mountain middle maroon felsic volcanic unit. Interpreted to cut Horn Mountain middle maroon volcanic unit. | |
| Late Triassic | Cake Hill pluton | **Cake Hill pluton (LTrCH*qm*)**. Hbl Qtz monzonite and rare Hbl (-rich) monzonite to monzogranite. Massive, equigranular (0.5-3 mm). Contains 10-35% blocky to tabular Hbl, 30-55% blocky Pl, 20-30% blocky to rectangular Kfs, and 5-30% Qtz. Moderately resistant, pinkish to white weathering. | Cuts Stuhini Group volcanic unit. Adjacent Stuhini Group volcanic unit displays features of contact metamorphism. | U-Pb zircon: 221±3 Ma[4]<br>K-Ar Hbl: 212±7 Ma[5]<br>ca. 222 Ma[5] |
| | Latham Creek pluton | **Latham Creek pluton (LTrLC*qd*).** Hbl-rich Qtz diorite. Commonly foliated, equigranular (0.5-4 mm). Contains 35-55% blocky to rectangular Hbl, 45-63% rectangular to blocky Pl, and 0-10% Qtz (0.5-1.5 mm). Moderately resistant, black and white weathering. | | |
| | Gabbro | **Gabbro (LTr*gb*).** Mafic-rich gabbro. Massive, typically equigranular (0.3-4 mm). Contains 30-85% mafic minerals (probably Cpx and Hbl) and 15-70% rectangular Pl. Resistant, medium grey to greenish weathering. | Locally contains xenoliths similar to Gnat Lakes ultramafite. | |
| | Gnat Lakes ultramafite | **Gnat Lakes ultramafite (LTrGL*um*)**. Hbl clinopyroxenite, hornblendite and gabbro [3]. Resistant, dark grey to dark greenish grey weathering. | Adjacent Tsaybahe group sedimentary unit and mafic intrusive unit (EMTr*m*) display features of contact metamorphism. | Ar-Ar Hbl: 223.3±2.0 Ma[1] |
| Early-Middle Triassic | Tsaybahe-related subvolcanic intrusions | **Mafic intrusive (EMTr*m*).** Pl-Aug- to Aug-phyric coherent rocks, interpreted as dikes, sills and intrusions. Contains 25-45% equant Aug (0.5-4 mm), 0-30% blocky to platy Pl (0.2-2 mm), set in a fine-grained dark sea-green groundmass. Median magnetic susceptibility 0.79 x $10^{-3}$ SI units. Resistant, dark grey to dark green weathering. | Cuts and includes xenoliths of Tsaybahe group sedimentary rocks. | |

Note: [1] Zagorevski (unpublished data); [2] Logan et al. (2012b); [3] Nixon et al. (1997; 1989); [4] Anderson and Bevier (1992); [5] Read (1984); [6] Stevens et al. (1982).

the Latham Creek pluton, and the Cake Hill pluton. The Gnat Lakes ultramafite is a 4.7 km$^2$ body exposed along Highway 37 (Fig. 2). It has been described as an Alaskan-type intrusion based on the presence of hornblende clinopyroxenite, hornblendite and gabbro, minor zoning, and distinctive whole-rock and mineral chemistry data (LTrGL*um*, Table 2; Nixon et al., 1989; 1997). An Ar-Ar hornblende analysis returned a 223.3 ±2.0 Ma cooling age (A. Zagorevski, unpublished data). The adjacent Tsaybahe group sedimentary unit (lmTrT*s*) and mafic intrusive unit (EMTr*m*) are strongly silicified and contain common disseminated pyrite as a result of contact metamorphism.

Small (<4 km$^2$) mafic-rich gabbro bodies are exposed in the eastern, northeastern, and northwestern parts of the map area (LTr*gb,* Table 2; Fig. 2). In the northeast, a 1.3 km$^2$ compositionally zoned gabbro body displays a central zone containing up to 80% clinopyroxene and a marginal zone to the north with 25-30% clinopyroxene. A significantly larger gabbroic pluton is exposed west of the map area (Caribou Meadows pluton; Read, 1983).

The Latham Creek pluton forms three separate bodies (up to 44 km$^2$ in size) in the southeastern part of the map area (Fig. 2) and consists of hornblende-rich quartz diorite that is commonly foliated (LTrLC*qd,* Table 2; Fig. 11).

The Cake Hill pluton is exposed in the eastern part of the map area (Fig. 2). It consists mainly of hornblende quartz monzonite and lacks xenoliths (LTrCH*qm,* Table 2). Decimetre-scale dikes of Cake Hill composition cut Stuhini Group augite-phyric coherent rocks (uTrST*vm*) along the pluton's western margin. A sample from the adjacent map area to the east returned a U-Pb zircon age of 221 ±3 Ma (Anderson and Bevier, 1992).

### 4.3. Early-Middle Jurassic subvolcanic intrusions

Augite-plagioclase-phyric and plagioclase-phyric coherent rocks (EMJ*m*, Table 2; Fig. 12) form relatively small (<1.5 km$^2$) bodies in the eastern part of the map area. The intrusions are texturally and mineralogically similar to volcanic clasts within the Horn Mountain middle maroon volcanic unit (lmJHM*Mv*); they likely represent feeder dikes. Rare augite- and coarse platy plagioclase-phyric dikes (EMJ*m.po*, Table 2) cut Early-Middle Triassic mafic intrusive rocks and Tsaybahe sedimentary rocks in the eastern part of the map area. These dikes are texturally similar to platy plagioclase-phyric intrusions that are cogenetic with Horn Mountain volcanism in the adjacent map area to the northwest (e.g., van Straaten and Gibson, 2017).


**Fig. 12.** Subvolcanic Horn Mountain mafic intrusive (EMJ*m*) with hexagonal chloritized and epidote-altered augite and plagioclase.

### 4.4. Middle Jurassic plutonic rocks

We mapped three Middle Jurassic plutonic bodies in the field area, the Three Sisters, Pallen Creek, and Tanzilla plutons (Fig. 2, Table 2). The Three Sisters pluton is exposed in the eastern part of the map area. The pluton is subdivided into a mafic phase (MJTS*qd*), a felsic phase (MJTS*qm*), and a potassic phase (MJTS*gr*). Several small (<1 km) mafic to mafic-rich quartz diorite bodies of the mafic phase are enclosed within the felsic phase in the northeastern part of the map area. A 3.5 km$^2$ coarse platy plagioclase porphyritic diorite body of a mafic subphase (MJTS*qd.po*; Fig. 13) is exposed in the northeastern part of the study area. It is texturally and compositionally similar to a hornblende-clinopyroxene diorite body with platy plagioclase described by van Straaten and Bichlmaier (2018a) on the eastern margin of the Three Sisters pluton. The felsic


**Fig. 11.** Latham Creek pluton (LTrLC*qd*). Foliated hornblende-rich quartz diorite.


**Fig. 13.** Three Sisters pluton plagioclase porphyritic mafic subphase (MJTS*qm.po*). Mafic-rich diorite with coarse platy plagioclase set in a fine-crystalline plagioclase-rich groundmass.

phase, exposed in the northeastern part of the map area, consists of hornblende-biotite quartz monzodiorite. The potassic phase extends along the eastern side of the map area, and consists of biotite-hornblende quartz monzonite to biotite monzogranite. A sample of the potassic phase returned a U-Pb zircon age of 171 ±1 Ma (Anderson and Bevier, 1992).

The Pallen Creek pluton forms a 30 km$^2$ body in the northwestern part of the map area. We identify a marginal phase (MJP*dr*) and a central phase (MJP*qm*; Table 2), corroborating previous work by Downing (1980). The marginal phase comprises biotite-hornblende quartz diorite, is locally foliated and contains minor fine-grained dioritic xenoliths (Fig. 14). The central phase of the Pallen Creek pluton consists of (hornblende-) biotite quartz monzonite to monzodiorite. A sample from the adjacent map sheet to the north returned a U-Pb zircon age of 172 ±1 Ma (Logan et al., 2012b).

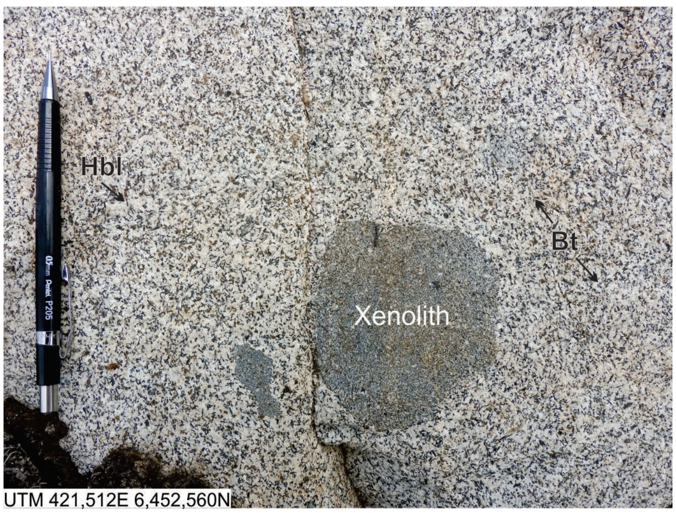


**Fig. 14.** Marginal phase of the Pallen Creek pluton (MJP*dr*). Biotite-hornblende quartz diorite with hornblende-rich microdiorite xenoliths.

The Tanzilla pluton forms a 15 km$^2$ body in the western part of the map area. It consists mainly of biotite-hornblende quartz monzodiorite to granodiorite (MJT*gd*, Table 2; Fig. 15). Although K-Ar biotite and hornblende analyses returned Early to Middle Jurassic cooling ages (Stevens et al., 1982), textural and mineralogical similarity to the Three Sisters and Pallen Creek plutons suggests it is most likely part of the Middle Jurassic plutonic suite.

## 5. Structure

Within the field area, penetrative deformation is limited to Stikine assemblage rocks. Triassic and Jurassic rocks generally lack penetrative fabrics.

### 5.1. Devonian-Permian rocks

Kilometre-scale tight folds are outlined by Stikine assemblage rocks in the northwestern part of the map area (Fig. 2). Rocks generally display a penetrative northwest-dipping phyllitic foliation and the folds display subhorizontal to gently northeast to southwest plunging axes (Fig. 16a). Bedding is commonly

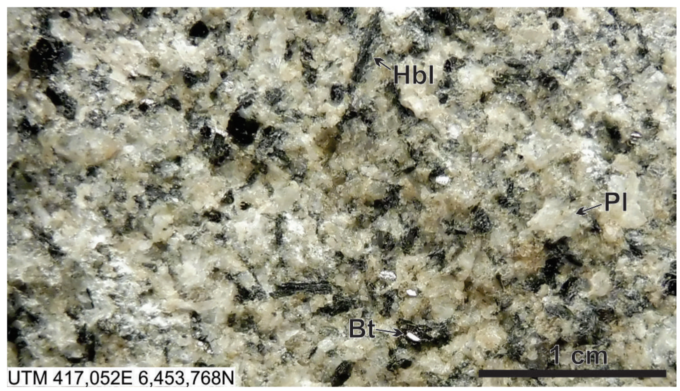


**Fig. 15.** Tanzilla pluton (MJT*gd*). Massive, biotite-hornblende quartz monzodiorite.

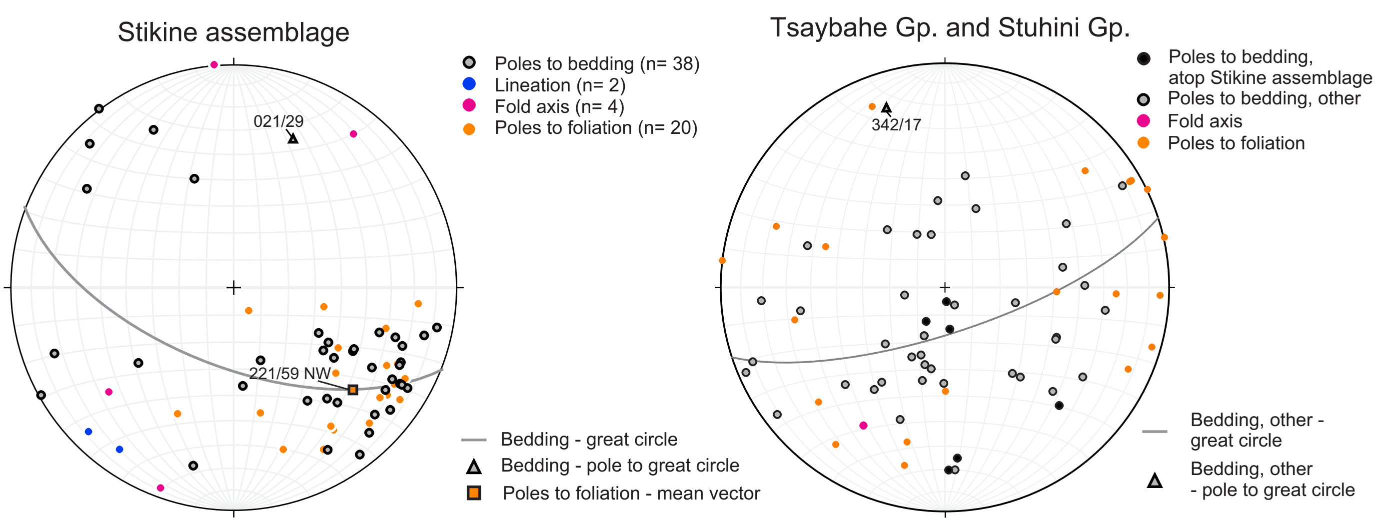


**Fig. 16.** Equal area lower hemisphere stereonet projections of structural data for **a)** Stikine assemblage (Devonian-Permian) rocks and **b)** Tsaybahe group and Stuhini Group (Triassic) rocks. In a), lineations include a bedding/cleavage intersection and a stretching lineation. Structural data from Logan et al., (2012a; b) and this study.

parallel to foliation (Fig. 16a). Although way-up indicators are lacking we infer the folds have one overturned limb. On the limb of the easternmost antiform along Itsillitu Creek, both bedding and foliation dip to the northwest, but bedding dips more shallowly, indicating that the limb is right-way-up and that the limestone unit overlies the meta-sedimentary unit.

The absence of penetrative deformation in unconformably overlying Tsaybahe and Stuhini groups suggests deformation postdates Stikine assemblage limestone formation (Early Permian) and predates Tsaybahe group deposition (Early Triassic). It correlates with the Tahltanian orogeny recognized throughout most of the Intermontane terranes (e.g., Wheeler, 1967; Logan and Koyanagi, 1994).

### 5.2. Triassic rocks

Triassic Tsaybahe and Stuhini Group rocks are only rarely foliated, and no outcrop-scale folds were observed. Bedding in basal Tsaybahe group generally dips away from Stikine assemblage basement (Fig. 2). Stereonet analysis of bedding variations within the Tsaybahe and Stuhini groups suggest they are folded about gently northerly plunging fold axes (Fig. 16b). The reinterpreted distribution of Tsaybahe and Stuhini units, particularly within 6 km north of the Stikine River (Fig. 2), could be most easily explained by gently southerly plunging map-scale folds. Inferred fold axes in the map area appear continuous with map-scale north-plunging folds noted by Logan et al. (2012a; b) in the adjacent map area to the north. The absence of north-south trending folds in late Early-Middle Jurassic strata (e.g., van Straaten and Gibson, 2017) may suggest deformation occurred in the latest Triassic to Early Jurassic. The change in fold plunge may be explained by north-south shortening during mid-Jurassic terrane accretion. Structures resulting from south-vergent fold and thrust belt development are widespread north of the King Salmon fault and moderately developed in footwall Whitehorse trough strata (e.g., Logan et al., 2012a; b; van Straaten and Gibson, 2017).

Northerly trending structures including the Gnat Pass shear zone (see van Straaten et al., 2012) and shear zones west of the Gnat Lakes ultramafite (Fig. 2) display a well-developed shear zone-parallel phyllitic foliation.

Read (1983; 1984) mapped the low-angle folded ‘Z-fault’ along Stikine River (Fig. 2). Erosion of the fault along the Stikine River exposes two windows of Tsaybahe sedimentary rocks containing Early to Middle Triassic fossils, cut by a hornblendite to gabbro body (Fig. 2). Read (1983; 1984) interpreted the structure as a gently dipping detachment fault along which Tsaybahe and Stuhini rocks in the hanging wall moved north to northeast. The fault was subsequently folded about a northeasterly axis; faulting and folding predates deposition of the Sustut Group (Cretaceous, Read, 1983; 1984).

### 5.3. Jurassic rocks

Bedding in the Hazelton Group mainly dips moderately to the southwest. Several northerly trending lineaments and faults cut the succession, with adjacent fault blocks showing moderate differences in bedding attitude, character of sedimentary rocks, and stratigraphic superposition. The change in character of sedimentary rocks from west to east, and absence of one of the volcanic units in a stratigraphic section in the northeast may be related to syn-depositional fault movement. Megascopic drag folding on the east wall of the easternmost fault (Fig. 7) suggests an east-side-down normal movement.

## 6. Mineral occurrences

A number of intrusion-related mineral occurrences lie within the field area. One is hosted in Late Triassic plutonic rocks, and five are likely related to Middle Jurassic intrusions. Several additional mineral occurrences near Highway 37 (e.g., Gnat Pass, Moss, Dalvenie and BCR; Fig. 2) are described in van Straaten et al. (2012) and van Straaten and Gibson (2016).

### 6.1. Late Triassic intrusion-hosted mineral occurrences

Hotai is a donut-shaped aeromagnetic anomaly in the Latham Creek pluton (Fig. 2). A soil geochemical survey indicated no anomalous metal values, an induced polarization survey showed a chargeability high coincident with part of the aeromagnetic high, and a grab sample from a bornite vein in weakly chlorite-altered hornblende diorite returned 0.56% Cu (sample 966971, Andrzjewski and Bui, 2012).

### 6.2. Middle Jurassic intrusion-related mineral occurrences

Geochemical sampling in the 1970s discovered molybdenum in the Pallen Creek pluton (Downing, 1980). We observed 1-3 vol.% fractures (1-3 mm wide) with pyrite and minor chalcopyrite with or without molybdenite in small pits at the Disco and Stikine showings (MINFILE 104J 019, 46); plutonic host rocks appear unaltered. At the Stikine Moly showing (MINFILE 104J 034) up to 4-6% disseminated and fracture-hosted pyrite is accompanied by minor molybdenite and chalcopyrite. A 1.5 m chip sample from Disco returned 0.30% Cu and 0.8 ppm Mo (sample 975162, Andrzjewski and Bui, 2012). Exploration by Quartz Mountain Resources Ltd. in 2012 did not generate significant soil geochemistry anomalies that correlate with induced polarization chargeability highs (Andrzjewski and Bui, 2012).

The Crown copper showing (MINFILE 104I 046) is 3.5 km northwest of Peak 1979 m (Fig. 2). A pyritic gossan and disseminated and vein-hosted chalcopyrite with K-feldspar and skarn alteration is hosted in Triassic volcanic rocks adjacent to a granodiorite to monzonite intrusion (BC Department of Mines and Petroleum Resources, 1972, p. 44; 1973, p. 538). Geophysical surveys, geochemical sampling, and two diamond drill holes were completed in the 1970s, but only geophysical results were reported (Fominoff and Adamson, 1971). We mapped nearby plutonic rocks as the felsic phase of the Three Sisters pluton. Work carried out by West Cirque Resources Ltd. in 2011 and 2012 identified an induced polarization chargeability and copper in soil anomalies (Luckman and Kuttai, 2012; Luckman, 2013).

The Kay 49 showing (MINFILE 104I 026) is in the northwestern part of the map area (Fig. 2). Exploration activities by Tanzilla Explorations Ltd. in the late 1960s and early 1970s identified a 27 m-wide altered and mineralized meta-volcanic outcrop that returned 0.04% Cu and 1.37 g/t Ag. The meta-volcanic rocks are bordered by extensive outcrops of unmineralized intrusive rocks to the southeast (Scott, 1970). The showing is in the felsic phase of the Three Sisters pluton, and possibly in a Stuhini Group pendant. At the nearby Kay 19 showing (MINFILE 104I 037) three drill holes intersected up to 0.09% Cu and 3.4 g/t Ag over 1 m, and a grab sample of nearby exposures returned 0.25% Cu (Aikins, 1971).

The Lode occurrence is in the cirque immediately east of Peak 1979 m. Anomalous silver in a stream-sediment sample (Andrzjewski et al., 2012) led to prospecting and soil geochemistry and induced polarization surveys (Andrzjewski and Bui, 2012). The surveys showed a moderate chargeability feature and coincident multi-element soil geochemical anomaly. We observed rusty weathering and strongly silicified Spatsizi Formation sedimentary rocks (Fig. 7) containing abundant disseminated pyrite and local arsenopyrite. Locally, calcareous sedimentary rocks contain garnet-diopside-epidote skarn assemblages. Alteration and mineralization are likely related to intrusion of the adjacent potassic phase of the Three Sisters pluton (Fig. 2). Significant copper and elevated gold and silver values were reported in several rock samples, including two grab samples that returned 1.05% Cu, 68 ppb Au, 5.9 g/t Ag (sample 975215), 13.0% Cu and 1012 ppb Au and 70.2 ppb Ag (sample 975233, Andrzjewski and Bui, 2012).

## 7. Discussion

### 7.1. Regional extent and significance of Tsaybahe group

Although the Triassic history of northern Stikinia is recorded mainly by Upper Triassic volcanic and related sedimentary rocks of the Stuhini Group (British Columbia) and Lewes River Group (Yukon), local remnants of Lower to Middle Triassic sedimentary and volcanic rocks are scattered across the region.

Approximately 100 km west-southwest of our study area and north of the Chutine River, Brown et al. (1996) mapped chert, ribbon chert, siliceous siltstone and tuff containing Early Permian and Middle Triassic radiolaria and conodonts. Contact relationships with underlying Lower Permian limestones are equivocal, and the succession that contains Middle Triassic conodonts "appears to grade abruptly upward into tuffaceous wacke of the Stuhini Group" (Brown et al., 1996). In the same area, Brown et al. (1996) documented a limestone block with Early Triassic conodonts in Upper Triassic volcaniclastic sandstone. About 55 kilometres farther southwest, at the toe of the Scud Glacier, Late Permian limestone, maroon tuff, and chert (Stikine assemblage) is either conformably or paraconformably overlain by an undated tuffaceous wacke and tuff unit correlated with either the Tsaybahe or Stuhini Group (Brown et al., 1996). Approximately 130 km to the southwest of the study area, and north and east of the Galore Creek Cu-Au porphyry deposit, Souther (1972) and Logan and Koyanagi (1994) described a Lower to Middle Triassic siliceous siltstone, limy siltstone and carbonaceous silty shale unit that paraconformably overlies Lower Permian limestone. Volcanic-bearing successions of Early to Middle Triassic age are even rarer than purely sedimentary units. Approximately 165 km to the south-southwest of the study area and near the lower Iskut River, Read et al (1989) mapped a Middle Triassic sedimentary unit containing sedimentary and volcanic breccia, sandstone, and argillite that interfingers with mafic volcanic breccia and tuff; he noted that the volcanic rocks are similar to extensive Middle Triassic augite-phyric volcanic rocks found near the Stikine River.

We suggest that the scattered occurrences summarized above, and coeval sedimentary rocks within the study area, may represent the rare remnants of an Early-Middle Triassic marine basin. Based on textural and compositional similarity between Tsaybahe and Stuhini volcanic rocks and a volcanic arc geochemical signature for both successions (Logan and Iverson, 2013) we further suggest that Middle Triassic volcanism may represent the onset of arc volcanism before the Late Triassic Stuhini-Lewes River arc was fully established. The onset of Tsaybahe group volcanism appears to coincide with the end of Permo-Triassic mafic and bimodal primitive intra-oceanic arc volcanism in the northern Cache Creek terrane (ca. 261-242 Ma, Childe and Thompson, 1997; Childe et al., 1998, Mihalynuk et al., 2003; English et al., 2010; Schiarizza, 2011; 2012a; b; Bickerton, 2014; Zagorevski et al., 2015; 2016; McGoldrick et al., 2018; Bordet, in press; Bordet et al., in press). It may indicate an inboard jump of the subduction zone resulting in termination of subduction below intra-oceanic volcanic arc segments within the Cache Creek terrane and initiation of subduction below Stikinia.

Lacking biostratigraphic and geochronologic constraints, Paleozoic, Jurassic and Eocene augite-phyric volcanic rocks throughout northwest British Columbia have inadvertently been included in the Stuhini Group (e.g., Mihalynuk et al., 1995; Mihalynuk, 1999; van Straaten and Nelson, 2016). Given its remarkable similarity to the Stuhini Group, we conclude that the Tsaybahe group is probably more extensive than currently recognized.

### 7.2. Criteria to distinguish Triassic-Jurassic volcano-sedimentary successions

Mapping by the British Columbia Geological Survey in the Dease Lake area during the last decade has largely focussed on separating three temporally distinct, but texturally similar, mafic volcanic successions: the Tsaybahe group (Lower-Middle Triassic), the Stuhini Group (Upper Triassic), and the upper part of the Hazelton Group (Lower to Middle Jurassic). In Table 3 we summarize key criteria that can be used to distinguish these three successions.

## 8. Conclusions

New 1:20,000-scale mapping in the Latham and Pallen Creek area, part of a multi-year project devoted to examining the geologic history and metallogeny of Stikine terrane near

**Table 3.** Summary of criteria to distinguish Triassic-Jurassic mafic volcanic successions in the Dease Lake area.

| | **Tsaybahe group** *(Early to Middle Triassic)* | **Stuhini Group** *(Late Triassic)* | **upper part of Hazelton Group** *(late Early to Middle Jurassic)* |
|---|---|---|---|
| *Volcanic rocks* | Predominantly dark green Pl-Aug-phyric mafic volcanic rocks; no felsic rocks reported | Predominantly dark green Pl-Aug-phyric mafic volcanic rocks dominate; no felsic rocks reported | Dark green Pl-Aug-phyric mafic volcanic rocks common; maroon to medium grey Pl-Aug- to (coarse platy) Pl-phyric mafic to intermediate volcanic rocks common; felsic volcanic rocks subordinate (Horn Mnt. Fm.) |
| *Sedimentary rocks* | Argillite, siltstone, sandstone, rare chert | Volcaniclastic sandstone | Argillite, siltstone, (volcaniclastic) sandstone, rare conglomerate with granitic clasts (Spatsizi Fm.) |
| *Lower contact* | Unconformably above Stikine assemblage | Unknown contact relationships with Tsaybahe group | Unconformably atop Stikine plutonic suite and Stuhini Group |
| *Upper contact* | Unknown contact relationships with Stuhini Group | Unconformably overlain by Hazelton Group | Generally conformably overlain by Bowser Lk. Gp. sedimentary rocks |
| *Relationship to plutonic rocks* | Cut by Stikine plutonic suite and younger intrusions | Cut by Stikine plutonic suite and younger intrusions | Cut by Three Sisters plutonic suite and younger intrusions |
| *Magnetic susceptibility* | Low ($0.88 \times 10^{-3}$ SI units for volcanic unit) | High ($23 \times 10^{-3}$ SI units for volcanic unit) | Variable |
| *Aeromagnetic signature* | Low | High, variable | Variable |
| *Structure* | Open map-scale folds, no outcrop-scale folds observed | Open map-scale folds, no outcrop-scale folds observed | Homoclinal to subhorizontal |
| *Metamorphic grade* | Lower greenschist | Lower greenschist | Possibly no higher than prehnite-pumpellyite |
| *Age* | Anisian-Ladinian, basal sedimentary rocks as old as Olenekian | Carnian | Toarcian to Bajocian |
| *Tectonic interpretation* | Early volcanic arc (?) | Volcanic arc | Syncollisional volcanism |

Dease Lake, focussed on separating three temporally distinct, but texturally similar, mafic volcanic successions: the Tsaybahe group (Early-Middle Triassic), the Stuhini Group (Late Triassic) and the upper part of the Hazelton Group (late Early to Middle Jurassic). We separate Tsaybahe volcanic rocks from those of the Stuhini Group, based on their stratigraphic position atop the Stikine assemblage (upper Paleozoic), rare Middle Triassic biostratigraphic ages, low magnetic susceptibility and low response on regional aeromagnetic surveys. In contrast, Stuhini Group rocks have a high magnetic susceptibility and display a high and variable response on regional aeromagnetic surveys.

The Tsaybahe group is unusual in northern Stikinia because it is older than most Triassic volcanic successions. Throughout northern Stikinia, augite-phyric mafic volcanic rocks have largely been assigned to the Stuhini Group where sparse biostratigraphic data suggest a mostly Late Triassic age. However, large tracts mapped as Stuhini Group lack age constraints. Rare documented Early-Middle Triassic exposures throughout northern Stikinia contain mainly fine-grained siliciclastic rocks which, in the Dease Lake area, are overlain by significant accumulations of Middle Triassic mafic volcanic rocks. These scattered occurrences of sedimentary rocks may represent rare remnants of an Early-Middle Triassic marine basin, followed by localized, or perhaps largely unrecognized, Middle Triassic volcanism representing the onset of arc volcanism before widespread Upper Triassic Stuhini arc activity. The onset of Tsaybahe group volcanism appears to coincide with the end of mafic and bimodal intra-oceanic arc volcanism in the Cache Creek terrane, and may suggest initiation of subduction below Stikinia resulting from an inboard jump of the subduction zone.

## Acknowledgments

We thank Natashia Drage and Sadye Butler for their capable and enthusiastic assistance during the field season, and Tundra Helicopters for safe flying. Previously unpublished mapping by Jim Logan, Larry Diakow, Olivia Iverson and David Moynihan in 2011 provided additional data for the Latham and Pallen Creek study area. Quartz Mountain Resources Ltd. are acknowledged for permission to use field data collected by the first author in 2012 while employed by Hunter Dickinson Inc. Thanks to Esther Bordet and JoAnne Nelson for constructive commentary that significantly improved the manuscript.

## References cited

Aeroquest Airborne, 2012. Report on a helicopter-borne magnetic survey (Aeroquest Job #11-046) for Geoscience BC. Geoscience BC Report 2012-2, 11 p.

Aikins, H.S., 1971. Tanzilla Explorations Ltd., kay, king, ko and king fr. mineral claims, Geological report - diamond drilling. British Columbia Ministry of Energy, Mines and Petroleum Resources, Assessment Report 3372, 10 p.

Anderson, R.G., and Bevier, M.L., 1992. New Late Triassic and Early Jurassic U-Pb zircon ages from the Hotailuh batholith, Cry Lake map area, north - central British Columbia. In: Radiogenic age and isotopic studies: Report 6, Geological Survey of Canada, Paper 92–02, pp. 145-152.

Andrzejewski, A., Willes, C., and Rebagliati, M., 2012. Assessment report on geochemical work on the Galaxie property. British Columbia Ministry of Energy, Mines and Petroleum Resources, Assessment Report 33349, 24 p.

Andrzejewski, A., and Bui, P., 2012. Geochemical, and geophysical work on the Galaxie property. British Columbia Ministry of Energy, Mines and Petroleum Resources, Assessment Report 33659, 39 p.

BC Department of Mines and Petroleum Resources, 1972. Geology, Exploration and Mining in British Columbia. 718 p.

BC Department of Mines and Petroleum Resources, 1973. Geology, Exploration and Mining in British Columbia. 718 p.

Bickerton, L., 2014. The northern Cache Creek terrane: record of Middle Triassic arc activity and Jurassic-Cretaceous terrane imbrication. Unpublished M.Sc. thesis, Simon Fraser University, Burnaby, BC, Canada, 89 p.

Bordet, E., in press. Bedrock geology map of the east Lake Laberge area; parts of Teslin Mountain (105E/6), Lake Laberge (NTS 105E/3), Lower Laberge (NTS 105E/2), Mason Landing (NTS 105E/7), Joe Mountain (NTS 105D/15) and Mount M'Clintock (NTS 105D/16). Yukon Geological Survey, Geoscience Map 2019-1, 1:50,000 scale.

Bordet, E., Crowley, J.L., and Piercey S.J., in press. Geology of the east Lake Laberge area (105E), south central Yukon. Yukon Geological Survey, Open File 2019-1.

Brown, D.A., Gunning, M.H., and Greig, C.J., 1996. The Stikine project: Geology of western Telegraph Creek map area, northwestern British Columbia. British Columbia Ministry of Employment and Investment, British Columbia Geological Survey Bulletin 95, 130 p.

Childe, F.C., and Thompson, J.F.H., 1997. Geological setting, U-Pb geochronology, and radiogenic isotopic characteristics of the Permo-Triassic Kutcho assemblage, north-central British Columbia. Canadian Journal of Earth Sciences, 34, 1310-1324.

Childe, F.C., Thompson, J.F.H., Mortensen, J.K., Friedman, R.M., Schiarizza, P., Bellefontaine, K., and Marr, J.M., 1998. Primitive Permo-Triassic volcanism in the Canadian Cordillera tectonic and metallogenic implications. Economic Geology, 93, 224-231.

Cohen, K.M., Finney, S.C., Gibbard, P.L., and Fan, J.-X., 2013. The ICS International Chronostratigraphic Chart. Episodes, 36, 199–204. Updated version (August, 2018) available from http://www.stratigraphy.org/.

Colpron, M., Crowley, J.L., Gehrels, G., Long, D.G.F., Murphy, D.C., Beranek, L., and Bickerton, L., 2015. Birth of the northern Cordilleran orogen, as recorded by detrital zircons in Jurassic synorogenic strata and regional exhumation in Yukon. Lithosphere, 7, 541-562.

Downing, B.W., 1980. Geochemical, geophysical and geological report on the Stikine moly property. British Columbia Ministry of Energy Mines and Petroleum Resources, Assessment Report 8505, 75 p.

English, J.M., Mihalynuk, M.G., and Johnston, S.T., 2010. Geochemistry of the northern Cache Creek terrane and implications for accretionary processes in the Canadian Cordillera. Canadian Journal of Earth Sciences, 47, 13-34.

Evenchick, C.A., McMechan, M.E., McNicoll, V.J., and Carr, S.D., 2007. A synthesis of the Jurassic–Cretaceous tectonic evolution of the central and southeastern Canadian Cordillera: Exploring links across the orogen. In: Sears, J.W., Harms, T.A., and Evenchick, C.A. (Eds.), Whence the Mountains? Inquiries into the Evolution of Orogenic Systems: A volume in Honor of Raymond A. Price. Geological Society of America Special Paper, 433, 117-145.

Fominoff, P.J., and Adamson, R., 1971. Report on magnetometer and induced polarization surveys, Crown property, Dease Lake Area. British Columbia Ministry of Energy Mines and Petroleum Resources, Assessment Report 3422, 17 p.

Gabrielse, H., 1998. Geology of Cry Lake and Dease Lake map areas, north-central British Columbia. Geological Survey of Canada, Bulletin 504, 147 p.

Gillespie, M.R., and Styles, M.T., 1999. BGS rock classification scheme. Volume 1. Classification of igneous rocks. British Geological Survey Research Report RR99-06, 52 p.

Golding, M.L., Orchard, M.J., and Zagorevski, A., 2017. Conodonts from the Stikine terrane in northern British Columbia and southern Yukon. Geological Survey of Canada, Open File 8278, 23 p.

Hallsworth, C.R., and Knox, R.W.O., 1999. BGS rock classification scheme. Volume 3. Classification of sediments and sedimentary rocks. British Geological Survey Research Report RR99-03, 44p.

Iverson, O., Mahoney, J.B., and Logan, J.M., 2012. Dease Lake geoscience project, part IV: Tsaybahe group: Lithological and geochemical characterization of Middle Triassic volcanism in the Stikine arch, north-central British Columbia. In: Geological Fieldwork 2011, British Columbia Ministry of Energy, Mines and Natural Gas, British Columbia Geological Survey Paper 2012-1, pp. 17-22.

Kretz, R., 1983. Symbols for rock-forming minerals. American Mineralogist, 68, 227-279.

Logan, J.M., and Iverson, O., 2013. Dease Lake geoscience project: Geochemical characterization of Tsaybahe, Stuhini and Hazelton volcanic rocks, northwestern British Columbia (NTS 104I, J). In: Summary of Activities 2012, Geoscience BC Report 2013-1, pp. 11-32.

Logan, J.M., and Koyanagi, V.M., 1994. Geology and mineral deposits of the Galore Creek area. British Columbia Ministry of Energy, Mines and Petroleum Resources, British Columbia Geological Survey Bulletin 92, 96 p.

Logan, J.M., and Mihalynuk, M.G., 2014. Tectonic controls on Early Mesozoic paired alkaline porphyry deposit belts (Cu-Au+/-Ag-Pt-Pd-Mo) within the Canadian Cordillera. Economic Geology, 109, 827-858.

Logan, J.M., Moynihan, D.P., and Diakow, L.J., 2012a. Dease Lake geoscience project, Part I: Geology and mineralization of the Dease Lake (NTS 104J/08) and East-Half of the Little Tuya River (NTS 104J/07E) map sheets, northern British Columbia. In: Geological Fieldwork 2011, British Columbia Ministry of Energy, Mines and Natural Gas, British Columbia Geological Survey Paper 2012-1, pp. 23-44.

Logan, J.M., Moynihan, D.P., Diakow, L.J., and van Straaten, B.I., 2012b. Dease Lake - Little Tuya River geology (NTS 104J/08, 07E). British Columbia Ministry of Energy, Mines and Natural Gas, British Columbia Geological Survey Open File 2012-04, scale: 1:50,000.

Luckman, N., and Kuttai, J., 2012. Induced polarization survey on the Tanzilla-Pliny property, British Columbia Ministry of Energy Mines and Petroleum Resources, Assessment Report 32714, 7 p.

Luckman, N., 2013. Soil geochemical survey on the Pliny property. British Columbia Ministry of Energy Mines and Petroleum Resources, Assessment Report 34550, 17 p.

Marsden, H., and Thorkelson, D.J., 1992. Geology of the Hazelton Volcanic Belt in British Columbia: Implications for the Early to Middle Jurassic evolution of Stikinia. Tectonics, 11, pp. 1266-1287.

McGoldrick, S., Zagorevski, A., and Canil, D., 2017. Geochemistry of volcanic and plutonic rocks from the Nahlin ophiolite with implications for a Permo-Triassic arc in the Cache Creek terrane, northwestern British Columbia. Canadian Journal of Earth

Sciences, 54, 1214-1227.
Mihalynuk, M.G., 1999. Geology and Mineral Resources of the Tagish Lake Area, (NTS 104M/8,9,10E, 15 and 104N/12W), Northwestern British Columbia. British Columbia Ministry of Energy and Mines, British Columbia Geological Survey Bulletin 105, 202 p.
Mihalynuk, M.G., Nelson, J., and Diakow, L.J., 1994. Cache Creek terrane entrapment: Oroclinal paradox within the Canadian Cordillera. Tectonics, 13, 575-595.
Mihalynuk, M.G., Meldrum, D.G., Sears, S., and Johannson, G., 1995. Geology and mineralization of the Stuhini Creek area. In: Geological Fieldwork 1994, British Columbia Ministry of Energy, Mines and Petroleum Resources, British Columbia Geological Survey Paper 1995-1, pp. 321-342.
Mihalynuk, M.G., Johnston, S.T., English, J.M., Cordey, F., Villeneuve, M.E., Rui, L., and Orchard, M.J., 2003. Atlin TGI, Part II: Regional geology and mineralization of the Nakina area (NTS 104N/2W and 3). In: Geological Fieldwork 2002, British Columbia Ministry of Energy and Mines, British Columbia Geological Survey Paper 2003-1, pp. 9-38.
Nelson, J., and Mihalynuk, M., 1993. Cache Creek ocean: Closure or enclosure? Geology, 21, 173-176.
Nelson, J., Colpron, M., and Israel, S., 2013. The Cordillera of British Columbia, Yukon and Alaska: tectonics and metallogeny. In: Colpron, M., Bissig, T., Rusk, B., and Thompson, J. F. H. (Eds.), Tectonics, metallogeny and discovery: The North American Cordillera and similar accretionary settings., Society of Economic Geologists, Special Publication 17, pp. 53-109.
Nixon, G.T., Ash, C.H., Connelly, J.N., and Case, G., 1989. Alaskan-type mafic-ultramafic rocks in British Columbia: The Gnat Lakes, Hickman, and Menard Creek complexes. In: Geological Fieldwork 1988, British Columbia Ministry of Energy, Mines and Petroleum Resources, British Columbia Geological Survey Paper 1989-1, pp. 429-442.
Nixon, G.T., Hammack, J.L., Ash, C.A., Cabri, L.J., Case, G., Connelly, J.N., Heaman, L.M., Laflamme, J.H.G., Nuttall, C., Paterson, W.P.E., and Wong, R.H., 1997. Geology and platinum-group-element mineralization of Alaskan-type ultramafic-mafic complexes in British Columbia. British Columbia Ministry of Employment and Investment, British Columbia Geological Survey Bulletin 93, 150 p.
Read, P.B., 1983. Geology, Classy Creek (104J/2E) and Stikine Canyon (104J/1W), British Columbia. Geological Survey of Canada, Open File 940, 1:50,000 scale.
Read, P.B., 1984. Geology, Klastine River east (104G/16E), Ealue Lake west (104H/13W), Cake Hill west (104I/4W) and Stikine Canyon east (104J/1E), British Columbia. Geological Survey of Canada, Open File 1080, 1:50,000 scale.
Read, P.B., Brown, R.L., Psutka, J.F., Moore, J.M., Journeay, M., Lane, L.S., and Orchard, M.J., 1989. Geology, More and Forrest Kerr creeks (parts of 104B/10,15,16 & 104G/1,2). Geological Survey of Canada, Open File 2094, 1:50,000 scale.
Read, P.B., and Psutka, J.F., 1990. Geology of Ealue Lake east-half (104H/13E) and Cullivan Creek (104H/14) map areas, British Columbia. Geological Survey of Canada, Open File 2241, 1:50,000 scale.
Schiarizza, P., 2011. Geology of the Kutcho assemblage between the Kutcho Creek and the Tucho river, northern British Columbia (NTS 104I/01). In: Geological Fieldwork 2010, British Columbia Ministry of Energy and Mines, British Columbia Geological Survey Paper 2011-1, pp. 99-118.
Schiarizza, P., 2012a. Geology of the Kutcho assemblage between the Kehlechoa and Tucho Rivers, northern British Columbia (NTS 104I/01, 02). In: Geological Fieldwork 2011, British Columbia Ministry of Energy and Mines, British Columbia Geological Survey Paper 2012-1, pp. 75-98.
Schiarizza, P., 2012b. Bedrock geology of the upper Kutcho Creek area (parts of NTS 104I/01, 02). British Columbia Ministry of Energy and Mines, British Columbia Geological Survey Open File 2012-8, 1:50,000 scale.
Scott, D.M., 1970. Tanzilla Explorations Ltd, King and King/Box groups, Report on geological, geochemical, and geophysical work. British Columbia Ministry of Energy Mines and Petroleum Resources, Assessment Report 2766, 12 p.
Souther, J.G., 1971. Geology and mineral deposits of Tulsequah map area, British Columbia (104K). Geological Survey of Canada, Memoir 362, 59 p.
Souther, J.G., 1972. Telegraph Creek map-area, British Columbia (104G). Geological Survey of Canada, Paper 71-44, Map 11-1971, 38 p.
Stevens, R.D., DeLabio, R.N., and Lachance, G.R., 1982. Age determinations and geological studies, K-Ar isotopic ages, Report 16. Geological Survey of Canada, Paper 82-2, 56 p.
Tipper, H.W., and Richards, T.A., 1976. Jurassic stratigraphy and history of north-central British Columbia. Geological Survey of Canada; Bulletin 270, 82 p.
van Straaten, B.I., and Bichlmaier, S., 2018a. Late Early to Middle Jurassic Hazelton Group volcanism and its tectonic setting, McBride River area, northwest British Columbia. In: Geological Fieldwork 2017, British Columbia Ministry of Energy and Mines, British Columbia Geological Survey Paper 2018-1, pp. 39-66.
van Straaten, B.I., and Bichlmaier, S.J., 2018b. Preliminary bedrock geology of the McBride River area (parts of NTS Sheets 104H/14,15; 104I/02, 03, 06). British Columbia Ministry of Energy, Mines and Petroleum Resources, British Columbia Geological Survey Open File 2018-3, 1:50,000 scale.
van Straaten, B.I., and Gibson, R., 2017. Late Early to Middle Jurassic Hazelton Group volcanism and mineral occurrences in the McBride-Tanzilla area, northwest British Columbia. In: Geological Fieldwork 2016, British Columbia Ministry of Energy Mines and Petroleum Resources, British Columbia Geological Survey Paper 2017-1, pp. 83-115.
van Straaten, B.I., and Nelson, J.L., 2016. Syncollisional late Early to early Late Jurassic volcanism, plutonism, and porphyry-style alteration on the northeastern margin of Stikinia. In: Geological Fieldwork 2015, British Columbia Ministry of Energy and Mines, British Columbia Geological Survey Paper 2016-1, pp. 113-143.
van Straaten, B.I., Logan, J.M., and Diakow, L.J., 2012. Mesozoic magmatism and metallogeny of the Hotailuh Batholith, northwestern British Columbia. British Columbia Ministry of Energy, Mines and Natural Gas, British Columbia Geological Survey Open File 2012-06, 58 p.
van Straaten, B.I., Gibson, R., and Nelson, J.L., 2017. Preliminary bedrock geology of the Tanzilla and McBride area (NTS 104I/03,04,05,06). British Columbia Ministry of Energy, Mines and Petroleum Resources, British Columbia Geological Survey Open File 2017-9, 1:50,000 scale.
Wheeler, J.O., 1967. Tectonics. In: Canadian Upper Mantle Report, Geological Survey of Canada, Paper 67–41, pp. 3-59.
Zagorevski, A., Corriveau, A.-S., McGoldrick, S., Bédard, J.H., Canil, D., Golding, M.L., Joyce, N., and Mihalynuk, M.G., 2015. Geological framework of ancient oceanic crust in northwestern British Columbia and southwestern Yukon, GEM 2 Cordillera. Geological Survey of Canada, Open File 7957, 12 p.
Zagorevski, A., Mihalynuk, M.G., McGoldrick, S., Bedard, J.H., Golding, M., Joyce, N., Lawley, C., Canil, D., Corriveau, A.-S., Bogatu, A., and Tremblay, A., 2016. Geological framework of ancient oceanic crust in northwestern British Columbia and southwestern Yukon: GEM 2 Cordillera. Geological Survey of Canada, Open File 8140, 13 p.

# Age constraints for rocks hosting massive sulphide mineralization at Rock and Roll and Granduc deposits between Iskut and Stewart, British Columbia

Mitchell G. Mihalynuk[1, a], Alexandre Zagorevski[2], James M. Logan[3], Richard M. Friedman[4], and Stephen T. Johnston[5]

[1] British Columbia Geological Survey, Ministry of Energy, Mines and Petroleum Resources, Victoria, BC, V8W 9N3
[2] Geological Survey of Canada, Ottawa, ON, K1A 0E8
[3] JLoGeologic, Victoria, BC, V8L 5Z9
[4] Pacific Centre for Isotopic and Geochemical Research, The University of British Columbia, Vancouver, BC, V6T 1Z4
[5] Earth & Atmospheric Science, University of Alberta, Edmonton, AB, T6G 2E1
[a] corresponding author: Mitch.Mihalynuk@gov.bc.ca

Recommended citation: Mihalynuk, M.G., Zagorevski, A., Logan, J.M., Friedman, R.M., and Johnston, S.T., 2019. Age constraints for rocks hosting massive sulphide mineralization at Rock and Roll and Granduc deposits between Iskut and Stewart, British Columbia. In: Geological Fieldwork 2018, British Columbia Ministry of Energy, Mines and Petroleum Resources, British Columbia Geological Survey Paper 2019-01, pp. 97-111.

**Abstract**

U-Pb geochronological results reported here for host rocks of the Rock and Roll and Granduc volcanogenic massive sulphide (VMS) deposits in the Iskut area of northwestern British Columbia are consistent with the Late Triassic age suggested by previous workers. Although a direct age determination is still lacking, we constrain mineralization to between ~222 Ma and <~208 Ma for Granduc and 292 Ma to 186 Ma for Rock and Roll. The Late Triassic age may mark an important VMS mineralizing event within the submarine Stuhini arc, with implications for regional mineral exploration. Data from this study also provides constraints on two phases of superimposed deformation to between 210 Ma and 183 Ma.

**Keywords:** Volcanogenic massive sulphide, VMS, Besshi, Rock and Roll, Iskut, Granduc, geochronology, detrital zircon, Stuhini Group, Late Triassic

## 1. Introduction

Most prominent Late Triassic-Early Jurassic mineral deposits in the Stikine terrane (Stikinia) of northwestern British Columbia are calc-alkaline and alkaline Cu-Au-Mo porphyries and porphyry-related gold veins (e.g., Logan and Mihalynuk, 2014). Paleozoic and Early Mesozoic volcanogenic massive sulphide (VMS) deposits are much less common but are economically significant. They include past-producing mines such as Tulsequah Chief (Late Mississippian; Childe, 1997), Eskay Creek (Middle Jurassic, Aalenian; Childe, 1996) and Granduc (Late Triassic; Childe, 1997). VMS deposits form as accumulations of base metals in hydrothermal fields near active submarine magmatic centers. VMS prospective environments, such as ocean ridges, and volcanic arc and back arc rifts and calderas, tend to produce clusters or belts of economic deposits (e.g., Galley et al., 2007), making identification of prospective time periods a key criterion in VMS exploration. Unfortunately, the lack of a detailed stratigraphic and geochronological framework for much of northwestern British Columbia hinders exploration away from known occurrences. In this contribution, we present new geochronological data from host rocks at the Granduc mine and the Rock and Roll VMS deposit (Figs. 1, 2).

Granduc is a Besshi-type massive sulphide Cu-Au-Ag deposit (Höy, 1991) located 40 km north-northwest of Stewart (Fig. 1). Between 1971 and 1984 Granduc produced 190,143.7 tonnes Cu, 124 million g Ag and 2 million g Au (Johnson, 2012; MINFILE 104B021). At the Main Zone, Measured, Indicated and Inferred resources are 5.16, 6.16 and 30.52 million tonnes with grades of 1.58, 1.39, and 1.40% Cu, 0.17 g/t Au, and 13.7, 11.4 and 13.3 g/t Ag (Morrison et al., 2013). Including the North Zone, total Inferred resources are 44.6 million tonnes grading 1.43% Cu, 0.19 g/t Au, and 10.7 g.t Ag; all at a 0.8% Cu-equivalent cut-off grade (Morrison et al., 2013).

Granduc was considered to be Late Triassic based on U-Pb dating of multi-grain zircon fractions separated from crosscutting mafic dikes and intensely sheared mafic igneous rocks within the 'Mine Series' (Childe, 1997). However, the dikes are restricted to the footwall of the deposit and may not be coeval with mineralization. In addition, the relationship of the 'Mine Series' sample to mineralization is uncertain due to intense deformation.

Lead isotopic ages are not quantitative, however, they can be used as a guide to the relative age of mineralization. Lead isotope signatures from Granduc sulphide mineralization (Childe, 1997) overlap of the $^{208}Pb/^{204}Pb$ cluster for the ~327 Ma Tulsequah VMS camp, but the $^{207}Pb/^{204}Pb$ cluster also overlaps data from the Schaft Creek porphyry copper deposit (Logan et al., 2000), which is well constrained as Late Triassic

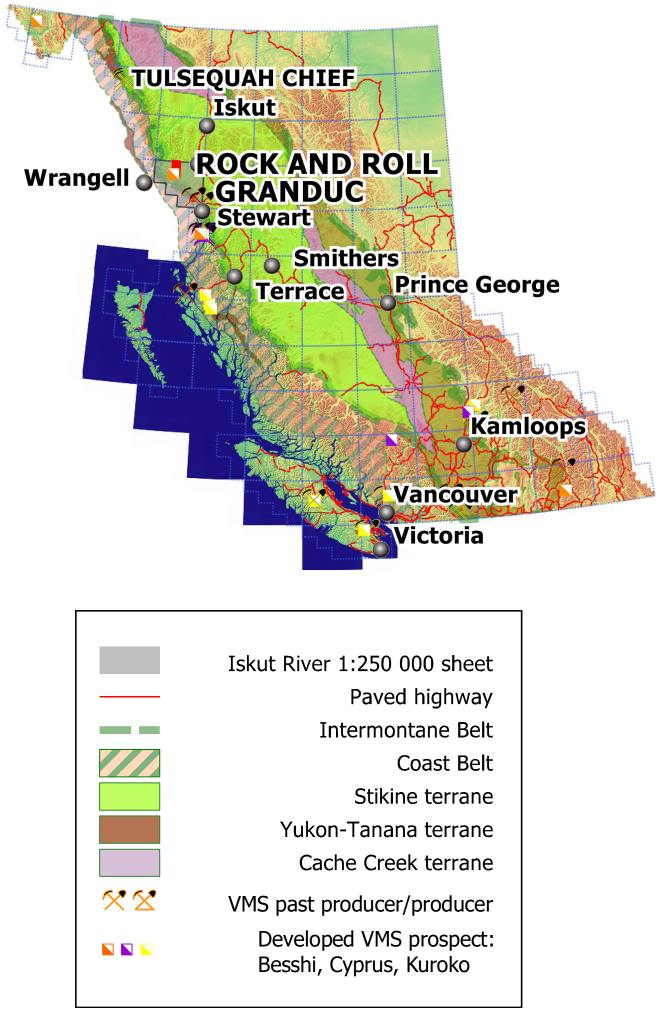


**Fig. 1.** Location of Rock and Roll and Granduc VMS deposits in northwest British Columbia. Terrane map modified after Wheeler et al. (1991).

by U-Pb dating of its host intrusive body (Scott et al., 2008). Thus, ambiguity remains as to whether Granduc lies within the Stikine assemblage (Upper Paleozoic) or the Stuhini Group (Upper Triassic).

Rock and Roll is a precious metal-rich polymetallic massive sulphide deposit (Montgomery et al., 1991) along the south side of the lower Iskut River valley (Fig. 2a), approximately 115 km northwest of Stewart. It contains an estimated Indicated resource of 2.155 million tonnes grading 0.68 g/t Au, 82.7 g/t Ag, 0.22% Cu, 0.22% Pb, and 0.94% Zn at an Au-equivalent cut-off grade of 0.5 g/t (Jones, 2011).

Geological mapping northeast of the Iskut River showed that layered rocks considered at the time to be part of the Stikine assemblage were lithologically more similar to rocks enclosing mineralization at the Rock and Roll deposit than they were to rocks of the Stuhini Group (Mihalynuk et al., 2010). However, geochronological and paleontological data to test this correlation, or to provide a direct age constraint on Rock and Roll mineralization, were lacking.

To address uncertainties regarding the age of the Granduc and Rock and Roll deposits, we collected samples of quartz-bearing clastic strata to establish maximum depositional ages using detrital zircon geochronology. In addition, we collected volcanic layers in the host stratigraphy and quartz diorite (that intrudes and shows irregular contacts with massive sulphide at Rock and Roll) for conventional CA-TIMS age determinations (Table 1). We also collected sulphide samples to determine suitability for Re-Os dating, but found these sulphides to be Re impoverished and unsuitable for dating.

## 2. Previous work and study rationale

'Mine Series' strata at Granduc include distinctive graphitic and tuffaceous limestone, laminated chert, mafic tuff, black argillite, heterolithic breccia (Fig. 3), and sulphides comprising 200-500 hundred metres of deformed section (Fig. 2b; Klepacki and McGuigan, unpublished map cited in McGuigan, 2005). The ~222 Ma age of the Granduc deposit is based on three U-Pb zircon age determinations that overlap within error (Childe, 1997). This age implies that Granduc is hosted by strata that are age equivalent to the Stuhini Group (Lewis, 2013), but these strata differ from the typical Stuhini Group, which is commonly characterized by augite-porphyritic volcanic rocks, polymictic conglomerate and other volcanic-derived sedimentary rocks,

**Table 1.** Synopsis of samples analyzed for geochronology and results.

| Sample | Description | Longitude | Latitude | Age (Ma) | Comment |
|---|---|---|---|---|---|
| *Rock and Roll* | | | | | |
| TST09-3-05 | Rhyolite lapilli tuff band in limestone | -131.2314 | 56.7143 | 209.7±0.9 | LA-ICP-MS (data in Mihalynuk et al., 2019) |
| TST09-3-02 | Rhyolite tuff and pyritic rhyolite tuff | -131.2323 | 56.7111 | | insufficient zircon recovery |
| TST09-3-16 | Cherty ash tuff | -131.2251 | 56.7143 | 291.7±1.0 | CA-TIMS, weighted average of 3 concordant and overlapping $^{206}Pb/^{238}U$ dates. |
| TST09-6-11 | Diorite | -131.2315 | 56.7184 | 185.6±0.5 | CA-TIMS, Maximum age of Based on $^{206}Pb/^{238}U$ date of youngest of 3 analyzed grain |
| TST09-7-01 | Felsic dike, DDH RR-91-70, 5.2-12.2m | -131.2289 | 56.7188 | 182.9±0.2 | CA-TIMS, weighted average of 4 concordant and overlapping $^{206}Pb/^{238}U$ dates. |
| *Granduc* | | | | | |
| 10JLO-10-51 | heterolithic breccia | -130.3505 | 56.1990 | | LA-ICP-MS (data in Mihalynuk et al., 2019) |

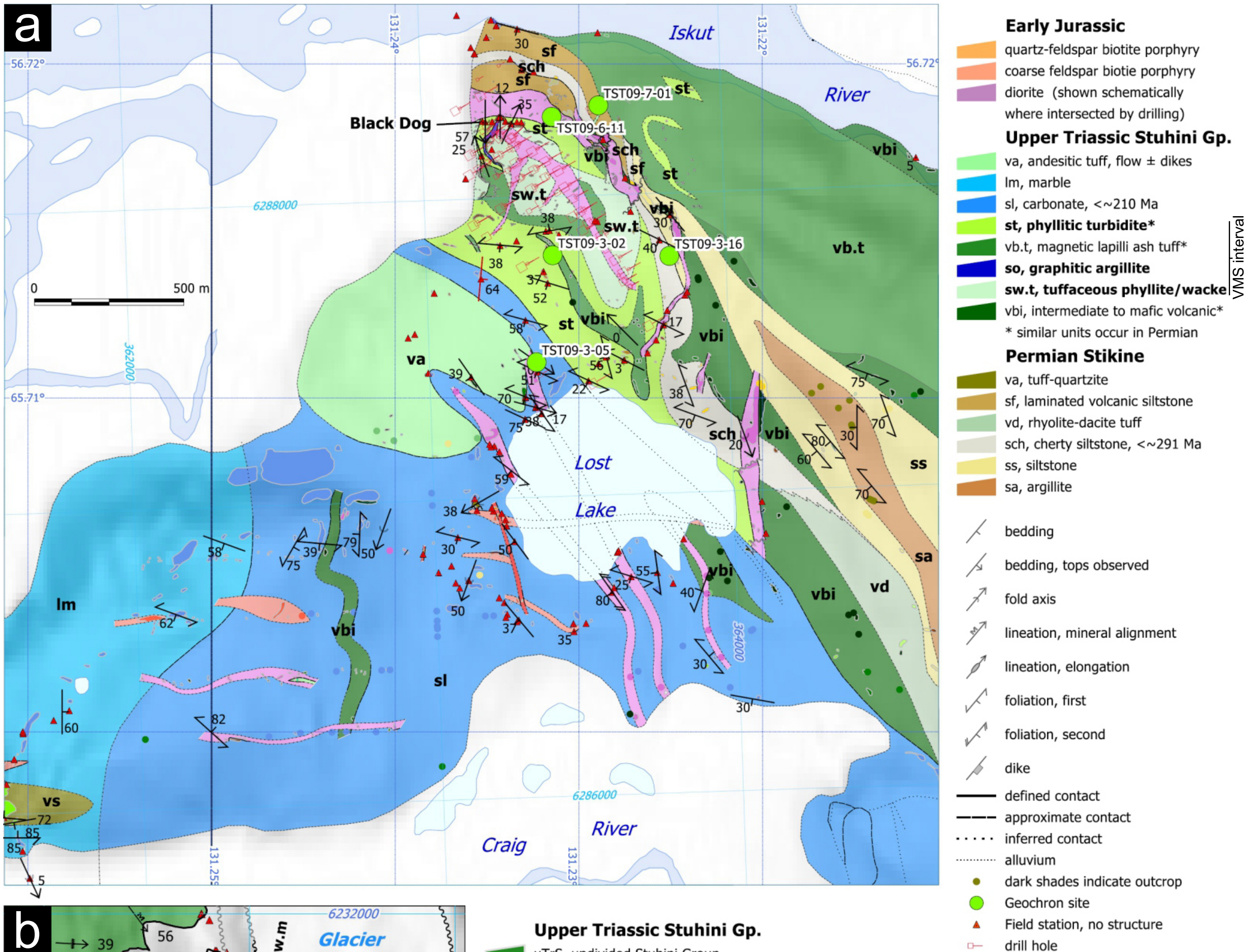


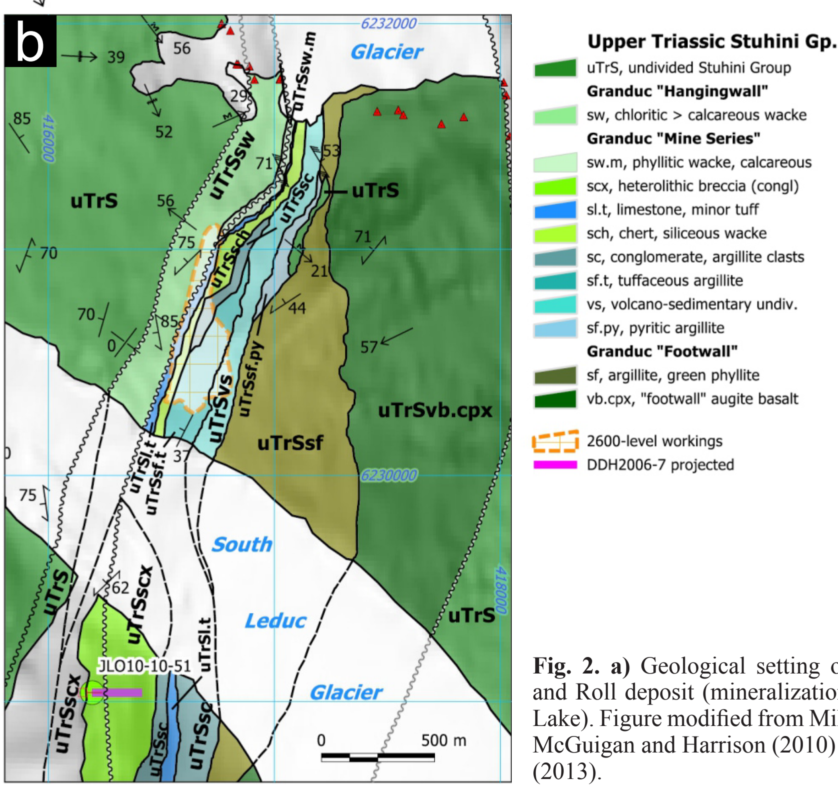


**Fig. 2. a)** Geological setting of samples collected for geochronology near the Rock and Roll deposit (mineralization outlined by concentration of drill holes north of Lost Lake). Figure modified from Mihalynuk et al. (2010). **b)** Map information compiled from McGuigan and Harrison (2010) in Morrison et al. (2013) and structural data from Lewis (2013).

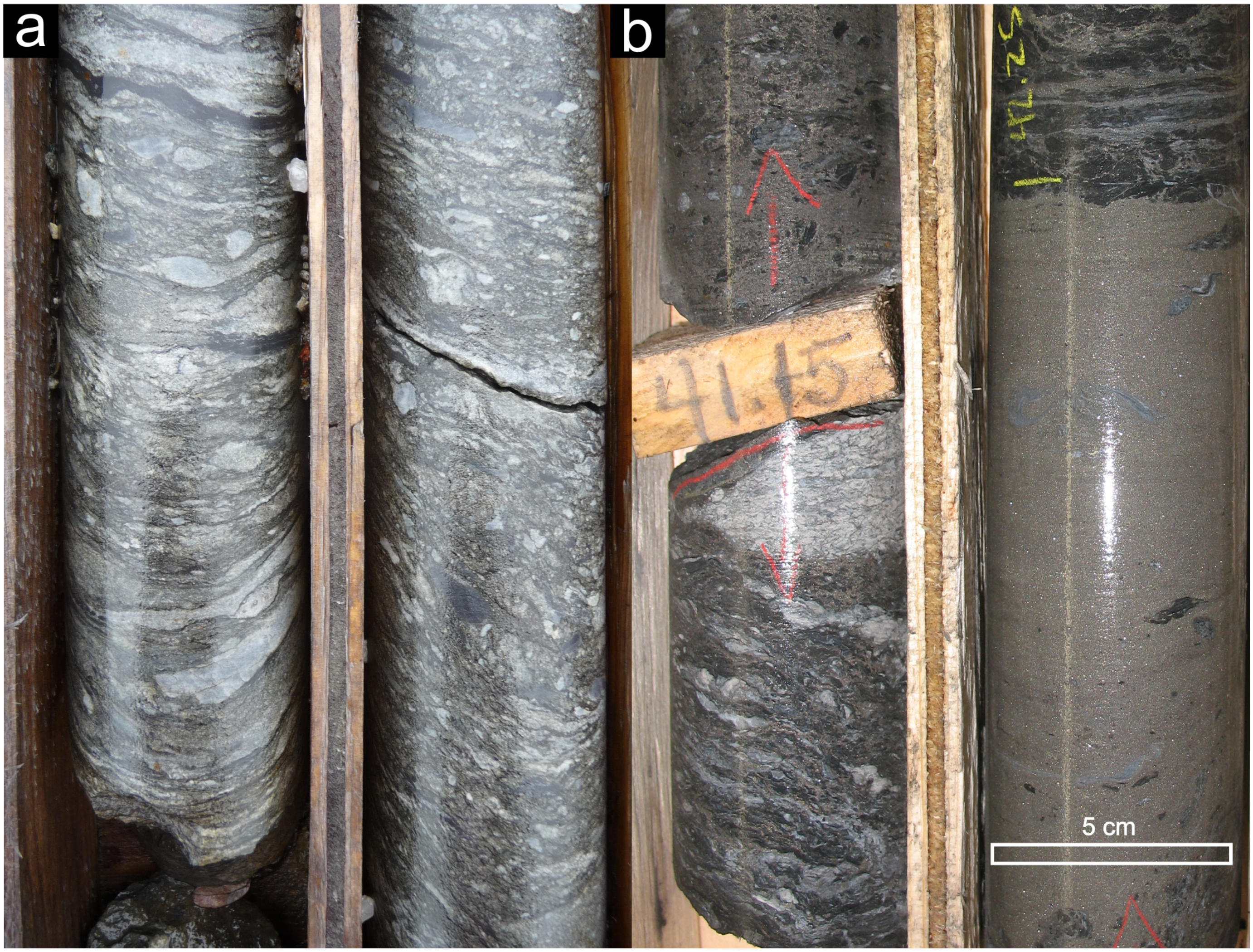


**Fig. 3.** A visual comparison of mineralized foliated heterolithic breccia units. **a)** Granduc deposit drill hole 2006-7, interval submitted for detrital zircon age determination**. b)** Rock and Roll deposit drill hole RR09-107, with carbonaceous argillite (top right) and massive sulphide (mid and lower right).

and limestone. Thus, establishing a Late Triassic age for these strata is important because the Granduc Mine sequence is a distinctive succession and, if within the Stuhini Group, would be a useful regional target for VMS mineral exploration.

Re-evaluating the Granduc samples that were collected for U-Pb zircon geochronology by Childe (1997), we conclude that they are possibly all of intrusive rather than volcanic origin. A drill core sample of quartz diorite sill in the deposit footwall yielded a 223 ±3 Ma weighted mean $^{207}$Pb/$^{206}$Pb age (Childe, 1997). The second drill core sample described as "...chlorite-altered basaltic composition flow, with poorly preserved metamorphic hornblende crystals...", also from the footwall (Childe, 1997; p. 59), yielded a 223 ±5 Ma weighted mean $^{207}$Pb/$^{206}$Pb age. Both samples produced discordant data. A third sample of "an intensely sheared rock of basaltic andesitic composition..." was collected from surface within the mineralized section. It yielded three fractions of partly resorbed (pitted and ovoid) zircons. Childe (1997) interpreted a crystallization age of 222 ±1 Ma from the concordant $^{206}$Pb/$^{238}$U ages of the three fractions. However, none of the dated samples preserve unequivocal volcanic protolith textures. All rock types sampled could be intrusive rocks that cut older strata of the succession. Therefore, we sampled strata in the immediate hangingwall of the mineralization for detrital zircons to obtain a maximum depositional age for the top of the host succession.

At the Rock and Roll prospect, previous geological investigations failed to establish the age of mineralization. Host strata are volcanogenic sedimentary rocks, sandstones, and a predominance of argillaceous to cherty strata with minor heterolithic breccia and carbonaceous argillite, which are associated with sulphide mineralization (Fig. 3). These rocks were interpreted as Triassic, overthrust by polydeformed limestone (Figs. 2a, 4) that was correlated with Paleozoic limestone elsewhere (Kerr, 1948; Mihalynuk et al., 2010). Mineralization was interpreted as stratiform (Montgomery et al., 1991). Association of stratiform mineralization with felsic volcanic rocks and high Cu-Zn (e.g., Kuroko style) suggest a syngenetic, VMS-style mineralization (Mihalynuk et al.,

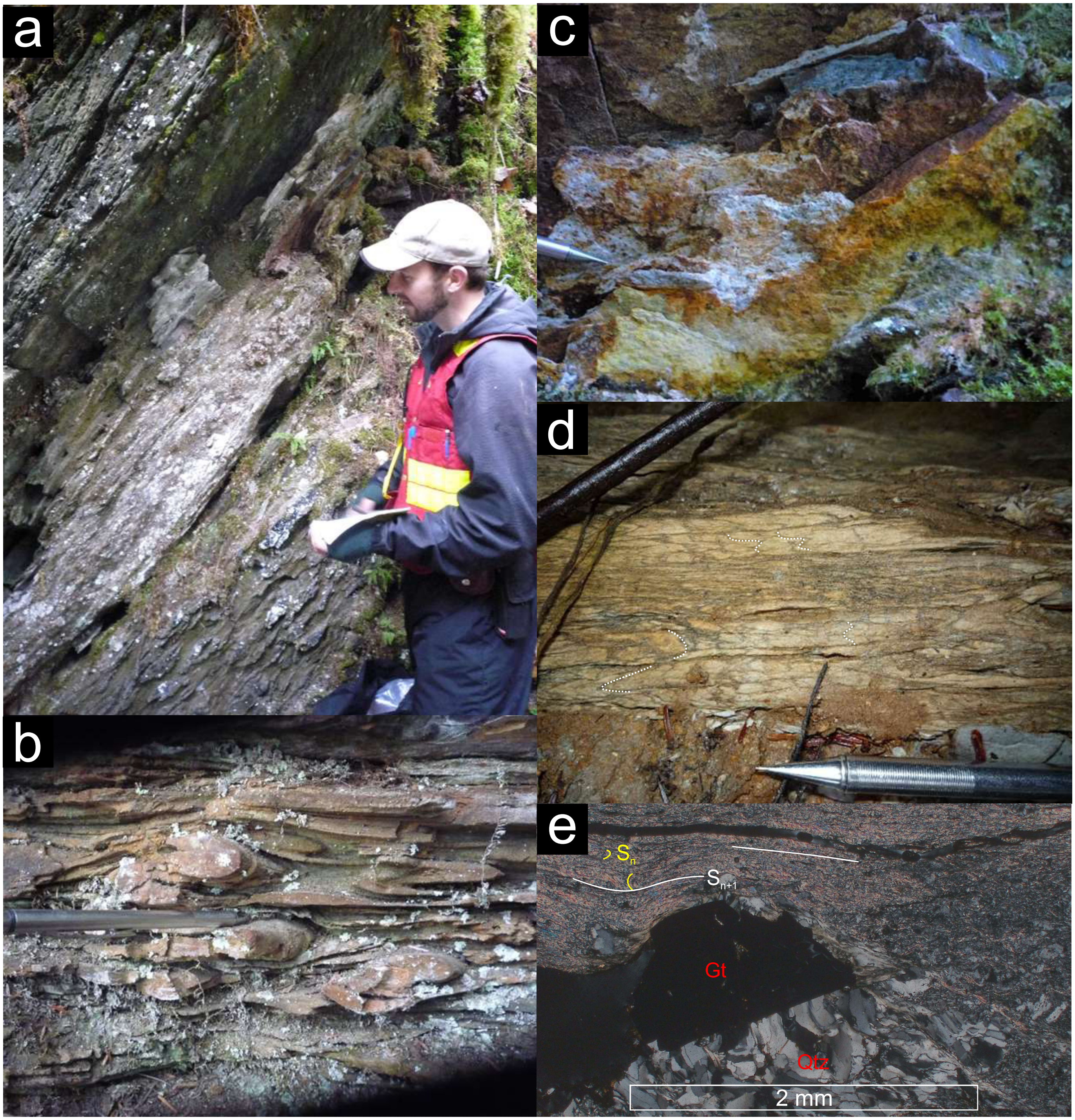


**Fig. 4.** Rock and Roll area. **a)** Outcrop of limestone with tuffaceous interbeds, like those sampled for geochronology. **b)** Limestone with isoclinal, locally rootless, folds delineated by differential weathering of resistant silty layers. Pen aligned with fold hinges. **c)** Bleached, pyritic zone of thickest tuff layer preferentially sampled for U-Pb age determination. **d)** A second phase penetrative cleavage in carbonate rocks (parallel to pen) is developed at a high angle to the earlier fabric (highlighted by dotted white curves). **e)** Photomicrograph of pyritic felsic tuff layer in limestone shows two penetrative fabrics intersecting at a high angle (Sn and Sn+1). A quartz (Qtz) pressure shadow formed as the pyrite grain rotated. Iron oxide/hydroxide, possibly goethite (Gt) pseudomorphs pyrite.

2010; Foley, 1991, unpublished report cited in Jones, 2011). Mineralization is cut by diorite dikes and sills up to tens of metres thick that locally contain sulphide apophyses and enclaves remobilized from the host volcano-sedimentary rock (Fig. 5a). If Rock and Roll is a syngenetic sulphide deposit, the age of enclosing strata should constrain the maximum age of that mineralization, whereas the age of the diorite would provide a minimum age of mineralization. We sampled both the host stratigraphy and crosscutting diorite for geochronology.

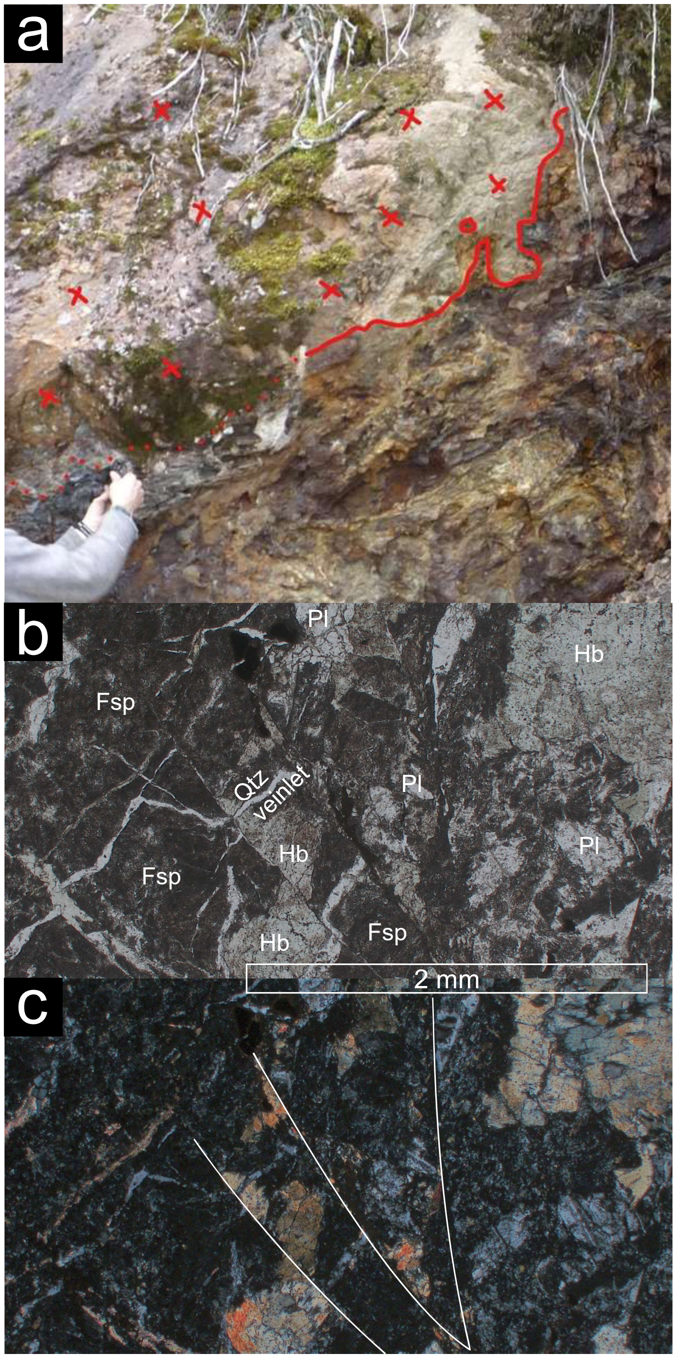


**Fig. 5. a)** Diorite cutting mineralized graphitic siltstone at the Black Dog occurrence, northwestern Rock and Roll deposit. Light-weathering massive diorite (above red line with red "x" pattern) cuts contorted, rusty, carbonaceous mudstone with massive pyrrhotite-sphalerite-chalcopyrite layers that are rusty, black orange and yellow-weathering. **b)** Plain polarized light photomicrographs of the diorite showing typically altered, turbid feldspar (Fsp) and less abundant, relatively fresh plagioclase (Pl), altered hornblende (Hb) and fine quartz veinlets (Qtz) that cut the rock along with microfaults showing variable offset. **c)** Same field of view as b) in cross polarized light; white lines highlight microfaults.

## 3. Methods

Sample preparation and analytical work for both the U-Pb Chemical Abrasion-Thermal Ionization Mass Spectrometry (CA-TIMS) and Laser Ablation-Inductively Coupled Mass Spectroscopy (LA-ICP-MS) isotopic ages presented herein was conducted at the Pacific Centre for Isotopic and Geochemical Research (PCIGR) at the Department of Earth and Ocean Sciences, The University of British Columbia. Zircon was separated from the samples (Table 1) using standard mineral separation techniques (crushing, grinding, Wilfley wet shaker table, heavy liquids and magnetic separation), followed by hand picking. Picked samples were microscopically evaluated to ensure purity (Fig. 6a, inset). Chemically abraded single zircon grains were analyzed.

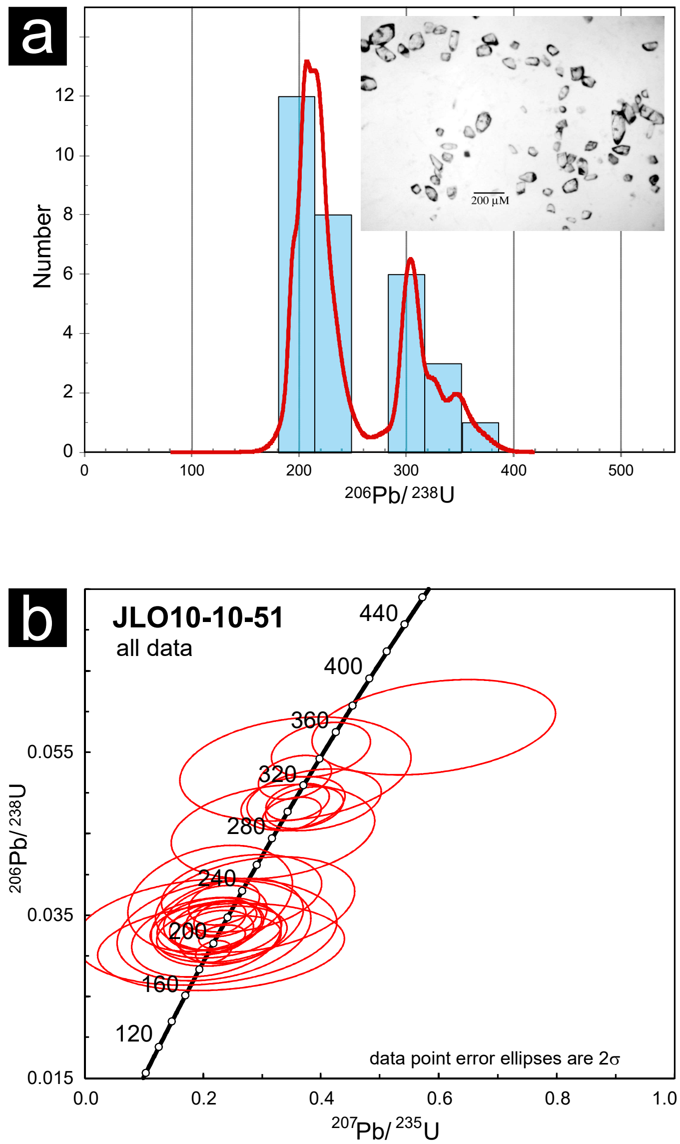


**Fig. 6. a)** Detrital zircon age histogram and distribution plot for detrital zircons obtained from heterolithic breccia within the Granduc mine stratigraphy (see Fig. 3 for sample analyzed). A representative zircon sample aliquot analyzed is shown in the inset. **b)** Concordia plot showing all of the analytical results with 2σ error envelopes.

### 3.1. CA-TIMS

CA-TIMS procedures described here are modified from Mundil et al. (2004), Mattinson (2005), and Scoates and Friedman (2008). After rock samples underwent standard mineral separation procedures, zircons were handpicked in alcohol. The clearest, crack- and inclusion-free grains were selected, photographed and then annealed in quartz glass crucibles at 900°C for 60 hours. Annealed grains were transferred into 3.5 mL PFA screw top beakers, ultrapure HF (up to 50% strength, 500 mL) and $HNO_3$ (up to 14N, 50 mL) were added and caps are closed finger tight. The beakers were placed in 125 mL PTFE liners (up to four per liner) and about 2 mL HF and 0.2 mL $HNO_3$ of the same strength as acid within beakers containing samples were added to the liners. The liners were then slid into stainless steel Parr™ high pressure dissolution devices, which were sealed and brought up to a maximum of 200°C for 8-16 hours (typically 175°C for 12 hours). Beakers were removed from liners and zircon was separated from leachate. Zircons were rinsed with >18 MΩ.cm water and subboiled acetone. Then 2 mL of subboiled 6N HCl was added and beakers were set on a hotplate at 80-130°C for 30 minutes and again rinsed with water and acetone. Masses were estimated from the dimensions (volumes) of grains. Single grains were transferred into clean 300 mL PFA microcapsules (crucibles), and 50 mL 50% HF and 5 mL 14N $HNO_3$ were added. Each was spiked with a $^{233\text{-}235}$U-$^{205}$Pb tracer solution (EARTHTIME ET535), capped and again placed in a Parr liner (8-15 microcapsules per liner). HF and nitric acids in a 10:1 ratio, respectively, were added to the liner, which was then placed in Parr high pressure device and dissolution was achieved at 240°C for 40 hours. The resulting solutions were dried on a hotplate at 130°C, 50 mL 6N HCl was added to microcapsules and fluorides were dissolved in high pressure Parr devices for 12 hours at 210°C. HCl solutions were transferred into clean 7 mL PFA beakers and dried with 2 mL of 0.5N $H_3PO_4$. Samples were loaded onto degassed, zone-refined Re filaments in 2 mL of silicic acid emitter (Gerstenberger and Haase, 1997).

Isotopic ratios were measured by a modified single collector VG-54R or 354S (with Sector 54 electronics) thermal ionization mass spectrometer equipped with analogue Daly photomultipliers. Analytical blanks are 0.2 pg for U and up to 3 pg for Pb. U fractionation was determined directly on individual runs using the EARTHTIME ET535 mixed $^{233\text{-}235}$U-$^{205}$Pb isotopic tracer and Pb isotopic ratios were corrected for fractionation of 0.23%/amu, based on replicate analyses of NBS-982 reference material and the values recommended by Thirlwall (2000). Data reduction employed the Excel-based program of Schmitz and Schoene (2007). Standard concordia diagrams were constructed and regression intercepts, weighted averages calculated with Isoplot (Ludwig, 2003). Unless otherwise noted, all errors are quoted at the 2 sigma or 95% level of confidence. Isotopic dates were calculated with the decay constants l238=1.55125E-10 and l235=9.8485E-10 (Jaffey et al., 1971). EARTHTIME U-Pb synthetic solutions were analysed on an on-going basis to monitor the accuracy of results.

### 3.2. LA-ICP-MS

LA-ICP-MS instrumentation included a New Wave UP-213 laser ablation system and a ThermoFinnigan Element2 single collector, double-focusing, magnetic sector ICP-MS. We used the data acquisition and reduction protocols detailed by Tafti et al. (2009), as summarized below. Zircons hand-picked from the heavy mineral concentrate were mounted in an epoxy puck along with grains of the Plešovice zircon standard (Sláma et al., 2008) and an in-house, 197 Ma standard zircon, and brought to a very high polish. High quality portions of each grain (free of alteration, inclusions, or possible inherited cores) were selected for analysis. The surface of the mount was washed for 10 minutes with dilute nitric acid and rinsed in ultraclean water before analysis. Line scans rather than spot analyses were employed to minimize elemental fractionation during the analyses. Backgrounds were measured with the laser shutter closed for ten seconds, followed by data collection with the laser firing for approximately 29 seconds. The time-integrated signals were analysed using GLITTER software (Van Actherbergh, 2001; Griffin, 2008), which automatically subtracts background measurements, propagates all analytical errors, and calculates isotopic ratios and ages. Corrections for mass and elemental fractionation were made by bracketing analyses of unknown grains with replicate analyses of the Plešovice zircon standard. A typical analytical session consisted of four analyses of the standard zircon, followed by four analyses of unknown zircons, two standard analyses, four unknown analyses, etc., and finally four standard analyses. The 197 Ma in-house zircon standard was analysed as an unknown to monitor the reproducibility of the age determinations on a run-to-run basis. Final interpretation and plotting of the analytical results used ISOPLOT software (Ludwig, 2003). Interpreted ages are based on a weighted average of the individual calculated $^{206}$Pb/$^{238}$U ages. Although zircons typically contain negligible amounts of initial common Pb, it is important to monitor the amount of $^{204}$Pb to evaluate the amount of initial common Pb, and/or blank Pb, in the zircons being analyzed. The argon that is used in an ICP-MS plasma commonly contains at least a small amount of Hg, and approximately 7% of natural Hg has a mass of 204. Measured count rates on mass 204 include $^{204}$Hg as well as any $^{204}$Pb that might be present, and direct measurement of $^{204}$Pb in a laser ablation analysis is therefore not possible. Instead, mass 202 is monitored; this corresponds exclusively to $^{202}$Hg. The expected count rate for $^{204}$Hg present in the analysis can then be calculated from the known isotopic composition of natural Hg, and any remaining counts at mass 204 can be attributed to $^{204}$Pb. Using this method, it is possible to conclude that there was no measurable $^{204}$Pb present in any of the analyses in this study.

## 4. Geochronology results

One sample was submitted from the mine succession at

Granduc, and five from host rocks and adjacent strata at the Rock and Roll deposit (one did not yield sufficient zircon). Uranium-lead isotopic age determinations obtained by LA-ICP-MS are plotted in Figures 6 and 7 (tabulated and ancillary data are presented in Mihalynuk et al., 2019); those obtained by CA-TIMS are listed in Tables 2, 3 and 4.

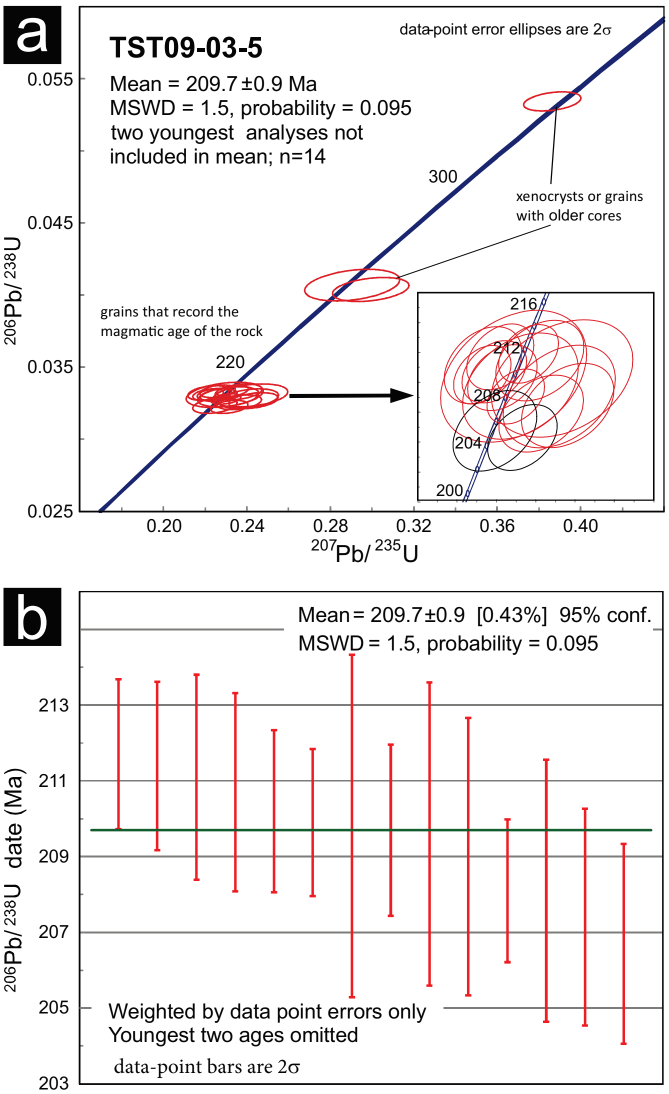


**Fig. 7. a)** Concordia plot for all zircons analyzed from sample TST09-03-5, a tuff band in deformed limestone from Rock and Roll. The inset shows details of the 14 data points used to calculate the age. **b)** Weighted mean $^{206}Pb/^{238}U$ age of 209.7 ±0.9 Ma calculated for the cluster of zircons in the inset.

### 4.1. Granduc

Clasts in heterolithic breccia of the mine series north and south of Leduc Glacier are primarily feldspar and lesser hornblende-feldspar porphyry. These strata have been included in the upper mine series and described as "green lapilli tuff, chert pebble conglomerate with a black calcareous matrix; minor dark green foliated volcanics" (Morrison et al., 2013, p. 68). Owing to the angularity of competent clasts in the sample analyzed, we refer to it as a breccia. The sample is a green volcanic clast-rich rock with a fine ash-rich matrix and includes minor black argillite and light coloured, rusty-weathering pyrite and pyrrhotite-veined clasts; strained incompetent altered clasts are aligned along the fabric and appear rounded (Fig. 3a).

Sample 10JLO-10-51 was collected from a 0.6 m interval (6.3 to 6.9 m) from fresh, cut core of diamond drill hole 2006-7 (azimuth 090°, inclined -58°, end of hole 389.9 m; McGuigan and Harrison, 2010, unpublished report cited in Morrison et al., 2013) that intersected mine series heterolithic breccia south of the Leduc Glacier (Fig. 2b). Historic drilling within this unit in the south zone intersected massive sulphide layers with true thicknesses of ~4-7 m and grading between 3 and 4% Cu (Morrison et al., 2013).

Abundant clear, doubly terminated zircons and fragments (Fig. 6a inset) were separated from the sample. Analysis of the zircons produced a spectrum of dates with a main peak at ~208 Ma, and a secondary peak at ~304 Ma. Several zircons yielded ages between ~325 and 348 Ma. The juvenile, mainly volcanic provenance of the units suggests that the ~208 Ma age broadly represents the depositional age of the sediment. In addition, we interpret mineralized clasts in the heterolithic breccia unit as either indicating deposition that is coeval with mineralization or representing eroded or collapsed parts of an anoxic, subaqueous mineralized or mineralizing volcano-hydrothermal system. Thus, the heterolithic breccia age should broadly date VMS mineralization. The biotite and chlorite alteration displayed by the sample may be related to the same hydrothermal system or may be unrelated and due to later igneous intrusion and thermal metamorphism.

### 4.2. Rock and Roll

#### 4.2.1. Tuff band in limestone sample TST09-3-05, 209.7 ±0.9 Ma

Strongly foliated and folded limestone west and northwest of Lost Lake (Fig. 2a) was previously considered to be Permian (Kerr, 1948). It contains layers packed with green lapilli and ash-sized clasts (Fig. 4a) and local resistant silty layers (Figs. 4a, b). The tuffaceous layers are typically less than 10 cm thick, although the sampled tuff layer is about 50 cm thick and pyritic, grading into pyritic carbonate. Pyrite grains within this layer display horizontal elongation in a southeast-northwest direction. Where sampled, the thick tuff layer is white and rust-weathering, possibly more felsic than other tuff layers (Fig. 4c).

Of the zircons separated from the sample, twenty grains were selected for LA-ICP-MS analysis. Fourteen of these grains define a mean $^{206}Pb/^{238}U$ age of 209.7 ±0.9 Ma (95% confidence, Fig. 7). This age is considered to represent the crystallization age of the tuff, coeval with the surrounding limestone. This age is consistent at the stage level with late Carnian to early Norian conodont ages (Golding et al., 2017) from limestone along strike, north of the Iskut River. At the substage level, the ~210 Ma age is younger than the conodont-bearing strata, because the early-middle Norian boundary is age calibrated at 224 Ma in British Columbia (Diakow et al., 2012) and globally (Kent et al., 2017 and citations therein). This suggests that

**Table 2.** U-Th-Pb isotopic data for sample TST09-3-16.

| | Compositional Parameters | | | | | | | | | Radiogenic Isotope Ratios | | | | | | | | | Isotopic Ages | | | | | |
|---|---|---|---|---|---|---|---|---|---|---|---|---|---|---|---|---|---|---|---|---|---|---|---|
| Sample | Wt. mg | U ppm | $\frac{Th}{U}$ | Pb ppm | $^{206}Pb^*$ $x10^{-13}$ mol | mol % $^{206}Pb^*$ | $\frac{Pb^*}{Pb_c}$ | Pb (pg) | $\frac{^{206}Pb}{^{204}Pb}$ | $\frac{^{208}Pb}{^{206}Pb}$ | $\frac{^{207}Pb}{^{206}Pb}$ | % err | $\frac{^{207}Pb}{^{235}U}$ | % err | $\frac{^{206}Pb}{^{238}U}$ | % err | corr. coef. | $\frac{^{207}Pb}{^{206}Pb}$ | ± | $\frac{^{207}Pb}{^{235}U}$ | ± | $\frac{^{206}Pb}{^{238}U}$ | ± |
| (a) | (b) | (c) | (d) | (c) | (e) | (e) | (e) | (e) | (f) | (g) | (g) | (h) | (g) | (h) | (g) | (h) | | (i) | (h) | (i) | (h) | (i) | (h) |
| **TST09-3-16** | | | | | | | | | | | | | | | | | | | | | | | |
| A | 0.0016 | 42 | 0.370 | 3.1 | 0.1285 | 85.56% | 2 | 1.78 | 128 | 0.118 | 0.052288 | 5.493 | 0.333028 | 5.833 | 0.046193 | 0.428 | 0.808 | 298.01 | 125.31 | 291.87 | 14.80 | 291.11 | 1.22 |
| B | 0.0014 | 33 | 0.483 | 2.9 | 0.0908 | 80.55% | 1 | 1.80 | 95 | 0.154 | 0.052606 | 7.880 | 0.336709 | 8.363 | 0.046421 | 0.593 | 0.828 | 311.84 | 179.30 | 294.68 | 21.39 | 292.51 | 1.69 |
| C | 0.0009 | 24 | 0.372 | 3.1 | 0.0414 | 65.31% | 1 | 1.81 | 53 | 0.122 | 0.054434 | 16.690 | 0.349883 | 17.722 | 0.046618 | 1.276 | 0.821 | 389.04 | 374.64 | 304.63 | 46.64 | 293.72 | 3.66 |
| D | 0.0013 | 255 | 0.340 | 15.8 | 0.7750 | 97.06% | 10 | 1.93 | 630 | 0.108 | 0.053775 | 0.990 | 0.415445 | 1.077 | 0.056031 | 0.164 | 0.584 | 361.64 | 22.33 | 352.79 | 3.21 | 351.44 | 0.56 |
| E | 0.0009 | 57 | 0.368 | 4.1 | 0.1032 | 87.40% | 2 | 1.22 | 147 | 0.114 | 0.051342 | 5.266 | 0.338763 | 5.588 | 0.047854 | 0.447 | 0.740 | 256.23 | 121.02 | 296.23 | 14.36 | 301.33 | 1.32 |

(a) A, B etc. are labels for fractions composed of single zircon grains or fragments; all fractions annealed and chemically abraded after Mattinson (2005) and Scoates and Friedman (2008).
(b) Nominal fraction weights estimated from photomicrographic grain dimensions, adjusted for partial dissolution during chemical abrasion.
(c) Nominal U and total Pb concentrations subject to uncertainty in photomicrographic estimation of weight and partial dissolution during chemical abrasion.
(d) Model Th/U ratio calculated from radiogenic $^{208}Pb/^{206}Pb$ ratio and $^{207}Pb/^{235}U$ age.
(e) Pb* and Pbc represent radiogenic and common Pb, respectively; mol% $^{206}Pb^*$ with respect to radiogenic, blank and initial common Pb.
(f) Measured ratio corrected for spike and fractionation only. Mass discrimination of 0.23%/amu based on analysis of NBS-982; all Daly analyses.
(g) Corrected for fractionation, spike, and common Pb; up to 3 pg of common Pb was assumed to be procedural blank: $^{206}Pb/^{204}Pb = 18.50 \pm 1.0\%$; $^{207}Pb/^{204}Pb = 15.50 \pm 1.0\%$; $^{208}Pb/^{204}Pb = 38.40 \pm 1.0\%$ (all uncertainties 1-sigma). Excess over blank was assigned to initial common Pb with S-K model Pb composition at 291 Ma.
(h) Errors are 2-sigma, propagated using the algorithms of Schmitz and Schoene (2007) and Crowley et al. (2007).
(i) Calculations are based on the decay constants of Jaffey et al. (1971). $^{206}Pb/^{238}U$ and $^{207}Pb/^{206}Pb$ ages corrected for initial disequilibrium in $^{230}Th/^{238}U$ using Th/U [magma] = 3.
(j) Corrected for fractionation, spike, and blank Pb only.

**Table 3.** U-Th-Pb isotopic data for sample TST09-6-11.

| | Compositional Parameters | | | | | | | | | Radiogenic Isotope Ratios | | | | | | | | | Isotopic Ages | | | | | |
|---|---|---|---|---|---|---|---|---|---|---|---|---|---|---|---|---|---|---|---|---|---|---|---|
| Sample | Wt. mg | U ppm | $\frac{Th}{U}$ | Pb ppm | $^{206}Pb^*$ $x10^{-13}$ mol | mol % $^{206}Pb^*$ | $\frac{Pb^*}{Pb_c}$ | Pb (pg) | $\frac{^{206}Pb}{^{204}Pb}$ | $\frac{^{208}Pb}{^{206}Pb}$ | $\frac{^{207}Pb}{^{206}Pb}$ | % err | $\frac{^{207}Pb}{^{235}U}$ | % err | $\frac{^{206}Pb}{^{238}U}$ | % err | corr. coef. | $\frac{^{207}Pb}{^{206}Pb}$ | ± | $\frac{^{207}Pb}{^{235}U}$ | ± | $\frac{^{206}Pb}{^{238}U}$ | ± |
| (a) | (b) | (c) | (d) | (c) | (e) | (e) | (e) | (e) | (f) | (g) | (g) | (h) | (g) | (h) | (g) | (h) | | (i) | (h) | (i) | (h) | (i) | (h) |
| **TST09-6-11** | | | | | | | | | | | | | | | | | | | | | | | |
| A | 0.0010 | 487 | 0.977 | 22.4 | 0.7463 | 97.58% | 14 | 1.50 | 764 | 0.308 | 0.050505 | 1.774 | 0.256056 | 1.822 | 0.036771 | 0.204 | 0.290 | 218.28 | 41.05 | 231.48 | 3.77 | 232.79 | 0.47 |
| B | 0.0012 | 658 | 1.165 | 25.4 | 0.9620 | 97.19% | 12 | 2.28 | 658 | 0.371 | 0.049821 | 1.158 | 0.200602 | 1.253 | 0.029203 | 0.262 | 0.451 | 186.63 | 26.96 | 185.64 | 2.13 | 185.56 | 0.48 |
| C | 0.0002 | 2026 | 1.070 | 93.7 | 0.6086 | 97.49% | 14 | 1.28 | 736 | 0.338 | 0.050402 | 1.235 | 0.250296 | 1.301 | 0.036017 | 0.221 | 0.375 | 213.57 | 28.61 | 226.82 | 2.64 | 228.10 | 0.49 |

Notes as in Table 2, except as follows:
(g) Corrected for fractionation, spike, and common Pb; up to 3 pg of common Pb was assumed to be procedural blank: $^{206}Pb/^{204}Pb = 18.50 \pm 1.0\%$; $^{207}Pb/^{204}Pb = 15.50 \pm 1.0\%$; $^{208}Pb/^{204}Pb = 38.40 \pm 1.0\%$ (all uncertainties 1-sigma). Excess over blank was assigned to initial common Pb with S-K model Pb composition at 185 Ma.

**Table 4.** U-Th-Pb isotopic data for sample TST09-7-01.

| | Compositional Parameters | | | | | | | | | Radiogenic Isotope Ratios | | | | | | | | | Isotopic Ages | | | | | |
|---|---|---|---|---|---|---|---|---|---|---|---|---|---|---|---|---|---|---|---|---|---|---|---|
| Sample | Wt. mg | U ppm | $\frac{Th}{U}$ | Pb ppm | $^{206}Pb^*$ $x10^{-13}$ mol | mol % $^{206}Pb^*$ | $\frac{Pb^*}{Pb_c}$ | Pb (pg) | $\frac{^{206}Pb}{^{204}Pb}$ | $\frac{^{208}Pb}{^{206}Pb}$ | $\frac{^{207}Pb}{^{206}Pb}$ | % err | $\frac{^{207}Pb}{^{235}U}$ | % err | $\frac{^{206}Pb}{^{238}U}$ | % err | corr. coef. | $\frac{^{207}Pb}{^{206}Pb}$ | ± | $\frac{^{207}Pb}{^{235}U}$ | ± | $\frac{^{206}Pb}{^{238}U}$ | ± |
| (a) | (b) | (c) | (d) | (c) | (e) | (e) | (e) | (e) | (f) | (g) | (g) | (h) | (g) | (h) | (g) | (h) | | (i) | (h) | (i) | (h) | (i) | (h) |
| **TST09-7-01** | | | | | | | | | | | | | | | | | | | | | | | |
| A | 0.0067 | 100 | 0.415 | 3.5 | 0.7995 | 94.16% | 5 | 4.08 | 317 | 0.132 | 0.049804 | 1.902 | 0.197524 | 2.047 | 0.028764 | 0.337 | 0.498 | 185.86 | 44.27 | 183.03 | 3.43 | 182.81 | 0.61 |
| B | 0.0067 | 174 | 0.467 | 5.3 | 1.3967 | 99.13% | 34 | 1.00 | 2134 | 0.149 | 0.050031 | 0.570 | 0.198494 | 0.648 | 0.028775 | 0.180 | 0.545 | 196.42 | 13.24 | 183.85 | 1.09 | 182.87 | 0.32 |
| C | 0.0081 | 103 | 0.620 | 3.4 | 1.0191 | 98.07% | 16 | 1.65 | 956 | 0.197 | 0.049800 | 1.622 | 0.200778 | 1.747 | 0.029241 | 0.269 | 0.527 | 185.66 | 37.75 | 185.78 | 2.97 | 185.79 | 0.49 |
| D | 0.0084 | 181 | 0.406 | 5.4 | 1.8269 | 99.26% | 40 | 1.11 | 2504 | 0.129 | 0.049582 | 0.482 | 0.197267 | 0.597 | 0.028856 | 0.300 | 0.599 | 175.45 | 11.24 | 182.81 | 1.00 | 183.38 | 0.54 |
| E | 0.0020 | 366 | 0.570 | 12.0 | 0.8774 | 97.66% | 13 | 1.73 | 791 | 0.180 | 0.049258 | 1.235 | 0.195337 | 1.338 | 0.028762 | 0.229 | 0.520 | 160.11 | 28.88 | 181.17 | 2.22 | 182.79 | 0.41 |

Notes as in Table 2, except as follows:
(g) Corrected for fractionation, spike, and common Pb; up to 3 pg of common Pb was assumed to be procedural blank: $^{206}Pb/^{204}Pb = 18.50 \pm 1.0\%$; $^{207}Pb/^{204}Pb = 15.50 \pm 1.0\%$; $^{208}Pb/^{204}Pb = 38.40 \pm 1.0\%$ (all uncertainties 1-sigma). Excess over blank was assigned to initial common Pb with S-K model Pb composition at 183 Ma.

limestone at Lost Lake was deposited over a protracted (>10 m.y.) period.

#### 4.2.2. Cherty siltstone
#### sample TST09-3-16, 291.7 ±1.0 Ma

Laminated, cream to rusty weathering, cherty, tuffaceous siltstone with a structural thickness of up to 100 m occurs to the north and east of Lost Lake (Fig. 2a). This tuffaceous siltstone (Fig. 8a) appears to grade to the southeast into felsic lapilli tuff. Other parts of the unit include cherty layers within fine siltstone, and argillite with siliceous ovoids interpreted as recrystallized radiolaria (Fig. 8b). We collected a sample from an outcrop of suspected rhyolitic dust tuff (near outcrop of Fig. 8a) to test for age equivalence with other tuffaceous layers, but petrographic analysis revealed little definitive evidence of volcanic textures.

Of the zircons separated from the sample, five were selected for CA-TIMS analysis. Three concordant and overlapping $^{206}Pb/^{238}U$ dates produced a weighted average age of 291.7 ±1.0 Ma; two older concordant analyses are interpreted as recording older sources or xenocrystic cores (Fig. 9). The 291.7 ±1.0 Ma age is interpreted as the crystallization age of the predominant source of the tuffaceous siltstone. This age is ~80 m.y. older than the other ages reported here and thus its significance is unclear. One possibility is that the sample is from a Triassic sequence that was predominantly derived from an Early Permian and older basement with $^{206}Pb/^{238}U$ ages of 301 ±1 Ma and 351.4 ±0. 6 Ma, such as igneous basement identified regionally by, for example, Logan et al. (2000). We consider this unlikely because it would require the depocentre be shielded somehow from sediments shed from the active Stuhini arc, which are amply represented by zircon-bearing Triassic volcanic and plutonic rocks regionally. An alternative and more likely explanation is that this rock is part of the Stikine assemblage (Paleozoic) and that there is either an unconformity or an unrecognized fault in this area.

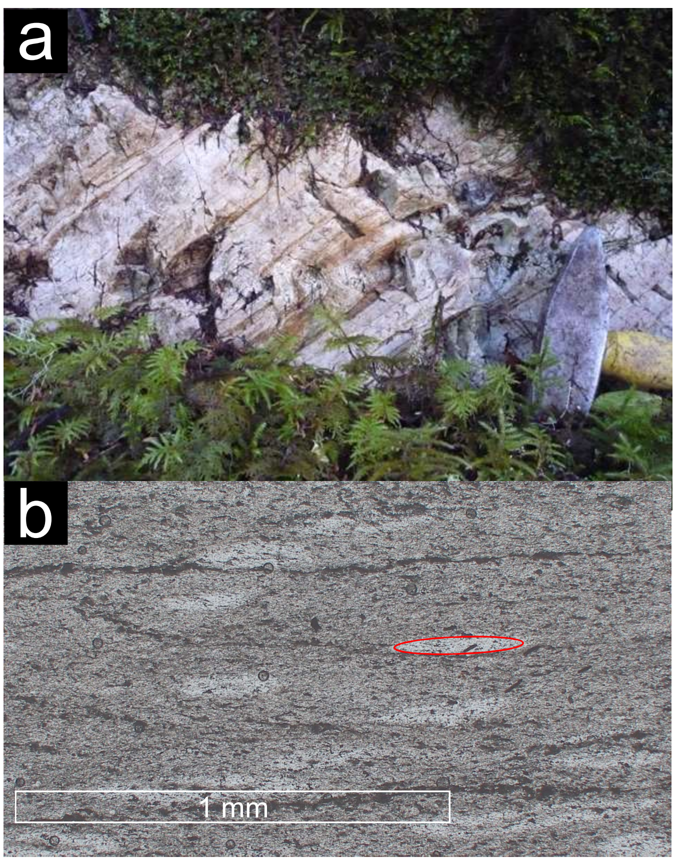


**Fig. 8. a)** Representative outcrop of cherty, tuffaceous siltstone at Rock and Roll like that sampled for age determination (Sample TST09-3-16). **b)** Plane polarized light photomicrograph of cherty and silty argillite sample. Clear ovoids (one highlighted by red oval) are interpreted as recrystallized radiolaria.

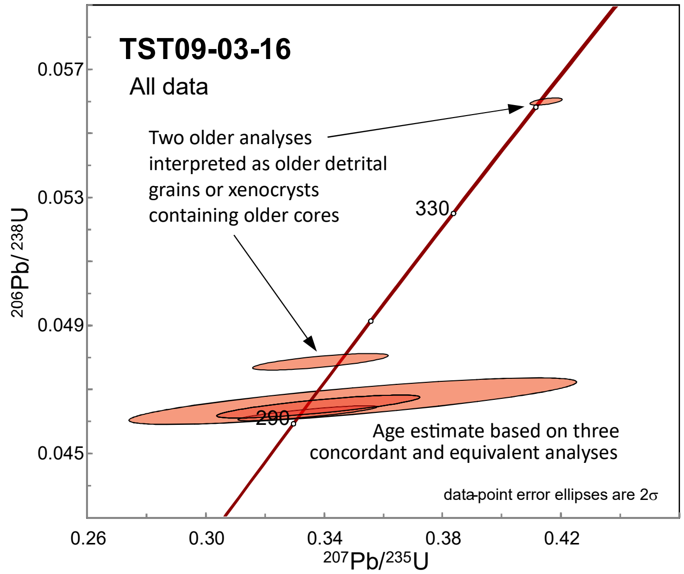


**Fig. 9.** Concordia plot of five grains analyzed by CA-TIMS from sample TST09-3-16. An age of the sample of 291.7 ±1.0 Ma is interpreted based on three overlapping and equivalent dates.

#### 4.2.3. Diorite
#### sample TST09-6-11, 185.6 ±0.5 Ma

Variably foliated, dark green and light grey-weathering diorite sills and dikes up to 50 m thick cut all lithologies around Lost Lake and form resistant rounded to blocky outcrops (Fig. 5a). Dikes are predominantly parallel and perpendicular to northwest-trending folds (Fig. 2a). A sample of medium-grained, hornblende-feldspar-titanite quartz diorite (~5% interstitial quartz) was sampled near the main Black Dog showing at the Rock and Roll property for CA-TIMS dating. The sample yielded very few zircons, and only three grains survived chemical abrasion pre-treatment intact. TIMS analysis of these grains produced a maximum age based on $^{206}Pb/^{238}U$ date of the youngest grain of 185.6 ±0.5 Ma (Fig. 10). This age is interpreted as the crystallization age of the quartz diorite, and because these dikes cut sulphide mineralization at the Black Dog occurrence (Fig. 2a), it provides an absolute minimum age for the mineralization.

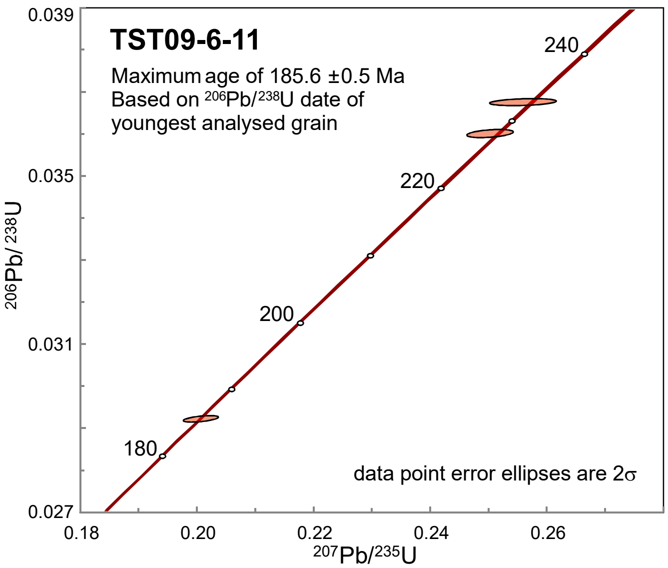


**Fig. 10.** Concordia plot of three grains analyzed by CA-TIMS from sample TST09-6-11. A maximum age of the sample of 185.6 ±0.5 Ma is interpreted based on the youngest grain.

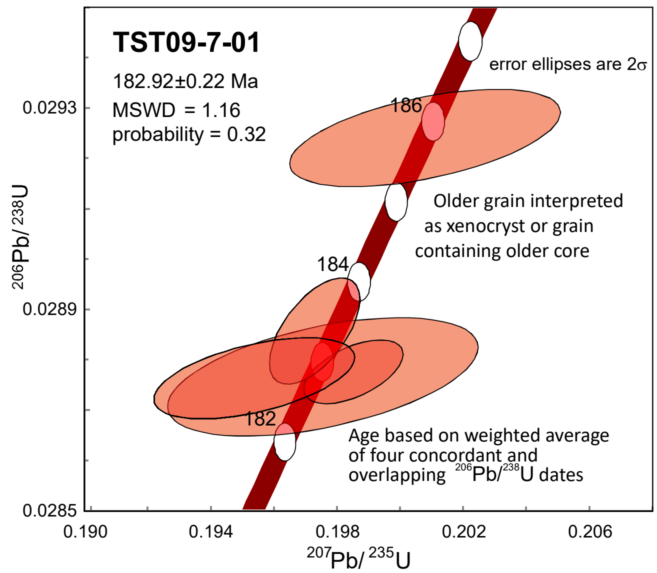


**Fig. 12.** Concordia plot of five grains analyzed by CA-TIMS from sample TST09-7-01. A relatively precise age of the sample of 182.92 ±0.22 Ma is interpreted based on four overlapping and equivalent dates.

### 4.2.4. Rhyodacitic dike sample TST09-7-01, 182.92 ±0.22 Ma

Diamond drill hole RR91-70 (Fig. 2a) north of Lost Lake intersected an interval of felsic rock within the laminated volcanic siltstone unit. Split core was retrieved from a 7 m interval (5.2-12.2 m) for dating. Petrographic analysis of a subsample shows preservation of delicate trachytic fabric with no sign of the penetrative foliation seen in all other samples (Fig. 11). The petrography and lack of foliation suggests that the felsic rock is likely a dike that cuts the laminated volcanic siltstone. Of the zircons separated from the sample, four grains were analysed by CA-TIMS producing concordant and overlapping dates with a $^{206}Pb/^{238}U$ weighted age of 182.92 ±0.22 Ma (Fig. 12). We interpret this as the crystallization age of a dike that postdates deformation. A slightly older ~186 Ma grain is interpreted as a xenocryst or a grain containing an older core, perhaps derived from one of the widespread diorite dikes of this age.

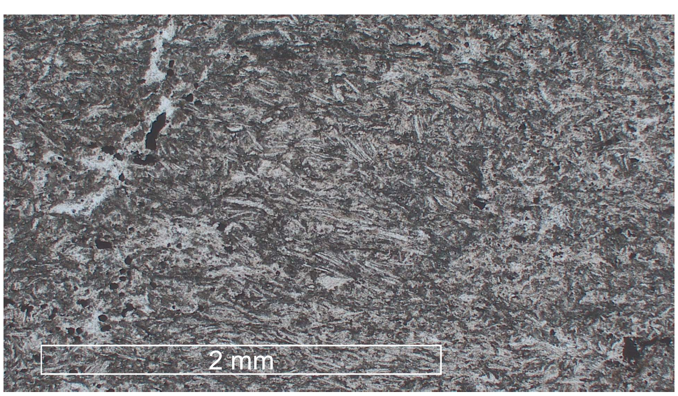


**Fig. 11.** Fine trachytic texture preserved in sample TST09-7-01 is outlined by feldspar microlites.

### 4.2.5. Rhyolite tuff and pyritic rhyolite tuff sample TST09-3-02, no age determination

Laminated, black to green-grey and rust to black weathering silty mudstone contains 1-1.5 cm thick, cream coloured quartz and feldspar-rich layers interpreted as volcanic tuff. In places the feldspar is altered and deformed around quartz eyes, which are up to 3 mm in diameter. However, petrographic analysis of these layers show that they contain a few percent by volume microperthite grains (Fig. 13), indicating a slowly cooled, not eruptive, igneous source. Repetition of laminated and graded layers within the silty mudstone are interpreted to record subaqueous mass flows. A sample of the tuff did not contain sufficient zircon for age determination.

## 5. Discussion

Ages obtained in this study help to constrain the timing of mineralization at Granduc and Rock and Roll. Our data indicate that the mineralization at Granduc may be younger than ~222 Ma (Childe, 1997), with its younger age limit approximately dated by the youngest zircon population, ~208 Ma, in the heterolithic breccia of the 'Mine Series'. Preservation of sulphide clasts suggests that deposition of breccia was either coeval with or shortly postdated the upper mineralized horizon at Granduc. Heterolithic breccias are common features of hydrothermal fields because the sub-basins in which they occur are bounded by active fault scarps that produce talus. In addition, hydrothermal mounds grow, over-steepen and collapse. Ancient and modern examples of heterolithic breccias are known worldwide: Canada, Peru, Turkey, Japan, Australia, Russia, TAG, PACMANUS, Middle Valley (Whalen et al., 2013; Tornos et al., 2015). Heterolithic breccia in many of these deposits are mixtures of volcanic, argillite, and sulphide clasts, lithologically similar to the heterolithic mine stratigraphy unit

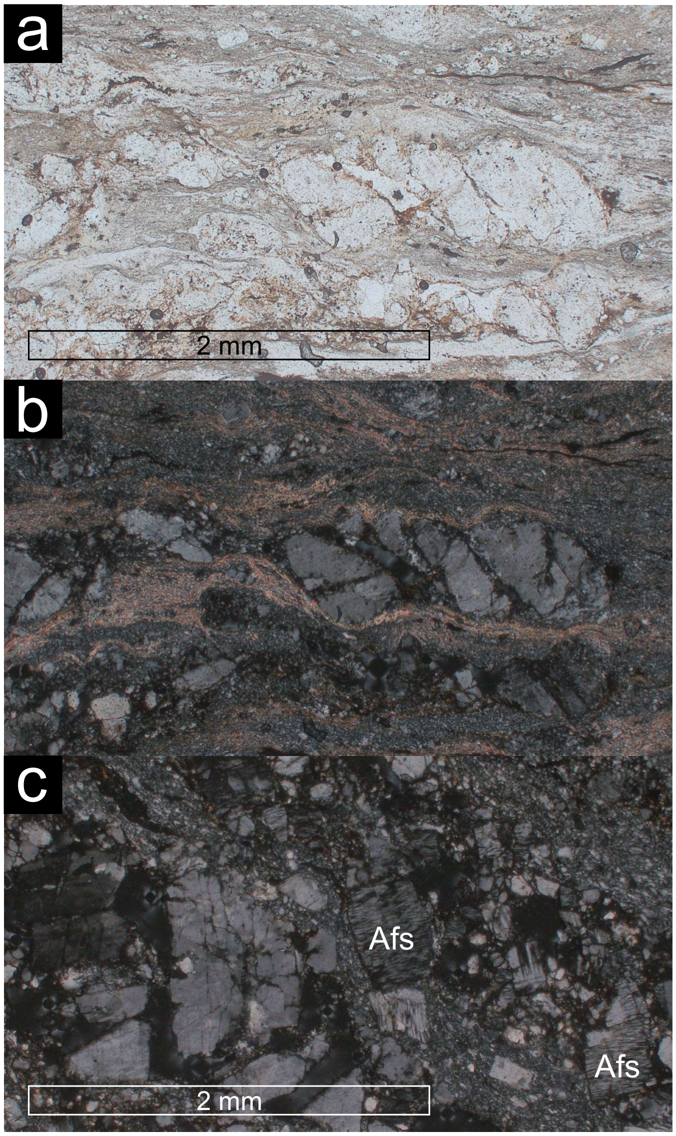


**Fig. 13.** Photomicrographs of coarse 'ash tuff' layer, a subsample of TST09-3-02. **a)** Plane polarized light showing cataclastic reduction of feldspar crystals and a well-devloped shear fabric. **b)** Same view in cross polarized light. **c)** Another view of the same thin section showing abundant microperthite grains (Afs: alkali feldspar) of probable intrusive origin.

at Granduc, which is strikingly similar to heterolithic breccia immediately overlying massive sulphide mineralization at the Rock and Roll (Fig. 3). Such similarity suggest that these deposits accumulated in basins with analogous flanking strata and modes of deposition.

At Rock and Roll, the oldest dated strata are ~292 Ma (Early Permian, Sakmarian; Cohen et al., 2013, updated 2018). Extensive carbonate rocks, previously presumed to be part of the Stikine assemblage (Permian), has now been confirmed as containing a ~210 Ma tuff layer (Fig. 7) and are therefore Late Triassic (Late Norian). This age is broadly consistent with conodont ages on correlative limestone within the Stuhini Group north of the Iskut River (Golding et al., 2017). The Norian age of the limestone negates the need for an interpreted southwest-dipping thrust fault at its base (e.g., as shown by Mihalynuk et al., 2010). It is likely that the immediate host strata of the Rock and Roll deposit lie stratigraphically between the Norian limestone unit and the Permian siltstone, with an age of between 210 Ma and 292 Ma. Although these age constraints are broad, they are consistent with the 222 to 208 Ma age of the Granduc deposit.

Lead isotopic signatures also support their correlation. The $^{207}Pb/^{204}Pb$ cluster from galena and pyrite mineralization at Granduc and galena at the Rock and Roll deposit are identical within error (Dean and Carr, 1991; Childe, 1997). Late Triassic model ages for Granduc and Rock and Roll coincide with those for Greens Creek VMS deposit (Alexander terrane) and the Schaft Creek porphyry copper deposit (Stikine terrane), both of which have independently dated Late Triassic hosts (Childe, 1997; Logan et al., 2000; Sack, 2009, Sack et al., 2016; Taylor et al., 2010). Overlap of lead $^{208}Pb/^{204}Pb$ clusters for Tulsequah and Granduc remains problematic. It may reveal some resetting of that isotopic system at Tulsequah, and requires re-evaluation.

Ages of minor pre-Triassic zircon populations in our samples help to further resolve the discontinuously exposed Paleozoic Stikine assemblage basement of northern Stikinia. Inherited and detrital zircons from Rock and Roll (~301 and 351 Ma) and Granduc (~304, 325 and 348 Ma) indicate that Stikine assemblage was present as adjacent highlands or basement to these sequences, suggesting that it extends beneath younger cover.

### 5.1. Late Triassic mineralization in Stikinia

Late Triassic Stikine and Quesnel terranes are mostly known for their Cu-Au ±Ag-Pt-Pd-Mo porphyry and related mineralization (Logan and Mihalynuk, 2014). Porphyry mineralization is known to be spatially associated with volcano-plutonic complexes. However, mineral deposit studies typically underappreciate that volcanic rocks were in many cases deposited in marine environments, as indicated by intercalated volcanic and marine sedimentary rocks, some bearing coeval marine fossils. Marine environments coeval and co-spatial with porphyry mineralization are commonly recorded by Mesozoic Stikinia and Quesnellia rocks. Arc-proximal, fault-bounded, restricted basins with slow sedimentation (e.g., containing carbonaceous argillite), and signs of hydrothermal alteration or exhalites, have significant potential for accumulations of VMS mineralization.

Although we now have a geochronological framework that is consistent with a Late Triassic age of massive sulphide mineralization at both Granduc and Rock and Roll deposits, the absolute age of mineralization has still not been determined. Units unequivocally contemporaneous with sulphide mineralization need to be dated, or the sulphide mineralization needs to be directly dated. Determining the age of sulphide mineralization may be possible using the Re-Os technique if sulphide minerals such as pyrrhotite, pyrite, sphalerite, chalcopyrite, galena at Rock and Roll contain sufficient radiogenic Re. Unfortunately, unlike graphitic shales elsewhere (Selby and Creaser, 2005), the two samples of Rock and Roll sulphide mineralization in graphitic shale at the Black Dog occurrence lacked sufficient rhenium for a direct Re/Os age determination. Because Re is concentrated in molybdenite, any trace of this mineral found in the VMS mineralization at either deposit should be collected for Re-Os age determination.

### 5.2. Early Jurassic magmatism and age constraints on deformation

Late syn- to post-kinematic ~186 Ma quartz diorite dikes at Rock and Roll are only locally foliated, but display pervasive mesoscopic brittle deformation and grain size reduction (Fig. 5), whereas the ~183 Ma felsic trachytic dike (drill core sample TST09-7-01) is undeformed (Fig. 11). The 186 Ma grain in the analyzed ~183 Ma dike sample, likely inherited when crosscutting the older quartz diorite dikes, is consistent with the relative age assignments of these intrusions.

The ages of the Rock and Roll dikes are coeval with younger part of the Texas Creek Plutonic suite (ca. 195-178 Ma; Lewis 2013) and are coeval with the most prolific Early Jurassic magmatic suite in the northern Cordillera, the Aishihik suite (sensu Johnston et al., 1996; Mihalynuk et al., 1999). The Texas Creek Plutonic suite includes plutons, stocks, and dikes that are widespread in the Iskut River area, and are considered to have fed extrusive magmatic rocks of the Betty Creek Formation (Lewis, 2013; Cutts et al., 2015). A nearby coeval, possible extrusive equivalent of the Rock and Roll diorite (sample TST09-6-11) in the Hoodoo Mountain area is a grey, hornblende (5-10%) and plagioclase (35-40%) porphyritic ash flow that returned 187.0 ±1.9 Ma zircons (MMI10-13-2; Mihalynuk et al., 2011). Zircons from the ash flow also contain ~560 and 1800 Ma inheritance (Zagorevski et al., 2015) not yet identified in the diorite dikes at Rock and Roll.

The ~183 Ma felsic trachytic dike (drill core sample TST09-7-01) is roughly coeval with tuffaceous sandstones near Hoodoo Mountain. There, a carbonate-cemented quartzite and pebble conglomerate cut by gabbro sills returned a unimodal detrital zircon population at 181.8 ±1.7Ma (N. Joyce, unpublished results from sample ZE10-294A) and 184.3 ±2.2Ma (N. Joyce, unpublished results from sample 14ZE842B).

Two deformation events fold and foliate rocks that we now know to be Late Triassic (Figs. 3, 4, 8, 13). Clear evidence of non-coaxial overprinting of an earlier foliation by a later foliation is common (Fig. 4). Late Early Jurassic bodies provide younger age constraints on the second penetrative deformation that affected Stuhini Group and older strata, ending in the lower Iskut River area between 186 and 183 Ma. The older of these two deformational events is amply represented along the Intermontane belt (Fig. 1) in late Norian to early Rhaetian, and is implicated in the formation of porphyry copper deposits (Logan and Mihalynuk, 2014). The younger event may be related to crustal thickening in northern Stikinia and at peak metamorphic pressures ~185 Ma (Mihalynuk et al., 1999). At the same time, widespread zircon lead loss (Mihalynuk et al., 2006) and contraction (Nixon et al., 1993) are recorded along the inboard margin of the northern Intermontane belt. Younger deformational episodes are not recorded by rocks at Rock and Roll. For example, they show little evidence of either the Middle Jurassic contraction affecting the entire northeast margin of Stikinia and which inverted the Whitehorse trough (Mihalynuk et al., 2004; Mihalynuk et al., 2017), nor of mid-Cretaceous shortening in adjacent Bowser Basin, manifested by the Skeena fold and thrust belt (Evenchick et al., 2007).

## 6. Summary

This study provides new age constraints on the Granduc past-producer and the Rock and Roll deposit. Host rocks of both are Upper Triassic and assigned to the Stuhini Group. A new detrital maximum depositional age for host strata in the 'Mine Series' at Granduc is ~208 Ma, distinctly younger than ~222 Ma U-Pb ages from igneous protoliths reported by Childe (1997). Host rocks at Rock and Roll formed between 292 and 210 Ma. Similarity of mineralization and of local deposit stratigraphy favours consideration of these two deposits as products of a VMS epoch within the Stuhini Group that may have regional potential.

## Acknowledgments

Samples were collected by Toby Stiers, University of Victoria. LA-ICP-MS analyses were by Kathryn Lucas, PCIGR, Department of Earth and Ocean Sciences, The University of British Columbia. Sample collection and geochronology was supported by a NSERC Discovery Grant to S.T. Johnston. Reviews by H. Awmack and J. Nelson significantly improved the manuscript.

## References cited

Childe, F., 1996. U-Pb geochronology and Nd and Pb isotope characteristics of the Au-Ag-rich Eskay Creek volcanogenic massive sulphide deposit, British Columbia. Economic Geology 91, 1209-1224.

Childe, F., 1997. Timing and tectonic setting of volcanogenic massive sulphide deposits in British Columbia: constraints from U-Pb geochronology, radiogenic isotopes, and geochemistry. Unpublished Ph.D. thesis, The University of British Columbia, 319 p.

Cohen, K.M., Finney, S.C., Gibbard, P.L., and Fan, J.X., 2013. The ICS International Chronostratigraphic Chart. Episodes, 36, 199-204.

Cutts, J.A., McNicoll, V.J., Zagorevski, A., Anderson, R.G., and Martin, K., 2015. U-Pb geochronology of the Hazelton Group in the McTagg anticlinorium, Iskut River area, northwestern British Columbia. In: Geological Fieldwork 2014, British Columbia Ministry of Energy and Mines, British Columbia Geological Survey Paper 2015-1, pp. 87-101.

Dean, J.A., and Carr, G.R., 1991. Report to Prime Exploration on the lead isotopic compositions of samples from Galore Creek and Iskut River, British Columbia, Unpublished Report SR 154, CSIRO Australia, 16 p.

Diakow, L.J., Orchard, M.J., and Friedman, R.M., 2012. Absolute ages for the Norian Stage: a further contribution from southern British Columbia, Canada. Cordilleran Tectonics Workshop, Geological Association Canada, Pacific Section, p. 2.

Evenchick, C.A., McMechan, M.E., McNicoll, V.J., and Carr, S.D.,

2007. A synthesis of the Jurassic-Cretaceous tectonic evolution of the central and southeastern Canadian Cordillera: Exploring links across the orogen. In: Sears, J.W., Harms, T.A., and Evenchick, C.A. (Eds.), Whence the Mountains? Inquiries into the Evolution of Orogenic Systems: A Volume in Honor of Raymond A. Price, Geological Society of America Special Paper, 433, pp. 117-145.

Gagnon, J.F., Barresi, T., Waldron, J.W.F., Nelson, J.L., Poulton, T.P., and Cordey, F., 2012. Stratigraphy of the upper Hazelton Group and Jurassic evolution of the Stikine terrane, British Columbia. Canadian Journal of Earth Sciences, 49, 1027-1052.

Galley, A.G., Hannington, M.D., and Jonasson, I.R., 2007. Volcanogenic massive sulphide deposits. In: Goodfellow, W.D., (Ed.), Mineral deposits of Canada: A synthesis of major deposit-types, district metallogeny, the evolution of geological provinces, and exploration methods. Geological Association of Canada, Mineral Deposits Division, Special Publication, 5, pp. 141-161.

Gerstenberger, H., and Haase, G., 1997. A highly effective emitter substance for mass spectrometric Pb isotope ratio determinations. Chemical Geology, 136, 309-312.

Golding, M., Orchard, M.J., and Zagorevski, A., 2017. Conodonts from the Stikine Terrane in northern British Columbia and southern Yukon. Geological Survey of Canada. Open File 8278, 23 p.

Griffin, W.L., Powell, W.J., Pearson, N.J, and O'Reilly, S.Y., 2008. Glitter: Data reduction software for laser ablation ICP-MS. In: Sylvester, P.J. (Ed.), Laser Ablation ICP-MS in the Earth Sciences: Current Practices and Outstanding Issues. Mineralogical Association of Canada Short Course 40, Vancouver, B.C., pp. 308-311.

Höy, T., 1991. Volcanogenic massive sulphide deposits in British Columbia. In: McMillan, W.J. (Ed.), Ore Deposits, Tectonics and Metallogeny in the Canadian Cordillera. British Columbia Ministry of Energy, Mines and Petroleum Resources, British Columbia Geological Survey Paper 1991-4, pp. 89-124.

Jaffey, A.H., Flynn, K.F., Glendenin, L.E., Bentley, W. T., and Essling, A.M., 1971. Precision measurement of half-lives and specific activities of U 235 and U 238. Physical Review C, 4, 1889-1906.

Johnston, S.T., Mortensens, J.K., and Erdmer, P., 1996. Igneous and metaigneous age constraints for the Aishihik metamorphic suite, southwest Yukon. Canadian Journal of Earth Sciences, 33, 1543-1555.

Jones, M., 2011. 2010 Geological and geochemical report on the Rock and Roll Property. Assessment Report AR32127, B.C. Ministry of Energy and Mines, 58 p.

Kent, D.V., Olsen, P.E., and Muttoni, G., 2017. Astrochronostratigraphic polarity time scale (APTS) for the Late Triassic and Early Jurassic from continental sediments and correlation with standard marine stages. Earth Science Reviews, 166, 153-180.

Kerr, F.A., 1948. Lower Stikine and Iskut River areas, British Columbia. Geological Survey of Canada, Memoir 246, 94 p.

Kyba, J., and Nelson, J., 2015. Stratigraphic and tectonic framework of the Khyber-Sericite-Pins mineralized trend, lower Iskut River, northwest British Columbia. In: Geological Fieldwork 2014, British Columbia Ministry of Energy and Mines, British Columbia Geological Survey Paper 2015-1, pp. 41-58.

Lewis, P.D., 2013. Iskut River Area Geology, Northwest British Columbia (104B/08, 09, 10 & part of 104B/01, 07, 11). Geoscience British Columbia Report 2013-05, 1:50,000 scale.

Logan, J.M., and Mihalynuk, M.G., 2014. Tectonic controls on early Mesozoic paired alkaline porphyry deposit belts (Cu-Au ±Ag-Pt-Pd-Mo) within the Canadian Cordillera. Economic Geology, 109, 827-858.

Logan, J.M., Drobe, J.R., and McClelland, W.C., 2000. Geology of the Forrest Kerr-Mess Creek Area. Northwestern British Columbia (NTS 104B/10, 15 & 104G/2 & 7W). British Columbia Ministry of Energy and Mines, British Columbia Geological Survey Bulletin, 104, 164 p.

Ludwig, K.R., 2003, Isoplot 3.09-A geochronological toolkit for Microsoft Excel: Berkeley Geochronology Center, Special Publication No. 4.

Mattinson, J.M., 2005. Zircon U-Pb chemical abrasion ("CA-TIMS") method: combined annealing and multi-step partial dissolution analysis for improved precision and accuracy of zircon ages. Chemical Geology, 220, 47-66.

McGuigan, P.J., 2005. Granduc property northwestern British Columbia, Canada. Unpublished report by Tecucomp Geological Inc. for Bell Resources Corporation, 52 p.

Mihalynuk, M.G., Mountjoy, K.J., Smith, M.T., Currie, L.D., Gabites, J.E., Tipper, H.W., Orchard, M.J., Poulton, T., P., and Cordey, F., 1999. Geology and mineral resources of the Tagish Lake area (NTS 104M/8, 9, 10E, 15 and 104N/12W), northwestern British Columbia. British Columbia Ministry of Energy, Mines and Petroleum Resources, British Columbia Geological Survey Bulletin 105, 235 p.

Mihalynuk, M.G., Erdmer, P., Ghent, E.D., Cordey, F., Archibald, D.A., Friedman, R.M., and Johannson, G.G., 2004. Coherent French Range blueschist: Subduction to exhumation in <2.5 my? Geological Society of America Bulletin, 116, 910-922.

Mihalynuk, M.G., Friedman, R.M., Devine, F.A., and Heaman, L.M., 2006. Protolith age and deformation history of the Big Salmon Complex, relics of a Paleozoic continental arc in northern British Columbia. In: Colpron, M. and Nelson, J.L. (Eds.), Paleozoic Evolution and Metallogeny of Pericratonic Terranes at the Ancient Pacific Margin of North America, Canadian and Alaska Cordillera. Geological Association of Canada Special Paper, 45, 179-200.

Mihalynuk, M.G., Stier, Toby J., Jones, Murray I., R.M., and Johnston, S.T., 2010. Stratigraphic and Structural Setting of the Rock and Roll Deposit, Northwestern British Columbia (NTS 104B/11). In: Geological Fieldwork 2009, British Columbia Ministry of Forests, Mines and Lands, British Columbia Geological Survey Paper 2010-1, pp. 7-18.

Mihalynuk, M.G., Logan, J.M., and Zagorevski, A., 2011. East Hoodoo Mountain - Iskut River Geology, NTS 104B/14E & 11NE. Geological Survey of Canada, Open File 6730; British Columbia Ministry of Energy and Mines, British Columbia Geological Survey Open File Map, 2011-4, 1:50,000 scale.

Mihalynuk, M.G., Zagorevski, A., English, J.M., Orchard, M.J., Bidgood, A.K., Joyce, N., and Friedman, R.M., 2017. Geology of the Sinwa Creek area, northwest BC (104K/14). In: Geological Fieldwork 2016, British Columbia Ministry of Energy and Mines, British Columbia Geological Survey Paper 2017-1, pp. 153-178.

Mihalynuk, M.G., Friedman, R.M., and Logan, J.M., 2019. Detrital zircon geochronological data from the Granduc and Rock and Roll deposits, northwest British Columbia. British Columbia Ministry of Energy, Mines and Petroleum Resources, British Columbia Geological Survey GeoFile, in press.

Montgomery, A.T., Todoruk, S.L., and Ikona, C.K., 1991. Eurus Resources Corp. Thios Resource Inc. Assessment Report on the Rock and Roll Project. British Columbia Ministry of Energy, Mines and Petroleum Resources, Assessment Report 20884, 203 p. plus figures, appendices and maps.

Morrison, R., McKinnon, C., Liukko, G., Kesavanathan, D., Gagnon, A., Abdel Hafez, S., Danon-Schaffer, M., McLaughlin, M., and Ouellet, J., 2013. Preliminary economic assessment of the Granduc copper project, northern British Columbia. NI 43-101, Report by Tetra Tech for Castle Resources, Toronto, ON, Canada, 299 p.

Mundil, R., Ludwig, K.R., Metcalfe, I., and Renne, P.R., 2004. Age and timing of the Permian mass extinctions: U/Pb dating of closed-system zircons. Science, 305, 1760-1763.

Nixon, G.T., Archibald, D.A., and Heaman, L.M., 1993. $^{40}Ar$-$^{39}Ar$ and U-Pb geochronometry of the Polaris alaskan-type complex, British Columbia; precise timing of Quesnellia-North America

interaction. In: Geological Association of Canada, Mineralogical Association of Canada, Canadian Geophysical Union Joint Annual Meeting, Program With Abstracts, p. 76.
Rhys, D.A., 1995. The Red Bluff gold-copper porphyry and associated precious and base metal veins, northwestern British Columbia. In: Schroeter, T.G. (Ed.), Porphyry Deposits of the Northwestern Cordillera of North America. Canadian Institute of Mining and Metallurgy Special Volume 46, pp. 838-850.
Sack, P.J., 2009. Characterization of footwall lithologies to the Greens Creek volcanic-hosted massive sulfide (VHMS) deposit, Alaska, USA. Unpublished Ph.D. thesis, University of Tasmania, Hobart, Australia, 415 p.
Sack, P.J., Berry, R.F., Gemmell, J.B., Meffre, S., and West, A., 2016. U-Pb zircon geochronology from the Alexander terrane, southeast Alaska: implications for the Greens Creek massive sulphide deposit. Canadian Journal of Earth Sciences, 53, 1458-1475.
Schmitz, M.D., and Schoene, B., 2007. Derivation of isotope ratios, errors, and error correlations for U-Pb geochronology using $^{205}$Pb-$^{235}$U-($^{233}$U)-spiked isotope dilution thermal ionization mass spectrometric data. Geochemistry, Geophysics, Geosystems, 8, 20 p.
Scoates, J.S., and Friedman, R.M., 2008. Precise age of the platiniferous Merensky Reef, Bushveld Complex, South Africa, by the U-Pb zircon chemical abrasion ID-TIMS technique. Economic Geology, 103, 465-471.
Selby, D., and Creaser, R.A., 2005. Direct radiometric dating of the Devonian-Mississippian time-scale boundary using the Re-Os black shale geochronometer. Geology, 33, 545-548.
Sláma, J., Košler, J., Condon, D.J., Crowley, J.L., Gerdes, A., Hanchar, J.M., Horstwood, M.S., Morris, G.A., Nasdala, L., and Norberg, N., 2008. Plešovice zircon-a new natural reference material for U-Pb and Hf isotopic microanalysis. Chemical Geology, 249, 1-35.
Tafti, R., Mortensen, J.K., Lang, J.R., Rebagliati, M., and Oliver, J.L., 2009. Jurassic U-Pb and Re-Os ages for the newly discovered Xietongmen Cu-Au porphyry district, Tibet, PRC: Implications for metallogenic epochs in the southern Gangdese belt. Economic Geology,104, 127-136.
Taylor, C.D, Premo, W.R., and Johnson, C.A., 2010. Sulfur and Lead Isotope characteristics of the Greens Creek polymetallic massive sulfide deposit, Admiralty Island, southeastern Alaska. In: Taylor, C.D., and Johnson, C.A. (Eds.), Geology, Geochemistry, and Genesis of the Greens Creek Massive Sulfide deposit, Admiralty Island, southeastern Alaska. U.S. Geological Survey Professional Paper 1763, pp. 241-282.
Thirlwall, M.F., 2000. Inter-laboratory and other errors in Pb isotope analyses investigated using a $^{207}$Pb-$^{204}$Pb double spike. Chemical Geology, 163, 299-322.
Tornos, F., Peter, J.M., Allen, R., and Conde, C., 2015. Controls on the siting and style of volcanogenic massive sulphide deposits. Ore Geology Reviews, 68, 142-163.
Van Achterbergh, E., Ryan, C.G., Jackson, S.E., and Griffin, W.L., 2001. Data reduction software for LA-ICP-MS: appendix. In: Sylvester, P.J. (Ed.), Laser Ablation-ICP Mass Spectrometry in the Earth Sciences: Principles and Applications. Mineralogical Association of Canada Short Course 29, Ottawa, Ontario, pp. 239-243.
Whalen, J.B., Zagorevski, A., McNicoll, V.J., and Rogers, N., 2013. Geochemistry, U-Pb geochronology, and genesis of granitoid clasts in transported volcanogenic massive sulfide ore deposits, Buchans, Newfoundland. Canadian Journal of Earth Sciences, 50, 1116-1133.
Wheeler, J.O., Brookfield, A.J., Gabrielse, H., Monger, J.W.H., Tipper, H.W., and Woodsworth, G.J., 1991. Terrane map of the Canadian Cordillera. Geological Survey of Canada, Map 1713A, 1:2,000,000 scale.
Zagorevski, A., Mihalynuk, M.G., Joyce, N., Friedman, R.M., Ryan, J.J., Chapman, J., Cutts, J.A., McNicoll, V.J., and Anderson, R.G., 2015. Geochronology of the Lower Jurassic Hazelton arc in northwestern British Columbia and Yukon. Mineral Exploration Roundup, Poster, Association for Mineral Exploration, Vancouver, BC.

# Characterization of primary fersmite from the Mount Brussilof magnesite deposit, southeastern British Columbia, Canada

George J. Simandl[1, a, 2], Joseph A. Petrus[3], Matthew I. Leybourne[4], Suzanne Paradis[5], and Carlee Akam[1]

[1] British Columbia Geological Survey, Ministry of Energy, Mines and Petroleum Resources, Victoria, BC, V8W 9N3
[2] School of Earth and Ocean Sciences, University of Victoria, BC, V8P 5C2
[3] Mineral Exploration Research Centre, Harquail School of Earth Sciences, Laurentian University, Sudbury, ON, P3E 2C6
[4] Queen's Facility for Isotope Research, Department of Geological Sciences and Geological Engineering, Kingston, ON, K7L 3N6
[5] Geological Survey of Canada, Natural Resources Canada, Sidney, BC, V8L 4B2
[a] corresponding author: George.Simandl@gov.bc.ca

Recommended citation: Simandl, G.J., Petrus, J.A., Leybourne, M.I., Paradis, S., and Akam, C., 2019. Characterization of primary fersmite from the Mount Brussilof magnesite deposit, southeastern British Columbia, Canada. In: Geological Fieldwork 2018, British Columbia Ministry of Energy, Mines and Petroleum Resources, British Columbia Geological Survey Paper 2019-01, pp. 113-123.

**Abstract**

Fersmite ($[Ca,Ce,Na][Nb,Ta,Ti]_2[O,OH,F]_6$) is a complex mineral, occurring commonly as a strongly metamict alteration product of pre-existing niobate minerals in carbonatites, alkaline and peralkaline intrusions, and rare element pegmatites. Most well-documented primary fersmite localities in Europe are 'alpine cleft', also referred to as 'alpine fissure', occurrences. At Mount Brussilof in southeastern British Columbia, fersmite occurs as an accessory mineral on sparry dolomite crosscutting and lining cavities in sparry magnesite. The fersmite forms brittle, black, submetallic to vitreous lustre, acicular to platy crystals up to 2 cm long. It also forms smaller, commonly fractured or broken, crystals (<3 mm) enclosed by sparry dolomite. Sparry dolomite is commonly associated with Mississippi Valley-type Zn-Pb deposits, both globally and within southeastern British Columbia. Electron microprobe and laser ablation inductively coupled plasma mass spectrometry mapping indicate that the Mount Brussilof fersmite is rich in Nb, Th, and heavy REE, and poor in Ta. Individual fersmite crystals are strongly zoned in terms of Na, Ti, Fe, Y, all REE, Ta, Pb isotopes ($^{204}Pb$, $^{206}Pb$, $^{207}Pb$, and $^{208}Pb$), Th, and U, suggesting that the chemical composition of hydrothermal or carbohydrothermal fluids from which fersmite precipitated evolved with time. The textural and chemical properties of the Mount Brussilof fersmite differ from those found in carbonatite- and pegmatite-related deposits. The zonation, non-metamict appearance, and enrichment in Nb relative to Ta of the Mount Brussilof fersmite may help to distinguish fersmite formed in similar settings (alpine-clefts) from fersmite formed in pegmatites, peralkaline intrusions, carbonatites, and other geological environments, and enhance its use as a direct indicator mineral.

**Keywords:** Primary fersmite, chemical zoning, Mount Brussilof, magnesite, sparry dolomite, dolomitization, Mississippi Valley-type deposits

## 1. Introduction

The Mount Brussilof sparry magnesite deposit, currently the only magnesite-producing mine in Canada, is 40 km northeast of Invermere in the Rocky Mountain Foreland Belt of the southern Canadian Cordillera (Fig. 1). The spatial relationship between the Mount Brussilof deposit and Mississippi Valley-type (MVT) deposits such as Shag, Hawk Creek, Kicking Horse, and Monarch, and their position along the Kicking Horse rim (Fig. 2) was highlighted by Aitken and McIlreath (1984), Simandl et al. (1992), and Paradis and Simandl (2017, 2018). At the Mount Brussilof deposit, sparry dolomite zones cut sparry magnesite (Simandl and Hancock, 1991). Fersmite ($[Ca,Ce,Na][Nb,Ta,Ti]_2[O,OH,F]_6$) is hosted by the sparry dolomite or by sugary dolomite enclosed in the sparry dolomite.

Globally, fersmite is the third most important Nb-ore mineral after pyrochlore supergroup minerals and columbite-tantalite solid solution series minerals (Mackay and Simandl, 2014; Simandl et al., 2018). However, the Mount Brussilof fersmite occurrence is too small to be of economic interest as a source of niobium. Nevertheless, it may have metallogenic implications. Assuming there is only one generation of sparry dolomite in southeastern British Columbia, or if fersmite is hosted by the youngest generation of sparry dolomite, then the circulation of Nb-bearing fluids along the faults related to the Cathedral escarpment post-dates MVT Zn-Pb, REE-Ba-fluorite, and magnesite mineralization in the region.

The objectives of this study are to: 1) describe the Mount Brussilof fersmite occurrence; 2) define the relationships between fersmite, sparry dolomite, and sparry magnesite; 3) characterize the compositional zoning observed in fersmite and present the most likely hypothesis regarding its origin; and 4) compare the physical and chemical properties of the Mount Brussilof fersmite to those of fersmite from carbonatite- and pegmatite-related deposits, furthering the value of fersmite as a direct indicator mineral.


**Fig. 1.** Location of the Mount Brussilof magnesite mine.

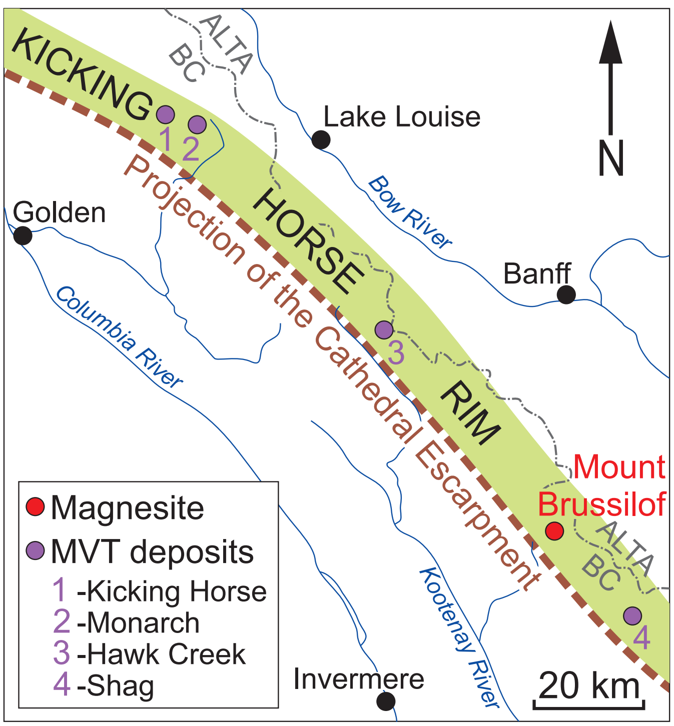


**Fig. 2.** Kicking Horse Rim bounded on the west by the projection of the Cathedral escarpment (Aitkin, 1971). Mount Brussilof magnesite mine and selected MVT deposits. 1- Kicking Horse mine; 2- Monarch mine; 3- Hawk Creek prospect; and 4- Shag prospect. All are northeast of the Cathedral Escarpment and hosted by carbonate rocks deposited in shallow-marine environments (modified from Simandl et al., 1992).

## 2. Geological setting

The Mount Brussilof magnesite deposit is along the Kicking Horse rim (Fig. 2), a north-northwest trending paleo-topographic high defined by Aitken (1971, 1989). The southwestern edge of the Kicking Horse rim coincides with the Cathedral escarpment, a Middle Cambrian reef margin (Aitken and McIlreath, 1984, 1990; Fritz, 1990). The rocks northeast of the escarpment (Fig. 2), including the Cathedral Formation (Middle Cambrian) that hosts the Mount Brussilof magnesite deposit, were deposited in a shallow-marine environment, whereas rocks of the Chancellor Group that outcrop southwest of the escarpment are off-reef, deeper water deposits (Aitken, 1978; Simandl and Hancock, 1991; Simandl et al., 1992). In the Mount Brussilof area, the projection of the Cathedral escarpment coincides with the ‘faulted facies change’ mapped by Leech (1966) and with the Mitchell River fault on the most recent regional map (McMechan and Leech, 2011). The stratigraphy of the Mount Brussilof mine area and geology of the deposit is summarized by Simandl and Hancock (1991). The relationships between dolomite, sparry magnesite, sparry dolomite, and Zn-Pb MVT mineralization is covered by Paradis and Simandl (2018). Fersmite post-dates sparry dolomite, which cross cuts sparry magnesite. The sparry magnesite is hosted by the Cathedral Formation (Middle Cambrian).

## 3. Fersmite

Aeschynite-group minerals and euxenite-group minerals, which include fersmite ($[Ca,Ce,Na][Nb,Ta,Ti]_2[O,OH,F]_6$), are orthorhombic. The groups share the formula $AB_2O_6$. The A-site is commonly occupied by Y, REE, Ca, Na, U, and Th, and the B-site contains Ti, Nb, and Ta. Despite similarities in occupancies of the A- and B-sites of these mineral groups, LREE are preferentially incorporated into the aeschynite-group minerals, whereas Y and HREE are preferentially incorporated into the euxenite group (Ercit, 2005; Škoda and Novák, 2007).

Globally, fersmite occurs mostly as a strongly metamict alteration product of pre-existing niobate minerals in carbonatites (e.g., Aley Carbonatite in British Columbia, Mäder, 1987; Chakhmouradian et al., 2015) and alkaline and peralkaline intrusions (e.g., Ilímaussaq complex in South Greenland; Karup-Møller et al., 2010). Rare element pegmatites (e.g., Prašivá in Slovakia, Uher et al., 1998; Wodgina in Western Australia, Sweetapple and Lumpkin, 2011; and pegmatites of the Třebíč Pluton in the Czech Republic, Škoda and Novák, 2007) are also known to contain secondary or late fersmite. Lumpkin and Ewing (1992) explain the mineral stability relationship between fersmite-ferrocolumbite ($FeNb_2O_6$) and pyrochlore ($[Na,Ca]_2Nb_2O_6[OH,F]$) in the Na-Ca-Fe-Nb-O-H system (which approximates magmatic-hydrothermal systems) in terms of $Na^+$, $Ca^{2+}$, and $Fe^{2+}$ activities.

Primary fersmite is less common. It occurs mainly as prismatic crystals that are predominantly tabular, blade-shaped, or acicular. Crystals are black, dark brown, or lemon-yellow to yellow-brown, and their luster varies from resinous to subvitreous or submetallic. Many dark-colored crystals are nearly opaque, fluoresce yellow-green to bluish-green under shortwave and longwave ultraviolet light, and have a pale blue cathodoluminescence (Anthony et al., 2017). Well-documented localities containing prismatic fersmite crystals correspond to 'alpine cleft' occurrences (also referred to as 'alpine fissures'), defined by Niggli et al. (1940) as open joints, vugs and other cavities partially filled with well crystallized (commonly euhedral) minerals formed during metamorphism and uplift of mountain belts. The origin of fluids carrying Nb and REE from which primary fersmite crystallizes has not been clearly identified in published studies.

At the Mount Brussilof magnesite deposit, fersmite is an erratically distributed trace mineral. The fersmite-bearing zone, now mined out, was approximately 10 m long, irregular, and porous. It consisted of sugary dolomite and sparry dolomite that cuts sparry magnesite. The zone was exposed a few metres from a pyrite stockwork in the sparry magnesite. The Mount Brussilof fersmite forms brittle, black, acicular to platy crystals up to 2 cm long with a submetallic to vitreous lustre that line cavities in sparry dolomite. In some cavities, fersmite occurs with euhedral quartz (Fig. 3). Fersmite also occurs as smaller crystals enclosed in dolomite (Fig. 4). The Mount Brussilof fersmite does not replace earlier Nb-bearing minerals and, resembling 'alpine cleft' varieties that have been described from sites in Europe, may be the first primary fersmite recognized in British Columbia. The samples selected for detailed geochemical studies consist of black, striated, prismatic fersmite crystals about 0.5 to 2.0 mm long.

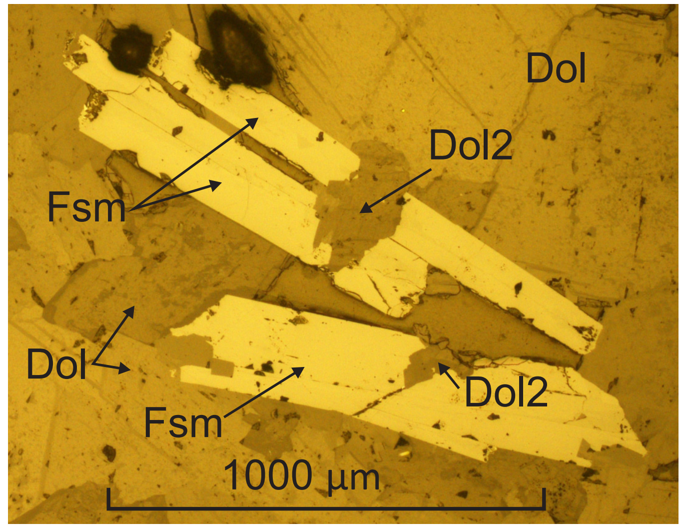


**Fig. 4.** Photomicrograph of zoned fersmite (Fsm) crystals enclosed in sparry dolomite (Dol), reflected light. Late dolomite (Dol2) fills fractures in fersmite. Mount Brussilof mine.

## 4. Analytical methods

Four fersmite-bearing polished thin sections were produced from samples collected at the Mount Brussilof deposit, and analyzed (MB-16-01, MB-16-02A, MB-16-02B, and MB-16-02C). Black, striated, grains suspected to be Nb-rutile or fersmite were selected for electron microprobe (EMP), laser ablation inductively coupled plasma mass spectrometry (LA-ICP-MS), and wavelength-dispersive sprectroscopy (WDS). Independently, a concentrate of the black striated grains intended for X-ray powder diffraction (XRD) analysis was produced by crushing the rock with a hammer and steel plate, and hand-picking under a binocular microscope. The results of XRD, EMP, and LA-ICP-MS analyses are essential to chemically characterize the Mount Brussilof fersmite.

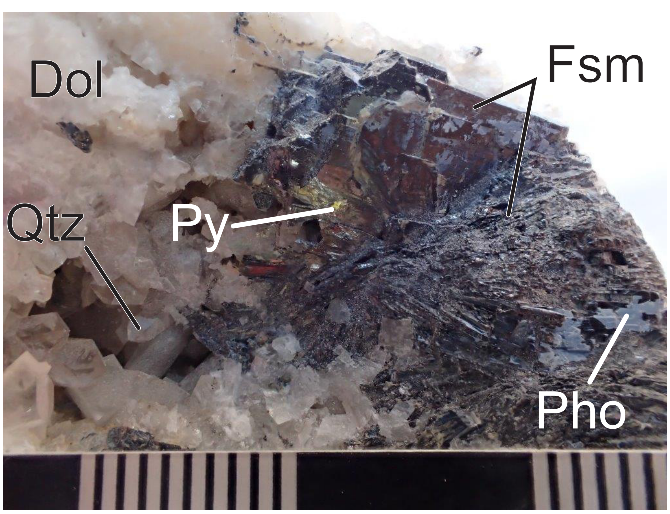


**Fig. 3.** Coarse fersmite crystals (Fsm) lining a cavity in sparry dolomite and locally intergrown with late sugary dolomite (Dol). Quartz (Qtz), pyrite (Py), and phosphate (Pho) are also present. Coarsest fersmite lining the cavity has apparent brownish reflections along cleavages. Mount Brussilof mine, scale in cm.

### 4.1. X-ray powder diffraction

A hand-picked concentrate of niobate minerals was analyzed at the University of British Columbia. The concentrate was ground under ethanol with a corundum mortar and pestle and dispersed onto a zero-diffraction quartz plate using ethanol. Continuous-scan XRD data were collected over a range 3-80° 2q with Co Kα radiation on a Bruker D8 Focus Bragg-Brentano diffractometer equipped with a Fe-monochromator foil, 0.6 mm (0.3°) divergence slit, incident- and diffracted-beam Soller slits and a LynxEye detector. The long fine-focus Co X-ray tube was operated at 35 kV and 40 mA, using a take-off angle of 6°. The XRD of the concentrate was needed to confirm the identity of the Ca-niobate, because fersmite has a similar Nb/Ca value to vigezzite (an aeschynite-group mineral with a generalized formulae $[Ca,Ce][Nb,Ta,Ti]_2O_6$).

### 4.2. Electron microprobe analyses

Selected fersmite grains were analyzed by EMP using a Cameca SX50 at the Central Analytical Facility, Laurentian University. Operating conditions were 20 kV and 20 nA using a focused beam and WDS acquisition and the correction procedure described by Pouchou and Pichoir (1984) was applied. Standards used were APS25 (F), Albite (Na), Wake Diopside (Ca), $CaTiO_3$ (Ti), $YPO_4$, (Y), $MnNb_2O_6$ (Nb), $CePO_4$ (Ce) and $LiTaO_3$ (Ta). Count times were 15 s (F, Y, Ce, Ta) and 30 s (Na, Ca, Ti, Nb).

### 4.3. Laser Ablation Inductively Coupled Plasma Mass Spectrometry

The trace element contents of fersmite were determined by LA-ICP-MS at Laurentian University, Ontario. The measurements were made in situ by ablating the grains with a Resonetics (now Australian Scientific Instruments) RESOlution M-50 laser ablation system employing a Coherent CompexPRO ArF 193 nm wavelength, 20 ns pulse duration laser and a Laurin Technic two-volume laser ablation cell (Müller et al., 2009). Ablation took place in ultra-pure He flowing at 650 ml/min. The He and ablation aerosol were combined with $N_2$ (6 ml/min) and Ar (750 ml/min) immediately outside the ablation cell and transferred to the torch of the ICP-MS by approximately 3 meters of tubing. The ablated material was analyzed by a Thermo X-Series II ICP-MS operating with a forward power of 1450 W. Prior to each session, the ICP-MS was tuned while ablating NIST612 to maximize sensitivity and minimize oxide production (<0.5%) while maintaining Th/U ~1. Different isotopes were analyzed in each session as the preceding measurements showed significant trace element variation. Dwell times during analysis were 5-10 ms for major and trace elements, and 20-40 ms for U-Th-Pb ($^{206}$Pb:30, $^{207}$Pb:40, $^{208}$Pb:20, $^{232}$Th:20, $^{238}$U:30). Spot data were collected using a beam diameter of 48 µm, repetition rate of 6 Hz, and fluence of 5 J/cm$^2$.

Because the chemistry of the initial spot analyses appeared to be complex, several grains were laser mapped to reveal the elemental relationships in more detail. The maps were acquired by ablating a series of parallel and adjacent traverses over the regions of interest. To improve the spatial resolution, a smaller spot size of 14 µm was used with a scan speed of 7 µm/s and repetition rate of 8 Hz.

Calibration was carried out using certified reference materials NIST610, NIST612, and BHVO2G, each of which were analyzed before, after, and periodically during each analytical session. The data were processed using Iolite version 3.4 (Paton et al., 2011). The trace element contents were calculated using the "TraceElements_IS" data reduction scheme of Iolite with NIST610 as the external standard and Nb (53.28 wt.%; mean of WDS data) as the internal standard.

## 5. Results

Exploratory EMP analysis determined that the grains of unknown, black mineral were either fersmite or vigezzite ($[Ca,Ce][Nb,Ta,Ti]_2O_6$). The XRD analyses confirmed conclusively that all black, striated grains with sub-vitreous luster previously analyzed by EMP and LA-ICP-MS are fersmite (Fig. 5).

Electron microprobe analyses of grains from samples MB-16-01 and MB-16-02 are listed in Table 1. A statistical summary of LA-ICP-MS analyses of REE in grains from these samples is presented in Table 2, and chondrite-normalized REE patterns for sample MB-16-02 first quartile, median, and third quartile based on 189 spot analyses are displayed in Figure 6. A series of compositional maps were produced to link the variations in chemical composition to their position within individual grains (e.g., Fig. 7). The Mount Brussilof fersmite is Nb-rich (Table 1), averages 53.3 wt.% Nb, and has low Ta contents (below the limit of quantification by EMP, 180 ppm) relative to fersmite from other geological environments. Compositional maps of fersmite crystals (e.g., Fig. 7) show well-developed zonation in terms of Na, Ti, Fe, Y, all REE, Ta, Pb isotopes ($^{204}$Pb, $^{206}$Pb, $^{207}$Pb, and $^{208}$Pb), Th, and U.

## 6. Discussion

Fersmite from the Mount Brussilof deposit is interpreted as primary based on its prismatic crystal form and textural habit (Figs. 3, 4). This is in contrast with other fersmite occurrences in British Columbia where fersmite is an alteration product of previously formed niobates. Euhedral fersmite crystals formed in open spaces on sparry dolomite (Fig. 3) but are locally transected by a later-stage dolomite (Dol 2 in Fig. 4). Thus fersmite crystallized between episodes of dolomite growth. Because the sparry dolomite crosscuts the magnesite ore, the fersmite also post-dates magnesite.

Coarse-grained, white sparry dolomite, referred to as 'saddle' dolomite in the exploration industry, forms by interaction of high temperature hydrothermal fluids with precursor carbonates and is commonly used as an exploration guide for MVT Zn-Pb mineralization (Leach et al., 2005; Paradis et al., 2007). Sparry magnesite may have a similar origin. For the Mount Brussilof sparry magnesite, one possible mechanism considers that carbonate minerals convert to magnesite under moderate fluid temperature conditions (<200°C), assuming a one mole concentration, and a one to one mole ratio of $Ca^{2+}$ to $Mg^{2+}$ equivalent of seawater (Rosenberg et al., 1967; Simandl and Hancock, 1991). An alternative mechanism involves the conversion of Mg-rich magnesite precursors precipitated in an evaporitic environment into magnesite (Simandl and Hancock, 1998).

The timing of sparry dolomitization in the Rocky Mountain Foreland belt of the Canadian Cordillera and the Western Canada Sedimentary Basin remains contentious. There is evidence for at least two periods of sparry dolomitization coinciding with tectonic activity (Al-Aasm et al., 2000; Al-Aasm, 2003); the first corresponds to the Late Devonian-Early Mississippian 'Antler Orogeny' (Root, 2001), and the second to the Late Cretaceous-Eocene fold and thrust belt (Laramide Orogeny; Symons et al., 1999). Studies by Al-Aasm (2003) and Mrad (2016) conducted in the northwestern portion of the Western Canada Sedimentary Basin suggest that distinction between different pulses of dolomitization may be possible based on, for example, $\delta^{18}O$ and $^{87}Sr/^{86}Sr$ values of sparry dolomite, and fluid salinity. A comparable study in the Rocky Mountain Foreland belt in southeastern British Columbia (Nesbitt and Prochaska, 1998) containing additional information on solute chemistry of fluid inclusions (Na/Br, Cl/Br, and I/Br values) in dolomite and magnesite suggests that formation of sparry dolomite, magnesite, talc, and MVT deposits hosted by Middle Cambrian carbonate rocks preceded the Laramide orogeny. This, in

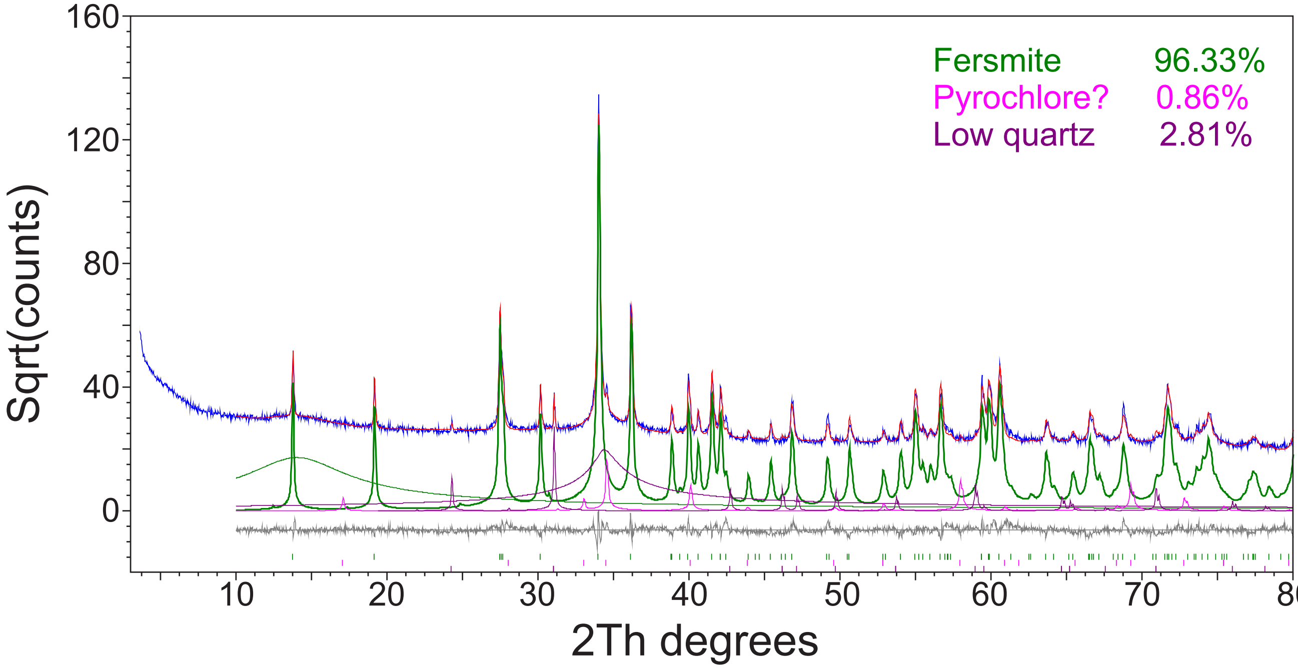


**Fig. 5.** Rietveld refinement plot of fersmite from sample MB16-01. Blue line - observed intensity at each step; red line - calculated pattern; solid grey line below - difference between observed and calculated intensities; vertical bars - positions of all Bragg reflections. Individual diffraction patterns of fersmite in green, of possible pyrochlore in pink, and of low quartz in purple.

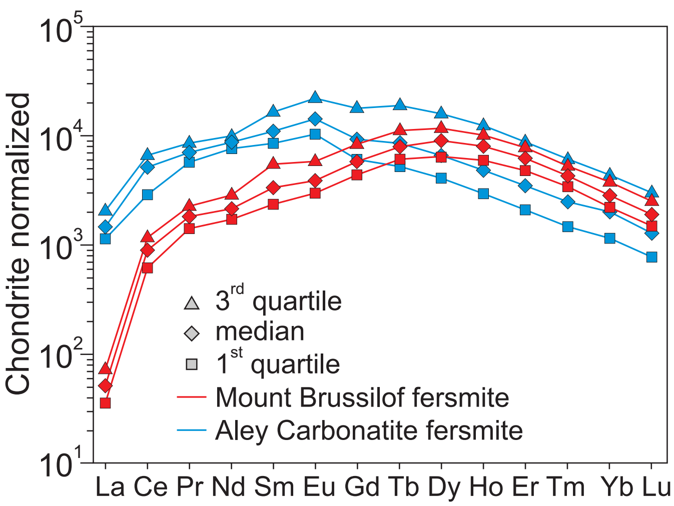


**Fig. 6.** Chondrite-normalized median, and upper and lower quartile REE distribution for fersmite from Mount Brussilof sample MB-16-02 (based on 189 spot analyses) and for fersmite from the Aley carbonatite (Chakhmouradian et al., 2015). Chondrite values are from McDonough and Sun (1995).

combination with the fluid flow model of Yao and Demicco (1995, 1997) and ongoing research of Paradis and Simandl (2017; 2018) will be components of a modern metallogenic synthesis of southeastern British Columbia. Fersmite, a Nb- and REE- bearing mineral, is hosted by sparry dolomite, which post-dates sparry magnesite. It also coexists with or pre-dates sugary dolomite, both of which post-date the sparry dolomite. These relationships may provide a key constraint on the timing of sparry dolomitization and MVT mineralization along the Kicking Horse rim, and possibly elsewhere. It may be relevant to interpreting the genesis of the sparry dolomite-associated Rock Canyon Creek REE-F deposit 73 km south-southeast from Mount Brussilof.

### 6.1. Chemical composition of fersmite

In Figure 8 we compare the weight proportions of Ca, Nb, and Ta x 10 of fersmite compositions from the Mount Brussilof magnesite deposit to fersmite compositions from Aley carbonatite in northeastern British Columbia (Chakhmouradian et al., 2015); Upper Fir carbonatite in east-central British Columbia (Chudy, 2013); Sunsas Belt placer deposit, Bolivia (Alfonso et al., 2015); Prasiva Pegmatites, Slovakia (Uher et al., 1998); Skoddefjellet Pegmatite, Norway (Prsek et al., 2010); Alpe Rosso Pegmatite, Italy (Guastoni et al., 2008); and Baveno Pegmatite, Italy (Aurisicchio et al., 2001). It also compares these weight proportions to the Huron Claim Pegmatite, Manitoba (average of two analyses) and Himalaya Pegmatite and King's Mountain Pegmatite (Foote Mine), USA (Foord and Mrose, 1978). The Ta content of fersmite from the Aley and Upper Fir carbonatites is probably representative of most fersmite-bearing carbonatites. Five of the values from the Aley carbonatite form a tight cluster and two plot within or near the cluster formed by fersmite from the Upper Fir carbonatite. The Upper Fir fersmite is expected to have relatively high Ta content relative to fersmite from most carbonatites because the Ta content of Upper Fir niobate minerals (pyrochlore and columbite) is relatively high (Simandl et al., 2002). Tantalum content of fersmite from pegmatites is more variable than that

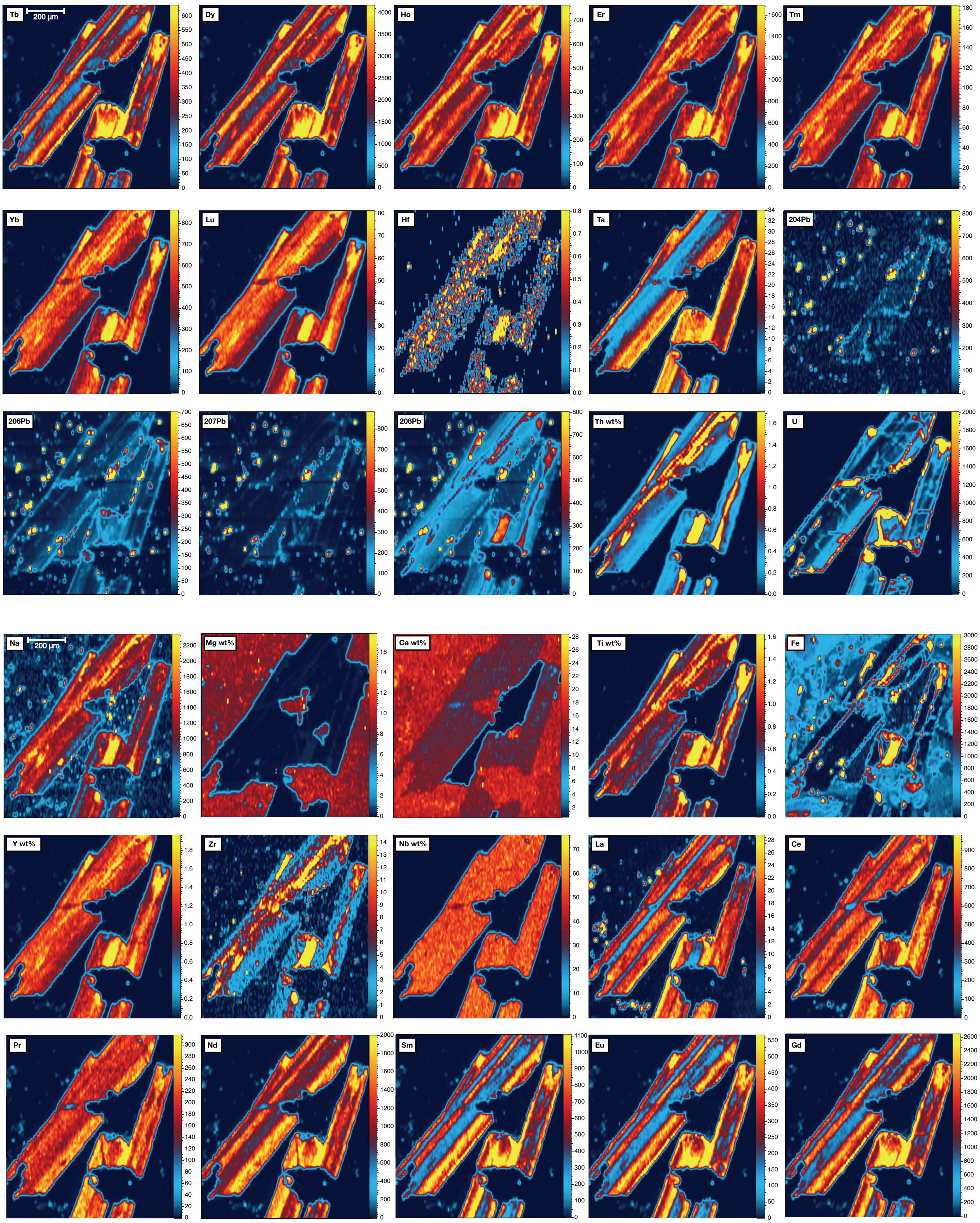


**Fig. 7.** Compositional LA-ICP-MS map of fersmite grains from sample MB-16-02A. The color scales are linear with minimums and maximums defined by the median ±3 standard deviations. Note that this implies that some pixels are below and above the color extremes. Concentrations are in ppm unless noted otherwise. Scale of 200 µm visible on the Na and Tb maps applies to all maps.

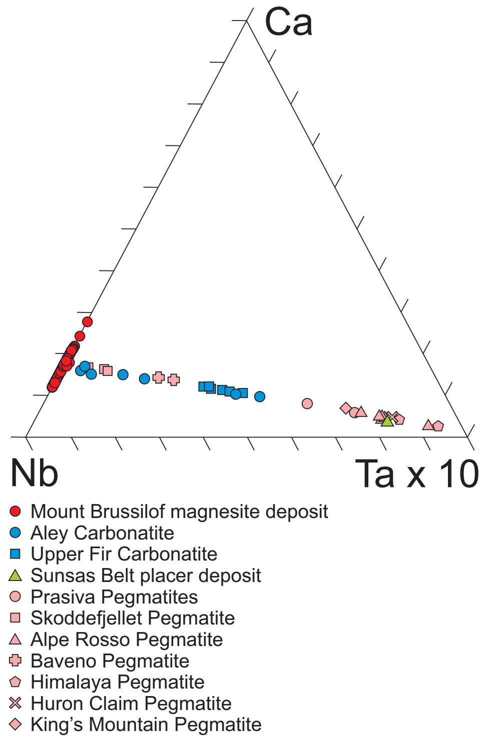


**Fig. 8.** Ca-Nb-Ta x 10 compositions in weight proportions of fersmite from the Mount Brussilof magnesite mine (red), carbonatite (blue), pegmatite (pink), and placer (green) deposits.

of fersmite from carbonatites, and extends closer to the Ta x 10 apex (Fig. 8). This ternary diagram is relevant to use of fersmite as a direct indicator mineral and for targeting specific Nb-Ta deposit types (see section 6.3).

Fersmite is a euxenite group mineral; consequently, it preferentially incorporates Y and HREE in its crystal structure relative to LREE (Ercit, 2005; Škoda and Novák, 2007). The chondrite-normalized REE pattern of the Mount Brussilof fersmite is smooth and convex-upward and similar to fersmite in the Aley carbonatite, albeit with lower LREE (Fig. 6). The maximum of the Mount Brussilof fersmite chondrite-normalized REE pattern is shifted towards heavier REE relative to the Aley carbonatite fersmite pattern, possibly indicating that the mineralizing system at Mount Brussilof had a higher HREE:LREE ratio than that at Aley. This observation may be important for mineral deposit targeting based on direct indicator minerals (see section 6.3) because carbonatites typically have a higher LREE:HREE ratio than other lithologies (e.g., Simandl and Paradis, 2018).

It is possible that the atypical (Nb-rich) composition of the Mount Brussilof fersmite reflects the composition of fluids from which it precipitated. Experimental studies of fluoride-rich systems suggest that as fluids interact with the country rocks and their composition evolves, the mobility of Nb remains higher than that of Ta at pH of 2, and up to a temperature of 250°C, over a wide range of HF concentrations (Timofeev et

**Table 1.** Electron microprobe analyses (wt.%) of fersmite in polished thin sections MB-16-01 and MB-16-02.

| Sample | $Na_2O$ | CaO | $TiO_2$ | $Y_2O_3$ | $Nb_2O_5$ | $Ce_2O_3$ | $Ta_2O_5$ | F | Total |
|---|---|---|---|---|---|---|---|---|---|
| MB-02-1 | 0.07 | 15.82 | 0.91 | 0.76 | 79.50 | 0.00 | 0.00 | 0.04 | 97.10 |
| MB-02-2 | 0.30 | 12.01 | 3.50 | 2.04 | 70.73 | 0.05 | 0.00 | 0.09 | 88.72 |
| MB-02-3 | 0.11 | 15.43 | 1.48 | 0.87 | 78.89 | 0.09 | 0.04 | 0.00 | 96.91 |
| MB-02-4 | 0.10 | 15.70 | 1.05 | 0.63 | 79.02 | 0.09 | 0.00 | 0.02 | 96.62 |
| MB-02-5 | 0.08 | 15.77 | 1.09 | 0.69 | 78.74 | 0.07 | 0.00 | 0.00 | 96.43 |
| MB-02-6 | 0.07 | 16.22 | 0.80 | 0.27 | 80.09 | 0.06 | 0.00 | 0.00 | 97.50 |
| MB-02-7 | 0.10 | 15.70 | 0.86 | 0.60 | 79.69 | 0.05 | 0.01 | 0.00 | 97.01 |
| MB-02-8 | 0.18 | 14.72 | 2.52 | 1.27 | 76.46 | 0.07 | 0.00 | 0.04 | 95.25 |
| MB-02-9 | 0.14 | 15.52 | 1.11 | 0.85 | 78.87 | 0.10 | 0.00 | 0.01 | 96.61 |
| MB-02-10 | 0.33 | 12.43 | 2.86 | 1.52 | 71.73 | 0.02 | 0.00 | 0.00 | 88.88 |
| MB-01-1 | 0.06 | 16.48 | 0.84 | 0.00 | 78.09 | 0.30 | 0.00 | 0.06 | 95.83 |
| MB-01-2 | 0.17 | 15.84 | 0.75 | 0.05 | 77.45 | 0.15 | 0.00 | 0.12 | 94.53 |
| MB-01-3 | 0.11 | 15.14 | 2.47 | 0.32 | 73.56 | 0.20 | 0.05 | 0.09 | 91.95 |
| MB-01-4 | 0.14 | 16.07 | 0.51 | 0.00 | 77.83 | 0.20 | 0.00 | 0.04 | 94.79 |
| MB-01-5 | 0.32 | 9.55 | 3.59 | 0.00 | 68.03 | 0.63 | 0.00 | 0.00 | 82.13 |
| MB-01-6 | 0.41 | 14.37 | 1.66 | 0.18 | 74.07 | 0.09 | 0.00 | 0.02 | 90.79 |
| MB-01-7 | 0.14 | 15.89 | 0.97 | 0.14 | 76.60 | 0.10 | 0.00 | 0.07 | 93.91 |
| MB-01-8 | 0.18 | 15.86 | 0.73 | 0.22 | 76.86 | 0.21 | 0.00 | 0.01 | 94.07 |
| MB-01-9 | 0.14 | 14.68 | 3.17 | 0.65 | 72.24 | 0.07 | 0.00 | 0.02 | 90.96 |
| MB-01-10 | 0.07 | 16.28 | 1.22 | 0.00 | 75.83 | 0.41 | 0.00 | 0.00 | 93.82 |

**Table 2.** Statistical summary of trace element composition (ppm) of fersmite for polished thin sections MB-16-01, MB-16-02A, MB-16-02B, and MB-16-02C.

| **Sample** | **MB-16-01** | **n=30** | | | | **MB-16-02A** | **n=61** | | | |
|---|---|---|---|---|---|---|---|---|---|---|
| Element | Minimum | $1^{st}$ Quartile | Median | $3^{rd}$ Quartile | Maximum | Minimum | $1^{st}$ Quartile | Median | $3^{rd}$ Quartile | Maximum |
| **Na** | 157.90 | 618.00 | 1185.00 | 1684.00 | 3333.00 | 744.00 | 1052.00 | 1155.00 | 1477.00 | 3022.00 |
| **Mg** | | | | | | 12.90 | 180.00 | 420.00 | 1971.00 | 16400.00 |
| **Si** | | | | | | | | | | |
| **Ca** | 102700.00 | 115250.00 | 119200.00 | 121250.00 | 127200.00 | 98900.00 | 108300.00 | 111800.00 | 113100.00 | 133900.00 |
| **Ti** | 3594.00 | 5087.50 | 8080.00 | 13132.50 | 23220.00 | 5840.00 | 7930.00 | 10180.00 | 14730.00 | 28610.00 |
| **Cr** | | | | | | 1.82 | 2.46 | 3.09 | 3.90 | 4.70 |
| **Fe** | | | | | | 6.40 | 85.68 | 402.00 | 1138.75 | 3027.00 |
| **Y** | | | | | | 10700.00 | 14260.00 | 15800.00 | 17960.00 | 26390.00 |
| **Zr** | | | | | | 1.65 | 5.11 | 7.24 | 11.34 | 26.22 |
| **La** | | | | | | 6.14 | 13.64 | 17.35 | 20.60 | 25.54 |
| **Ce** | 773.00 | 1021.75 | 1271.50 | 1670.00 | 2512.00 | 471.00 | 586.00 | 660.00 | 754.00 | 845.00 |
| **Pr** | | | | | | 176.50 | 211.70 | 230.70 | 247.90 | 333.10 |
| **Nd** | | | | | | 913.00 | 1163.00 | 1380.00 | 1802.00 | 2649.00 |
| **Sm** | 591.00 | 1688.00 | 2252.00 | 3359.50 | 8110.00 | 287.90 | 481.00 | 640.00 | 990.00 | 1563.00 |
| **Eu** | | | | | | 136.20 | 227.60 | 323.20 | 477.00 | 798.00 |
| **Gd** | | | | | | 797.00 | 1232.00 | 1789.00 | 2396.00 | 4120.00 |
| **Tb** | | | | | | 208.60 | 307.00 | 438.00 | 554.00 | 870.00 |
| **Dy** | | | | | | 1783.00 | 2411.00 | 2920.00 | 3454.00 | 5960.00 |
| **Ho** | | | | | | 398.90 | 499.00 | 561.00 | 701.00 | 1099.00 |
| **Er** | | | | | | 943.00 | 1186.00 | 1332.00 | 1643.00 | 2452.00 |
| **Tm** | | | | | | 93.70 | 129.30 | 139.90 | 170.60 | 280.20 |
| **Yb** | 48.90 | 141.95 | 255.30 | 377.98 | 621.00 | 419.00 | 604.00 | 679.00 | 801.00 | 1204.00 |
| **Lu** | | | | | | 37.95 | 59.54 | 67.50 | 76.30 | 105.60 |
| **Hf** | | | | | | 0.16 | 0.30 | 0.39 | 0.55 | 1.29 |
| **Ta** | 2.91 | 5.26 | 10.16 | 14.83 | 20.48 | 5.89 | 11.10 | 18.19 | 27.50 | 44.55 |
| **W** | | | | | | | | | | |
| **$^{204}$Pb** | 1.04 | 1.43 | 1.70 | 2.47 | 9.50 | 1.00 | 2.65 | 4.40 | 9.40 | 29.50 |
| **$^{206}$Pb** | 8.44 | 17.70 | 49.65 | 90.70 | 453.00 | 5.39 | 14.09 | 25.00 | 50.10 | 128.80 |
| **$^{207}$Pb** | 1.74 | 3.10 | 4.55 | 6.46 | 25.20 | 1.79 | 3.18 | 4.76 | 11.60 | 29.00 |
| **$^{208}$Pb** | 57.00 | 87.65 | 169.90 | 259.35 | 507.00 | 45.70 | 97.80 | 165.30 | 252.40 | 820.00 |
| **Bi** | | | | | | | | | | |
| **Th** | 3998.00 | 6079.75 | 11025.00 | 17627.50 | 35880.00 | 3020.00 | 6510.00 | 10750.00 | 16480.00 | 52100.00 |
| **U** | 75.80 | 154.50 | 607.00 | 999.00 | 4739.00 | 47.90 | 140.00 | 274.30 | 622.00 | 1171.00 |

al., 2017). Under such conditions, both Nb and Ta are expected to precipitate rapidly upon removal of fluoride from an acidic brine (Timofeev et al., 2015, 2017). Fluorite was not observed close to the Mount Brussilof fersmite occurrence, suggesting that this fersmite may have formed from distal, relatively low concentration fluids (some F may have been incorporated by the crystal structure of mica found locally in the magnesite mine area). Because the fersmite occurrence is small, it is also possible that fersmite precipitated due to fluid mixing. More work is required to clarify the origin of the Mount Brussilof fersmite occurrence.

### 6.2. Compositional maps of individual fersmite crystals

The systematic zonation shown on the compositional maps of fersmite (Fig. 7) explains the relatively high degree of variability in the spot data, and indirectly confirms the internal consistency of the trace element data (Table 2). This zonation suggests a mineralizing system that evolved during fersmite crystallization. In combination with the non-metamict appearance of the Mount Brussilof fersmite, the zonation helps distinguish the Mount Brussilof and possibly 'alpine cleft' fersmite from that formed in pegmatites, peralkaline intrusions, carbonatites, and other geological environments.

### 6.3. Fersmite as direct indicator mineral

The physical and chemical properties of primary fersmite make it a useful direct indicator mineral for carbonatites and related deposits. Indicator minerals are defined by McClenaghan (2005, p. 233) as "mineral species that, when appearing as transported grains in clastic sediments, indicate the presence in bedrock of a specific type of mineralization, hydrothermal alteration or lithology. Their physical and chemical characteristics, including a relatively high density, facilitate their preservation and identification and allow them to be readily recovered at the parts per billion level from sample media such as till, stream sediments or soil producing large exploration targets". An indicator mineral that contains pathfinder elements characteristic of a targeted deposit in

**Table 2.** Continued.

| **Sample** | **MB-16-02B** | **n=46** | | | | **MB-16-02C** | **n=82** | | | |
|---|---|---|---|---|---|---|---|---|---|---|
| Element | Minimum | 1st Quartile | Median | 3rd Quartile | Maximum | Minimum | 1st Quartile | Median | 3rd Quartile | Maximum |
| **Na** | 652.00 | 805.25 | 1033.00 | 1425.25 | 2236.00 | 248.80 | 422.25 | 561.00 | 683.50 | 2281.00 |
| **Mg** | 12.00 | 50.70 | 305.50 | 1216.25 | 4600.00 | 14.30 | 32.90 | 128.50 | 799.75 | 31900.00 |
| **Si** | | | | | | 1600.00 | 2150.00 | 2500.00 | 2800.00 | 4900.00 |
| **Ca** | 76200.00 | 96125.00 | 100600.00 | 105575.00 | 203000.00 | 71400.00 | 82825.00 | 84950.00 | 89400.00 | 142000.00 |
| **Ti** | 3400.00 | 4647.50 | 5271.00 | 6692.50 | 9240.00 | 2200.00 | 3580.00 | 4352.50 | 6002.50 | 12400.00 |
| **Cr** | 1.33 | 1.54 | 1.65 | 1.94 | 2.80 | 1.86 | 2.10 | 2.42 | 3.00 | 6.20 |
| **Fe** | 6.20 | 87.60 | 256.50 | 667.00 | 3158.00 | 4.50 | 15.68 | 65.25 | 514.25 | 2690.00 |
| **Y** | 9070.00 | 10900.00 | 13385.00 | 15095.00 | 21420.00 | 10560.00 | 13235.00 | 14015.00 | 15322.50 | 23270.00 |
| **Zr** | 2.28 | 4.09 | 7.14 | 10.28 | 17.95 | 0.91 | 3.19 | 4.03 | 5.88 | 21.70 |
| **La** | 4.58 | 14.38 | 15.76 | 18.40 | 48.60 | 1.41 | 6.56 | 8.59 | 10.47 | 22.20 |
| **Ce** | 343.00 | 516.00 | 547.70 | 604.50 | 813.00 | 117.90 | 286.50 | 334.60 | 404.05 | 580.00 |
| **Pr** | 140.30 | 160.88 | 178.50 | 203.53 | 238.50 | 81.70 | 101.83 | 122.00 | 141.53 | 205.90 |
| **Nd** | 619.00 | 899.50 | 1032.00 | 1336.50 | 1656.00 | 382.00 | 619.50 | 758.00 | 930.25 | 1467.00 |
| **Sm** | 187.20 | 342.75 | 450.50 | 776.50 | 1001.00 | 139.30 | 260.00 | 354.50 | 451.50 | 796.00 |
| **Eu** | 90.40 | 163.93 | 222.65 | 366.15 | 476.00 | 68.60 | 128.50 | 174.70 | 224.78 | 449.00 |
| **Gd** | 495.00 | 884.75 | 1162.00 | 1664.00 | 2278.00 | 373.00 | 674.75 | 926.50 | 1189.25 | 2350.00 |
| **Tb** | 128.40 | 228.95 | 295.60 | 399.00 | 619.00 | 97.00 | 171.45 | 227.00 | 303.68 | 1200.00 |
| **Dy** | 1104.00 | 1866.00 | 2171.00 | 2650.25 | 4250.00 | 775.00 | 1228.00 | 1559.50 | 2289.50 | 8570.00 |
| **Ho** | 252.30 | 374.48 | 420.35 | 504.25 | 887.00 | 171.10 | 254.45 | 323.40 | 394.75 | 1614.00 |
| **Er** | 660.00 | 835.25 | 972.00 | 1167.50 | 1834.00 | 434.00 | 598.25 | 758.00 | 892.75 | 2060.00 |
| **Tm** | 73.30 | 89.00 | 106.20 | 125.53 | 179.50 | 46.90 | 65.18 | 81.45 | 96.78 | 164.10 |
| **Yb** | 322.00 | 418.00 | 501.50 | 611.75 | 772.00 | 201.30 | 313.48 | 383.50 | 440.00 | 697.00 |
| **Lu** | 29.68 | 42.20 | 51.70 | 60.93 | 73.80 | 19.04 | 31.69 | 36.59 | 42.15 | 68.60 |
| **Hf** | 1.30 | 2.04 | 2.35 | 2.78 | 4.34 | 0.19 | 0.45 | 0.66 | 0.87 | 1.86 |
| **Ta** | 4.49 | 6.85 | 11.05 | 19.35 | 23.54 | 1.98 | 3.54 | 5.22 | 9.78 | 16.55 |
| **W** | | | | | | 140.40 | 754.00 | 1064.50 | 1276.00 | 1806.00 |
| **$^{204}$Pb** | 1.23 | 2.18 | 2.60 | 3.15 | 11.00 | 2.60 | 3.50 | 4.20 | 5.20 | 15.50 |
| **$^{206}$Pb** | 3.03 | 8.98 | 20.44 | 27.69 | 76.30 | 2.05 | 4.47 | 8.05 | 15.93 | 74.60 |
| **$^{207}$Pb** | 1.16 | 1.96 | 2.41 | 3.03 | 13.79 | 0.85 | 1.42 | 1.85 | 3.00 | 17.80 |
| **$^{208}$Pb** | 42.40 | 60.15 | 126.75 | 234.50 | 533.00 | 20.93 | 56.13 | 72.40 | 125.28 | 478.00 |
| **Bi** | | | | | | 0.03 | 0.04 | 0.04 | 0.05 | 0.09 |
| **Th** | 4020.00 | 6177.50 | 11120.00 | 20045.00 | 53100.00 | 4440.00 | 9275.00 | 11220.00 | 19385.00 | 62100.00 |
| **U** | 9.26 | 101.50 | 239.45 | 319.28 | 614.00 | 3.88 | 39.85 | 91.75 | 179.48 | 1270.00 |

concentrations detectable by commonly applied analytical methods such as portable XRF or traditional, laboratory-based analytical methods is referred to as a ‘direct’ indicator mineral (Simandl et al., 2017).

The direct indicator mineral concept involves using traditional geochemical methods to identify sediment samples with anomalous concentrations of pathfinder elements, followed by analysis of anomalous samples by Quantitative Evaluation of Materials by Scanning Electron Microscopy, or QEMSCAN®(Simandl et al., 2017). This two-step approach provides the equivalent of geochemical and indicator mineral surveys without expensive and time-consuming traditional indicator mineral surveys involving hand-picking. Fersmite, as well as pyrochlore supergroup and columbite-tantalite series minerals, REE-fluorocarbonates, and monazite, were used as direct indicator minerals in orientation surveys targeting carbonatites and related deposits in British Columbia (Mackay et al., 2016; Simandl et al., 2018). Fersmite from carbonatites and related deposits is Nb-rich, whereas fersmite from pegmatites may have significantly higher Ta content (Fig. 8). It remains unclear if the composition of fersmite from Mount Brusilof is representative of ‘alpine-cleft’ style fersmite occurrences. More work is required to determine which the case is; nevertheless, our summary (Fig. 8) is the first step in developing a fersmite discrimination diagram for mineral exploration and deposit targeting.

## 7. Summary

The Mount Brussilof fersmite is characterized by strongly zoned euhedral crystals growing on the walls of cavities, or enclosed in a sugary dolomite matrix within sparry dolomite zones that crosscut magnesite ore. It post-dates sparry dolomitization and formation of magnesite ore. The Mount Brussilof fersmite shares textural similarities with niobate mineral occurrences reported in ‘alpine cleft’ occurrences in Europe, and differs texturally and compositionally from fersmite in carbonatite-related Nb mineralization where it is considered secondary and derived from pre-existing niobate minerals. The Mount Brussilof fersmite probably precipitated from hydrothermal fluids. Fersmite has potential as a direct indicator mineral.

**Acknowledgments**

This study is part of the Targeted Geoscience Initiative 5 spearheaded by Natural Resources Canada. We thank Baymag Inc. and the mine manager Ian Knuckey for permission to study and sample the Mount Brussilof deposit. Former mine geologist Chris Pilarski first attracted our attention to the unknown mineral later identified to be fersmite. Some of the fersmite samples used in this study were provided by Alex Hogg or Brody Myers, mine geologists at Mount Brussilof mine. Dr. Mati Raudsepp, formerly with the Electron-Microbeam/X-Ray Diffraction Facility, Department of Earth, Ocean and Atmospheric Sciences, University of British Columbia provided timely XRD analysis.

**References cited**

Aitken, J.D., 1971. Control of Lower Paleozoic Sedimentary Facies by the Kicking Horse Rim, Southern Rocky Mountains, Canada. Bulletin of Canadian Petroleum Geology, 19, 557-569.

Aitken, J.D., 1978. Revised models for depositional grand cycles, Cambrian of the southern Rocky Mountains, Canada. Bulletin of Canadian Petroleum Geology, 26, 515-542.

Aitken, J.D., 1989. Birth, Growth and Death of the Middle Cambrian Cathedral Lithosome, Southern Rocky Mountains; Bulletin of Canadian Petroleum Geology, 37, 316-333.

Aitken, J.D., and McIlreath, L.A., 1984. The Cathedral Reef Escarpment, a Cambrian Great Wall with Humble Origins. Geoscience, 13, 17-19.

Aitken, J.D., and McIlreath, L.A., 1990. Comment on "The Burgess Shale: Not in the Shadow of the Cathedral Escarpment". Geoscience Canada, 17, 111-115.

Al-Aasm, I., 2003. Origin and characterization of hydrothermal dolomite in the Western Canadian Sedimentary Basin. Journal of Geochemical Exploration, 78, 9-15.

Al-Aasm, I., Lonnee, J., and Clarke, J., 2000. Multiple fluid flow events and the formation of saddle dolomite: examples from Middle Devonian carbonates of the Western Canada Sedimentary Basin, Journal of Geochemical Exploration, 69, 11-15.

Alfonso, P., Oliva, J., Calvo, D., Parcerisa, D., and Garcia-Valles, M., 2015. Nb-Ta oxide minerals of alluvial placers from the Sunas Belt, Precambrian shield of Bolivia. In: Mineral Resources in a Sustainable World, 13th SGA Biennial Meeting 2015, proceedings, 2, pp. 667-670.

Anthony, J.W., Bideaux, R.A., Bladh, K.W., and Nichols, M.C., Eds., 2017. Handbook of Mineralogy, Mineralogical Society of America, Chantilly, VA 20151-1110, USA. <http://www.handbookofmineralogy.org/> Accessed November 2017.

Aurisicchio, C., De Vito, C., Ferrini, V., and Orlandi, P., 2001. Nb-Ta oxide minerals from miarolitic pegmatites of the Baveno pink granite, NW Italy. Mineralogical Magazine, 65, 509-522.

Chakhmouradian, A.R., Reguir, E.P., Kressall, R.D., Crozier, J., Pisiak, L.K., Sidhu, R., and Yang, P., 2015. Carbonatite-hosted niobium deposit at Aley, northern British Columbia (Canada): Mineralogy, geochemistry and petrogenesis. Ore Geology Reviews, 64, 642-666.

Chudy, T.C., 2013. The petrogenesis of th Ta-bearing Fir Carbonatite system, east-central British Columbia, Canada. PhD thesis, University of British Columbia, British Columbia, Canada, 553 p.

Ercit, T.S., 2005. Identification and alteration trends of granitic-pegmatite-hosted (Y,REE,U,Th)-(Nb,Ta,Ti) oxide minerals: a statistical approach. Canadian Mineralogist, 43, 1291-1303.

Foord, E.E., and Mrose, M.E., 1978. Rynersonite, $Ca(Ta,Nb)_2O_6$, a new mineral from San Diego County, California. American Mineralogist, 63, 709-714.

Fritz, W.H., 1990. Comment: In Defence of the Escarpment near the Burgess Shale Fossil Locality. Geoscience Canada, 17, 106-110.

Guastoni, A., Diella, V., and Pezzotta, F., 2008. Vigezzite and associated oxides of Nb-Ta from emerald-bearing pegmatites of the Vigezzo Valley, Western Alps, Italy. The Canadian Mineralogist, 46, 619-633.

Karup-Møller, S., Rose-Hansen, J., and Sørensen, H., 2010. Eudialyte decomposition minerals with new hitherto undescribed phases from the Ilímaussaq complex, South Greenland. Bulletin of the Geological Society of Denmark, 58, pp. 75-88.

Leach, D.L., Sangster, D.F., Kelley, K.D., Large, R.R., Garven, G., Allen, C.R., Gutzmer, J., and Walters, S.G., 2005. Sediment-hosted lead-zinc deposits: a global perspective. Society of Economic Geologists, Economic Geology One Hundredth Anniversary Volume 1905-2005, 561-607.

Leech, G.B., 1966. Kananaskis Lakes. Geological Survey of Canada, Open File map 634 scale 1:126,720.

Lumpkin, G.R., and Ewing, R.C., 1992. Geochemical alteration of pyrochlore group minerals: Microlite subgroup. American Mineralogist, 77, 179-188.

Mäder, U.K., 1987. The Aley Carbonatite complex, northern Rocky Mountains, British Columbia. In: Geological Fieldwork 1986, British Columbia Ministry of Energy, Mines and Petroleum Resources, British Columbia Geological Survey Paper 1987-1, pp. 283-288.

Mackay, D.A.R., and Simandl, G.J., 2014. Geology, market and supply chain of niobium and tantalum-a review. Mineralium Deposita, 49, p. 1025-1047.

Mackay, D.A.R., Simandl, G.J., Ma, W., Redfearn, M., and Gravel, J., 2016. Indicator mineral-based exploration for carbonatites and related specialty metal deposits-A QEMSCAN® orientation survey, British Columbia, Canada. Journal of Geochemical Exploration, 165, 159-173.

McClenaghan, M.B., 2005. Indicator mineral methods in mineral exploration. Geochemistry: Exploration, Environment, Analysis, 5, 233-245.

McDonough, W.F., and Sun, S.S., 1995. The composition of the Earth. Chemical geology, 120, 223-253.

McMechan, M.E., and Leech, G.B., 2011. Geology, Mount Assiniboine, British Columbia. Geological Survey of Canada, Canadian Geoscience Map 13, scale 1:50,000.

Mrad, C., 2016. Fluid compartmentalization of Devonian and Mississippian dolostones, Western Canada Sedimentary Basin; evidence from fracture mineralization. M.Sc. thesis, University of Windsor, Ontario, Canada, 114 p.

Nesbitt, B.E., and Prochaska, W., 1998. Solute chemistry of inclusion fluids from sparry dolomites and magnesites in Middle Cambrian carbonate rocks of the southern Canadian Rocky Mountains. Canadian Journal of Earth Sciences, 35, 546-555.

Niggli, P., Koenigsbergejr, J., and Parker, R.L., 1940. Die Mineralien der Schweizeralpen-2 Bände. Basel, Wepf & Co.

Paradis, S., and Simandl, G.J., 2017. Is there a genetic link between the SEDEX and MVT deposits of the Canadian Cordillera? In: Rogers, N., (Ed.), Targeted Geoscience Initiative, 2016 Report of Activities, Geological Survey of Canada, Open File 8199, pp. 107-113.

Paradis, S., and Simandl, G.J., 2018. Are there genetic links between carbonate-hosted barite-zinc-lead sulphide deposits and magnesite mineralization in southeast British Columbia? In: Rogers, N., (Ed.), Targeted Geoscience Initiative, 2016 Report of Activities, Geological Survey of Canada, Open File 8358, pp. 217-227.

Paradis, S., Hannigan, P., and Dewing, K., 2007. Mississippi Valley-type lead-zinc deposits. In: Goodfellow, W.D., (Ed.), Mineral Deposits of Canada: A Synthesis of Major Deposit-Types, District Metallogeny, the Evolution of Geological Provinces, and Exploration Methods, Geological Association of Canada, Mineral Deposits Division, Special Publication No. 5, pp. 185-203.

Paton, C., Hellstrom, J., Paul, B., Woodhead, J., and Hergt, J., 2011.

Iolite: freeware for the visualisation and processing of mass spectrometric data. Journal of Analytical Atomic Spectrometry, 26, 2508-2518.

Pouchou, J.L., and Pichoir, F., 1984. Un nouveau modèle de calcul pour la microanalyse quantitative par spectrométrie des rayons X. La Recherche Aérospatiale, 3, 167-192.

Prsek, J.,Majka, J., Uher, P., and Chudik, P., 2010. Niobium-tantalum minerals in the Skoddefjellet NYF granitic pegmatite, Svalbard Archipelago, Norway: Primary versus secondary assemblage. Neues Jahrbuch für Mineralogie-Abhandlungen, 187, 235-248.

Root, K.G., 2001. Devonian Antler fold and thrust belt and foreland basin development in the southern Canadian Cordillera: Implication for the Western Canadian Sedimentary Basin. Bulletin of Canadian Petroleum Geology, 49, 7-36.

Rosenberg., P.E., Burt, D.M., and Holland, H.D., 1967. Calcite - dolomite - magnesite stability relations in solutions: The effect of ionic strength. Geochimica et Cosmochimica Acta, 31, 39l-396.

Simandl, G.J., and Hancock, K.D., 1991. Geology of the Mount Brussilof magnesite deposit, SE British Columbia. In: Geological Fieldwork 1990, British Columbia Ministry of Energy, Mines and Petroleum Resources, British Columbia Geological Survey Paper 1991-1, pp. 269-278.

Simandl, G.J., and Hancock, K.D., 1998. Sparry Magnesite. In: Geological Fieldwork 1997, British Columbia Ministry of Employment and Investment, Geological Survey Paper 1998-1, pp. 24E-1-24E-3.

Simandl, G.J., and Paradis, S., 2018. Carbonatites: related ore deposits, resources, footprint, and exploration methods. Applied Earth Science, 127, 123-152.

Simandl, G.J., Hancock, K.D., Hora, D.Z., and MacLean, M.E., 1992. Regional geology of the Mount Brussilof carbonate-hosted magnesite deposit, southeastern British Columbia, Canada. In: Hora, Z.D., Hamilton, W.N., Grant, B., and Kelly, P.D. (Eds.), Industrial Minerals of Alberta and British Columbia, Canada, proceedings of the 27th Forum on the Geology of Industrial Minerals, May 5-10, 1991, British Columbia Geological Survey Open File 1991-23 and Alberta Geological Survey Information Series 115, pp. 57-65.

Simandl, G.J., Jones, P.C., and Rotella M., 2002. Blue River Carbonatites, British Columbia-Primary Exploration Targets for Tantalum. In: Exploration and Mining in British Columbia 2001, pp. 73-82.

Simandl, G.J., Mackay, D.A.R., Ma, X., Luck, P., Gravel, J., and Akam, C., 2017. The direct indicator mineral concept and QEMSCAN® applied to exploration for carbonatite and carbonatite-related ore deposits. In: Ferbey, T., Plouffe, A., and Hickin, A.S., (Eds.), Indicator Minerals in Till and Stream Sediments of the Canadian Cordillera. Geological Association of Canada Special Paper Volume 50, and Mineralogical Association of Canada Topics in Mineral Sciences Volume 47, pp. 175-190.

Simandl, G.J., Burt, R.O., Trueman, D.L., and Paradis, S., 2018. Tantalum and Niobium: Deposits, resources, exploration methods, and market-primer for geoscientists. Geoscience Canada, vol. 45, p. 85-96. https://journals.lib.unb.ca/index.php/GC/article/view/26003/1882519204.

Škoda, R., and Novák, M., 2007. Y,REE,Nb,Ta,Ti-oxide ($AB_2O_6$) minerals from REL-REE euxenite-subtype pegmatites of the Třebíč Pluton, Czech Republic; substitutions and fractionation trends. Lithos, 95, 43-57.

Sweetapple, M.T., and Lumpkin, G.R., 2011. Secondary Ta-Nb oxide minerals of the Archaean Wodgina Pegmatite district, Western Australia, and their significance. Asociación Geológica Argentina, Serie D, Publicación Especial No. 14, 209-212.

Symons, D.T.A., Enkin, R.J., and Cioppa, M.T., 1999. Paleomagnetism in the Western Canada Sedimentary Basin: dating fluid flow and deformation events. Bulletin of Canadian Petroleum Geology, 47, 534-547.

Timofeev, A., Migdisov, A.A., and Williams-Jones, A.E., 2015. An experimental study of the solubility and speciation of niobium in fluoride-bearing aqueous solutions at elevated temperature. Geochimica et Cosmochimica Acta, 158, 103-111.

Timofeev, A., Migdisov, A.A., and Williams-Jones, A.E., 2017. An experimental study of the solubility and speciation of tantalum in fluoride-bearing aqueous solutions at elevated temperature. Geochimica et Cosmochimica Acta, 197, 294-304.

Uher, P., Cerny, P., and Chapman, R., 1998. Evolution of Nb,Ta-oxide minerals in the Prasiva granitic pegmatites, Slovakia. II. External hydrothermal Pb, Sb overprint. Canadian Mineralogist, 36, 535-545.

Yao, Q.J., and Demicco, R.V., 1995. Paleoflow patterns of dolomitizing fluids and paleo hydrogeology of the southern Canadian Rocky Mountains: evidence from dolomite geometry and numerical modeling. Geology, 23, 791-794.

Yao, Q.J, and Demicco, R.V., 1997. Dolomitization of the Cambrian carbonate platform, Southern Canadian Rocky Mountains: Dolomite front geometry, fluid inclusion geochemistry, isotopic signature, and hydrologic modelling studies. American Journal of Science, 297, 892-938.

# A skeleton data model for geochemical databases at the British Columbia Geological Survey

Tian Han[1, a], Alexei S. Rukhlov[1], Janet M. Riddell[1], and Travis Ferbey[1]

[1] British Columbia Geological Survey, Ministry of Energy, Mines and Petroleum Resources, Victoria, BC, V8W 9N3
[a] corresponding author: Tian.Han@gov.bc.ca

Recommended citation: Han, T., Rukhlov, A.S., Riddell, J.M., and Ferbey, T., 2019. A skeleton data model for geochemical databases at the British Columbia Geological Survey. In: Geological Fieldwork 2018, British Columbia Ministry of Energy, Mines and Petroleum Resources, British Columbia Geological Survey Paper 2019-01, pp. 125-135.

**Abstract**

Data modelling is a key component to developing any database. In the past, the British Columbia Geological Survey has modelled geochemical data sets individually. Herein we propose a skeleton data model capable of capturing and representing the commonalities of individual sets by focusing on the entities, attributes, and relationships common to most geochemical data sets. We use this skeleton data model to update existing models for four province-wide data sets (lithogeochemical, regional drainage, till, and coal ash), capturing the unique characteristics of each. Applying the skeleton data model streamlines data handling steps, from data compilation to product generation, and establishes a reliable flow for managing geochemical data at the British Columbia Geological Survey.

**Keywords:** Geochemical data model, database, entities, attributes, relationships, data lifecycle activities, operation, query, SQL, data access, analytical methods, chemical element abundance

## 1. Introduction

The British Colombia Geological Survey (BCGS) is currently the custodian of four province-wide geochemical data sets: lithogeochemical; regional drainage geochemical surveys (RGS); till; and coal ash. The lithogeochemical data set contains analyses from bedrock samples; the RGS data set contains analyses from water and stream-, lake- and moss mat- sediment samples; the till geochemical data set contains analyses from subglacial till samples; and the coal ash data set contains analyses of the inorganic residue remaining after coal combustion. These data sets were extracted from reports produced or archived by the BCGS in PDF, Excel, or ASCII formats. The BCGS has begun systematically compiling and migrating these geochemical data sets to relational databases, where data are centrally maintained and managed for easy access, efficient update, enhanced consistency, effective quality control, and long-term storage. Previously, we created individual data models for each of the four province-wide data sets (Han et al., 2016, 2017; Bustard et al., 2017; Riddell and Han, 2017). However, although the data sets are derived from samples of different media, they all record values of abundances of chemical elements or compounds and thus share commonalities that can be expressed in terms of generic entities, common attributes, and intrinsic relationships. This led us to develop a skeleton data model to capture these commonalities across all geochemical data sets that could be used as a base for developing data set-specific models. These data set-specific models are created by customizing the skeleton model to incorporate the unique characteristics of the corresponding data sets, rather than by building an entirely new model. This approach helps standardize geochemical data attribution, management, reconciliation, publication, and quality control.

In this paper, we present the skeleton data model, describe how it is adapted for each of the four province-wide geochemical data sets, present the corresponding detailed data model, and outline the post-data modeling work, including the streamlined process built around these databases to support geochemical data lifecycle activities.

## 2. Developing a skeleton data model for geochemical data

Database development is typically done in four stages: requirement analysis; logical design; implementation; and database population (Connolly and Begg, 1999). The result of logical design is a data model conceived to represent the data of interest in a database environment. A data model is obtained through a process called data modeling by: 1) determining the data entities; 2) defining the attributes for each data entity; and 3) resolving the relationship between data entities. Each of the lithogeochemical, RGS, till, and coal ash geochemical data sets has multiple entities, attributes, and relationships. Some are unique to a specific data set, whereas others are common to all data sets. Below we consider the common ones and outline a skeleton data model capable of representing them all (Fig. 1). To complement the 'structural view' portrayed by the skeleton data model (Fig. 1), a 'data view' (Fig. 2) shows the appearance of the data model once it is populated with real data. To avoid confusion in the following discussion, we present entity names in boldface and attribute names in italics.

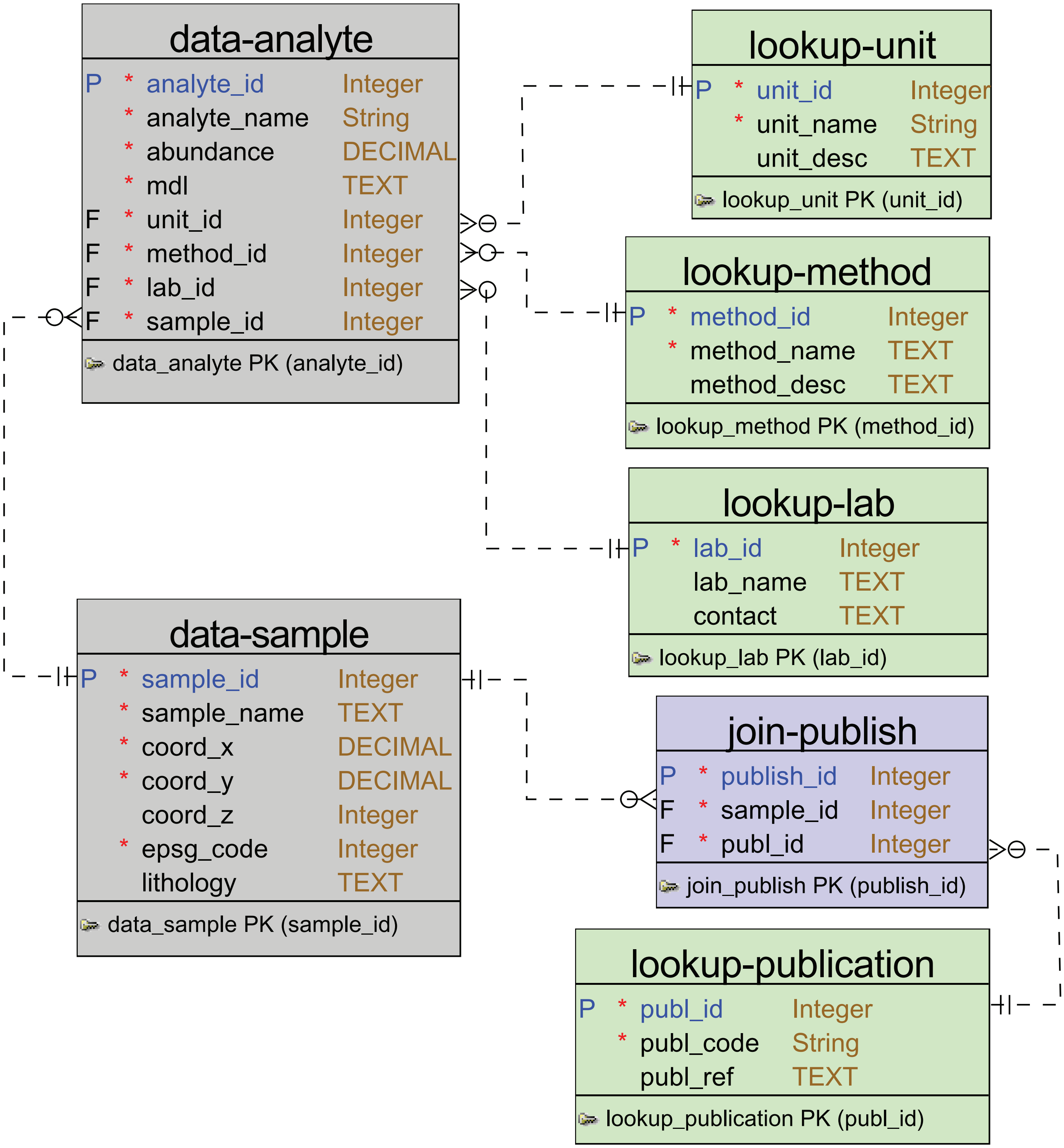


**Fig. 1.** Skeleton data model for geochemical data. Each of the seven boxes represents an entity. The dashed lines connecting the boxes depict entity relationships. The name of each entity is shown in boldface; attribute names are on the left, related data types on the right. The bottom row of each box is the attribute that functions as the primary key of the entity. Mandatory attributes are indicated by an asterisk.

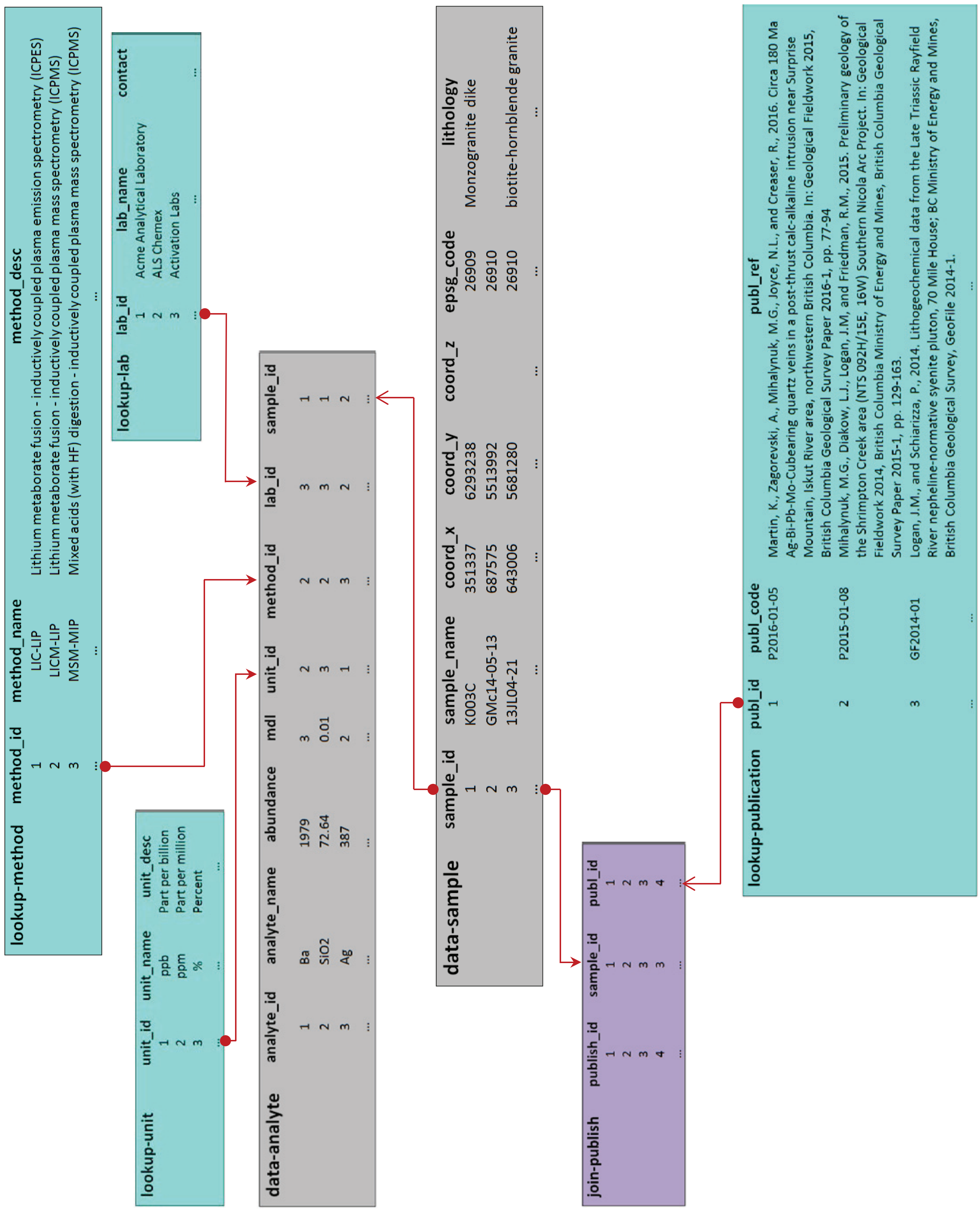


**Fig. 2.** Skeleton data model populated with real data in ‘data view’.

## 2.1. Entities

In general, a geochemical data set comprises two generic entities: sample and analyte, and several related auxiliary entities. The sample entity comprises a suite of common attributes, including sample name, location, geology, lithology, and other properties. In the case where one field sample is split into several fractions, each split is a sub-sample, which is treated as a formal record in the sample entity and is assigned with a unique *sample_id*. These sub-samples can be further named in the *sample_name* attribute so that the 'parent-children' relationship between a field sample and its sub-samples is made obvious. The analyte entity captures analytical values representing concentrations of chemical elements or compounds. The common attributes of the analyte entity are analytical value, unit, analytical method, and the laboratory responsible for the analysis. These two entities and their associated attributes are typically common to all geochemical data sets. The skeleton data model (Fig.1) has the sample and analyte entities, along with five other auxiliary entities, where each entity is depicted as a table with a list of entries for its attributes and data types.

Among the five auxiliary entities included in the skeleton data model (Fig. 1), the **lookup-unit** holds all common units that can be assumed by the analyte abundance values; the **lookup-method** captures all the analytical methods used for sample analysis; the **lookup-lab** maintains the analytical laboratories and contact information; and the **lookup-publication** provides source references for samples included in the database. All these entities have names starting with 'lookup', indicating they function as lookup tables. Though these entities could be combined with either the **data-sample** or **data-analyte** entities, keeping them separate is preferred for categorizing logic data, normalizing between entities, and enhancing data integrity and performance. For example, if an analytical laboratory changes its name from X to Y and the laboratory information is stored in the **data-analyte** entity, we would have to update all the records of analytes that were done by X. Missing any one of them would compromise data integrity. By keeping laboratory information separately as shown in Figure 1, we only have to update one record in the **lookup-lab** entity.

## 2.2. Attributes

The sample entity, named **data-sample** in the skeleton data model, contains a list of nine attributes. These attributes are *sample_id* for record identification; *sample_name* for sample name; *coord_x* and *coord_y* for sample location coordinates; *coord_z* for sample elevation; *epsg_code* for geospatial reference system code defined by the European Petroleum Survey Group (EPSG; IOGP, 2018); *collect_date* for date of sample collection; and *lithology* and *sample_desc*. Using EPSG code enables us to represent sample coordinates concisely in their original spatial reference systems and avoid unnecessary re-projection calculations. The analyte entity, named **data-analyte** in the skeleton data model, has eight attributes, of which *analyte_id* is for record identification; *analyte_name* is for analyte name; *abundance* is for analyte abundance value; and *mdl* is for minimum detection limit.

## 2.3. Relationships

Having determined entities and their associated attributes, we then resolve relationships between entities. For each entity of the skeleton data model, the first attribute is created for record identification with a name that ends with 'id'. Although without real physical meaning, this attribute is called the primary key, and is a unique identifier that can be used to locate specific records and facilitate efficient joining between entities. Other attributes with names ending with 'id' in each entity (Fig. 1) are used for linking related entities. These attributes are called foreign keys. A foreign key in one entity is commonly the primary key in another. For example, *sample_id* is a foreign key in **data-analyte** entity but the primary key in **data-sample** entity.

The relationship between the entities **data-sample** and **data-analyte** is determined by the *sample-id* in both. It is a 'one-to-many relationship', meaning that one sample may have many analytes. This is common in geochemical data sets because samples are routinely analyzed for multiple elements. One-to-many relationships also exist between **lookup-unit** and **data-analyte** defined by *unit_id*; **lookup-method** and **data-analyte** by *method_id*; and **lookup-lab** and **data-analyte** by *lab_id*. These relationships are depicted using a 'crow foot' symbol (Connolly and Begg, 1999) in Figure 1.

The **data-sample** and **lookup-publication** entities commonly have a 'many-to-many relationship', such as where one sample is reported in multiple publications or, as is generally the case, a single publication reports results from multiple samples. It would be difficult and inefficient to implement this relationship directly because it would result in many duplicated or blank attributes. As a result, a special entity, **join-publish**, is introduced and is embedded between **data-sample** and **lookup-publication**. It joins the two (hence the name starting with join-) and turns the many-to-many relationship into two one-to-many relationships; one between **data-sample** and **join-publish** and the other between **lookup-publication** and **join-publish**.

## 2.4. Query support

Our skeleton data model also considers user query requirements. The model and derived databases are designed to accommodate common query requirements such as looking up records of samples or analytes that satisfy certain criteria. For example, a user may want to see samples with Ag concentrations above 50 ppm that were analyzed with AAS (aqua regia-cold vapour atomic absorption spectrometry). Or the user may want to identify samples with Au and As concentrations (analyzed using Instrumental Neutron Activation) both above 95$^{th}$ percentile. The model is able to accommodate unique identification and extraction of samples efficiently with simple Structured Query Language (SQL) statements.

The model also supports spatial queries. Geochemical sample sites are treated as points with coordinates specified in geospatial reference systems using EPSG codes (a standard in geospatial information technology and recognized by the Open Geospatial Consortium). Sample coordinates can be extracted and used for spatial visualization and further examination against other geological data sets.

## 3. Adapting the skeleton model to suit different geochemical data sets

The skeleton data model presented in Figure 1 aligns well with the Open Geoscience data model (Granitto et al, 2012; Watson and Evans, 2012). It is our intention to use it as the framework to model all geochemical data sets currently hosted by the BCGS. It is a base that can be built upon to address the unique entities, attributes, and relationships existing in the corresponding data sets. Below we present the data model for each of the four province-wide data sets and discuss the customization details.

### 3.1. Data model for lithogeochemical data set

The BCGS lithogeochemical data set consists of more than 11,000 samples with about a quarter million determinations generated by 26 different analytical methods carried out at 21 laboratories. The data were compiled from reports published since 1986 by BCGS geoscientists and research partners from the Geological Survey of Canada (GSC) and Canadian universities.

We reconstructed the data model used by Han et al (2016) based on the skeleton model. The updated lithogeochemical data model (Fig. 3) retains all components of the skeleton model with the addition of several lithogeochemistry-specific attributes and two entities. A **lookup-geologist** entity was added to identify who collected a sample and a **lookup-preparation** entity was included to record how samples were prepared before analysis.

### 3.2. Data model for RGS geochemical data set

The regional geochemical survey data set includes results from drainage samples (stream-, lake-, and moss mat-sediment, and water), collected by the Geological Survey of Canada, BCGS, and Geoscience BC since 1976. About 80% of the province has been sampled at a density of one sample per 7 to 13 km$^2$ (Lett and Rukhlov, 2017). Province-wide RGS compilations were released by Lett (2005), Lett (2011), and Rukhlov and Naziri (2015). Han and Rukhlov (2017) presented a data model in which all RGS data were consolidated into a unified relational database. Currently, the data set has about 65,000 samples and 5 million analyses generated by 18 analytical methods at 18 laboratories.

In the updated RGS geochemical data model (Fig. 4) we added three new entities to the skeleton data model: **data-lake** (with attributes specific to lake sediment and water samples), **data-stream** (with attributes specific to stream sediment and water samples), and **data-moss** (with attributes specific to sediment trapped by moss mats). Each of the three has a one-to-one relationship with the **data-sample** entity, meaning that theoretically, they could all be incorporated into the **data-sample** entity. However, doing so would result in many blank attributes for most of the records.

### 3.3. Data model for till geochemical data set

Till geochemical surveys typically sample subglacial tills, which are commonly considered a first derivative of bedrock (Shilts, 1993). Till has a relatively straightforward transport history that reflects the ice-flow history of an area, and the sediment geochemistry thus can be used to characterize and locate buried mineralization (Levson, 2001). Historically, till geochemical surveys conducted in British Columbia also collected other sediment types, including other till facies (ablation till, colluviated till) and glaciogenic sediments (glaciomarine, glaciofluvial), and colluvium. These deposits commonly have a more complex transport history, and identifying the source of geochemical anomalies may be difficult. The most recent regional-scale till geochemical data release (Bustard et al., 2017) was compiled from 39 reports published between 1992 and 2017 by the BCGS, GSC, and Geoscience BC. The data set has geochemical data for 10,454 samples derived from analyzing the clay (<2 µm) and silt plus clay (<63 µm) size fractions by methods including: inductively coupled plasma mass spectrometry (ICP-MS) or inductively coupled plasma emission spectrometry (ICP-ES) after an aqua regia (or modified aqua regia) digestion; lithium metaborate fusion; and instrumental neutron activation (INAA).

The reconstructed till data model (Fig. 5) fits the till geochemical data model used by Bustard et al. (2017) without adding entities or modifying relationships between entities. Only a few attributes were added to the **data-sample** and **data-analyte** entities, including *azimuth*, *dip*, *size_frac* (for size fraction), which are specific for till geochemical data.

### 3.4. Data model for coal ash chemical data set

Coal ash is the inorganic residue remain after coal combusts. It is composed of oxides of the mineral content in the coal. Coal ash chemistry can have a significant influence on coke strength after reaction (CSR), an important measure of coking coal quality. Riddell and Han (2017) designed a data model and database and filled it with coal ash oxides and related analyses for 478 samples from the Gates, Gething, Minnes and Boulder Creek formations in the Peace River coalfields in northeastern British Columbia, and from the Mist Mountain Formation in the Elk River and Crowsnest coalfields of southeastern British Columbia.

As with the till geochemical data, we found that the skeleton data model suits the coal ash chemical data well (Fig. 6). Using the same entities and relationships, the skeleton model with addition of a few coal ash specific attributes represents and describes the coal ash data completely. The additional attributes, including *coal_deposit*, *seam*, and *basis*, were added to **data_sample** and **data_analyte** entities.

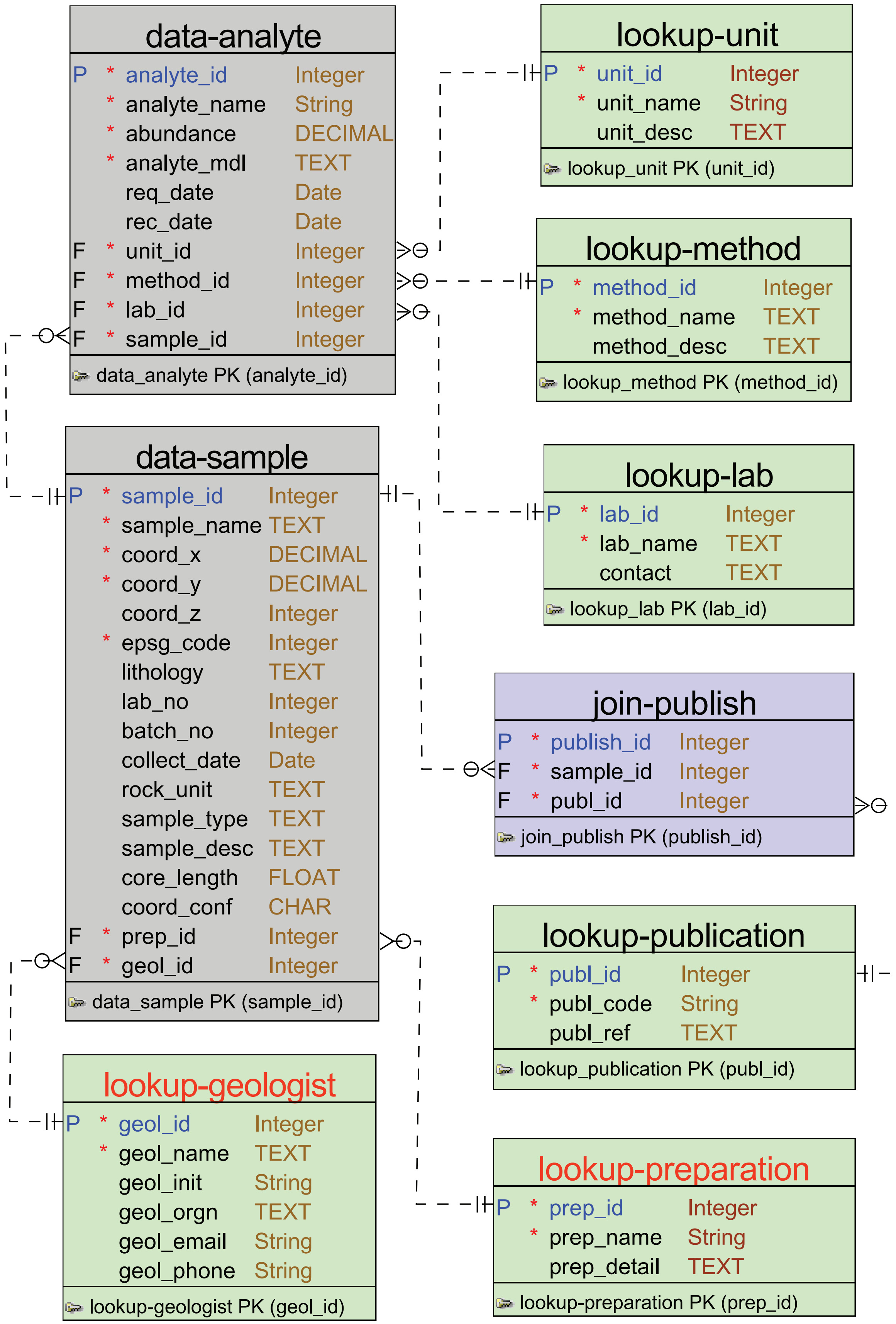


**Fig. 3.** Lithogeochemical data model reconstructed from the data model used by Han et al. (2016) by customizing the skeleton data model shown in Figure 1.

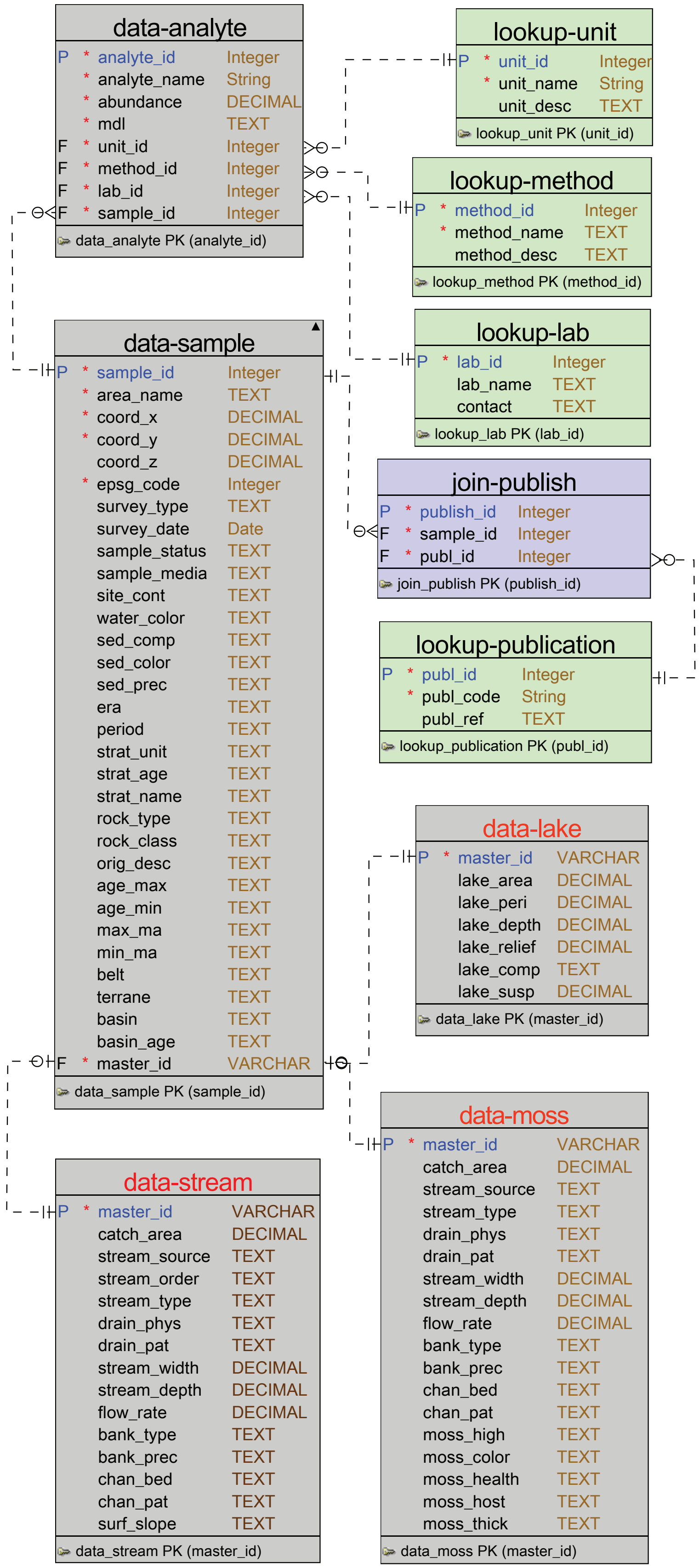


**Fig. 4.** RGS data model reconstructed from the data model used by Han and Rukhlov (2017) by customizing the skeleton data model shown in Figure 1.

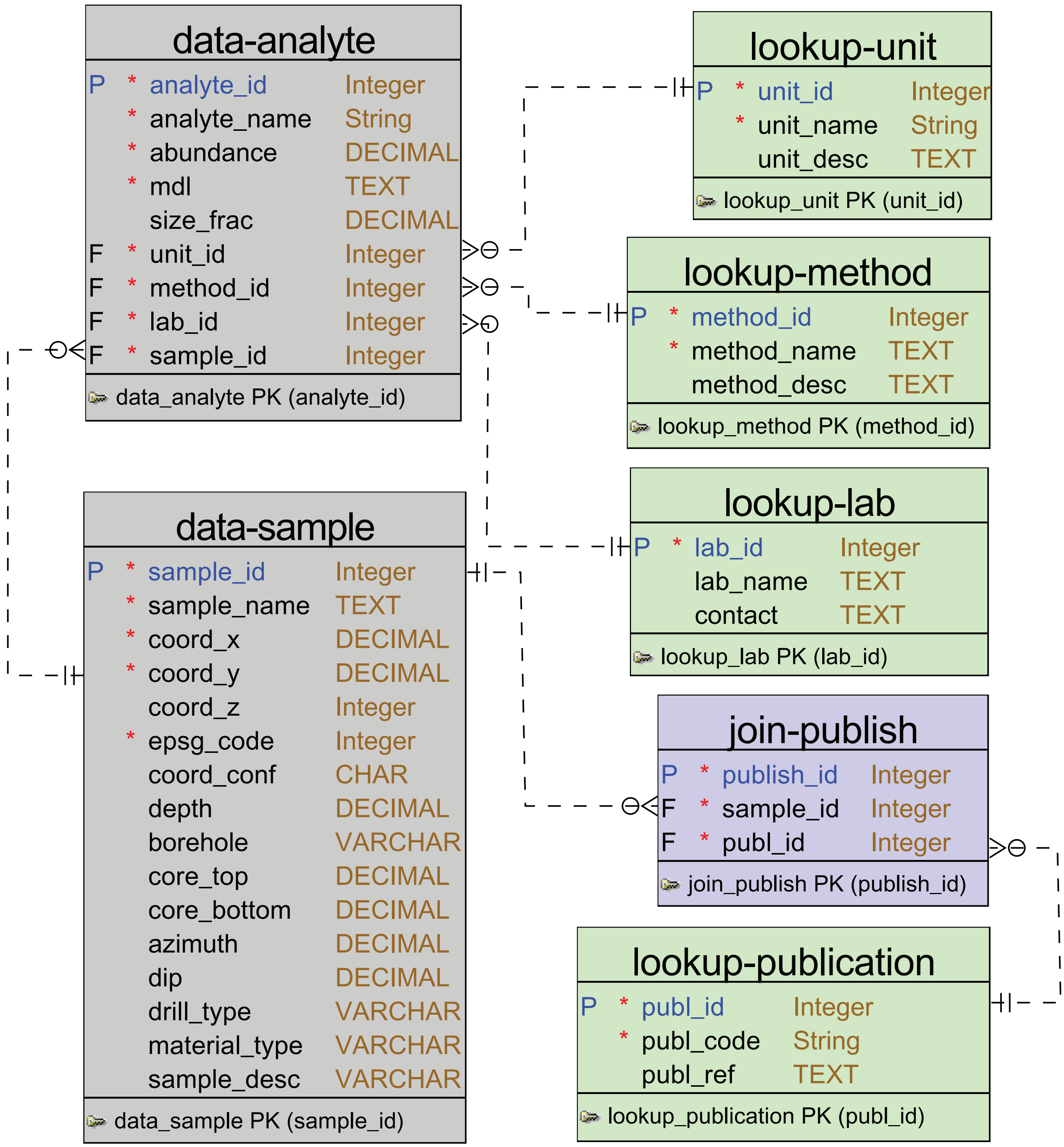


**Fig. 5.** Till geochemical data model reconstructed from the data model used by Bustard et al. (2017) by customizing the skeleton data model shown in Figure 1.

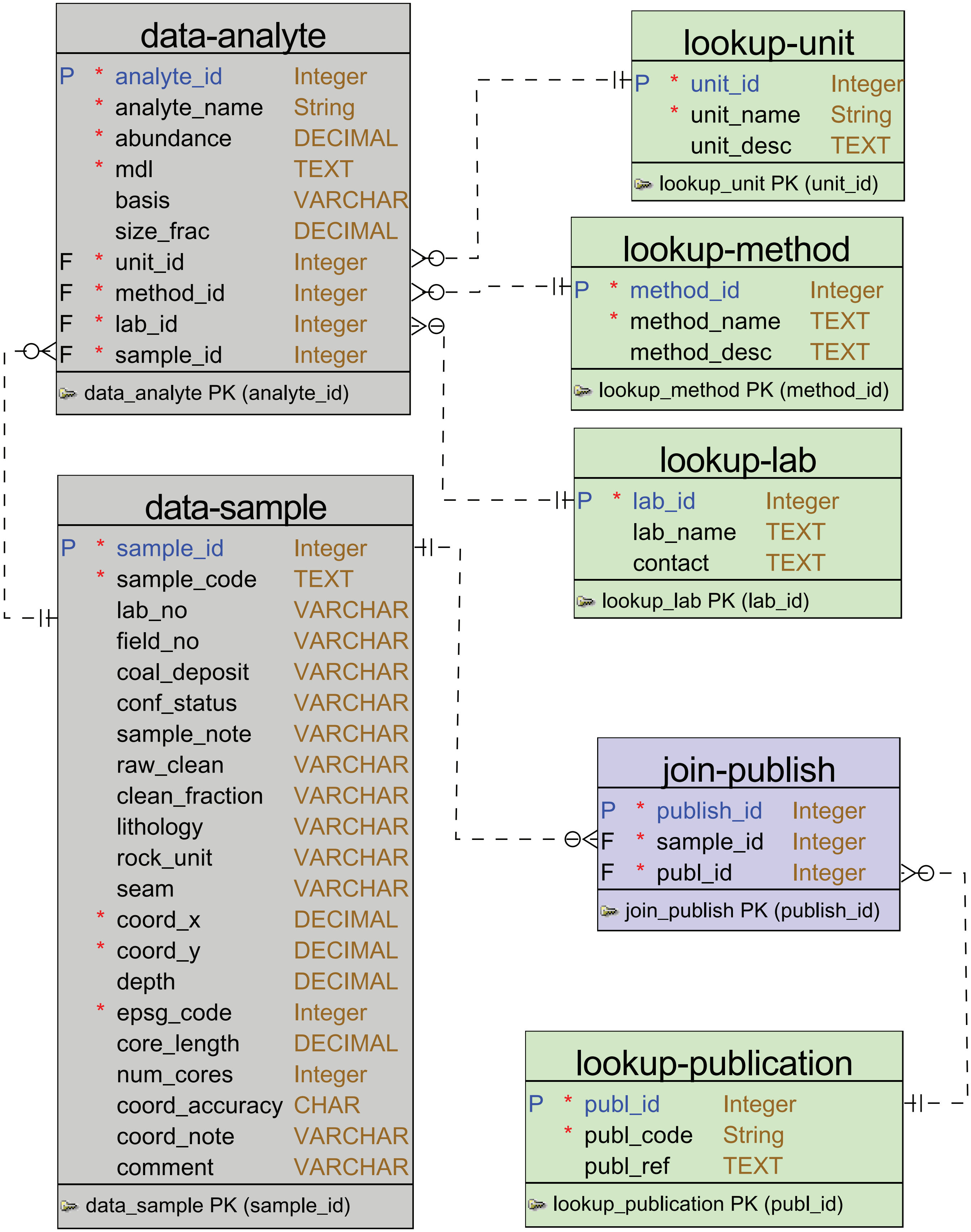


**Fig. 6.** Coal ash chemical data model reconstructed from the data model used by Riddell and Han (2017) by customizing the skeleton data model shown in Figure 1.

## 4. Development of BCGS geochemical databases

A database can be developed by implementing the corresponding data model using any database language. For the BCGS geochemical databases, we implemented the data models described above using Microsoft Access. Among the many considerations needed to develop a reliable database we paid close attention to: 1) supporting data lifecycle activities; 2) accounting for geochemical data that change with time; and 3) integrating data and metadata.

### 4.1. Supporting data lifecycle

Geoscience data, including geochemical data, live a lifecycle of six stages, from planning, acquisition, processing, analysis, storage, to publication or sharing, as defined by Faundeen et al., (2013). Except for the first two, these stages commonly occur in a database environment. This is particularly the case when geoscience data need to be long-lived, continually updated, and used by people from both within and outside an organization.

### 4.2. Accounting for geochemical data that change with time

Geochemical data sets evolve because of changes in survey techniques, improvements in data acquisition and advances in analytical instrumentation. Furthermore, previously collected and analyzed geological samples are commonly re-analyzed using different standards and techniques. For example, about 5500 of the RGS stream-sediment samples were reanalyzed using ICP-MS, with improved detection limits relative to earlier analytical methods (Jackaman, 2017). Failing to accommodate such changes in the data model could limit the usefulness of the database.

### 4.3. Integrating data and metadata

A geochemical data set typically contains two types of data: raw data (represented by **data-sample** and **data-analyte** entities in the skeleton data model); and metadata (represented by entities with names beginning with **"lookup"** for analytical method, lab, and value unit). Results from samples with, for example, high Au contents (raw data) are meaningless if the analytical method (metadata) used to determine concentrations, are unknown. To prevent separation or loss of metadata, we unite the metadata with the corresponding raw data by enforcing the foreign key constraint between the related data and metadata entities.

## 5. Operation

To operate the four province-wide BCGS geochemical databases we built four sets of applications, using the Python scripting language, to interface with the database. These applications automate routine data management tasks, including geochemical data compilation, quality control, update, and product generation. This flow of data through these programs consists of five steps (Fig. 7): 1) data compilation; 2) initial quality control and quality assurance (QA/QC); 3) data loading; 4) product generating; and 5) product QA/QC.

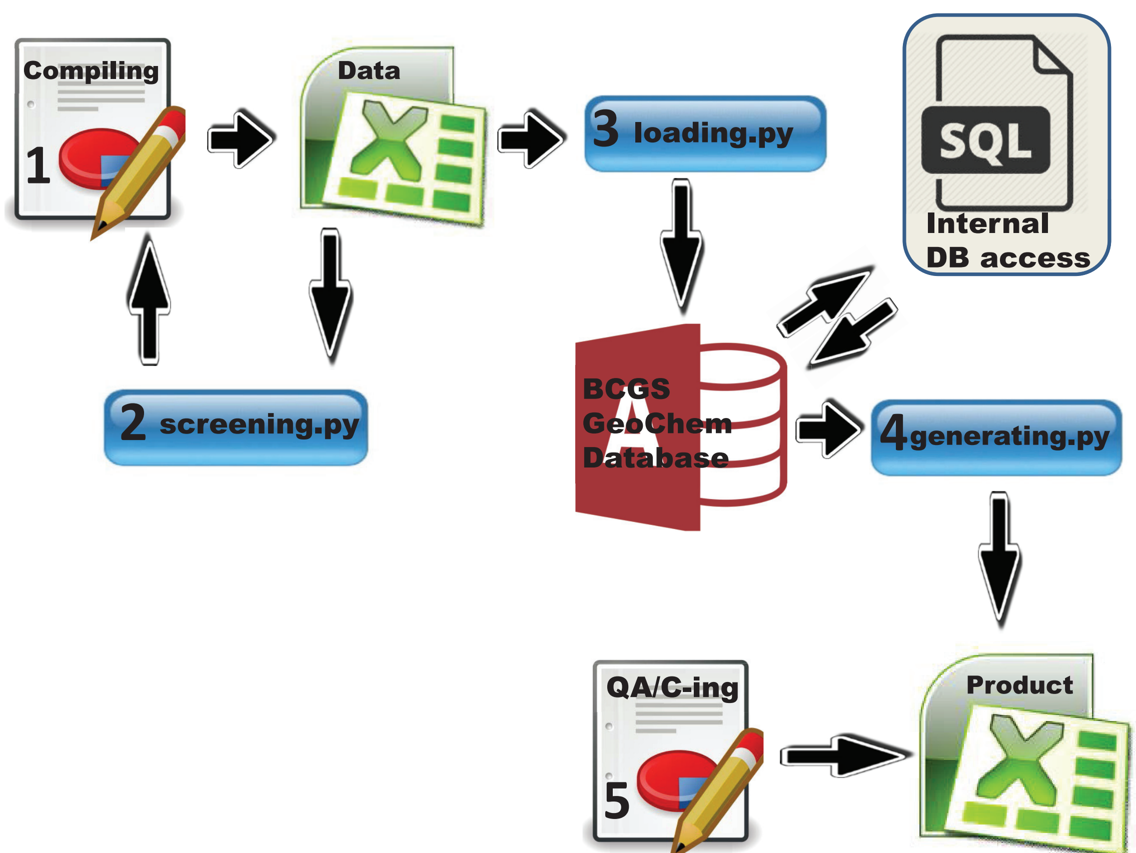


**Fig. 7.** British Columbia Geological Survey geochemical data flow.

During compilation (Step 1), data are retrieved from different sources and saved as Excel files in a predetermined format. Data QA/QC (Step 2) is then conducted using the corresponding Python script (screening.py), designed to flag common data errors either present in the source or introduced during data compilation. The errors flagged may include unrealistic determinations and units, improper methods, inconsistent handling of censored data (e.g., values below the detection limit), wrong sample locations, and redundant samples. The flagged errors are then manually examined and corrected. After this step, data are loaded into the database (Step 3). This is done automatically by executing the Python script (loading.py). Generating derived data products (Step 4) is also done using a Python script (generating.py), which retrieves and outputs data in simple formats, such as Comma Separated-Value (CSV), ESRI shapefiles, or MS Excel files. If errors are found in the generated data products, Steps 1 to 4 are repeated.

The geochemical databases discussed in this paper are not designed for direct access by data users but for data management personnel who are responsible for operating, maintaining, and updating these databases. As indicated in Figure 7, data management personnel prepare and release data products derived from these databases to users in simple tabular formats.

## 6. Conclusion

In this paper we present a simplified geochemical data model that is capable of capturing and representing generic entities, common attributes, and intrinsic relationships existing across different geochemical data sets. This skeleton data model has the potential for us to consolidate the four province-wide geochemical databases that currently operate independently into a unified one, improving the efficiency and standardization of our geochemical data management.

Data modeling is typically an incremental process. It is common to start with a simple data model that satisfies immediate needs and to later add in complexities to meet requirements that were unforeseen in the initial analysis of database requirements. The skeleton data model is not meant to be one that is all-inclusive, all-purpose. For example, because the geochemical data currently stored in the BCGS geochemical databases are only from field samples, we kept the data model simple and excluded analytical duplicates, blanks, and reference materials. But the skeleton data model is capable of expanding to include such samples. It currently includes all the basic elements found across geochemical data sets at the BCGS, and can be built on.


## Acknowledgments

We would like to express our sincere appreciation to Ray Lett, British Columbia Geological Survey Emeritus Scientist, for reviewing this paper and many discussions about the geochemical data sets involved in this paper. We thank Stephen W. Adcock, Geological Survey of Canada, for reviewing and commenting. We are grateful to Gabe Fortin, British Columbia Geological Survey for help with the writing.


## References cited


Bustard, A.L., Han, T., and Ferbey, T., 2017. Compiled till geochemical data for British Columbia. British Columbia Ministry of Energy and Mines, British Columbia Geological Survey GeoFile 2017-9, 7 p.

Connolly, T., and Begg, C., 1999. Database Sytems – A Practical Approach to Design, Implementation, and Management, 2nd Edition, Addison-Wesley, 113 p.

International Association of Oil & Gas Producers (IOGP), EPSG Geodetic Parameter Dataset, http://www.epsg-registry.org/, 2018.

Faundeen, J.L., Burley, T.E., Carlino, J.A., Govoni, D.L., Henkel, H.S., Holl, S.L., Hutchison, V.B., Martín, E., Montgomery, E.T., Ladino, C.C., Tessler, S., and Zolly, L.S., 2013. The United States Geological Survey Science Data Lifecycle Model: U.S. Geological Survey Open-File Report 2013-1265, 4 p., http://dx.doi.org/10.3133/ofr20131265.

Granitto, M., Schmidt, J.M., Labay, K.A., Shew, N.B., and Gamble, B.M., 2012. Alaska geochemical database-Mineral exploration tool for the 21st century. U.S. Geological Survey Open-File Report 2012-1060, 33 p.

Han, T., Rukhlov, A.S., Naziri, M., and Moy, A., 2016. New British Columbia lithogeochemical database: Development and preliminary data release. British Columbia Ministry of Energy and Mines, British Columbia Geological Survey GeoFile 2016-4, 6 p.

Han, T., and Rukhlov, A.S., 2017. Regional Geochemical Survey (RGS) data update and release using the newly developed RGS database. British Columbia Ministry of Energy and Mines, British Columbia Geological Survey GeoFile 2017-11, 7 p.

Jackaman, W., 2017. RGS Sample reanalysis project (parts of NTS 082G, 082J, 092N, 093E, 093H, 103O, 103P and 104N), GeoScience BC Report 2017-04.

Lett, R.E., 2005. Regional Geochemical Survey Database on CD. British Columbia Ministry of Energy and Mines, British Columbia Geological Survey GeoFile 2005-17.

Lett, R.E., 2011. Regional Geochemical Survey Database 2011. British Columbia Ministry of Energy and Mines, British Columbia Geological Survey GeoFile 2011-7.

Lett, R., and Rukhlov, A.S., 2017. A review of analytical methods for regional geochemical survey (RGS) programs in the Canadian Cordillera. In: Ferbey, T., Plouffe, A., and Hickin, A.S., (Eds.), Indicator Minerals in Till and Stream Sediments of the Canadian Cordillera. Geological Association of Canada Special Paper Volume 50, and Mineralogical Association of Canada Topics in Mineral Sciences Volume 47, pp. 53-108.

Levson, V.M., 2001. Regional till geochemical surveys in the Canadian Cordillera: sample media, methods, and anomaly evalutation. In: McClenaghan, M.B., Bobrowsky, P.T., Hall, G.E.M., and Cook, S.J. (Eds.), Drift Exploration in Glaciated Terrain, Geological Society of London, Special Publication 185, pp. 45-68.

Riddell, J., and Han, T., 2017. Ash chemistry database for British Columbia Rocky Mountain bituminous coals. Ministry of Energy and Mines, British Columbia Geological Survey GeoFile 2017-10, 15 p.

Rukhlov, A., and Naziri, M., 2015. Regional Geochemical Survey database. British Columbia Ministry of Energy and Mines, British Columbia Geological Survey GeoFile 2015-3.

Shilts, W.W., 1993. Geological Survey of Canada's contributions to understanding the composition of glacial sediments. Canadian Journal of Earth Sciences, 30, 333-353.

Watson, C., and Evans, I., 2012. Geochemistry data model summary, British Geological Survey, http://www.bgs.ac.uk/services/dataModels/geochemistry.html. Last accessed November 2016.

# Appendix: British Columbia Geological Survey publications and peer-reviewed journal papers authored by BCGS staff and released in 2018

All BCGS publications are available for download, free of charge, from https://www2.gov.bc.ca/gov/content/industry/mineral-exploration-mining/british-columbia-geological-survey/publications

To receive notification of our latest releases email Geological.Survey@gov.bc.ca


## Papers

Paper 2018-1

Geological fieldwork 2017, a summary of field activities and current research, 234 p.

Hickin, A.S., Jones, L.D., and Clarke, G., 2018. British Columbia Geological Survey annual program review 2017-2018. In: Geological Fieldwork 2017, British Columbia Ministry of Energy, Mines and Petroleum Resources, British Columbia Geological Survey Paper 2018-1, pp. 1-13.

Nelson, J., Waldron, J., van Straaten, B., Zagoresvski, A., and Rees, C., 2018. Revised stratigraphy of the Hazelton Group in the Iskut River region, northwestern British Columbia. In: Geological Fieldwork 2017, British Columbia Ministry of Energy, Mines and Petroleum Resources, British Columbia Geological Survey Paper 2018-1, pp. 15-38.

van Straaten, B.I., and Bichlmaier, S., 2018. Late Early to Middle Jurassic Hazelton Group volcanism and its tectonic setting, McBride River area, northwest British Columbia. In: Geological Fieldwork 2017, British Columbia Ministry of Energy, Mines and Petroleum Resources, British Columbia Geological Survey Paper 2018-1, pp. 39-66.

Ootes, L., Castonguay, S., Friedman, R., Devine, F., and Simmonds, R., 2018. Testing the relationship between the Llewellyn fault, Tally-Ho shear zone, and gold mineralization in northwest British Columbia. In: Geological Fieldwork 2017, British Columbia Ministry of Energy, Mines and Petroleum Resources, British Columbia Geological Survey Paper 2018-1, pp. 67-81.

Mihalynuk, M.G., Zagorevski, A., Milidragovic, D., Tsekhmistrenko, M., Friedman, R.M., Joyce, N., Camacho, A., and Golding, M., 2018. Geologic and geochronologic update of the Turtle Lake area, NTS 104M/16, northwest British Columbia. In: Geological Fieldwork 2017, British Columbia Ministry of Energy, Mines and Petroleum Resources, British Columbia Geological Survey Paper 2018-1, pp. 83-128.

Milidragovic, D., Grundy, R., and Schiarizza, P., 2018. Geology of the Decar area north of Trembleur Lake, NTS 93K/14. In: Geological Fieldwork 2017, British Columbia Ministry of Energy, Mines and Petroleum Resources, British Columbia Geological Survey Paper 2018-1, pp. 129-142.

Schiarizza, P., 2018. Geology of the Spanish Lake area, south-central British Columbia. In: Geological Fieldwork 2017, British Columbia Ministry of Energy, Mines and Petroleum Resources, British Columbia Geological Survey Paper 2018-1, pp. 143-156.

Hora, Z.D., Stein, H., Žák, K., and Dobeš, P., 2018. Eaglet property, southeastern British Columbia: Re-Os geochronology, sulphur isotopes, and thermobarometry. In: Geological Fieldwork 2017, British Columbia Ministry of Energy, Mines and Petroleum Resources, British Columbia Geological Survey Paper 2018-1, pp. 157-166.

Rukhlov, A.S., Mao, M., and Rippon, C., 2018. Rapid identification of sand-size mineral grains using portable XRF: A new method for indicator mineral surveys. In: Geological Fieldwork 2017, British Columbia Ministry of Energy, Mines and Petroleum Resources, British Columbia Geological Survey Paper 2018-1, pp. 167-182.

Cui, Y., Zhao, S., Fortin, G., Meredith-Jones, S., and Jones, L.D., 2018. Development of MapPlace 2 geospatial web service to disseminate geoscience in British Columbia. In: Geological Fieldwork 2017, British Columbia Ministry of Energy, Mines and Petroleum Resources, British Columbia Geological Survey Paper 2018-1, pp. 183-195.

Cui, Y., Hickin, A.S., Schiarizza, P., Miller, D., Nixon, G.T., Nelson, J.L., and Ferri, F., 2018. Methods to update the digital geology of British Columbia and synopses of recently integrated mapping programs. In: Geological Fieldwork 2017, British Columbia Ministry of Energy, Mines and Petroleum Resources, British Columbia Geological Survey Paper 2018-1, pp. 197-215.

Rowins, S.M., Miller, D.R., and Cui, Y., 2018. Estimating the thickness of drift using a 3D depth-to-bedrock GOCAD model in the Ootsa Lake porphyry Cu-Mo-Au district of west-central British Columbia In: Geological Fieldwork 2017, Ministry of Energy, Mines and Petroleum Resources, British Columbia Geological Survey Paper 2018-1, pp. 217-227.

## Geoscience Maps

GM 2018-1
Plouffe, A., and Ferbey, T., 2018. Surficial geology of the Highland Valley Copper mine area (parts of NTS 092I/06, 7, 10 and 11), British Columbia, 1:50,000 scale.

## Open Files

OF 2018-1
Clarke, G., Northcote, B., Katay, F., and DeGrace, J.R., 2018. Operating mines and selected exploration projects in British Columbia, 2017.

OF 2018-2
Nixon, G.T., Geology of the Tulameen Alaskan-type ultramafic-mafic intrusion, British Columbia, scale 1:20,000.

OF 2018-3
van Straaten, B.I., and S.J. Bichlmaier, S.J., 2018. Preliminary geology of the McBride River area, scale 1:50,000.

## GeoFiles

GF 2018-1
Rukhlov, A.S., Mao, M., Spence, J., Creaser, R.A., Czech, E., and Gabites, J., 2018. Mineral chemistry and isotopic systematics of carbonatites and related rocks from the Blue River area. (Poster)

GF 2018-2
Nixon, G.T., Manor, M.J., and Scoates, J.S., 2018. Cu-PGE sulphide mineralization in the Tulameen Alaskan-type intrusion: Analogue for Cu-PGE reefs in layered intrusions? (Poster)

GF 2018-3
Mihalynuk, M.G., Friedman, R.M., Joyce, N., Camacho, A., and Zagorevski, A., 2018. Geochronologic data from samples collected in the Turtle Lake area, NTS 104M/16, northwest British Columbia.

GF 2018-4
Lett, R.E., 2018. Compilation of geochemical data between Lillooet and French Bar Creek, south-central British Columbia, 42 p.

GF 2018-5
Lett, R.E., 2018. Regional moss mat-sediment geochemical survey in the Porcher Island, Grenville Channel, and Dundas Island area, central British Columbia coast, 32 p.

GF 2018-6
Rukhlov, A.S., Chudy, T.C., Arnold, H., and Miller, D., 2018. Field trip guidebook to the Upper Fir carbonatite-hosted Ta-Nb deposit, Blue River area, east-central British Columbia, 67 p.

GF 2018-7
Lett, R.E., 2018. Digital data release for a multimedia geochemical survey in the McLeod Lake map area (NTS 093J/5, 6, 12), central British Columbia, 2 p.

GF 2018-8
Ferbey, T., Plouffe, A., and Hickin, A.S., 2018. Geochemistry and mineralogy of subsurface till samples recovered from diamond drill hole R17-01, Rateria property (porphyry Cu±Mo), south-central British Columbia, 15 p.

## Information Circulars

IC 2018-1
Clarke, G., Northcote, B., Katay, F., and DeGrace, J.R., 2018. Provincial overview of exploration and mining in British Columbia, 2016. British Columbia Ministry of Energy, Mines and Petroleum Resources, British Columbia Geological Survey Information Circular 2018-1, 139 p.

Clarke, G., Northcote, B., Katay, F., and DeGrace, J.R., 2018. Exploration and mining in British Columbia, 2017: A summary. In: Provincial Overview of Exploration and Mining in British Columbia, 2017. British Columbia Ministry of Energy, Mines and Petroleum Resources, British Columbia Geological Survey, Information Circular 2018-1, pp. 1-33.

Northcote, B., 2018. Exploration and mining in the South Central Region, British Columbia. In: Provincial Overview of Exploration and Mining in British Columbia, 2017. British Columbia Ministry of Energy, Mines and Petroleum Resources, British Columbia Geological Survey, Information Circular 2018-1, pp. 85-103.

Northcote, B., 2018. Exploration and mining in the Southwest Region, British Columbia. In: Provincial Overview of Exploration and Mining in British Columbia, 2017. British Columbia Ministry of Energy, Mines and Petroleum Resources, British Columbia Geological Survey, Information Circular 2018-1, pp. 105-119.

Clarke, G., 2018. Exploration and mining in the Northwest Region, British Columbia. In: Provincial Overview of Exploration and Mining in British Columbia, 2017. British Columbia Ministry of Energy, Mines and Petroleum Resources, British Columbia Geological Survey, Information Circular 2018-1, pp. 121-139.

IC 2018-2
British Columbia Geological Survey, 2018. British Columbia coal industry overview 2017, 14 p.

IC 2018-3
Saanich Inlet, southern Vancouver Island, geology of an Aspiring Global Geopark, 8 p. (Brochure)

IC 2018-4
British Columbia bedrock geology. (Flyer)

IC 2018-5
The Golden Triangle of northwestern British Columbia, 8 p. (Brochure)

IC2018-6
The East Kootenay coalfields. (Poster)

IC2018-7
The Peace River coalfields. (Poster)

IC2018-8
British Columbia Geological Survey, 20 p. (Brochure)

IC2018-9
Online databases at the British Columbia Geological Survey, 16 p. (Brochure)

IC2018-10
Mineral Development Office, 4 p. (Brochure)

IC2018-11
Low-carbon energy technologies and metals mining in British Columbia, 8 p. (Brochure)

## Peer-reviewed journal publications

Acosta-Góngora, P., Gleeson, S.A., Samson, I.M., Corriveau, L., Ootes, L., Jackson, S.E., and Taylor, B.E., 2018, Origin of sulfur and crustal recycling of copper in polymetallic (Cu-Au-Co-Bi-U±Ag) iron-oxide-dominated systems in the Great Bear Magmatic Zone, NWT, Canada. Mineralium Deposita, 53, 353-376.

Eyster, A., Ferri, F., Schmitz, M.D., and Macdonald, F.A., 2018. One diamictite and two rifts: Stratigraphy and geochronology of the Gataga Mountain of northern British Columbia. American Journal of Science, 318, 167-207.

McMechan, M., Currie, L., Richards, B., Ferri, F., Matthews, W., and Sullivan, P., 2018. Zircon provenance of the Carboniferous Mattson delta complex, western Laurentian margin, Canada: record of a Greenland-sourced pancontinental river system. Canadian Journal of Earth Science, 55, 1129-1138.

Milidragovic, D., Zagorevski, A., Weis, D., Joyce, N., and Chapman, J.B., 2018. Picrite "intelligence" from the Middle-Late Triassic Stikine arc: Composition of mantle wedge asthenosphere. Lithos, 308-309, 446-461. https://doi.org/10.1016/j.lithos.2018.03.014.

Simandl, G.J., and Paradis, S., 2018. Carbonatites: Related ore deposits, resources, footprint, and exploration methods. Applied Earth Science, Transactions of the Institutions of Mining and Metallurgy, 127, 123-152. https://www.tandfonline.com/doi/full/10.1080/25726838.2018.1516935.

Simandl, G.J., Akam, C., Yakimoski, M., Richardson, D., Teucher, A., Cui, Y., Paradis, S., McPhail, S., and Ferri, F., 2018. Elements in oil and gas field related produced waters, British Columbia, Canada. CIM Journal, 9, 195-214. https://doi.org/10.15834/cimj.2018.19.

Simandl, G.J., Burt, R.O., Trueman, D.L., and Paradis, S., 2018. Tantalum and niobium: Deposits, resources, exploration methods, and market – primer for geoscientists. Geoscience Canada, 45, 85-96. https://doi.org/10.12789/geocanj.2018.45.135.

Verbaas, J., Thorkelson, D.J., Crowley, J., Davis, W.J., Foster, D.A., Gibson, H.D., Marshall, D., and Milidragovic, D., 2018. A sedimentary overlap assemblage links Australia to northwestern Laurentia at 1.6 Ga. Precambrian Research, 305, 19-39. https://doi.org/10.1016/j.precamres.2017.10.001.

Verbaas, J., Thorkelson, D.J., Milidragovic, D., Crowley, J.L., Foster, D., Daniel Gibson, H., and Marshall, D., 2018. Rifting of western Laurentia at 1.38 Ga: The Hart River sills of Yukon, Canada. Lithos, 316-317, 243-260. https://doi.org/10.1016/j.lithos.2018.06.018.

## Contributions to partner publications

McMechan, M.E., Ferri, F., and Matthews, W., 2018. Triassic formations in Liard Basin, northeastern British Columbia: sample descriptions, and detrital zircon U-Pb geochronology, methodology, results, and data tables. Geological Survey of Canada, Open File 8370, 14 p.

Pană, D.I., Rukhlov, A.S., Heaman, L.M., and Hamilton, M., 2018. Geochronology of selected igneous rocks in the Alberta Rocky Mountains, with an overview of the age constraints on the host formations. Alberta Energy Regulator, Alberta Geological Survey, Open File Report 2018-03, 60 p. https://www.ags.aer.ca/publications/OFR_2018_03.html.

Paradis, S., and Simandl, G.J., 2018. Are there genetic links between carbonate-hosted barite-zinc-lead sulphide deposits and magnesite mineralization in southeast British Columbia? In: Rogers, N. (Ed.), Targeted Geoscience Initiative -2017, Report of Activities, Geological Survey of Canada, Open File 8358, pp. 217-227.

British Columbia Geological Survey
Ministry of Energy, Mines and Petroleum Resources